

Universiteit
Leiden
The Netherlands

From clouds to comets: tracing the molecular journey of interstellar ices in the JWST era

Slavicinska, K.

Citation
Slavicinska, K. (2026, June 10). *From clouds to comets: tracing the molecular journey of interstellar ices in the JWST era*. Retrieved from https://hdl.handle.net/1887/4305137

Version:	Publisher's Version
License:	Licence agreement concerning inclusion of doctoral thesis in the Institutional Repository of the University of Leiden
Downloaded from:	https://hdl.handle.net/1887/4305137

Note: To cite this publication please use the final published version (if applicable).

From Clouds to Comets

Tracing the Molecular Journey of Interstellar Ices in the JWST Era

Proefschrift

ter verkrijging van
de graad van doctor aan de Universiteit Leiden,
op gezag van rector magnificus prof. dr. S. de Rijcke,
volgens besluit van het college voor promoties
te verdedigen op woensdag 10 juni 2026
klokke 11:30 uur

door

Kateřina Slavičinská
geboren te Brno, Tsjechische Republiek
in 1997

Promotores

Prof. dr. E. F. van Dishoeck
Prof. dr. H. V. J. Linnartz†

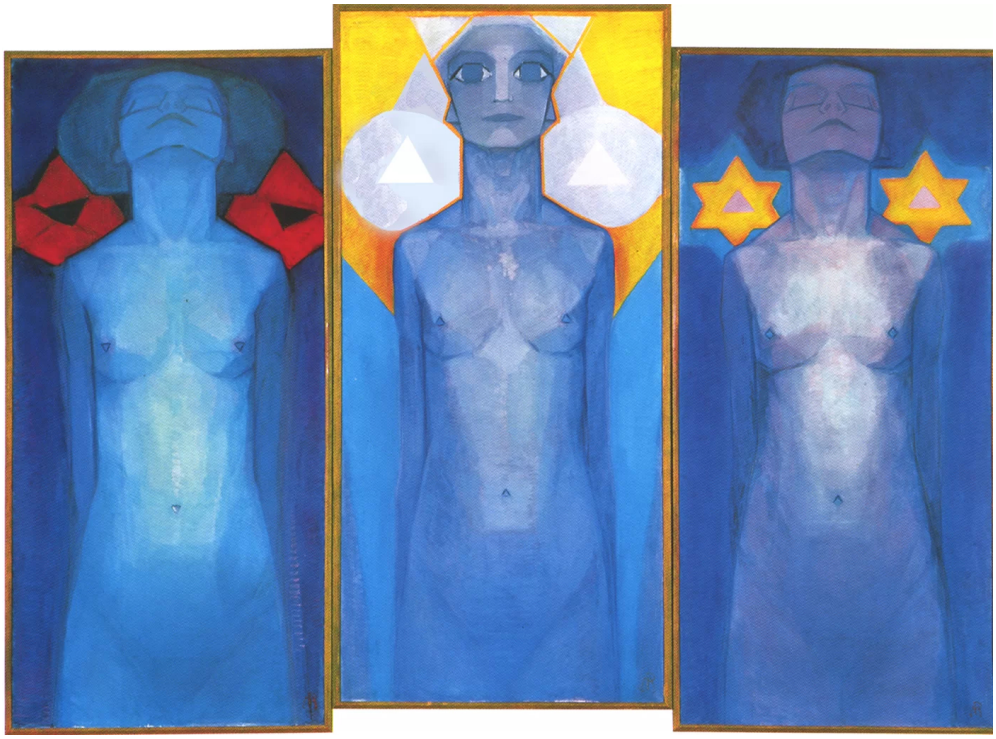
Co-promotor

Dr. K. -J. Chuang

Promotiecommissie

Prof. dr. I. A. G. Snellen	
Prof. dr. S. Viti	
Prof. dr. P. Ehrenfreund	
Dr. M. E. Palumbo	INAF - Osservatorio Astrofisico di Catania
Dr. P. Gerakines	NASA Goddard Space Flight Center

Copyright © *2026 Katerina Slavicinska*.
Cover art: *Surfaces and Depths (bottom half).* Illustrated by Katie Slavicinska in Adobe Photoshop. Inspired by the collaborative artworks of Stephen Muldoon and Robert Wyland. See Brian Ferrari's thesis for top half.



Evolution
Piet Mondrian, 1911

Contents

1 Introduction **1**
- 1.1 Seeds of life in surprising places . . . 1
- 1.2 Ice chemistry during star and planet formation . . . 3
  - 1.2.1 Molecular clouds . . . 3
  - 1.2.2 Protostars and protoplanetary disks . . . 8
  - 1.2.3 Planetary bodies . . . 11
- 1.3 Infrared spectroscopy of ices . . . 12
  - 1.3.1 Observational methods . . . 14
  - 1.3.2 Laboratory methods . . . 20
- 1.4 Thesis overview . . . 25
  - 1.4.1 Aims . . . 25
  - 1.4.2 Chapter summary . . . 26
  - 1.4.3 Scientific significance and future directions . . . 27
- 1.B Bibliography . . . 29

2 JWST detections of amorphous and crystalline HDO ice toward massive protostars **33**
- 2.1 Introduction . . . 34
- 2.2 Methods . . . 37
  - 2.2.1 Investigated sources . . . 37
  - 2.2.2 Observations and data reduction . . . 40
  - 2.2.3 Gas emission subtraction . . . 40
  - 2.2.4 Laboratory data collection . . . 40
- 2.3 Results . . . 41
  - 2.3.1 CH_3OH ice . . . 42
  - 2.3.2 4 μm region: CH_3OH, S-bearing species, and HDO . . . 44
  - 2.3.3 HDO ice . . . 46
  - 2.3.4 H_2O ice . . . 48
- 2.4 Discussion . . . 50
  - 2.4.1 Inferred ice HDO/H_2O ratios . . . 50
  - 2.4.2 Comparing ice and gas HDO/H_2O ratios . . . 51
  - 2.4.3 Ice envelope evolution . . . 53
- 2.5 Conclusions . . . 55
- 2.6 Acknowledgements . . . 55
- 2.A Appendix . . . 56
  - 2.A.1 Laboratory data . . . 56
  - 2.A.2 χ^2 plots . . . 64
  - 2.A.3 Estimated continuum errors . . . 64
  - 2.A.4 Literature HDO/H_2O values . . . 68
- 2.B Bibliography . . . 69

3 HDO ice detected toward an isolated low-mass protostar with JWST 73
3.1 Introduction . . . 74
3.2 Methods . . . 76
3.2.1 Observations . . . 76
3.2.2 Ice fitting . . . 78
3.3 Results and discussion . . . 80
3.3.1 HDO ice . . . 80
3.3.2 H_2O ice . . . 81
3.3.3 HDO/H_2O ratio . . . 83
3.4 Conclusions . . . 85
3.5 Acknowedgments . . . 86
3.A Appendix . . . 87
3.A.1 Observations . . . 87
3.A.2 Continuum, silicate, and CH_3OH ice fitting . . . 87
3.A.3 Comparing NIRSpec and MIRI bands of the same ice species . . . 92
3.A.4 Ice fitting uncertainties . . . 94
3.A.5 Comparison with AKARI results . . . 97
3.A.6 Literature HDO/H_2O values . . . 99
3.B Bibliography . . . 101

4 Ammonium hydrosulfide (NH_4SH) as a potentially significant sulfur sink in interstellar ices 103
4.1 Introduction . . . 104
4.2 Methodology . . . 107
4.2.1 Experimental . . . 107
4.2.2 Observational . . . 111
4.3 Spectroscopic characterization . . . 113
4.3.1 NH_3:H_2S . . . 113
4.3.2 H_2O:NH_3:H_2S . . . 117
4.4 Comparing NH_4SH:H_2O laboratory spectra to observations . . . 124
4.4.1 NH_4^+ ν_4 mode . . . 124
4.4.2 Redshift of the 6.85 μm feature . . . 128
4.4.3 SH^- stretching mode . . . 131
4.4.4 NH_4^+ ν_4 and SH^- libration combination mode . . . 133
4.4.5 Other anions (OCN^-, CN^-, $HCOO^-$, Cl^-) . . . 134
4.5 Astronomical implications . . . 135
4.5.1 Sulfur budgets . . . 135
4.5.2 NH_4SH ice desorption front . . . 136
4.6 Conclusions . . . 137
4.7 Acknowledgements . . . 138
4.A Appendix . . . 138
4.A.1 Calibration procedure supplementary information . . . 138
4.A.2 Beer's law plot errors . . . 139
4.A.3 Pure NH_4SH supplementary laboratory data . . . 139
4.A.4 NH_4SH:H_2O supplementary laboratory data . . . 144
4.A.5 Observational supplementary data . . . 154

4.B Bibliography . . . 158

5 Laboratory infrared spectra and band strengths of carbonyl sulfide (OCS) in CH_3OH- and CO-rich ice mixtures for analyzing interstellar ice observations 161
5.1 Introduction . . . 162
5.2 Methods . . . 164
5.2.1 Experimental setup . . . 164
5.2.2 Mixing ratio calibration . . . 165
5.2.3 Apparent band strengths . . . 166
5.3 Results . . . 167
5.3.1 Pure OCS ice . . . 167
5.3.2 OCS ice mixtures . . . 169
5.4 Astronomical implications . . . 175
5.5 Conclusions . . . 177
5.6 Acknowledgements . . . 178
5.A Supplemental Information . . . 178
5.A.1 OCS ν_3 peak positions, FWHMs, and relative integrated absorbances 178
5.B Bibliography . . . 184

6 The hunt for formamide in interstellar ices 185
6.1 Introduction . . . 186
6.2 Formamide formation mechanism debate . . . 189
6.3 Methodology . . . 191
6.4 Results . . . 193
6.4.1 C=O stretching and NH_2 scissoring features ($\sim$1700 and 1630 cm^{-1}) 197
6.4.2 CH bending and CN stretching features ($\sim$1388 and 1328 cm^{-1}) . . . 199
6.5 Astronomical implications . . . 201
6.6 Conclusions . . . 208
6.7 Acknowledgements . . . 209
6.A Appendix . . . 209
6.A.1 Peak positions and FWHMs of formamide in pure and mixed ices . . . 209
6.A.2 Relative apparent band strengths of formamide in pure and mixed ices 214
6.A.3 QMS calibration of an independent tri-dosing leak valve system and mixing ratio determination . . . 216
6.B Bibliography . . . 221

English summary 225

Nederlandse samenvatting 233

České shrnutí 243

Publications 251

Curriculum vitae 257

Acknowledgments 259

1 Introduction

1.1 Seeds of life in surprising places

Deep in some of the most remote parts of Earth's oceans along the boundaries of Earth's tectonic plates, hot plumes of liquids and gases bubble through towering mineral chimneys that grow from the bottom of the seafloor. Such *hydrothermal vents* arise when seawater leaks through seafloor cracks and is heated in Earth's mantle, producing fluids rich in reduced gases and dissolved crustal minerals. When these hot fluids are re-expelled into the ocean and meet the near-freezing seawater, the dissolved minerals within them precipitate, resulting in forests of vent chimneys similar in appearance to cave stalagmites (Fig. 1.1).

Given their complete lack of sunlight and the noxious nature of many vent fluid constituents (e.g., H_2S), one may expect hydrothermal vents to be rather desolate in terms of life. Yet despite their seemingly hostile conditions, hydrothermal vents are home to an eclectic collection of benthic creatures: long red tube worms, massive clams, "yeti" crabs with furry claws, eyeless shrimp, pale white octopuses. What's more, these bizarre ecosystems function largely independently of the light-powered world above, fueled primarily by local *chemosynthetic* bacteria and archaea, which harness chemical energy by oxidizing reduced compounds like H_2S to build organic molecules. And while such lifeforms may seem quite alien to us H_2S-averse land-dwellers, there are numerous indications that the last universal common ancestor, from which all currently known life on Earth evolved, was a similar chemosynthetic organism that lived in hot hydrothermal conditions (Pace 1991; Di Giulio 2003; Weiss et al. 2016; Moody et al. 2024). Some origins of life scientists even argue that the abundance of reduced species and catalytic minerals in hydrothermal vents make them prime candidate environments for the origin of life on Earth (Corliss et al. 1981; Russell et al. 1988; Russell & Martin 2004; Martin et al. 2008).

The hydrothermal origin hypothesis is one that remains hotly contested and debated. However, most origins of life researchers and astrobiologists can come to a consensus on one thing: wherever life first formed, there was water. It is the primary molecular constituent of all known life forms; no other molecule comes close to its ability to serve as the ubiquitous solvent of biochemical reactions (Frenkel-Pinter et al. 2021). For this reason, astrobiologists have adopted the motto "follow the water" – initially coined by Mars mission scientists (Hubbard et al. 2002) – to guide the search for extraterrestrial life in the solar system and beyond.

This thesis co-opts this guiding principle, but not in search for extraterrestrial life – rather, in search for the origins of life's most fundamental molecular ingredients. It follows the water



Figure 1.1: Earthly and heavenly pillars of creation. Left: carbonate chimneys in the the Lost City Hydrothermal Field, suggested to be chemically analogous to ancient hydrothermal vents where life may have first formed (Martin et al. 2008). Image credit: D. Kelley/M. Elend/UW/URI-IAO/NOAA/The Lost City Science Team. Right: columnar clouds of interstellar gas and dust in the Serpens star-forming region, as observed by the MIRI instrument onboard the *James Webb* Space Telescope. In the deepest parts of these cloud pillars, copious water and reduced molecules are produced in ice layers on the surfaces of dust grains. Image credit: J. DePasquale/A. Pagan/NASA/ESA/CSA/STScI.

backwards through time in the star and planet formation sequence all the way to its birthplace, another remarkably dark and seemingly desolate place: dense interstellar dust clouds (Fig. 1.1).

The dust in these clouds was expelled into the depths of the interstellar medium by dying stars undergoing mass loss, quite like how organic waste from light-powered ocean life rains down on and fertilizes the ocean's benthic zones. In fact, one could consider this expelled stardust, made of silicates and refractory carbonaceous matter, an effective fertilizer of interstellar chemistry. By blocking radiation and providing catalytic mineral surfaces, this dust creates ideal conditions for forming a plethora of volatile biogenic molecules in ice layers that grow on top of the dust grains.

The most abundant of these molecules is water, which is produced particularly efficiently under these dark and dusty conditions. However, various other species can also be found in these ices, with many of them in reduced form due to the high abundance of hydrogen atoms (e.g., CH_3OH and NH_3), and some of them are quite toxic (e.g., H_2CO and H_2S). Eventually, if the dust cloud gravitationally collapses, causing a star to begin forming at its center, these volatile-enriched dust grains feed the growing star and its surrounding protoplanetary disk, where its planets form. In this way, the ices grown within interstellar dust clouds become one of the primary ingredients of planetary systems and serve as a key source of biogenic volatiles during planet formation.

The work presented in this thesis investigates 1) the chemistry that occurs in interstellar

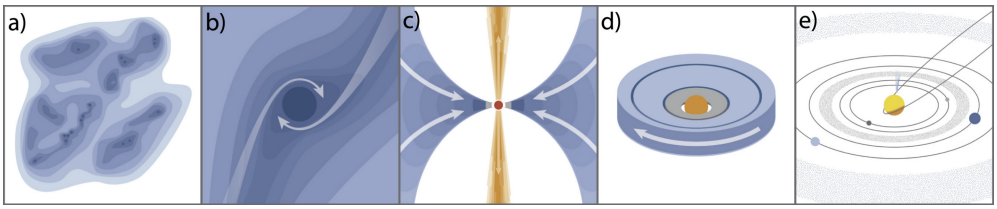


Figure 1.2: Schematic of the star and planetary system formation stages. a) Clouds of dust, ice, and gas with varying densities coalesce in the interstellar medium. b) Gravitational collapse within the densest regions of the clouds triggers star formation. c) A protostar forms and accretes material from its surrounding envelope of cloud material. To conserve angular momentum, the accreted envelope material flattens into a disk shape, and outflows of accreted material are ejected from the source poles. d) The surrounding envelope eventually completely dissipates via accretion or outflows. A protoplanetary disk of accreted material, in which planetesimals form, remains. e) The remaining disk material is either accreted or dissipated, leaving behind a star and its orbiting planetary bodies. Figure from Öberg & Bergin (2021).

ices during these earliest stages of star and planet formation, and 2) how that chemistry sets the stage for the formation of solar systems like our own and the distributions of volatiles within them. To do so, it employs infrared (IR) spectroscopy in a combined experimental and observational approach, where data collected in Earth-based laboratories that simulate interstellar conditions are used to analyze interstellar spectra observed by powerful IR facilities like the *James Webb* Space Telescope (JWST) and its predecessors. The presented studies largely target molecules that have been detected in volatile-rich and primitive small solar system bodies – particularly comets – to assess the chemical link between the interstellar medium and planetary systems. This chapter introduces the reader to the key physical and chemical processes that fundamentally govern interstellar ice chemistry throughout star and planet formation, the techniques used to illuminate these processes, some of the knowledge gaps in the preceding literature, and an overview of how the subsequent chapters of this thesis address them.

1.2 Ice chemistry during star and planet formation

1.2.1 Molecular clouds

The interstellar medium (ISM) – the parts of the universe between stars and their planetary systems – is not just empty space, although its most diffuse regions come very close to it. Here, atomic densities are on the order of $n{\sim}10^2$ cm^{-3}, mainly consisting of hydrogen and some helium atoms formed via fusion shortly after the Big Bang. Additionally, outflows from exploding dying stars supply interstellar space with heavier elements like carbon, nitrogen, oxygen, and sulfur that formed during stellar nucleosynthesis, as well as highly refractory molecules like silicates and polycyclic aromatic hydrocarbons (PAHs) that formed in dense stellar atmospheres and outflows during the end stages of stars' life cycles. Few other molecules can exist in these harsh regions because of extremely high UV and cosmic ray fluxes generated by surrounding stars and supernovae, which destroy all but the strongest chemical bonds.

Some of the refractory materials are expelled from the dying stars in the form of dust

grains with sizes on the order of nm to μm. These grains serve as catalysts, energy sinks, and radiation shields, and they ultimately enable vast networks of chemical reactions to develop in these hostile environments. One of the most important molecules to form on dust grains in the diffuse ISM is H_2 (Hollenbach & Salpeter 1971; Vidali 2013; Wakelam et al. 2017), which would be immediately dissociated by the excess energy released during its formation if formed in the gas phase because H_2 has no allowed rotational or vibrational transitions by which it could release its excess energy of formation. On a grain surface, however, the grain can absorb this energy excess.

The formation of H_2 on grain surfaces kickstarts a gas-phase chemical network by which other molecules (*e.g.*, CO, CH, and CN) form, largely through ion-molecule reactions (Smith 1992). Formation of these molecules competes with their photodissociation via external interstellar radiation. As gravitational instabilities cause the interstellar cloud to grow denser, the external radiation is increasingly shielded from the cloud's interior. The dust within the cloud also scatters light preferentially at shorter wavelengths, leading to the extinction and reddening of incident light. Furthermore, line emission by molecules with dipoles like CO and thermal emission by the dust grains radiatively cools the cloud (Klessen & Glover 2015), increasing the sticking probabilities of atoms and molecules on the dust grain surfaces.

Eventually, temperatures become low enough for the ices studied in this thesis to begin growing on the dust grain surfaces ($\lesssim$20-30 K). These ices form via addition reactions between adsorbed atoms and molecules (Tielens & Hagen 1982). Hydrogen atoms are light and volatile enough to diffuse along the surfaces and hydrogenate larger adsorbed atoms like oxygen, carbon, and nitrogen, leading to the production of reduced species such as H_2O, CH_4, and NH_3 in the form of ices on the grains. The hydrogenation of oxygen into water is particularly efficient; up to $\sim$20% of volatile oxygen atoms within molecular clouds end up locked up in water ice (van Dishoeck et al. 2021). Furthermore, gaseous species can collide with the grains and react with adsorbed atoms and radicals – for example, gaseous CO can react with surface hydroxyl radicals via the HOCO pathway to form CO_2 ice (Oba et al. 2010) and hydrogen atoms to form H_2CO and CH_3OH ice (Hiraoka et al. 1994; Watanabe & Kouchi 2002).

Water ice is observed early at cloud densities on the order of $n\sim10^3$ ($A_v\sim1.5$) (Boogert et al. 2013; Whittet et al. 2013); it is by far the most abundant ice produced at this stage, so this first layer of ices is often referred to as the *polar* ice layer. Other reduced species that form during this stage include CH_4 (Öberg et al. 2008; Qasim et al. 2020) and NH_3 (Hiraoka et al. 1995; Bottinelli et al. 2010). A significant fraction of the NH_3 formed at this stage is converted into NH_4^+ salts via solid-state acid-base reactions, as evidenced by the early appearance of an absorption feature at 6.85 μm (Boogert et al. 2013). The chemical identities of the acids that react with NH_3 to form NH_4^+ salts in the early cloud stage remains a topic of debate; Chapter 4 of this thesis presents an overview of this debate and argues that H_2S is likely the acid responsible for the majority of interstellar NH_4^+ salt formation. Additionally, OH radicals formed on the grains react with CO to produce CO_2 (Whittet et al. 2007; Oba et al. 2010), the second-most abundant observable ice species formed at this stage. Some OH radicals may also react with CH_4 to produce CH_3OH, but in limited quantities compared to later stages (Qasim et al. 2018).

Around $A_v\gtrsim$2-3, CO self-shielding of interstellar radiation becomes extremely efficient, leading to a dramatic increase in gas-phase CO production that further enhances self-shielding in a snowball effect (van Dishoeck & Black 1988; van Dishoeck 1992). Subsequently, as densities continue to increase ($n\gtrsim10^4$, $A_v\gtrsim$3-4), temperatures further drop ($\leq$20 K), enabling the

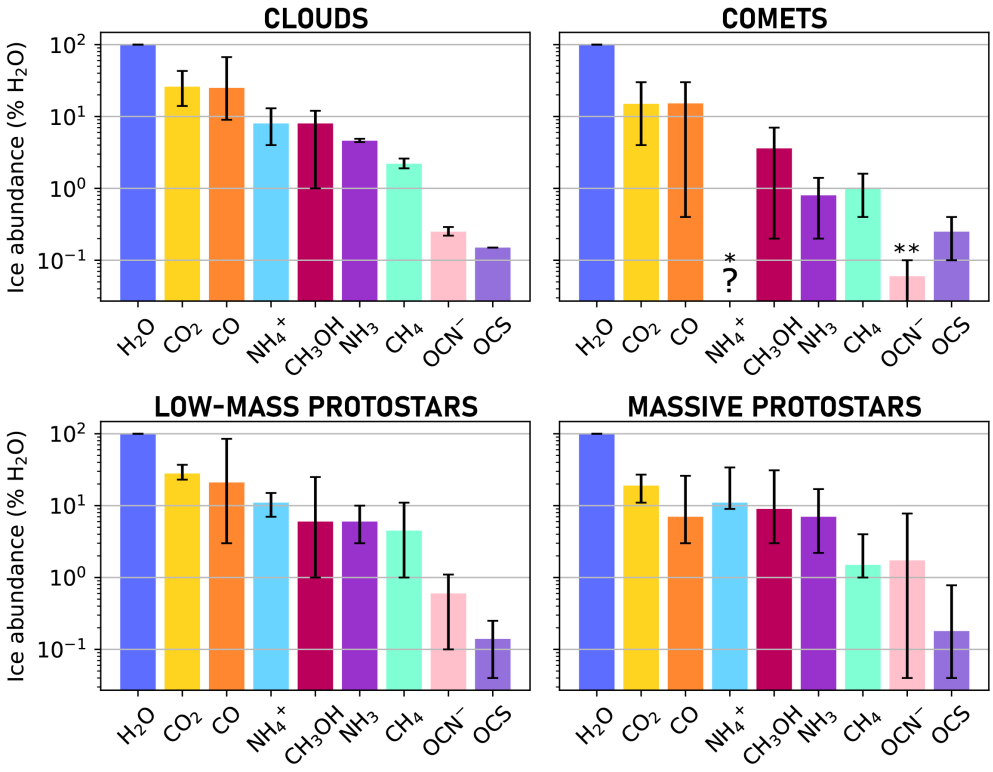


Figure 1.3: Relative ice abundances (with respect to H_2O ice) measured in various stages of star formation and in comets. Cloud values for CO_2, CO, NH_4^+, and CH_3OH are from Boogert et al. (2015); NH_3, CH_4, OCN^-, and OCS values are from McClure et al. (2023). Low-mass protostellar values for all species except OCS are from Boogert et al. (2015); OCS is from in prep work by the author of this thesis. Massive protostellar values for CO_2, CO, NH_4^+, and CH_3OH are from Boogert et al. (2015); NH_3 and CH_4 values are from Gibb et al. (2004); OCN^-, and OCS values are from Boogert et al. (2022). Cometary values for all species except CO_2 are from Mumma & Charnley (2011); CO_2 values are from Ootsubo et al. (2012). *NH_4^+ abundances with respect to water in cometary comae are not known, but presence of NH_4^+ salts in comets has been confirmed with both IR spectroscopy (Poch et al. 2020) and mass spectrometry (Altwegg et al. 2022). **Assumes all HNCO detected in cometary comae is a product of desorbed OCN^- salts.

freeze-out of some of the CO gas on the dust grains. Thus, an *apolar* ice layer begins to grow, dominated by CO, CO_2 produced via CO oxygenation, and likely other more volatile apolar species like N_2 and O_2, although their presence in ices cannot be observationally confirmed due to their IR inactivity (see Section 1.3).

Densities $n \gtrsim 10^5$ ($A_v \gtrsim 9$) mark the beginning of the *catastrophic CO freeze-out* stage, in which conditions are so cold and dense that the vast majority of the cloud CO is frozen out on the grains (Pontoppidan 2006). At these high densities, the hydrogenation of CO ice proceeds rapidly, producing the majority of the CH_3OH ice observed in molecular clouds. For this reason the ice layers grown at these high cloud densities are often referred to as the *CH_3OH-rich*

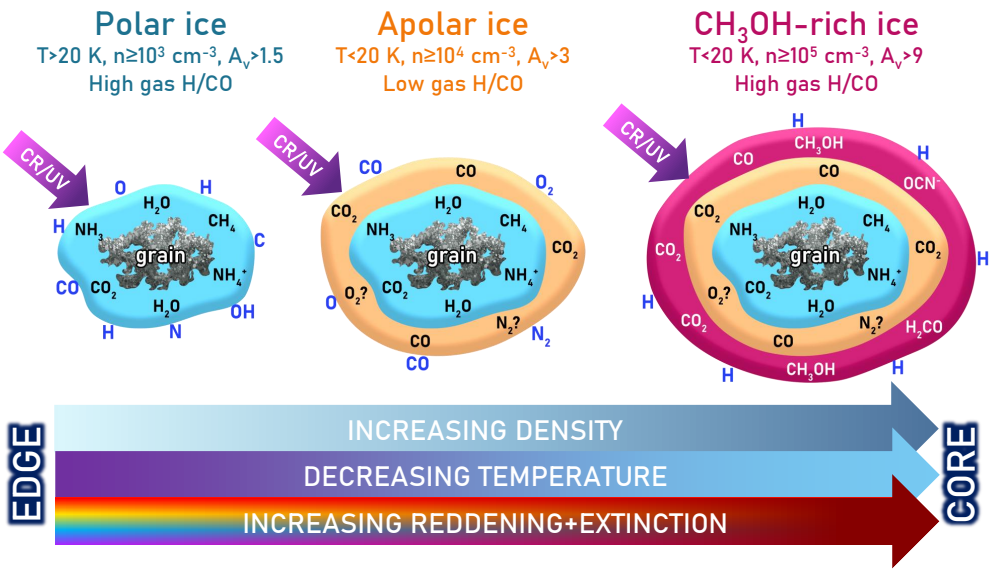


Figure 1.4: Different stages of ice growth in molecular clouds. In the first ice layers grown in the less dense translucent regions closer to the cloud edges, H_2O, CO_2, and hydrogenated species like NH_3 and CH_4 form. As densities increase, temperatures drop, enabling the growth of an apolar layer dominated by CO and CO_2. In the densest regions, CO is efficiently hydrogenated to form CH_3OH, resulting in a CH_3OH-rich layer that includes other species formed from CO like CO_2, OCS, and OCN^-.

layers. In this stage, CO also reacts with S- and N-species to respectively form OCS (Palumbo et al. 1997; Santos et al. 2024) and HNCO (Fedoseev et al. 2015), the latter of which is mostly consumed in acid-base reactions to form OCN^- (Novozamsky et al. 2001; van Broekhuizen et al. 2004). Laboratory experiments show that a myriad of other more complex and potentially prebiotically relevant organic molecules such as glycolaldehyde, methyl formate, glycerol, and propanol can form via CO hydrogenation as well (Chuang et al. 2016; Fedoseev et al. 2017; Qasim et al. 2019), although expected relative abundances of these species in the ices are low and, even when present, their weak IR signatures can be challenging to disentangle (*e.g.*, Chen et al. 2024).

This model of multiple chemically distinct ice growth stages shown in Fig. 1.4 is observationally supported in multiple ways. First, in clouds where multiple lines of sight with different densities can be probed, the lines of sight in denser regions show larger fractions of apolar species like CO and CO_2 in the total ice column density (Fig. 1.5). Furthermore, differences in x-intercepts when plotting various ice column densities in molecular clouds versus A_v (where the x-intercept of a given species indicates the minimum cloud density required for growth of that species in ices to begin) support a formation sequence where species like H_2O and CO_2 form first, followed by CO freeze-out and then CH_3OH formation at the highest A_v (see Fig. 7 in Boogert et al. 2008). Additionally, ice band profiles are sensitive to chemical environments (see Section 1.3.1), and the ice bands observed toward molecular clouds are consistent with multiple chemically distinct ice phases. However, the triphasic model described here is still only a simplified approximation of the complex chemical stratification expected

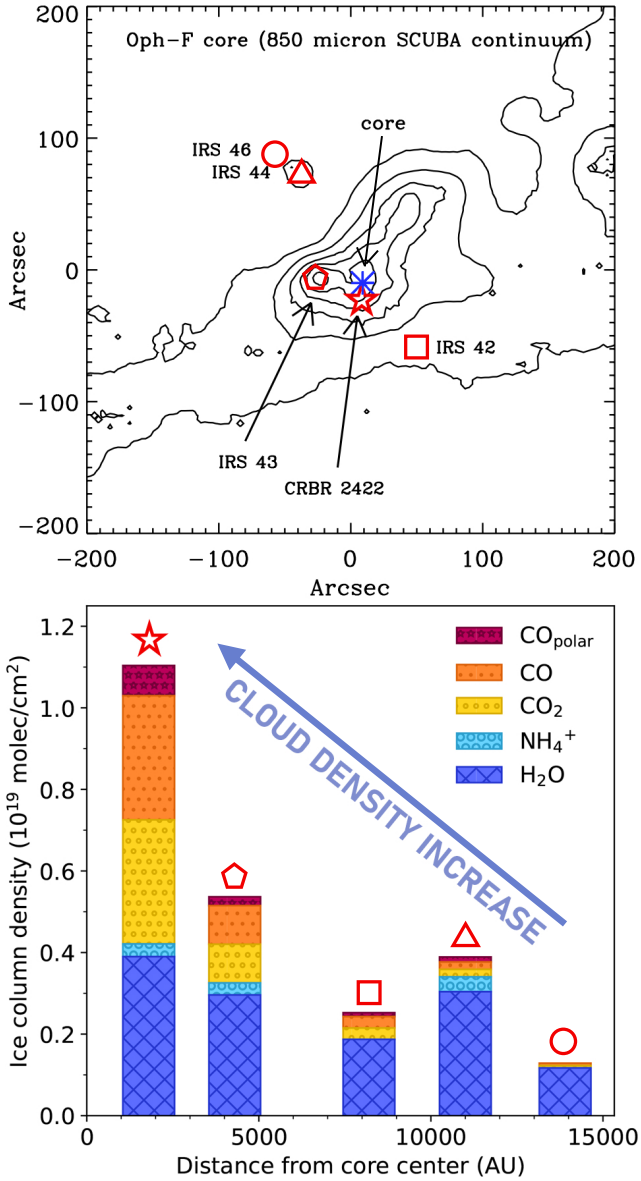


Figure 1.5: Spatial changes in ice column densities observed around the Oph-F cloud core. Top: 850 μm dust emission map of the Oph-F core. Blue star: core center; red shapes: 5 surrounding IR sources. Bottom: ice column densities observed toward the 5 IR sources in the Oph-F core. Lines of sight toward the outer, less dense core regions are dominated by water ice. Closer to the core center, the relative and absolute contributions of apolar species CO and CO_2 to the total ice column density increase. A significant column density of CO in a polar matrix (likely dominated by CH_3OH) is observed toward the source closest to the dense core.

within interstellar ices, and the transitions between the different ice phases are expected to be gradual rather than discrete as shown in Fig. 1.4.

Finally, it is important to note that the ice chemistry discussed thus far – the chemistry thought to be responsible for the formation of the cloud ice species presented in Fig. 1.3 – is primarily thought to be *non-energetic*, consisting of atom addition or acid-base reactions that do not require external energy input to proceed under interstellar conditions (Cuppen et al. 2024). However, it has long been proposed that *energetic processes* contribute to molecular cloud ice chemistry as well (Arumainayagam et al. 2019). Although dense molecular clouds are shielded from the external interstellar UV radiation field as discussed above, cosmic rays (high-energy ions and nuclei) are still able to penetrate the clouds and interact with the ice and gas within them. These cosmic rays can also generate a *secondary UV field* within the cloud by exciting local gas-phase H_2, which emit Lyman and Werner photons in the VUV range (6.9-13.6 eV) upon relaxation to ground state (Prasad & Tarafdar 1983). The UV flux expected from this process ($\sim 10^4$ photons cm^{-2} s^{-1}, Shen et al. 2004) is much lower than that of the interstellar UV field ($\sim 10^8$ photons cm^{-2} s^{-1}, Draine 1978), but it is nonetheless expected to trigger some photochemistry in the cloud ices.

Over the past few decades, plenty of laboratory experiments have shown that the sky is the limit when it comes to the molecules that can form via such energetic ice chemistry. Simulated cosmic ray or UV irradiation of interstellar ice analogs composed of the simple molecules in Fig. 1.3 can produce a myriad of more chemically complex and prebiotically relevant molecules, including heavy hitters like formamide, amino acids, and nucleobases (Munoz Caro et al. 2002; Bernstein et al. 2002; Kaňuchová et al. 2016; Öberg 2016; Oba et al. 2019; Chuang et al. 2022). However, no species of an indisputable energetic origin (*i.e.*, species that cannot form via non-energetic chemistry) have been detected in molecular cloud ices thus far (Boogert et al. 2015).

1.2.2 Protostars and protoplanetary disks

If a molecular cloud is sufficiently massive and dense, gravitational instabilities and turbulence can trigger the cloud's gravitational collapse, initiating the formation of a protostellar core. The nascent protostar then follows an evolutionary sequence that ultimately ends in the formation of a fully-fledged, hydrogen-fusing star in hydrostatic equilibrium.

In the case of low-mass stars (<8 M$_\odot$), the most common stars in our galaxy and the hosts of most known planetary systems, this evolutionary sequence lasts $\sim 10^6$-10^7 yr and can be roughly divided into four stages that are often conflated with spectroscopically defined *Classes* (Robitaille et al. 2006; Dunham et al. 2014). During the earliest stages following cloud collapse, an envelope of molecular cloud material as well as streamers from nearby clouds (Pineda et al. 2020; Valdivia-Mena et al. 2024) feed the core source. Gravitational potential energy is converted into thermal energy as the material collapses, heating the surrounding envelope in a thermal gradient that extends radially from the source. As temperatures rise, the dust within the heated parts of the envelope begins to thermally emit radiation that peaks in the far-IR and submillimeter ranges. Blackbody radiation from the central source itself is absorbed, re-radiated, scattered, and reddened by the surrounding envelope dust, extending the source spectral energy distribution (SED) into the IR range (Class 0). At this stage, the source is considered *deeply embedded* because most of its mass resides in its surrounding envelope rather than in the protostellar core source.

As the protostar continues to accrete surrounding envelope material, conservation of angular momentum results in outflows of accreted material from the source poles as well as the flattening of the inner portion of the envelope into a *protoplanetary disk*. Matter within the disk starts to coagulate into larger bodies, forming disk rings, gaps, and cavities, marking the beginnings of planetary formation (Segura-Cox et al. 2020). The envelope and disk continue to warm through source blackbody emission, and the SED profile of the source shifts to shorter wavelengths as envelope matter thins and the source grows hotter and more massive (Class I). Eventually the envelope material is completely depleted via outflows and accretion, leaving only the disk and a central pre-main sequence star that is hot and massive enough to be observable in the near-IR and visible ranges (Class II). Finally, the disk material is also depleted via disk winds and accretion by the source or disk planetesimals (Class III).

In the case of massive stars (>8 $M_\odot$), evolutionary stages during their formation are more difficult to define because they are more rare than low-mass stars in our galaxy, and their formation timescales are shorter ($\sim 10^5$ yr). Furthermore, massive protostars typically form in clusters where individual sources can be difficult to resolve. Nevertheless, their formation sequence also involves the gravitational collapse of a cloud, heating of the surrounding envelope material within which they are embedded, and formation of a disk (Beuther et al. 2007, 2025).

During the protostellar and protoplanetary disk stages, ices formed during the molecular cloud stage are inherited by the protostellar envelope and disk, where they can transform through various physical processes (Fig. 1.6). One of the processes most central to this transformation is the desorption of ice species into the gas phase, which is governed by molecular *snowlines*: the thermal boundaries that define the regions where envelope or disk temperatures become warm enough to sublimate specific ice species. Snowlines are not only important to accurately model the solid-state and gas-phase chemistry that occurs in envelopes and disks – they also govern the chemical composition of the planetesimals that form in the disk (see Section 1.2.3).

In younger and colder protostellar envelopes as well as the coldest, outermost regions of more evolved protostellar envelopes and the cold midplanes of protoplanetary disks, the molecular cloud ices can remain largely intact. As the ices move into warmer regions, they cross molecular snowlines in order of decreasing volatility, effectively *distilling* the ice layers as various ice species sublimate. Hypervolatile species like CO have snowlines around T$\sim$20 K and are the first to sublimate from the ices, water ice has a snowline around $T \sim 100$ K, and the snowlines of most of the other species shown in Fig. 1.3 are somewhere in-between. However, some species may still remain in ices past their snowlines if they are sufficiently *entrapped* within a matrix of ices with higher desorption temperatures. For example, some protostars with warmed envelopes and protoplanetary disks show CO profiles that are characteristic of CO trapped in ice matrices of less volatile species (like CO_2, CH_3OH, and H_2O, Pontoppidan et al. 2008; Cuppen et al. 2011; Bergner et al. 2024). For this reason, the water snowline is often considered the most important when modeling or analyzing gas-grain chemistry in protostellar envelopes and protoplanetary disks – given water's high abundance in ices, many ice species (especially less abundant ones like complex organics) are expected to be entrapped within a water-dominated matrix and thus co-desorb with water ice (Collings et al. 2004; Busch et al. 2022).

Before inducing desorption, warmer temperatures also increase the mobility of species within the ices, leading to ice restructuring. This restructuring explains the presence of pure CO_2 and CH_3OH ice features toward warmer sources: these species gradually *segregate* from

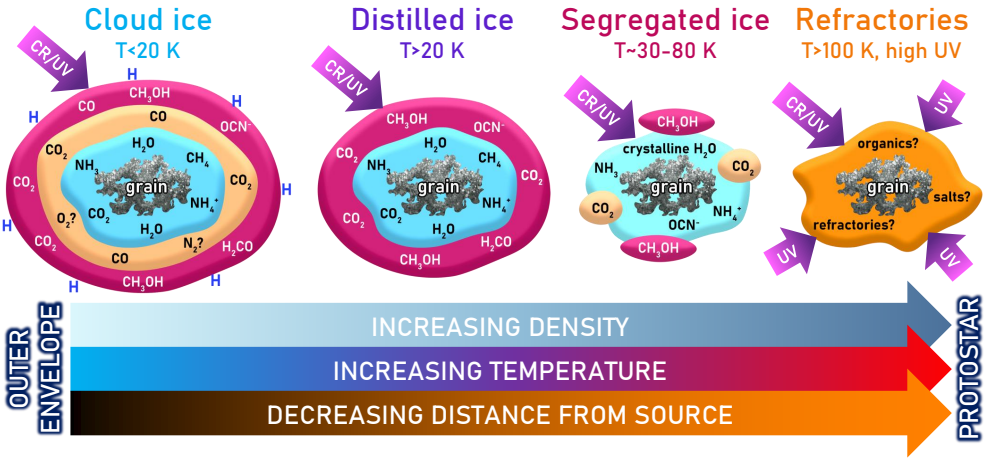


Figure 1.6: Changes in ice chemistry during thermal (and possibly energetic) processing in protostellar envelopes and protoplanetary disks. In the coldest envelope and disk regions, ice structures mimic those seen toward molecular clouds (see Fig. 1.4). As the ices move into warmer regions, hypervolatile species like CO desorb into the gas phase, distilling the ice. Even warmer temperatures drive the segregation of certain species (most notably CO_2) within the ice matrix and crystallization of the amorphous ices. Past 100 K, most of the volatile ices are expected to have desorbed into the gas, leaving behind on the grain more refractory species like salts and larger complex organics that may form via energetic processing.

other matrix constituents upon heating (*e.g.*, Ehrenfreund et al. 1998; Brunken et al. 2024b). Crystallization of amorphous ices is another form of ice restructuring that is observed toward warm sources, particularly in the case of water (*e.g.*, Dartois & d'Hendecourt 2001). Additionally, increased mobility can allow more species to overcome diffusion barriers and in turn increase rates of reactions that involve heavier species, such as recombination of radicals formed during ice energetic processing (Garrod & Herbst 2006) or acid-base reactions (van Broekhuizen et al. 2004). Although directly distinguishing ice species formed via thermally-driven diffusion is observationally challenging, chemical models often require diffusion to reproduce gas-phase abundances measured in the hot inner regions of protostellar envelopes, indirectly supporting their importance (*e.g.*, Garrod et al. 2008).

As is the case for molecular clouds, it is suspected energetic processing plays a role in the ice chemistry in protostellar envelopes and protoplanetary disks, both via the cosmic ray-induced secondary UV field and potentially the protostellar radiation field within certain envelope or disk regions. Although the latter internal UV field is expected to be very weak in the high-density envelope and disk midplane where most ices reside, ices that end up in less dense envelope regions close to the source or outflow cavity walls may experience UV fields with fluxes up to several orders of magnitude greater than the cosmic-ray generated field (Drozdovskaya et al. 2014). It has been suggested that a broad absorption feature in the 6-8 μm region isolated via empirical decompositions of protostellar spectra could be due to refractory organics produced by such UV irradiation of simpler ices, although purely thermal chemistry cannot be ruled out (Boogert et al. 2008). Such organics could potentially be refractory enough to survive past the water snowline and eventually serve to deliver volatile

elements into the inner solar system (see Section 1.2.3).

Finally, the journey of ice species within protostellar envelopes and protoplanetary disks is not expected to be linear in the sense of moving only in the direction of colder to warmer, ice phase to gas phase. Some degree of thermal cycling within the envelope is expected due to events like accretion bursts (see Chapter 2). Furthermore, accreted disk material can be transported from hotter to colder disk regions via outward radial or inward vertical diffusion and viscous spreading, especially in early stages when disk pressures are high and grain sizes are small (*e.g.*, Stevenson & Lunine 1988; Yang et al. 2013; Williams et al. 2025). Thus, interstellar volatiles can cycle multiple times between the ice and gas phase throughout the evolution of a protostellar system.

1.2.3 Planetary bodies

The disk snowlines discussed in Section 1.2.2 are a key factor that partially dictates the compositions of planetary objects based on their formation locations within the disk. Namely, a given species can be accreted by planetesimals that form outside of the snowline of that species, so the starting material that forms a planetary body will depend on where that body lies in the protoplanetary disk in relation to molecular snowlines. This initial chemical record is subsequently altered as snowlines change due to gradual dissipation of the protoplanetary disk and as planetary bodies undergo scattering and collision events due to dynamic interactions with other bodies. Geologic, atmospheric, or space-weathering processes on the planetary bodies further alter the chemical record once the protoplanetary disk has fully dissipated.

In our solar system, small airless bodies that formed in the outermost reaches of the solar system are thought to contain some of the most pristine records of inherited volatiles from interstellar ices because their small sizes preclude significant geologic or atmospheric processing, and their formation locations in the outer solar system allowed them to retain considerable amounts of volatiles after their formation. Comets are a prime example, and the outgassing of volatiles in their comae allow for direct comparisons between their volatile inventories and those of interstellar ices and protostellar gases, which have revealed some striking similarities (Öberg et al. 2011; Drozdovskaya et al. 2019, see also Chapter 4). However, systematic differences between cometary and interstellar volatile abundances as well as the presence of crystalline silicates in cometary dust (Zolensky et al. 2006) also point toward cometary material undergoing at least some degree of chemical processing within the protoplanetary disk.

The isotopic ratio of deuterium to hydrogen (D/H) in water is particularly sensitive to physicochemical conditions. Thus, this ratio has been used to evaluate the extent to which protostellar water is processed in the disk before it is accreted by comets (Persson et al. 2014; Cleeves et al. 2014). Interpretations of these comparisons are complicated by the large scatter in water D/H observed in both cometary and protostellar values (*e.g.*, Paganini et al. 2017; Jensen et al. 2019), as well as potential fractionation effects during cometary ice sublimation (Mandt et al. 2024). Furthermore, protostellar gas water D/H values have often been used as a proxy for ice D/H values because HDO ice could not be robustly detected toward protostars prior to JWST, but gas-phase reprocessing may cause differences in ice and gas D/H values. Chapters 2 & 3 of this thesis present the first reliable detections of protostellar HDO ice and calculations of protostellar water ice D/H values, marking an important advance in our ability to characterize how water chemically evolved during its journey from the interstellar medium to outer solar system bodies. The measured ice values in these chapters show agreement with

the highest protostellar envelope and protoplanetary disk water gas D/H values on the order of $\sim$ a couple 10^{-3}. These values are elevated by factors of $\sim$2-10 with respect to cometary water D/H values that are typically on the order of 10^{-4}, which could indicate either some level of chemical reprocessing of interstellar water ice within our past protoplanetary disk or a diversity in interstellar water ice D/H values that reflect differences in prestellar temperatures, densities, or timescales (see Chapters 2 & 3 for further discussion).

Isotopic ratios have also been used to argue an interstellar origin for some of the organic molecules found on carbonaceous chondrite meteorites, which originate from carbonaceous asteroids. Today these bodies are primarily found in the asteroid belt between Mars and Jupiter, but they may have been dynamically scattered there from a location further out (perhaps as far as where Saturn formed, Alexander 2017). Their high carbon abundances and signatures of past water presence indicate they inherited significant quantities of volatiles from the protoplanetary disk, although these volatiles were likely less chemically pristine than those inherited by comets given the more inward formation locations. Accretion of the radiogenic isotope ^{26}Al by these bodies also caused secondary parent body processes like aqueous alteration and thermal metamorphism that further changed their chemical inventories. Nevertheless, the high D/H ratios of organics present on carbonaceous chondrites point to possible origins within ices either in the interstellar medium or in the outermost regions of the protoplanetary disk. Specifically, energetic processing of simpler organic ices in these regions has been suggested as a possible pathway to produce the highly refractory and chemically complex insoluble organic matter found in carbonaceous chondrites (Alexander et al. 2007).

1.3 Infrared spectroscopy of ices

Molecular spectroscopy is the study of how molecules interact with light. These interactions are governed by the laws of quantum mechanics, whereby molecules can absorb or emit photons by transitioning between their quantized electronic, vibrational, or rotational energy states. Transitions from lower to higher energy states result in photon absorption, whereas transitions from higher to lower energy states result in photon emission. The energy difference between the molecular energy levels involved in a transition defines the energy (*i.e.*, wavelength) of the emitted or absorbed photon (Fig. 1.7). Electronic transitions typically correspond to the energy of UV to visible photons, vibrational transitions to infrared (IR) photons, and rotational transitions to microwave and radio photons.

Molecules in space can be identified and quantified by their unique emission or absorption features in telescopic spectra. The vast majority of interstellar molecules have been observed in the gas phase via emission lines at millimeter or centimeter wavelengths – *i.e.*, rotational spectroscopy (McGuire 2022). This spectral range is particularly useful for interstellar observations in part because little thermal energy is required to populate excited rotational levels due to their small energy gaps, so molecular emission lines can often be detected even in very cold environments (*e.g.*, Kaifu et al. 2004). However, in the case of ices, confinement within a solid matrix restricts their rotational motion, making them unobservable with rotational spectroscopy. Instead, the ice chemistry described in Section 1.2 has been uncovered entirely using IR wavelengths – *i.e.*, vibrational spectroscopy.

The vibrational transitions of a molecule are associated with *vibrational modes*, which

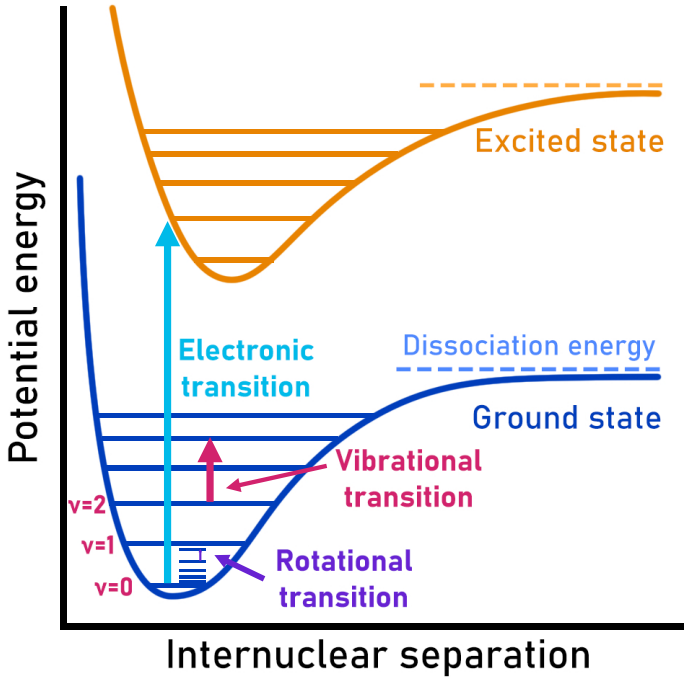


Figure 1.7: Electronic, vibrational, and rotational transitions shown in a molecular potential energy well diagram. The energy gap between the two levels involved dictate the wavelength of light that is emitted or absorbed during a transition.

correspond to specific motions of the molecule's atoms relative to each other. Every molecule has a certain number of *fundamental modes* that arise from transitions between a ground vibrational state v=0 and the first excited state v=1. Examples of fundamental modes include stretching, bending, or twisting motions as shown in Fig. 1.8. Transitions between ground states and excited states $v \geq 2$ are called *overtones*, and *combination modes* arise when a single photon induces two transitions simultaneously. Additionally, collective vibrations of molecules bound together in a solid or liquid result in *librations* and *lattice modes*. Fundamental modes typically produce the strongest observed features, whereas overtones, combination modes, and lattice modes are weaker and thus more difficult to observe unless the carrier molecule is very abundant.

Not all vibrational modes can be observed. As dictated by spectroscopic selection rules, only the vibrational modes in which the molecule's dipole moment changes as a result of the vibration will result in the absorption of an IR photon. These modes are referred to as *IR active*. Modes that result in no net dipole moment change, *IR inactive* modes, will therefore not appear in IR spectra. For some molecules, this means that only some of their vibrational modes can be observed; others, like homonuclear diatomics, have no IR active vibrational modes and thus cannot be observed in the IR (unless they are bound within a matrix that induces a weak dipole between the two atoms). As a result, the presence of molecules like N_2 and O_2 in interstellar ices cannot be spectroscopically confirmed nor well-constrained,

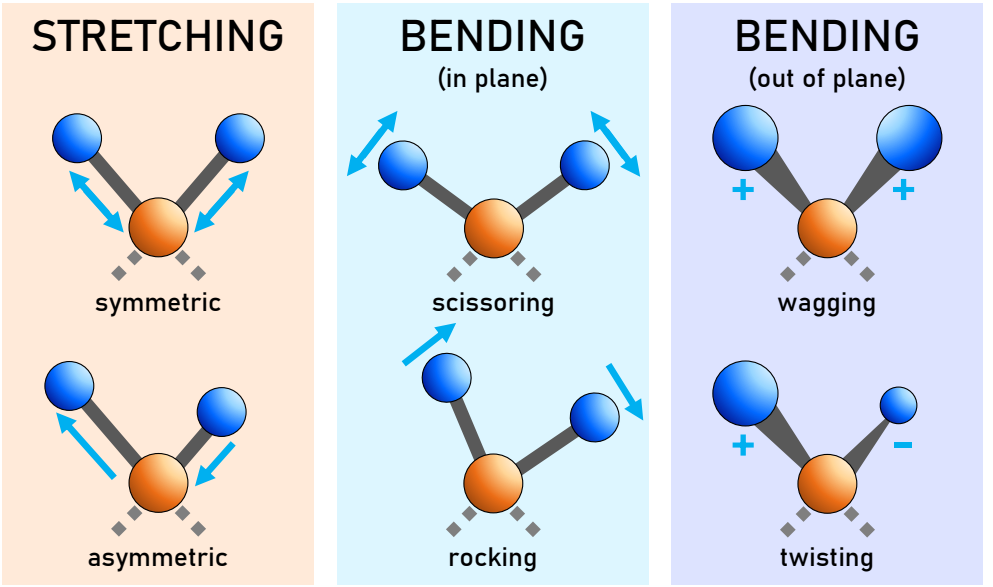


Figure 1.8: Six examples of fundamental molecular vibrational modes.

although it is strongly suspected (Ehrenfreund & van Dishoeck 1998; van Dishoeck et al. 2025).

The specific peak positions, profiles, and intensities of IR vibrational modes observed toward interstellar regions contain a wealth of information about the chemical identities, quantities, and even the physical and chemical environments of the molecules present in the ices. Extracting this information requires an integrated approach in which observations are compared to models that employ laboratory data. The following sections explain how both observational and laboratory data of such ices are acquired and analyzed.

1.3.1 Observational methods

Fig. 1.9 provides a schematic of the observing geometry used to acquire interstellar ice spectra. The telescope is aimed toward an IR light source, which can be either an extincted background star located behind the interstellar cloud of interest, or it can be a protostar that is embedded within the cloud. Molecular absorptions or emissions from species located along the line of sight from the light source to the telescope are then observed against the (proto)stellar continuum. In the case of background stars behind molecular clouds, cold ice bands are observed in addition to lines from gaseous species within the background star's photosphere (*e.g.*, McClure et al. 2023). In the case of protostars, the line of sight typically follows a thermal gradient where temperature decreases with distance from the protostar. Thus, species detected toward protostars can include pristine ices in the colder outer regions of the envelope, thermally-processed ices in the warmer inner regions of the envelope, and gas-phase molecules in the hot core region closest to the source (*e.g.*, van Dishoeck et al. 2025). Additionally, the line of sight in ground-based data includes absorptions from IR-active species

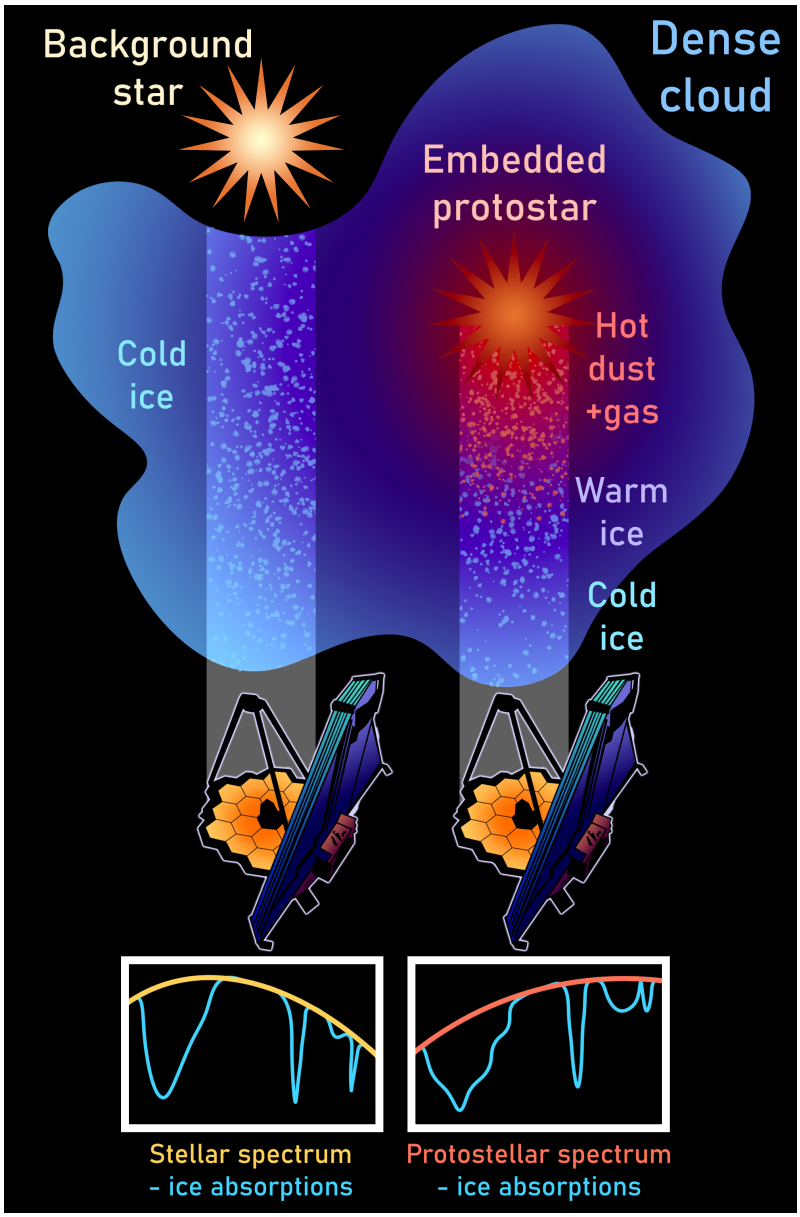


Figure 1.9: A schematic of how telescopes observe absorption features of interstellar ices in dense clouds and protostellar envelopes. The ices are observed along a pencil beam that traces the path from an IR light source (either an extincted background star or a protostar) to the telescope.

in Earth's atmosphere like CO_2 and H_2O; space-based telescopes eliminate this contaminant from the line of sight and are thus considered optimal for observing interstellar ices, although ground-based data remains valuable for analyzing interstellar ice features in spectral windows

free of atmospheric contaminants and can often offer higher spectral resolution than space-based telescopes in these windows (*e.g.*, Pontoppidan et al. 2003; Boogert et al. 2022).

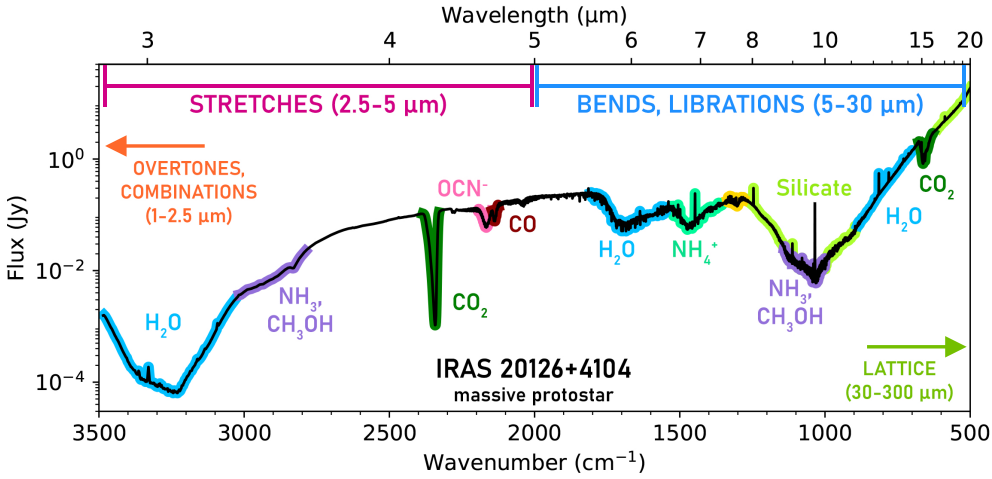


Figure 1.10: Example IR spectrum of a massive protostar (IRAS 20126+4104) showing interstellar ice and dust absorption features upon the protostellar continuum.

An example mid-IR (2.5-30 μm) spectrum of interstellar ices observed toward a protostar is presented in Fig. 5. This spectral window is dominated by fundamentals, specifically stretching modes from 3-6 μm and bending and libration modes from 6-30 μm. The near-IR region (1-2.5 μm) is dominated by weak combination and overtone features. The far-IR region (30-300 μm) is dominated by lattice modes. Almost all ice IR features are observed in absorption because the thermal energy required to significantly populate excited vibrational states of ices typically exceeds ice binding energies and would lead to ice desorption, with the exception of a few low-energy lattice modes in the far-IR that are occasionally observed in emission (*e.g.*, Omont et al. 1990).

A specific molecule can be identified or "assigned" in an interstellar IR spectrum if its characteristic IR features, defined via controlled laboratory experiments or theoretical quantum calculations, are observed. Sometimes, assignments to specific molecules are not trivial because molecules that share chemical functional groups (*i.e.*, bond structures) often have similar or overlapping IR signatures. In the case of such a degeneracy, the presence or absence of other characteristic features of the assigned molecule (or its isotopolog) can corroborate or refute the assignment. Assignments can also be ascertained by comparing how closely observed parameters like peak position and full width half maximum match those in laboratory data. Attempts have been made to establish a classification scheme that characterizes the reliability of ice feature assignments using terms like *secure*, *likely*, or *tentative* based on a set of criteria (Boogert et al. 2015), but use of these criteria is not standardized across the current literature (*e.g.*, Öberg et al. 2011; Rocha et al. 2024).

Once assigned, an IR peak can be used to quantify the *column density* of a molecule along the line of sight. Column density N is defined as the density of molecules n integrated along a given path ℓ, in this case the line of sight:

$$N = \int n \, d\ell \tag{1.1}$$

To obtain N of a given species from an observed IR feature, a portion of the observed spectrum that contains the feature must first be converted from the flux scale to the optical depth τ scale via the equation:

$$\tau = -ln(I/I_o) \tag{1.2}$$

where I is the observed flux, and I_o is the modeled (proto)stellar continuum flux without ice absorptions. I_o can be modeled using template stellar spectra, extincted blackbody curves, or polynomial fits to manually-defined continuum points. N can then be calculated via:

$$N = \frac{\int_{\nu_1}^{\nu_2} \tau_\nu \, d\nu}{A} \tag{1.3}$$

where the numerator of the fraction represents the integrated optical depth of the IR feature over a defined frequency range $\nu_1 - \nu_2$ expressed in wavenumbers (cm^{-1}) and A is the experimentally-determined *band strength* of the feature (discussed further in Section 1.3.2).

In addition, observed IR feature profiles can be used to infer the physical and chemical properties of their ice carriers. This is because intermolecular interactions (*e.g.*, hydrogen bonds, van der Waals forces) with surrounding matrix species can affect a molecule's electron density and geometry (*i.e.*, bond lengths and angles), altering its vibrational energy levels and, in turn, the peak properties of its IR features – most notably position and width. Fig. 1.11 presents two examples of how IR profiles of ices change with physical and chemical environments in the case of H_2O (left) and CO_2 (right) ices, respectively.

The top left panel presents the 3 μm O-H stretching mode in three pure H_2O laboratory ices with different morphologies: porous amorphous, compact amorphous, and crystalline. The feature appears significantly broader in the amorphous samples than in the crystalline sample. The narrowing of ice IR features upon transitions from amorphous to crystalline morphologies is observed in many species because crystalline structures have less disorder and thus less possible configurations of molecules within the matrix – more possible configurations result in a larger distribution of possible electron densities, bond distances, and angles, leading to peak broadening in amorphous ices (Mastrapa et al. 2009). In the case of the 3 μm H_2O band, the crystalline peak position is also significantly redshifted from the amorphous peak positions. Such band profile differences can be exploited when analyzing observations to determine whether the ice along the line of sight is amorphous or crystalline (*e.g.*, Smith et al. 1989). For example, the bottom left panel shows the 5 μm continuum flux map of an intermediate-mass protostar, HOPS 370, from the NIRSpec instrument aboard JWST (see Section 1.3.1). Two spectra (middle left panel) are extracted from the datacube: one using an aperture centered on a shocked knot (Tyagi et al. 2025) in the inner regions of the envelope close to the protostar, and one using an aperture centered on an outer part of the envelope illuminated by scattered light in the outflow cavity. The 3 μm water feature in the spectrum extracted closer to the protostar shows a greater relative contribution of crystalline water ice and a lesser relative contribution of amorphous water ice, demonstrating how thermal processing in the warmer, inner regions of the protostellar envelope crystallizes water ice.

The top right panel of Fig. 1.11 presents the 4.4 μm asymmetric stretching mode of the

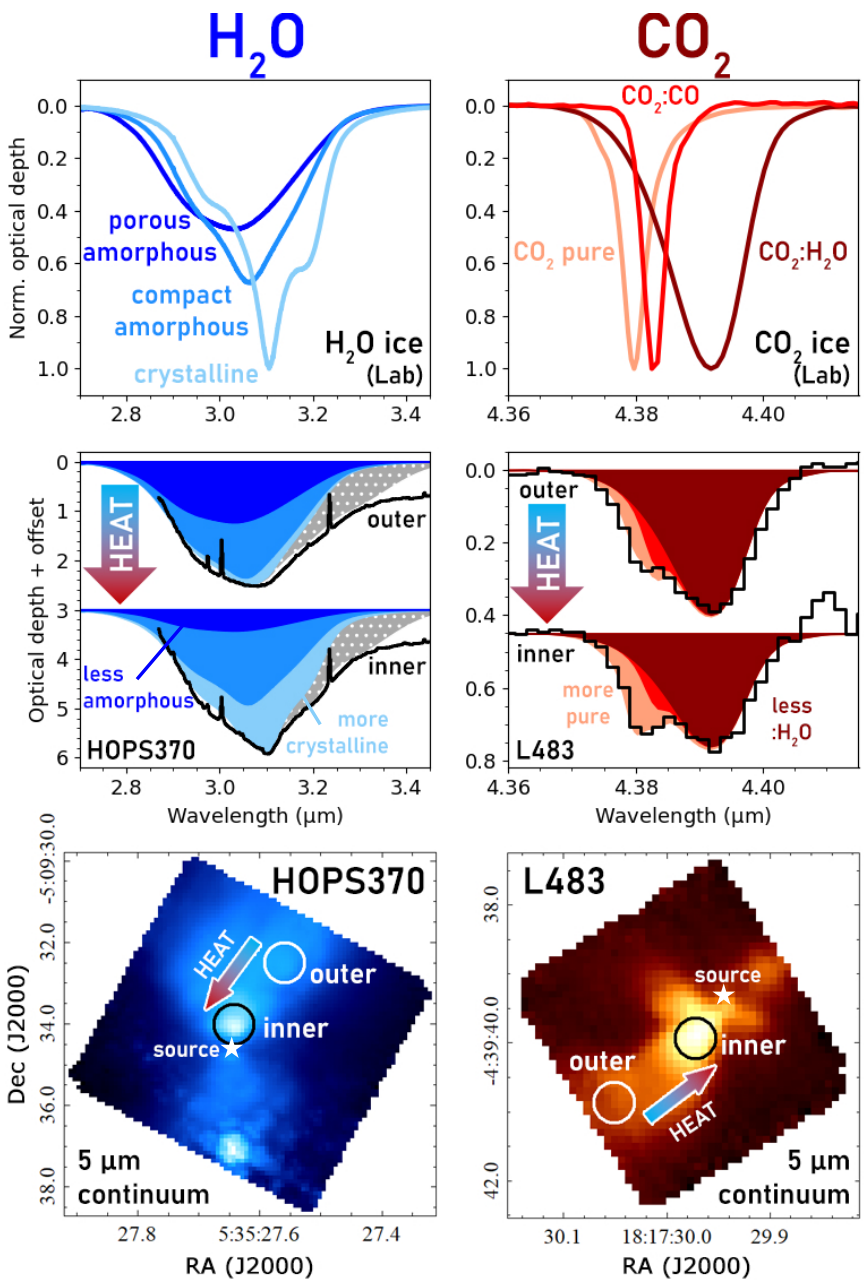


Figure 1.11: Differences in band profiles of H_2O (left) and CO_2 (right) ices caused by changes in ice morphology (left) and chemical environment (right). Top: laboratory spectra. Middle: observed protostellar spectra. Bottom: continuum maps showing the protostellar regions from which the spectra in the middle panels were extracted.

$^{13}CO_2$ isotopolog in three laboratory ices containing CO_2: a pure CO_2 ice, a mixed CO_2:CO ice, and a mixed CO_2:H_2O ice. The peak position and profile of the band differ significantly between the three chemical environments. Such profile changes are often most drastic between polar and apolar matrices (*i.e.*, matrices with and without hydrogen bonds), where polar matrices often result in broader IR features due to greater intermolecular forces that affect the dipole moments of the embedded molecules of interest (Ehrenfreund et al. 1997). Such differences can again be exploited to determine the chemical environments of various interstellar ice species (*e.g.*, Boogert et al. 2000). For example, the bottom right panel shows the 5 μm continuum flux map of a low-mass protostar, L483, from the NIRSpec instrument aboard JWST (see Section 1.3.1). Two spectra (middle right panel) are extracted from the datacube: one using an aperture centered on a bright spot in the outflow in the inner regions of the envelope close to the protostar, and one using an aperture again centered on an outer part of the envelope illuminated by scattered light in the outflow cavity. The 4.4 μm $^{13}CO_2$ feature in the spectrum extracted closer to the protostar shows a greater relative contribution of pure CO_2 ice and a lesser relative contribution of CO_2 ice mixed with water, demonstrating how thermal processing in the warmer, inner regions of the protostellar envelope promotes segregation of CO_2 from the previously mixed ice matrix.

The size, shape, and mineralogy of an icy dust grain can also influence the profiles of its ice features. Grain shape and size effects are most pronounced in strong and sharp features of the most abundant ices (Dartois & d'Hendecourt 2001; Dartois et al. 2022). These effects can be modeled using ice opacities generated from optical constants of laboratory ices, rather than the laboratory ice absorbance spectra often used to empirically fit weaker ice features. Such effects become increasingly important to account for as grain sizes grow (Dartois et al. 2024).

JWST

A large portion of the observational work utilized in this thesis was collected with the *James Webb* Space Telescope (JWST), which launched on December 25, 2021, approximately a month before this thesis work began.[1]

Prior to JWST, most of the IR spectra that informed the ice chemistry models laid out in Section 1.2 were collected either using the Infrared Space Observatory (ISO, 1995-1998) or the *Spitzer* Space Telescope (2003-2020). The short- and long-wavelength spectrometers on board ISO covered a broad spectroscopic range (2.5-200 μm) and provided moderate spectral resolving power in the mid-IR (R∼800-3000), but its low sensitivity (a few Jy) limited the sources that could be observed to the brightest massive objects (Gibb et al. 2004). *Spitzer* offered a sensitivity improvement of several orders of magnitude, creating a new opportunity to observe fainter low-mass protostars as well as more extincted background stars (Öberg et al. 2011). Nevertheless, the spectral range of its IR spectrograph (5-37 μm) neglected to cover the essential 2-5 μm spectral region where several major ice features lie, and its low spectral resolving power below 10 μm (R∼100) made it impossible to fully resolve narrow ice features or disentangle ice absorptions from gas phase emissions.

The combination of the Near-Infrared Spectrograph (NIRSpec) and the Mid-Infrared Instrument (MIRI) aboard JWST offers spectral coverage from 0.6-28 μm with comparable resolving power to ISO (R up to 2700 in the near-IR and up to 3500 in the mid-IR) and sensitivity orders of magnitude better than *Spitzer* (10^{-3}-10^{-2} mJy in the near-IR, 10^{-2}-10^{-1}

[1] Christmas day was a fitting launch date, as the results from this telescope have been an immense gift to the field.

mJy in the mid-IR). Furthermore, integral field units (IFUs) can be used to collect spatially resolved spectral datacubes with angular resolution on the order of up to ∼0.1", enabling the mapping of ice absorptions in the case of sources with extended emission.

In addition to the work discussed in this thesis, the improved capabilities of JWST have over the past few years led to observations of various weak features attributed to complex organic molecules (*e.g.*, Rocha et al. 2024; Chen et al. 2024; Nazari et al. 2024) as well as previously unobservable overtones and dangling modes of major ice species (*e.g.*, Brunken et al. 2024a; Noble et al. 2024) in protostellar envelopes. They have also enabled more comprehensive characterizations of the chemical environments of ices and the detection of trace ice species like NH_3, OCN^-, OCS, and $^{13}CO_2$ in dense clouds with record-high extinctions (*e.g.*, McClure et al. 2023) and Class II protoplanetary disks (*e.g.*, Sturm et al. 2023; Bergner et al. 2024). And finally, data from the IFUs have revealed changes in ice morphology throughout protostellar envelopes on spatial scales that were previously unresolvable in the IR (*e.g.*, Tyagi et al. 2025).

1.3.2 Laboratory methods

Laboratory measurements provide experimental data that is essential to interpreting the observations of ices described in Section 1.3.1. In such experiments, interstellar ice analogs with precisely controlled compositions are deposited upon a cryo-cooled flat substrate within an ultrahigh vacuum chamber with typical pressures on the order of $\leq 10^{-8}$-10^{-10} mbar. The resulting thin ice slab grown on the substrate is a physical approximation of the thin ice layers on top of interstellar dust grains observed toward background stars and protostars. When an IR-transmissive material (*e.g.*, KBr, CsI, Ge) is used as the substrate, an IR spectrum of the deposited ice can be collected in transmission using a Fourier-transform IR spectrometer (FTIR) whose beam path travels through the substrate and the ice layers deposited on top of it. This geometry is in some ways comparable to the transmissive observing geometry displayed in Fig. 1.9. Some UHV setups optimized for investigating interstellar ice chemistry utilize metal reflective substrates instead (*e.g.*, gold) to collect spectra in reflection-absorption mode at grazing incidence angles. This geometry yields greater sensitivity for the purpose of detecting extremely weak features or trace reaction products, but the resulting spectra are not directly comparable to observations.

The thickness of the deposited ice can be measured using the principles of thin film interference. A laser beam is aimed at the ice, and the intensity of the reflected beam is measured. During the deposition of the ice, the intensity of this reflected beam oscillates depending on the ice thickness due to the portion of laser light that is immediately reflected at the vacuum-ice interface interfering with the portion of laser light that is refracted at the vacuum-ice interface and reflected at the ice-substrate interface (see Fig. 1.12). Intensity maxima, resulting from constructive interference of the two interacting beams, are achieved at ice thicknesses d dictated by the following equation:

$$d = \frac{m\,\lambda}{2\sqrt{n^2 - sin^2\theta}} \tag{1.4}$$

where m is the integer number of constructive interference fringes, λ is the wavelength of the laser beam, n is the ice refractive index at wavelength λ, and θ is the angle of incidence

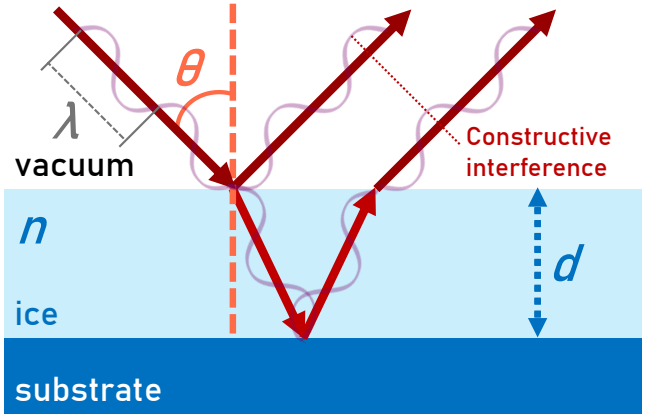


Figure 1.12: Schematic demonstrating the principle that results in an interference pattern when light is reflected off a growing thin film. The case of constructive interference is shown; changing the thickness of the ice d will result in changes in the observed interference.

of the laser beam. The refractive index n of the ice can be obtained by measuring the interference pattern of two laser beams positioned at two different incidence angles during an ice deposition using the following equation:

$$n = \sqrt{\frac{sin^2\theta_1 - \gamma^2 sin^2\theta_2}{1-\gamma^2}} \tag{1.5}$$

where θ_1 and θ_2 are the respective angles of incidence of the two laser beams and γ is equal to the ratio of the respective periods T_2/T_1 of the two resulting interference patterns.

The thickness of an ice can then be used to calculate the apparent band strength A' of various IR absorption features of a given ice species:

$$A' = \frac{M\,\ell n 10}{\rho\, d\, N_A} \int_{\nu_1}^{\nu_2} abs_\nu \, d\nu \tag{1.6}$$

where M is the molar mass of the ice species, ρ is the ice density, d is the thickness calculated from Eq. 1.3.2, N_A is Avogadro's number, and the integral is the absorbance of the ice feature of interest integrated over frequencies ν_1-ν_2 expressed in wavenumbers. The ice density ρ can be obtained from measurements using a *quartz crystal microbalance*, which detects extremely small changes in mass during ice deposition upon a quartz crystal substrate via changes in the crystal's resonance frequency (Allodi et al. 2013).

The laboratory IR spectra collected in such experiments can be directly compared to ice observations to identify the chemical species present in ices, and their column densities can be quantified using A' values. This empirical treatment is usually sufficient for analyzing ices observed toward dense clouds and Class 0 and I protostars, *i.e.*, the pencil-beam scenario. In the case of more evolved Class I or II protostars with hefty, optically thick disks, the photon paths toward the observer are less straightforward and thus require radiative transfer models that use ice optical constants as input rather than ice absorbance spectra (*e.g.*, Sturm et al.

2023; Bergner et al. 2024). Additionally, the profiles of strong and sharp ice features of the most abundant ice species (*i.e.*, H_2O, CO_2, CO) can differ significantly between the laboratory thin ice slab scenario and the interstellar ice layer on a μm-sized dust grain scenario due to spectral contributions from scattering, especially when grain sizes grow large. In such cases, the observed ice absorptions require modeling via their optical constants, which can be calculated from laboratory ice slab absorbance spectra (*e.g.*, Baratta & Palumbo 1998; Gerakines & Hudson 2020). The work in this thesis primarily focuses on less abundant ice species and younger, less geometrically complex observational targets. Therefore, ice optical constants are not measured nor extensively utilized – with the exception of Chapter 3, in which H_2O ice optical constants were used to account for scattering effects in the H_2O ice bands when calculating HDO/H_2O ice ratios toward a Class 0/I source with a disk.

IRASIS

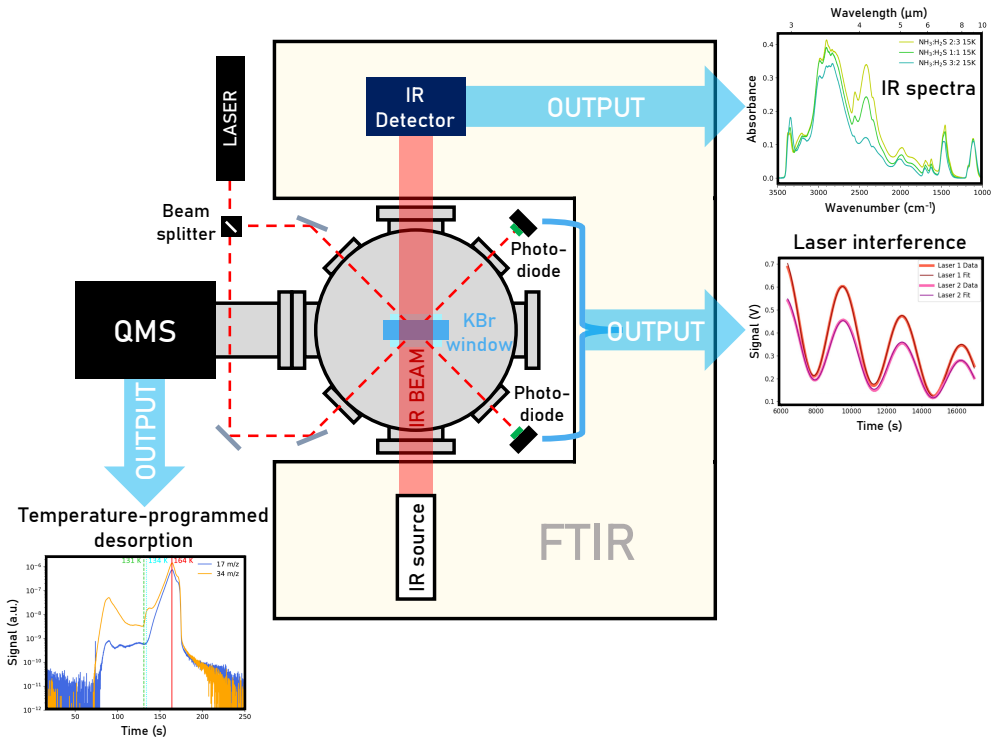


Figure 1.13: Top-view schematic of IRASIS in the configuration used during the work in this thesis.

The Infrared Absorption Set-up for Ice Spectroscopy (IRASIS) is an ultrahigh vacuum (UHV) setup in the Leiden Laboratory for Astrophysics (Rachid et al. 2021) that was used in this thesis to obtain experimental transmission spectra and band strengths of interstellar ice analogs. Its central chamber has a base pressure of $<1\times10^{-9}$ mbar, corresponding to a density on the order of $\sim10^{7}$ molecules cm^{-3}. Fig. 1.13 presents a schematic of the setup.

At the center of the UHV chamber, an IR-transmissive window substrate is attached to the arm of a cryostat that is capable of cooling the window down to ∼12 K. Both KBr and Ge substrates were used in the setup during the work presented in this thesis. The temperature of the substrate can be controlled from 15 K to room temperature via a resistive heater attached close to the substrate on the cryostat arm. The heater output is managed via proportional-integral-derivative control with a LakeShore controller to achieve a desired temperature or ramp rate (usually ∼0.4-1 K min^{-1}) in the case of warm-up experiments.

Ice samples are grown on both sides of the cryo-cooled substrate simultaneously by dosing gases and vapors of species of interest into the chamber via three leak valves, each attached to three independent gas manifold lines. This system enables controlled background deposition of ice mixtures containing up to three different chemical species. Using separate dosing lines for each species significantly improves accuracy in the reported mixing ratios compared to previous versions of the system, in which species were pre-mixed in the gas manifold and entered the chamber together through a single leak valve (*e.g.*, Terwisscha van Scheltinga et al. 2018). More detailed discussions of the benefits of using independent dosing lines to deposit ice mixtures can be found in the appendix of Chapter 6 as well as Yarnall & Hudson (2022).

This substrate lies normal to the path of a collimated infrared beam generated by an FTIR, which passes into and out of the chamber through two ZnSe windows parallel to the substrate. With this geometry, IR spectra are collected in transmission mode, directly comparable to the ice transmission spectra collected in astronomical observations. The chamber also includes four smaller ZnSe windows that enable laser interference measurements of ice sample growth and thickness. Two visible laser beams enter the chamber, one on each side of the substrate, and reflect off the substrate at 45° incidence into two photodiode detectors outside the chamber. The experiments presented in this thesis employed either a 633 or 543 nm HeNe laser, depending on the wavelength at which visible refractive index values were available for a given ice of interest.

Additionally, a quadrupole mass spectrometer (QMS), which can monitor the gas-phase species in the chamber during experiments, is positioned at 90° with respect to the IR beam path. The two primary purposes of the QMS on IRASIS are 1) leak valve calibration to yield ices with specific column densities and mixing ratios, and 2) temperature-programmed desorption (TPD) experiments. The QMS can also be used to detect IR-inactive contaminants during deposition, evaluate the cleanliness of the chamber prior to an experiment, and identify any possible solid-state reaction products during desorption.

Multiple procedures exist for leak valve calibration via the QMS. A procedure for depositing ice mixtures including only species that are either gaseous or have high vapor pressures at room temperature is described in Chapter 5; a procedure for depositing ice mixtures including species with extremely low vapor pressures at room temperature (*e.g.*, formamide) is described in Chapter 6.

During experiments that include TPD, the QMS monitors gas-phase species in the chamber as the ice sample is warmed at a constant rate. Once ices in the sample reach their desorption temperatures and sublimate, they are detected by the QMS. Thus, TPD experiments can yield the desorption temperatures or trapping efficiencies of ice species in various chemical environments. Because heating timescales in these experiments are orders of magnitude slower than the heating timescales (10^4-10^6 years) experienced by ices in environments like protostellar envelopes (Viti & Williams 1999), the laboratory desorption temperature of a given

species will be higher than its interstellar desorption temperature (Brown & Bolina 2007).

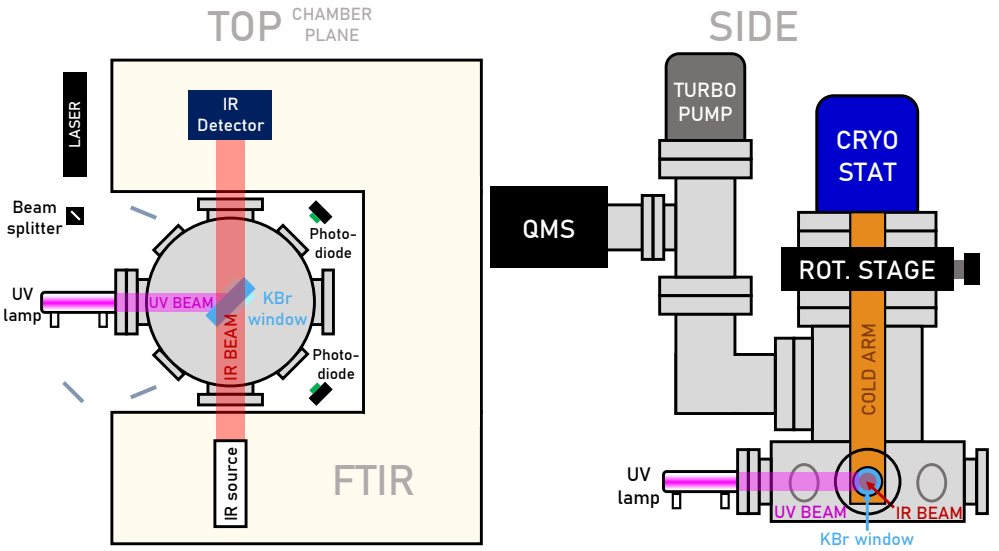


Figure 1.14: Top- and side-view schematics of IRASIS in the updated configuration that enables ice sample UV irradiation.

Following the work done in Chapters 2-6, IRASIS was upgraded to enable the IR characterization of species formed via UV irradiation of interstellar ice analogs. A schematic view of the chamber after this upgrade is presented in Fig. 1.14. Am F-type microwave discharge hydrogen-flow lamp (MDHL) replaced the QMS on the port perpendicular to the IR beam windows, and the QMS was moved to a port further from the sample and closer to the system turbomolecular pump. The MDHL generates Lyman-α photons at 121.6 nm as well as a broader molecular hydrogen emission profile centered around 160 nm (Ligterink et al. 2015).

To irradiate the ice sample, the substrate can be rotated via the chamber rotational stage to be either oblique (usually 45°) or perpendicular to the impinging UV beam. In the former case, collection of IR spectra can proceed simultaneously with UV irradiation, but longitudinal optical (LO) modes will be present in the spectra (Palumbo et al. 2006). The ice thickness cannot be monitored with laser interference in either of these geometries, so the ice sample is typically deposited with the substrate positioned perpendicular to the path of the IR beam (as shown in Fig. 1.13) before the sample is rotated for UV irradiation. It is important to note that with this geometry, only one side of the substrate is irradiated because KBr is opaque at the UV wavelengths generated by the lamp, which must be taken into account when yields are calculated.

1.4 Thesis overview

1.4.1 Aims

Since the first successful observation of interstellar ices in the Orion Nebula half a century ago (Gillett & Forrest 1973), the symbiotic relationship between IR telescopic observations and laboratory work has continually revealed that these ices host a rich solid-state chemistry that is foundational to the formation and transport of volatiles during the formation of planetary systems. However, a number of pressing questions about this chemistry also remained unanswered when this thesis work began:

- **To what extent is interstellar ice inherited versus chemically reprocessed in protostellar envelopes and protoplanetary disks before its accretion into planetary objects?** Comparisons of volatile abundances between interstellar ices and primitive solar system objects like comets show both striking similarities as well as key differences, suggesting that interstellar ices play an important role in setting planetary compositions but do also experience some level of chemical alteration throughout the star formation process (see Section 1.2.3). At what points during this process are interstellar ices preserved, and at what points are they reprocessed? *(addressed in Chapters 1 & 2)*

- **What species are the major sulfur sinks in the densest stages of star formation?** Sulfur is a key biogenic element, and its elemental abundance observed in the interstellar medium (Esteban et al. 2004) is close to the abundance observed in the sun and in primitive meteorites (Lodders 2003; Asplund et al. 2009). However, the sulfur abundance observed in the most dense stages of star formation (*e.g.*, molecular clouds and protostellar envelopes) can be up to 2-3 orders of magnitude lower than these interstellar and solar values. Models have long suggested much of the sulfur is expected to freeze out on the dust grains and form S-bearing ices, particularly H_2S (*e.g.*, Garrod et al. 2007), yet measured abundances of S-ices in these dense environments remain too low to account for the missing sulfur. In what chemical form is sulfur hiding in dense interstellar regions? And why are upper limits of species like H_2S so low despite model predictions? *(addressed in Chapters 3 & 4)*

- **Which of the many complex organic molecules detected in the gas phase in protostars can be found also in ices, and what does that tell us about their formation histories?** Despite the hundreds of chemically unique molecules detected in star-forming regions, very few molecules have been securely detected in interstellar ices – the so-called *gas-grain* gap. Some of the species detected in the gas phase may not be detected in ices because the species are produced via gas phase chemical routes, but others may not have been detected yet due to observational limitations or a lack of the necessary laboratory data. By how much will the combination of new facilities with improved sensitivity and spectral resolution like JWST and growing databases of laboratory data close this gap? *(addressed in Chapter 6)*

1.4.2 Chapter summary

Water ice D/H ratios as a probe of ice inheritance

Chapter 2: This work uses the increased sensitivity and resolution of JWST to make the first robust detections of the O-D stretching mode of HDO ice at 4.1 μm. It then presents a method for quantifying ice HDO/H_2O ratios toward protostellar lines of sight with thermal gradients and uses this method to find this ratio toward two massive protostars observed with JWST. For this work, new laboratory IR spectra of ice mixtures containing HDO, H_2O, CH_3OH, and CO were collected to aid in the fitting and chemical interpretation of the observed spectra. HDO ice is detected above the 3σ level toward both sources, with fits requiring a combination of HDO in mixtures with amorphous and crystalline H_2O. Ice HDO/H_2O ratios of $4.6\pm1.8\times10^{-3}$ and $2.6\pm1.2\times10^{-3}$ are obtained for the two sources. These ratios are similar to the highest reported gas HDO/H_2O ratios measured toward massive protostars and the hot inner regions of isolated low-mass protostars, suggesting that at least some of the gas HDO/H_2O ratios measured toward massive hot cores are representative of those in ices.

Chapter 3: This work presents the first detection of the 4.1 μm HDO ice feature with JWST toward a low-mass protostar, L1527 IRS, which may eventually grow to a Sun-like mass The method developed in Chapter 2 is used to measure an ice HDO/H_2O ratio of $4.4^{+3.7}_{-1.7}\times10^{-3}$, similar to the gas HDO/H_2O ratios measured in the warm inner cores of other low-mass protostellar envelopes and protoplanetary disks found in comparably isolated star-forming regions. Such a similarity tentatively supports the assumption that water vapor detected in these regions is not significantly altered by gas-phase reactions following ice sublimation. It also supports the hypothesis that pre- and protostellar water ice is largely inherited in a chemically unaltered state by outer protoplanetary disks. However, the fraction is a factor of $\sim$4-10 times higher than the gas HDO/H_2O ratios measured toward comets and low-mass protostars in clustered star-forming regions. This difference may be due to either gas-phase water reprocessing in protostellar envelopes and protoplanetary disks or differences between prestellar conditions of isolated dense cores and the clustered star-forming regions that are more analogous to the environment in which our Sun formed.

Sulfur ice chemistry

Chapter 4: Laboratory transmission IR spectra of both pure and H_2O-rich ices containing NH_4SH salt were collected to spectroscopically investigate the plausibility of NH_4SH serving as a sulfur reservoir and a carrier of the 6.85 μm band in interstellar ices. Peak positions, full width half maxima, and apparent band strengths of the NH_4^+ asymmetric bending mode and the SH^- stretching mode in H_2O-rich ices were obtained. The IR features of the laboratory salts were compared to those observed toward a sample of four protostars and two cold dense clouds. The observed 6.85 μm feature toward these sources is fit well with the laboratory NH_4SH:H_2O ice spectra, and the fits provide NH_4^+ column densities that range from 8–23% with respect to H_2O. Furthermore, the redshift of the 6.85 μm feature correlates with higher abundances of NH_4^+ with respect to H_2O in both the laboratory and observational data. The apparent band strength of the SH^- feature is likely too low for the feature to be detectable, but the 5.3 μm $NH_4^+ + SH^-$ combination mode may be an alternative means of detection. Its tentative assignment adds to mounting evidence supporting the presence of NH_4^+ salts in ices and is the first tentative observation of the SH^- anion toward interstellar ices. The combined

upper limits of four other counter-anion candidates, OCN^-, CN^-, $HCOO^-$, and Cl^-, are determined to be $\lesssim$15–20% of the total NH_4^+ column densities toward three of the protostars. If the majority ($\gtrsim$80–85%) of the NH_4^+ cations quantified toward the investigated sources in this work are bound to SH^- anions, then NH_4SH salts could account for up to 17–18% of their sulfur budgets.

Chapter 5: This chapter provides a library of new laboratory IR transmission spectra of OCS in CH_3OH- and CO-rich ice mixtures, some of which also include H_2S and H_2O, to aid future studies of the abundance, physicochemical environment, and evolutionary history of interstellar OCS ice. Of these new laboratory spectra, the tertiary OCS:CO:CH_3OH ice mixtures provide the best fits to observations of high-mass protostars, providing further support for the hypothesis that OCS forms with CH_3OH, possibly via chemical pathways involving frozen-out CO. The apparent band strengths of the ν_3 mode in OCS:CH_3OH and OCS:CO:CH_3OH ice mixtures are calculated. The derived values are consistent (within uncertainties) with the apparent band strength of the feature in pure OCS ice. A calibration method for producing ice mixtures using gases and high vapor pressure liquids is described.

Hunt for complex organic molecules in ices

Chapter 6: Gaseous formamide has been detected in many interstellar regions, but whether it forms in the ice or gas is a topic of great debate. However, more laboratory data are needed to hunt for its presence in interstellar ices. This chapter characterizes the IR spectra of formamide in its pure form as well as in mixtures of the most abundant interstellar ices. Apparent band strengths and positions of eight IR bands of formamide at various temperatures are provided. Three of these bands are identified as potential formamide tracers in observational ice spectra: the overlapping C=O stretch and NH_2 scissor bands at 5.88 and 6.13 μm, the CH bend at 7.20 μm, and the CN stretch at 7.53 μm. The laboratory spectra are compared to observational spectra of low- and high-mass protostars as well as prestellar cores. A comparison between the formamide CH bend in laboratory data and the 7.24 μm band in the observations tentatively indicates that, if formamide ice is contributing significantly to the observed absorption, it is more likely in a polar matrix, but other species like $HCOO^-$ and CH_3CH_2OH provide better fits to this feature and are more likely to be the main carriers of this band. Upper limits ranging from 0.35-5.1% with respect to H_2O were calculated. These upper limits are in agreement with gas-phase protostellar as well as cometary formamide abundances.

1.4.3 Scientific significance and future directions

The key scientific takeaways of this thesis can be summarized as follows:

- HDO ice is now robustly detectable in star-forming regions with JWST. Similarities between ice and gas water D/H ratios measured toward protostars and the gas water D/H measured toward protoplanetary disks suggest interstellar ice inheritance between protostellar envelopes and protoplanetary disks.

- Comparisons between water D/H values in protostellar ices and cometary comae suggest either some level of gas-phase water reprocessing in the protoplanetary disk *or* or

an environmentally-driven diversity in prestellar water ice D/H values across different star-forming regions in our galaxy.

- Up to ∼20% of the sulfur in dense star-forming regions like molecular clouds and protostellar envelopes may be locked up in salts like NH_4SH, potentially resolving the decades-long puzzle of why H_2S is not detected in interstellar ices despite predictions from chemical models.
- Given their higher desorption temperatures relative to their neutral acid-base counterparts, salts like NH_4SH may have facilitated the transport of the volatile elements N and S into the inner solar system, where they could eventually be accreted by volatile-rich bodies like carbonaceous asteroids.[2]
- Even with JWST, it may not be possible to unambiguously detect the absorption features of many of the less abundant and semi-refractory complex organic molecules like formamide due to overlaps with absorptions from more abundant and volatile organics.

Looking forward, a larger sample of ice water D/H measured toward protostars spanning a variety of environments will be needed to better constrain the ice water D/H ratio that was likely inherited by our solar system. Furthermore, a large fraction of the interstellar sulfur still remains missing. If it is in minerals or allotropes as suggested by others (Jiménez-Escobar & Caro 2011; Shingledecker et al. 2020), chances for direct detections of such species are not promising. But wherever this missing sulfur may be, it is time for an updated sulfur ice survey with JWST data to update previous constraints on species like H_2S and OCS, which primarily used outdated band strengths and focused on high-mass systems. The laboratory data presented in this thesis enable such surveys. And finally, observationally targeting lines of sight with low volatile ice-to-dust ratios but high dust columns (*i.e.*, protostellar envelopes that are still dense but have beeen highly thermally or energetically processed) may provide better opportunities for identifying more refractory trace ice species whose absorptions are typically overshadowed by the strong absorptions of the more abundant volatiles.

[2]For example, the liquid H_2O:NH_3 inclusions within iron sulfide grains found in recently returned samples from the carbonaceous asteroid Bennu may be a result of the aqueous alteration of this salt within Bennu's parent body (Prince et al. 2025).

1.B Bibliography

Alexander, C. M. 2017, Phil. Trans. R. Soc. A, Math. Phys. Eng. Sci., 375
Alexander, C. O., Fogel, M., Yabuta, H., & Cody, G. 2007, GCA, 71, 4380
Allodi, M., Baragiola, R., Baratta, G., et al. 2013, SSRv, 180, 101
Altwegg, K., Combi, M., Fuselier, S., et al. 2022, MNRAS, 516, 3900
Arumainayagam, C. R., Garrod, R. T., Boyer, M. C., et al. 2019, Chem. Soc. Rev., 48, 2293
Asplund, M., Grevesse, N., Sauval, A. J., & Scott, P. 2009, ARA&A, 47, 481
Baratta, G. & Palumbo, M. 1998, J. Opt. Soc. Am. A, 15, 3076
Bergner, J. B., Sturm, J., Piacentino, E. L., et al. 2024, ApJ, 975, 166
Bernstein, M. P., Dworkin, J. P., Sandford, S. A., Cooper, G. W., & Allamandola, L. J. 2002, Nature, 416, 401
Beuther, H., Churchwell, E. B., McKee, C. F., & Tan, J. C. 2007, Protostars and Planets V, 165
Beuther, H., Kuiper, R., & Tafalla, M. 2025, ARA&A, 63
Boogert, A., Brewer, K., Brittain, A., & Emerson, K. 2022, ApJ, 941, 32
Boogert, A., Chiar, J., Knez, C., et al. 2013, ApJ, 777, 73
Boogert, A., Ehrenfreund, P., Gerakines, P., et al. 2000, A&A, 353, 349
Boogert, A. A., Gerakines, P. A., & Whittet, D. C. 2015, ARA&A, 53, 541
Boogert, A. C., Pontoppidan, K. M., Knez, C., et al. 2008, ApJ, 678, 985
Bottinelli, S., Boogert, A. A., Bouwman, J., et al. 2010, ApJ, 718, 1100
Brown, W. A. & Bolina, A. S. 2007, MNRAS, 374, 1006
Brunken, N., van Dishoeck, E., Slavicinska, K., et al. 2024a, A&A, 692, A163
Brunken, N. G., Rocha, W. R., van Dishoeck, E. F., et al. 2024b, A&A, 685, A27
Busch, L. A., Belloche, A., Garrod, R. T., Müller, H. S., & Menten, K. M. 2022, A&A, 665, A96
Chen, Y., Rocha, W. R. M., van Dishoeck, E. F., et al. 2024, A&A, 690, A205
Chuang, K.-J., Fedoseev, G., Ioppolo, S., van Dishoeck, E., & Linnartz, H. 2016, MNRAS, 455, 1702
Chuang, K.-J., Jäger, C., Krasnokutski, S., Fulvio, D., & Henning, T. 2022, ApJ, 933, 107
Cleeves, L. I., Bergin, E. A., Alexander, C. M. O., et al. 2014, Science, 345, 1590
Collings, M. P., Anderson, M. A., Chen, R., et al. 2004, MNRAS, 354, 1133
Corliss, J. B., Baross, J., & Hoffman, S. 1981, Oceanol. Acta, 59
Cuppen, H., Penteado, E., Isokoski, K., van der Marel, N., & Linnartz, H. 2011, MNRAS, 417, 2809
Cuppen, H. M., Linnartz, H., & Ioppolo, S. 2024, ARA&A, 62
Dartois, E. & d'Hendecourt, L. 2001, A&A, 365, 144
Dartois, E., Noble, J. A., Caselli, P., et al. 2024, Nat. Astro., 8, 359
Dartois, E., Noble, J. A., Ysard, N., Demyk, K., & Chabot, M. 2022, A&A, 666, A153
Di Giulio, M. 2003, J. Theor. Biol., 221, 425
Draine, B. T. 1978, ApJS, 36, 595
Drozdovskaya, M. N., van Dishoeck, E. F., Rubin, M., Jørgensen, J. K., & Altwegg, K. 2019, MNRAS, 490, 50
Drozdovskaya, M. N., Walsh, C., Visser, R., Harsono, D., & van Dishoeck, E. F. 2014, MNRAS, 445, 913
Dunham, M. M., Stutz, A. M., Allen, L. E., et al. 2014, Protostars and Planets VI, 195

Ehrenfreund, P., Boogert, A., Gerakines, P., Tielens, A., & van Dishoeck, E. 1997, A&A, 328, 649
Ehrenfreund, P., Dartois, E., Demyk, K., & d'Hendecourt, L. 1998, A&A, 339, L17
Ehrenfreund, P. & van Dishoeck, E. 1998, Adv. Space Res., 21, 15
Esteban, C., Peimbert, M., García-Rojas, J., et al. 2004, MNRAS, 355, 229
Fedoseev, G., Chuang, K.-J., Ioppolo, S., et al. 2017, ApJ, 842, 52
Fedoseev, G., Ioppolo, S., Zhao, D., Lamberts, T., & Linnartz, H. 2015, MNRAS, 446, 439
Frenkel-Pinter, M., Rajaei, V., Glass, J. B., Hud, N. V., & Williams, L. D. 2021, J. Mol. Evol., 89, 2
Garrod, R. T. & Herbst, E. 2006, A&A, 457, 927
Garrod, R. T., Wakelam, V., & Herbst, E. 2007, A&A, 467, 1103
Garrod, R. T., Weaver, S. L. W., & Herbst, E. 2008, ApJ, 682, 283
Gerakines, P. A. & Hudson, R. L. 2020, ApJ, 901, 52
Gibb, E., Whittet, D., Boogert, A., & Tielens, A. 2004, ApJS, 151, 35
Gillett, F. & Forrest, W. 1973, ApJ, 179, 483
Hiraoka, K., Ohashi, N., Kihara, Y., et al. 1994, Chem. Phys. Lett., 229, 408
Hiraoka, K., Yamashita, A., Yachi, Y., et al. 1995, ApJ, 443, 363
Hollenbach, D. & Salpeter, E. 1971, ApJ, 163, 155
Hubbard, G. S., Naderi, F. M., & Garvin, J. B. 2002, Acta Astronaut., 51, 337
Jensen, S., Jørgensen, J., Kristensen, L., et al. 2019, A&A, 631, A25
Jiménez-Escobar, A. & Caro, G. M. 2011, A&A, 536, A91
Kaifu, N., Ohishi, M., Kawaguchi, K., et al. 2004, PASJ, 56, 69
Kaňuchová, Z., Urso, R., Baratta, G., et al. 2016, A&A, 585, A155
Klessen, R. S. & Glover, S. C. 2015, in Star Formation in Galaxy Evolution: Connecting Numerical Models to Reality: Saas-Fee Advanced Course 43. Swiss Society for Astrophysics and Astronomy (Springer), 85–249
Ligterink, N., Paardekooper, D., Chuang, K.-J., et al. 2015, A&A, 584, A56
Lodders, K. 2003, ApJ, 591, 1220
Mandt, K. E., Lustig-Yaeger, J., Luspay-Kuti, A., et al. 2024, Sci. Adv., 10, eadp2191
Martin, W., Baross, J., Kelley, D., & Russell, M. J. 2008, Nat. Rev. Microbiol., 6, 805
Mastrapa, R., Sandford, S., Roush, T., Cruikshank, D., & Dalle Ore, C. 2009, ApJ, 701, 1347
McClure, M. K., Rocha, W., Pontoppidan, K., et al. 2023, Nat. Astro., 7, 431
McGuire, B. A. 2022, ApJS, 259, 30
Moody, E. R., Álvarez-Carretero, S., Mahendrarajah, T. A., et al. 2024, Nat. Ecol. Evol., 8, 1654
Mumma, M. J. & Charnley, S. B. 2011, ARA&A, 49, 471
Munoz Caro, G., Meierhenrich, U. J., Schutte, W. A., et al. 2002, Nature, 416, 403
Nazari, P., Rocha, W., Rubinstein, A., et al. 2024, A&A, 686, A71
Noble, J. A., Fraser, H., Smith, Z., et al. 2024, Nat. Astro., 8, 1169
Novozamsky, J., Schutte, W., & Keane, J. 2001, A&A, 379, 588
Oba, Y., Takano, Y., Naraoka, H., Watanabe, N., & Kouchi, A. 2019, Nat. Comm., 10, 4413
Oba, Y., Watanabe, N., Kouchi, A., Hama, T., & Pirronello, V. 2010, ApJL, 712, L174
Öberg, K. I. 2016, Chem. Rev., 116, 9631
Öberg, K. I. & Bergin, E. A. 2021, Phys. Rep., 893, 1
Öberg, K. I., Boogert, A. A., Pontoppidan, K. M., et al. 2008, ApJ, 678, 1032
Öberg, K. I., Boogert, A. A., Pontoppidan, K. M., et al. 2011, ApJ, 740, 109

Omont, A., Moseley, S., Forveille, T., et al. 1990, ApJL, 355, L27
Ootsubo, T., Kawakita, H., Hamada, S., et al. 2012, ApJ, 752, 15
Pace, N. R. 1991, Cell, 65, 531
Paganini, L., Mumma, M., Gibb, E., & Villanueva, G. L. 2017, ApJL, 836, L25
Palumbo, M., Geballe, T., & Tielens, A. G. 1997, ApJ, 479, 839
Palumbo, M. E., Baratta, G. A., Collings, M. P., & McCoustra, M. R. 2006, PCCP, 8, 279
Persson, M., Jørgensen, J., van Dishoeck, E., & Harsono, D. 2014, A&A, 563, A74
Pineda, J. E., Segura-Cox, D., Caselli, P., et al. 2020, Nat. Astro., 4, 1158
Poch, O., Istiqomah, I., Quirico, E., et al. 2020, Science, 367, eaaw7462
Pontoppidan, K., Fraser, H., Dartois, E., et al. 2003, A&A, 408, 981
Pontoppidan, K. M. 2006, A&A, 453, L47
Pontoppidan, K. M., Boogert, A. C., Fraser, H. J., et al. 2008, ApJ, 678, 1005
Prasad, S. S. & Tarafdar, S. P. 1983, ApJ, 267, 603
Prince, B. S., Gainsforth, Z., Benner, M. C., & Zega, T. J. 2025, Microsc. Microanal., 31, 1447
Qasim, D., Chuang, K.-J., Fedoseev, G., et al. 2018, A&A, 612, A83
Qasim, D., Fedoseev, G., Chuang, K.-J., et al. 2020, Nat. Astro., 4, 781
Qasim, D., Fedoseev, G., Chuang, K.-J., et al. 2019, A&A, 627, A1
Rachid, M., Brunken, N., De Boe, D., et al. 2021, A&A, 653, A116
Robitaille, T. P., Whitney, B. A., Indebetouw, R., Wood, K., & Denzmore, P. 2006, ApJS, 167, 256
Rocha, W., van Dishoeck, E., Ressler, M., et al. 2024, A&A, 683, A124
Russell, M., Hall, A., Cairns-Smith, A., & Braterman, P. 1988, Nature, 336, 117
Russell, M. J. & Martin, W. 2004, Trends Biochem. Sci., 29, 358
Santos, J. C., Linnartz, H., & Chuang, K.-J. 2024, A&A, 690, A24
Segura-Cox, D. M., Schmiedeke, A., Pineda, J. E., et al. 2020, Nature, 586, 228
Shen, C., Greenberg, J., Schutte, W., & van Dishoeck, E. 2004, A&A, 415, 203
Shingledecker, C. N., Lamberts, T., Laas, J. C., et al. 2020, ApJ, 888, 52
Smith, D. 1992, Chem. Rev., 92, 1473
Smith, R. G., Sellgren, K., & Tokunaga, A. T. 1989, ApJ, 344, 413
Stevenson, D. J. & Lunine, J. I. 1988, Icarus, 75, 146
Sturm, J., McClure, M., Beck, T., et al. 2023, A&A, 679, A138
Terwisscha van Scheltinga, J., Ligterink, N., Boogert, A., van Dishoeck, E., & Linnartz, H. 2018, A&A, 611
Tielens, A. & Hagen, W. 1982, A&A, 114, 245
Tyagi, H., Manoj, P., Narang, M., et al. 2025, ApJ, 983, 110
Valdivia-Mena, M. T., Pineda, J. E., Caselli, P., et al. 2024, A&A, 687, A71
van Broekhuizen, F., Keane, J., & Schutte, W. 2004, A&A, 415, 425
van Dishoeck, E. 1992, in Symposium-International Astronomical Union, Vol. 150, Cambridge University Press, 143–151
van Dishoeck, E. F. & Black, J. H. 1988, ApJ, 334, 771
van Dishoeck, E. F., Kristensen, L. E., Mottram, J. C., et al. 2021, A&A, 648, A24
van Dishoeck, E. F., Tychoniec, Ł., Rocha, W. R. M., et al. 2025, A&A, 699, A361
Vidali, G. 2013, Chem. Rev., 113, 8762
Viti, S. & Williams, D. A. 1999, MNRAS, 305, 755
Wakelam, V., Bron, E., Cazaux, S., et al. 2017, Mol. Astrophys., 9, 1

Watanabe, N. & Kouchi, A. 2002, ApJ, 571, L173
Weiss, M. C., Sousa, F. L., Mrnjavac, N., et al. 2016, Nat. Microbiol., 1, 1
Whittet, D., Poteet, C., Chiar, J., et al. 2013, ApJ, 774, 102
Whittet, D., Shenoy, S., Bergin, E., et al. 2007, ApJ, 655, 332
Williams, J., Krijt, S., Bitsch, B., Houge, A., & Bergner, J. 2025, MNRAS, 544, 3562
Yang, L., Ciesla, F. J., & Alexander, C. M. 2013, Icarus, 226, 256
Yarnall, Y. Y. & Hudson, R. L. 2022, ApJL, 931, L4
Zolensky, M. E., Zega, T. J., Yano, H., et al. 2006, Science, 314, 1735

2

JWST detections of amorphous and crystalline HDO ice toward massive protostars

Katerina Slavicinska, Ewine F. van Dishoeck, Łukasz Tychoniec, Pooneh Nazari, Adam E. Rubinstein, Robert Gutermuth, Himanshu Tyagi, Yuan Chen, Nashanty G. C. Brunken, Will R. M. Rocha, P. Manoj, Mayank Narang, S. Thomas Megeath, Yao-Lun Yang, Leslie W. Looney, John J. Tobin, Henrik Beuther, Tyler L. Bourke, Harold Linnartz, Samuel Federman, Dan M. Watson, Hendrik Linz

Astronomy & Astrophysics (2024), 688, A29

Abstract

Context. Tracing the origin and evolution of interstellar water is key to understanding many of the physical and chemical processes involved in star and planet formation. Deuterium fractionation offers a window into the physicochemical history of water due to its sensitivity to local conditions.

Aims. This work aims to utilize the increased sensitivity and resolution of the *James Webb* Space Telescope (JWST) to quantify the HDO/H_2O ratio in ices toward young stellar objects (YSOs) and to determine if the HDO/H_2O ratios measured in the gas phase toward massive YSOs (MYSOs) are representative of the ratios in their ice envelopes.

Methods. Two protostars observed in the Investigating Protostellar Accretion (IPA) program using JWST NIRSpec were analyzed: HOPS 370, an intermediate-mass YSO (IMYSO), and IRAS 20126+4104, a massive YSO (MYSO). The HDO ice toward these sources was quantified via its 4.1 μm band. The contributions from the CH_3OH combination modes to the observed optical depth in this spectral region were constrained via the CH_3OH 3.53 μm band to ensure that the integrated optical depth of the HDO feature was not overestimated. H_2O ice was quantified via its 3 μm band. New laboratory IR spectra of ice mixtures containing HDO, H_2O, CH_3OH, and CO were collected to aid in the fitting and chemical interpretation of the observed spectra.

Results. HDO ice is detected above the 3σ level in both sources. It requires a minimum of two components, one amorphous and one crystalline, to obtain satisfactory fits. The H_2O ice band at 3 μm similarly requires both amorphous and crystalline components. The observed peak positions of the crystalline HDO component are consistent with those of annealed laboratory ices, which could be evidence for heating and subsequent re-cooling of the ice envelope (i.e., thermal cycling). The CH_3OH 3.53 μm band is fit best with two cold components, one consisting of pure CH_3OH and the other of CH_3OH in an H_2O-rich mixture. From these fits, ice HDO/H_2O abundance ratios of $4.6\pm1.8\times10^{-3}$ and $2.6\pm1.2\times10^{-3}$ are obtained for HOPS 370 and IRAS 20126+4104, respectively.

Conclusions. The simultaneous detections of both crystalline HDO and crystalline H_2O corroborate the assignment of the observed feature at 4.1 μm to HDO ice. The ice HDO/H_2O ratios are similar to the highest reported gas HDO/H_2O ratios measured toward MYSOs as well as the hot inner regions of isolated low-mass protostars, suggesting that at least some of the gas HDO/H_2O ratios measured toward massive hot cores are representative of the HDO/H_2O ratios in ices. The need for an H_2O-rich CH_3OH component in the CH_3OH ice analysis supports recent experimental and observational results that indicate that some CH_3OH ice may form prior to the CO freeze-out stage in H_2O-rich ice layers.

2.1 Introduction

Water is one of the most abundantly detected interstellar molecules in both the gas and solid phase, and it plays countless essential roles in physical and chemical processes involved in the birth and evolution of stars, planets, and life as we know it (e.g., van Dishoeck et al. 2013, 2021). Despite this significance and ubiquity, its formation and evolution in the star formation cycle are still not fully understood.

Detections of abundant water ice toward molecular clouds and dense prestellar cores show

that significant quantities of water can be produced in the solid state even before the earliest stages of star formation (Tanaka et al. 1990; Knez et al. 2005; Boogert et al. 2011, 2013; McClure et al. 2023). In these environments, water forms on the surfaces of silicate and carbonaceous interstellar grains via cold atom addition chemistry along with other simple species like CO_2, NH_3, and CH_4, resulting in the growth of ice layers that can be observed via infrared spectroscopy (Boogert et al. 2015 and references therein). There is mounting evidence that these water-rich prestellar ice mantles also serve as the birthplace and reservoir of many other more complex molecules, some of which could have prebiotic relevance (Herbst & van Dishoeck 2009; Jørgensen et al. 2020; Nazari et al. 2022; McClure et al. 2023; Chen et al. 2023; Rocha et al. 2024; Nazari et al. 2024).

However, it is uncertain how much of this primordial water ice and its associated chemical complexity survive the subsequent intense thermal and radiative processes that occur upon the formation of protostars and protoplanetary disks. Once a protostellar source forms from a prestellar core and begins to generate radiation, it can cause its surrounding water ice to sublimate into the gas phase via photo- or thermal desorption, where it may be destroyed and subsequently reformed via hot gas-phase neutral-neutral reactions (Bergin et al. 1998; Harada et al. 2010; Visser et al. 2011; Furuya et al. 2013; van Dishoeck et al. 2014; Owen & Jacquet 2015). The extent to which such processing of the prestellar water ice occurs within the hot, radiation-dominated regions of protostellar envelopes and protoplanetary disks has important implications for not only the physicochemical processes that drive their evolution, but also for the chemical inventory available to the planetesimals that eventually begin to form and grow in these environments (i.e., the question of *inheritance versus reset*, van Dishoeck 2017; Öberg & Bergin 2021).

Quantifying the deuterium fractions (D/H ratios) of water offers a promising path to understanding the extent of this processing because deuterium fractionation reactions are extremely sensitive to the physicochemical conditions in which they occur. Therefore, a molecule's D/H ratios reflect the environment in which it formed and existed. In molecular clouds and prestellar cores, molecules are thought to be deuterium enriched due to an increase in the relative abundance of available atomic D (with respect to atomic H) caused by the enhanced gas-phase formation of H_2D^+ (Roberts et al. 2003):

$$H_3{}^+ + HD \rightleftharpoons H_2D^+ + H_2 + 232K$$

At the low temperatures relevant to ice formation (T <50 K), this reaction mostly proceeds in the forward direction due to its energy barrier. The following dissociative recombination reaction can then free D atoms, increasing deuterium atoms that can land on cold dust grains and react to form a higher abundance of deuterated molecules (Tielens 1983):

$$H_2D^+ + e^- \rightarrow H_2 + D$$

Water formed in cold prestellar environments is therefore expected to be deuterium enriched relative to bulk interstellar and solar D/H values (2.0×10^{-5}, corresponding to an HDO/H_2O ratio of 4×10^{-5} if there is no fractionation, Prodanović et al. 2010; Geiss & Gloeckler 2003). The relative abundance of H_2D^+ is further enhanced in the absence of neutral species like O and CO that destroy $H_3{}^+$ and its isotopologs, so deuterium enrichment is expected to be even greater in the molecules formed during the coldest (<20 K) and densest

stages of prestellar cores, when O and CO are depleted from the gas phase as they freeze out on the grains.

Interstellar HDO was first detected in the gas phase in the massive star-forming region Orion KL (Turner et al. 1975). The relatively high brightness of the hot (>100 K) inner cores of such massive young stellar objects (MYSOs) allows multiple lines of HDO to be detected relatively easily with millimeter spectroscopy. The detection of these lines, along with the lines of $H_2^{18}O$, a water isotopolog that is usually optically thin, has enabled the determination of the gas HDO/H_2O ratios toward many of these objects in the last few decades. These ratios typically range between 10^{-4} to a few 10^{-3} (Helmich et al. 1996; van der Tak et al. 2006; Neill et al. 2013; Emprechtinger et al. 2013; Coutens et al. 2014b), an enhancement of up to two orders of magnitude relative to the cosmic standard D/H. Highly sensitive millimeter interferometers also enable reliable measurement of gas HDO/H_2O ratios in the hot inner regions of the much dimmer low-mass young stellar objects (LYSOs), whose ratios see a similar enhancement (Persson et al. 2013, 2014; Jensen et al. 2019, 2021).

This enhancement has been interpreted as evidence that at least some of the water gas detected in protostars has its origins in prestellar ices, in line with the assumption that many of the gas-phase species detected in protostellar hot cores and corinos come directly from ices via thermal desorption. Additionally, the gas HDO/H_2O ratios of clustered LYSOs are remarkably similar to those measured in comets, suggesting that prestellar water ice and its associated chemical complexity may be largely inherited by the planetesimals that grow in the outer protoplanetary disk (Persson et al. 2014).

While studying HDO/H_2O ratios in the gas phase has clearly improved our understanding of the chemical history of water throughout star formation across a range of stellar masses, a glaring question remains: are the HDO/H_2O ratios measured in protostellar hot gas actually representative of the protostellar HDO/H_2O ice ratios, or has the detected water gas already experienced substantial alteration by gas-phase reactions? To answer this question, the HDO/H_2O ratio in ices must be probed directly.

Despite H_2O being the most abundant observable hydrogen-bearing ice by a large margin, a secure detection of its deuterated isotopologs is an exceptional observational challenge. Because it begins to form in the earliest stages of cloud formation, its D/H ratio in the gas phase is a couple orders of magnitude below that of molecules like CH_3OH and H_2CO thought to form only in the later colder stages of cloud formation (Cazaux et al. 2011; Taquet et al. 2012; Caselli & Ceccarelli 2012; Ceccarelli et al. 2014; Furuya et al. 2016), so the column density of HDO ice is expected to be very low. Furthermore, the strongest IR band of HDO, its O-D stretching mode at $\sim$4.1 μm ($\sim$2440 cm^{-1}), lies next to the short-wavelength wing of the strong asymmetric C=O stretching mode of CO_2 ice, which sometimes warps the continuum due to grain shape effects and complicates the detection and quantification of spectrally adjacent species (Dartois et al. 2022, 2024). In the amorphous state, the O-D stretch of HDO is also broad and relatively weak (Dartois et al. 2003; Gálvez et al. 2011).

The first tentative HDO ice detection at 4.1 μm was reported in data from the Infrared Space Observatory (ISO) more than two decades ago by Teixeira et al. (1999), but the detection was soon called into question by Dartois et al. (2003), who pointed out, among several other concerns, that the observed absorption could also be attributed to a weak CH_3OH combination mode whose wavelength overlaps with that of the HDO O-D stretch. They went on to report HDO upper limits ranging from 0.16-1.1% with respect to H_2O toward four intermediate-mass and massive young stellar objects (IMYSOs and MYSOs) with low

CH_3OH column densities. Parise et al. (2003) expanded the search for HDO ice to low-mass young stellar objects (LYSOs) and also derived upper limits, ranging from 0.5-2% with respect to H_2O. Almost a decade later, Aikawa et al. (2012) reported tentative detections and measured very high HDO/H_2O ratios (2-22%) toward four LYSOs, but they cautioned that the HDO ice models did not provide a perfect fit to the observations, and their analysis did not take into account contribution from CH_3OH ice to the HDO ice spectral region. Furthermore, given the recent characterization of how grain growth affects the continuum around the CO_2 ice feature (Dartois et al. 2022), it is possible that some of the observed "broad absorption" that was attributed to HDO ice by Aikawa et al. (2012) was caused by a warping of the local continuum via grain shape effects, particularly in the case of IRAS 04302+2247.

It is evident that the infrared telescopes capable of observing ices in the 4 μm range thus far have lacked sufficient sensitivity to conclusively detect solid-state HDO. The unprecedented sensitivity of the Near Infrared Spectrograph (NIRSpec) instrument on the recently launched *James Webb* Space Telescope (JWST) provides a prime opportunity to revisit the search for interstellar HDO ice.

Here we report HDO ice detections toward two protostars, HOPS 370, and IRAS 20126+4104 (hereafter IRAS 20126), observed with JWST's NIRSpec integral field unit (IFUs) as part of the GO program 1802, Investigating Protostellar Accretion (IPA) across the mass spectrum (Program ID 1802, PI Tom Megeath; Megeath et al. 2021). Care is taken to ensure that the observed HDO ice detections cannot be attributed to the CH_3OH combination mode at 4 μm by establishing a CH_3OH column density via fitting high-resolution laboratory spectra to the 3.53 μm band. Additional high-resolution laboratory spectra of HDO are collected to enable the fitting of the observational spectra and subsequently derive HDO column densities. The laboratory spectra measured and used in this work are made publicly available via the Leiden Ice Database (LIDA, Rocha et al. 2022). Comparisons are made between the derived HDO ice abundances to those measured in the gas phase in the interstellar medium. The resulting implications for the chemical evolution of water throughout the star formation process are then discussed.

2.2 Methods

2.2.1 Investigated sources

Table 2.1: Source parameters and aperture coordinates used to extract spectra from the NIRSpec IFU datacubes.

Source	Distance (pc)	L ($L_\odot$)	RA	Dec
HOPS 370	390[(a)]	314[(b)]	05:35:27.6417	-05:09:33.944
IRAS 20126+4104	1550[(c)]	1.1×10^4[(d)]	20:14:26.2358	+41:13:32.445

[(a)] Tobin et al. (2020a). [(b)] Tobin et al. (2020b). [(c)] Reid et al. (2019). [(d)] Cesaroni et al. (2023)

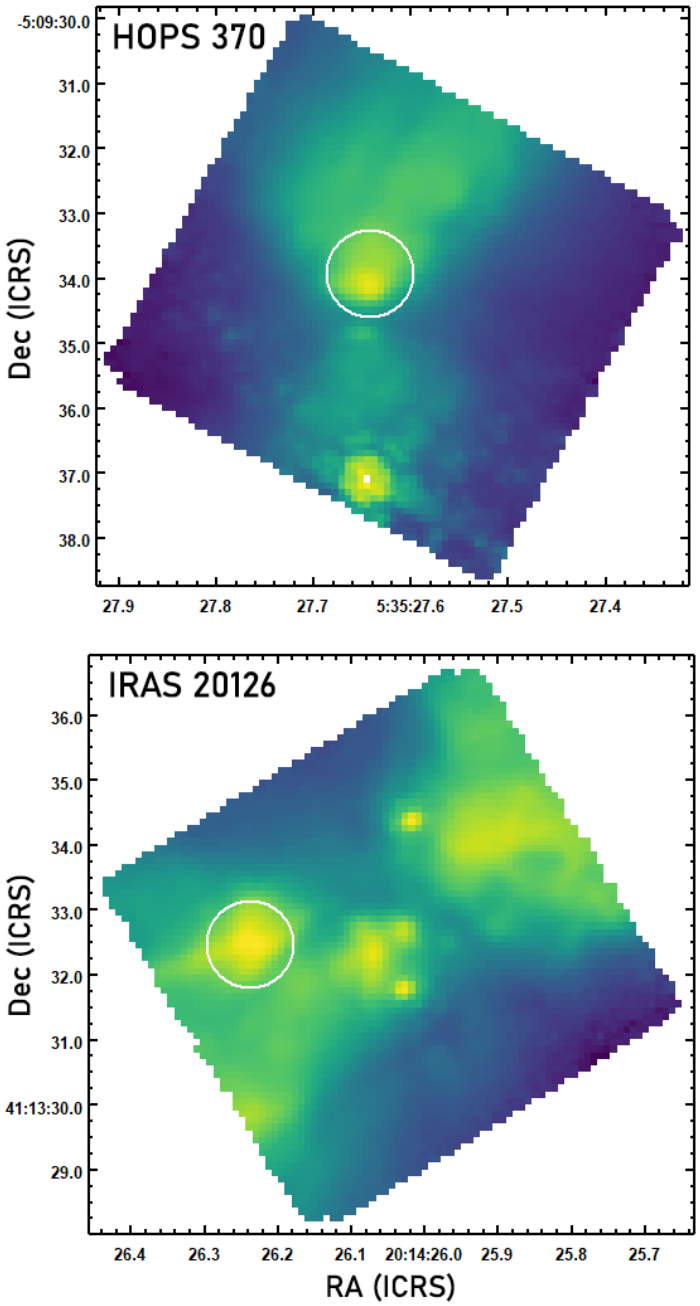


Figure 2.1: 5 μm continuum maps with the aperture used to extract the analyzed spectra at 5 μm shown in white (7$\times$ diffraction-limited radius at 5 μm=0.678").

The IPA program observed five YSOs in their primary accretion phase, with their bolometric luminosities spanning approximately six orders of magnitude, using the NIRSpec IFU (Federman et al. 2024). Out of these sources, two are presently analyzed due to their high S/N and because their IFUs contain lines of sight that have a non-saturated 3 μm O-H stretching feature of H_2O ice, enabling quantification of its column density and characterization of its morphology. Table 4.3 presents an overview of these sources.

HOPS 370 is an IMYSO with a spectral energy distribution (SED) near the Class 0/Class I border located within the very clustered OMC-2 star-forming region in the Orion A molecular cloud. It is likely currently experiencing a high accretion rate, and its compact complex organic molecule (COM) emission is similar to those of hot corinos (Tobin et al. 2020b). It is driving a powerful bipolar outflow observed in the far IR, millimeter, and centimeter wavelength ranges (Shimajiri et al. 2008; González-García et al. 2016; Osorio et al. 2017; Sato et al. 2023).

IRAS 20126 is a deeply embedded MYSO, the most massive and luminous protostar of the sample. The source contains a hot and massive disk (Chen et al. 2016) as well as jet-driven outflows (Caratti o Garatti et al. 2008). Although initial observations suggested that its environment is unusually isolated for a MYSO (Qiu et al. 2008), later observations revealed the presence of a young cluster within a 1.2 pc vicinity (Montes et al. 2015). Two likely companion YSOs are present within the 6"x6" FOV in the NIRSpec IFU of this source (**?**).

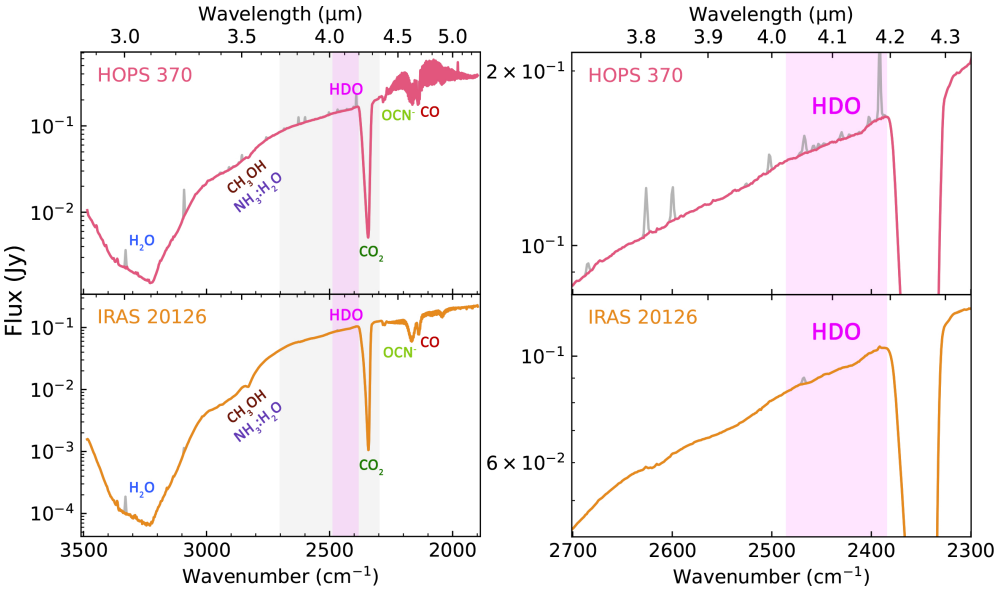


Figure 2.2: Extracted spectra of the investigated sources. Left: full NIRSpec spectra with major ice features labeled. The original spectra before gas emission subtraction are plotted in gray. The spectral region of the strongest HDO absorption, the O-D stretching mode, is indicated via magenta shading. The spectral region plotted on the right is indicated via gray shading. Right: a zoomed-in view of the spectral region of interest for HDO ice.

2.2.2 Observations and data reduction

The investigated spectra were collected with the NIRSpec IFU using the G395M grating (R=$\lambda/\Delta\lambda$∼700-1300, Rubinstein et al. 2024), providing data from 2.9-5.1 μm (3450-1960 cm^{-1}) with no detector gaps, unlike the higher-resolution G395H grating, which has a detector gap in the IFU at 4.1 μm, where the strongest HDO IR band is found. A 4-point dither pattern was used to obtain a 6"×6" mosaic with a 0.2" spatial resolution. Detailed descriptions of the data reduction are provided in **?** and Narang et al. (2024).

The regions in the IFUs from which spectra were extracted for analysis were chosen by searching through the datacube for the highest S/N lines of sight in which the H_2O 3 μm feature is not saturated or extincted. In both cases, the ice features in the selected positions are from the cold envelopes seen in projection in front of bright scattered light emission from the protostars. The HOPS 370 spectrum was extracted near the source center over a knot of shocked gas. Spectra extracted near the central position of IRAS 20126 cannot be used for the analysis in this work because the flux at 3 μm at these coordinates is so low that the profile of the H_2O feature is contaminated by an extended weak emission that may originate from a photodissociation region along the line of sight. Extended weak emission is present toward all of the IPA sources and is seen most distinctly at the edges of the datacubes, where the source continuum fluxes are minimal and a weak PAH emission feature at 3.3 μm is clearly observed. The analyzed spectrum of IRAS 20126 is therefore extracted from a bright position toward an outflow cavity, where the PAH emission flux is negligible relative to the overall observed flux.

The coordinates of the apertures used to extract the spectra are provided in Table 4.3 and are shown on the IFU continuum maps in Figure 2.1. A wavelength-dependent extraction aperture of 7 times the diffraction-limited radius was used, which results in an aperture that is >3 times the full width at half maximum (FWHM) of the NIRSpec IFU point spread function over the entire spectrum. Because the investigated sources have small radial velocities relative to the spectral resolution, the final extracted spectra are not corrected for source velocity (Brunken et al. 2024).

2.2.3 Gas emission subtraction

Both spectra contain gas emission features, including those of H_2, H I, [Fe II], and CO (**?**Narang et al. 2024; Rubinstein et al. 2024). The strongest of these features were subtracted out of the spectral regions of interest (3.33-4.18 μm) via Gaussian fits to prevent their interference with the fitting functions used to analyze the ice features. Most of the gas emission lines are well-resolved from other neighboring gas lines and thus required only single Gaussian profiles to be subtracted out. The few emission lines that are blended were subtracted out using multiple Gaussian profiles.

In all subsequent spectral figures, the original spectra before gas emission subtraction are plotted in gray, and the emission-subtracted spectra are over-plotted in color.

2.2.4 Laboratory data collection

High-resolution (0.5 cm^{-1}) spectra of various laboratory ice mixtures containing HDO, H_2O, CO, and CH_3OH ranging from temperatures of 15-150 K were collected on the InfraRed Absorption Setup for Ice Spectroscopy (IRASIS) in the Leiden Laboratory for Astrophysics

Table 2.2: Laboratory spectra collected for this work.

Mixture	Ratio
$HDO:H_2O$	0.4:100 (thick)*
	0.4:100 (thin)
CH_3OH	pure
$CH_3OH:H_2O$	2:1
	1:1
	1:2
	1:5
$CH_3OH:CO$	2:1
	1:1
	1:2*
	1:5*

* indicates that the strongest peak of the primary matrix component is saturated.

for use in fitting the observed spectra. A schematic of the set-up can be found in Rachid et al. (2021), and recent upgrades to the set-up are described in Slavicinska et al. (2023). The method used to create ice mixtures with specific ratios is similar to that described in Yarnall & Hudson (2022). The chemical compositions and mixing ratios of the laboratory ice mixtures are presented in Table 2.2. Additional experimental details can be found in Appendix 2.A.1.

All of the spectra are made available for public use and enjoyment via LIDA (Rocha et al. 2022). As much of this work focuses on fitting very weak features (i.e., the O-D stretch of highly diluted HDO at 4.1 μm and the combination modes of CH_3OH at 3.9 μm), the strongest peak of the primary ice matrix component (i.e., the C≡O stretching mode of CO or the O-H stretching mode of H_2O) was allowed to saturate in three of the experiments so that the weaker ice features have sufficient S/N for accurate fitting. The spectra with such a saturated peak are indicated with an asterisk (*) in Table 2.2. We strongly warn against using the saturated peaks in these spectra to fit observational data.

The peak positions, FWHMs, and apparent band strengths of the O-D stretching mode from 15 to 150 K were extracted from the $HDO:H_2O$ mixtures for both the amorphous and crystalline phases and are presented in Table 2.A.7 and Figures 2.A.10 and 2.A.11. As discussed in detail in Section 2.3.3, the variation in amorphous HDO band strength with respect to temperature has particularly important ramifications on the derived amorphous HDO abundances. The peak positions of the CH_3OH 3.53 μm band from 15 to 150 K in all of the CH_3OH-containing spectra are presented in Tables 2.A.8 and 2.A.9 and Figure 2.A.12.

2.3 Results

The full extracted spectra of both sources are presented in Figure 5.3. At first glance, it is apparent that in both spectra, the 3 μm O-H stretching modes of H_2O ice have sharp peaks at 3.1 μm, characteristic of a crystalline component (Hagen et al. 1981; Smith et al. 1989). This

indicates that the ices along these lines of sight have experienced enough thermal processing to crystallize some of the water ice. The presence of pure CO_2 components in the $^{13}CO_2$ bands (Brunken et al. 2024), enhanced OCN^- abundances (Nazari et al. 2024), and the relatively low absorptions of the CO ice features at 4.67 μm relative to the CO_2 features at 4.27 μm further corroborate that a significant portion of the ices toward these sources have experienced a substantial degree of thermal processing.

The ice species of interest to this work were analyzed as follows: first, the CH_3OH ice column densities and physicochemical environments were determined from the ∼3.53 μm (∼2830 cm^{-1}) C-H stretching mode (Section 2.3.1). This was done prior to the analysis of the HDO ice because CH_3OH has several weak combination modes between ∼3.7-4.2 μm (∼2700-2400 cm^{-1}), one of which overlaps with the HDO O-D stretching mode at 4.1 μm; therefore, pre-constraining the expected contribution of CH_3OH ice to this region via a column density derived from a stronger band in a different region is necessary to ensure that any CH_3OH absorption at 4 μm is not misattributed to HDO ice (Section 2.3.2), a concern previously raised by Dartois et al. (2003). The HDO ice column densities and morphologies were then determined via fitting the observed absorptions in the ∼3.7-4.2 μm region (Section 2.3.3). Finally, the 3 μm (∼3300 cm^{-1}) H_2O O-H stretching mode was fit to corroborate the morphologies found for HDO ice and to determine the ice HDO/H_2O ratios toward these sources (Section 2.3.4).

2.3.1 CH_3OH ice

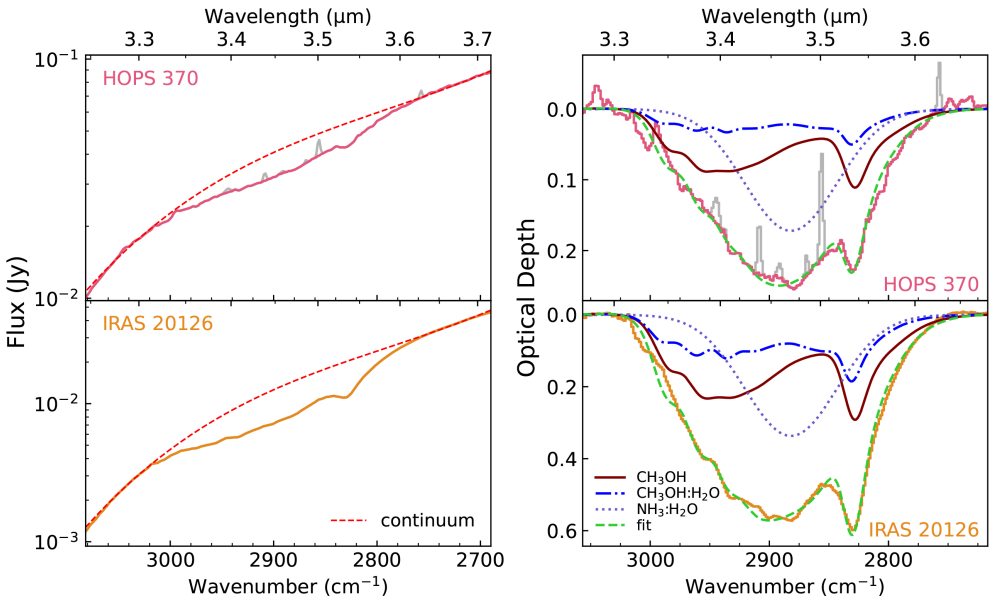


Figure 2.3: Extraction and fitting of the CH_3OH 3.53 μm band. Left: adopted local continua. Right: fits to the extracted optical depth spectra. Some of the substructures present at 3.4 μm in the high S/N spectrum of IRAS 20126 are well reproduced by the more prominent CH_3OH overtones and C-H asymmetric stretching modes that emerge in H_2O-rich CH_3OH spectra.

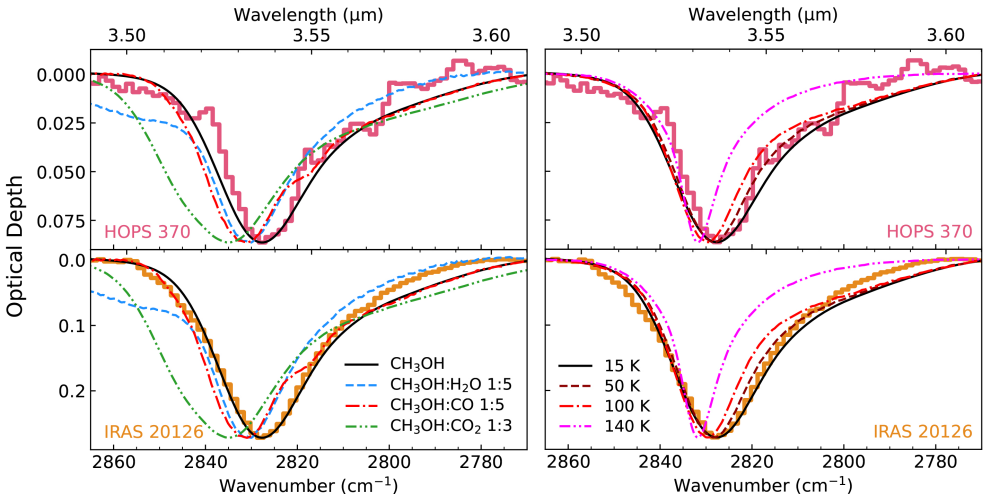


Figure 2.4: The observed CH_3OH C-H symmetric stretching modes compared to select laboratory data. The peaks were extracted from the 3.5 μm absorption complexes via a local continuum fit using baseline points between ∼3.47-3.50 and 3.60-3.62 μm (Figure 3.A.9). It is clear from these comparisons that cold, amorphous, and relatively pure CH_3OH is the major contributor to this feature. Left: observed peaks versus laboratory spectra of CH_3OH ice in various chemical environments. All spectra were collected at 15 K except the CH_3OH:CO_2 spectrum, which was collected at 10 K (Ehrenfreund et al. 1999). Right: observed peaks versus laboratory spectra of pure CH_3OH ice at various temperatures.

Both sources present a clear CH_3OH C-H stretching mode at 3.53 μm. The CH_3OH ice column density can be obtained from this mode via a procedure outlined in Brooke et al. (1999) and Boogert et al. (2022). Briefly, this involves subtracting a local continuum using data points ∼3.25-3.3 and 3.6-3.7 μm and then fitting a Gaussian representing ammonia hydrates with a peak position of 3.47 μm (2881.844 cm^{-1}) and a full-width half maximum (FWHM) of 0.11 μm (91.4 cm^{-1}) along with laboratory CH_3OH ice spectra to the extracted feature. An identical local continuum subtraction is performed on the laboratory data as well prior to fitting the observed data to isolate the C-H stretching modes from the strong and broad O-H stretching feature with which they overlap. The resulting CH_3OH fits, along with the local continuum subtractions used to extract the CH_3OH features into the optical depth scale, are shown in Figure 3.A.9.

Toward both sources, the peak position of the 3.53 μm band is most consistent with laboratory data of cold (<60 K), amorphous, relatively pure CH_3OH ice (Figures 2.4 and 2.A.12). The 3.53 μm bands of laboratory CH_3OH ices that is warm, crystalline, or diluted with any of the three most abundant observable interstellar ice components (H_2O, CO, and CO_2) are too blue-shifted to fit the observed absorption. However, fitting the entire 3.5 μm region with only pure amorphous CH_3OH ice results in the spectrum being overfit at 3.4 μm by the blended CH_3OH overtones and C-H asymmetric stretching modes.

This issue of pure CH_3OH ice spectra causing overfitting at 3.4 μm has previously been documented toward some LYSOs and MYSOs and was solved by using spectra of CH_3OH mixed with H_2O (Brooke et al. 1999; Pontoppidan et al. 2003), which decreases the optical depth of the 3.4 μm features relative to that of the 3.53 μm feature. Such a decrease is not observed in CO- or CO_2-rich CH_3OH mixtures or in crystalline CH_3OH ices. Using a combi-

nation of two laboratory amorphous CH_3OH spectra, one of pure CH_3OH ice and an H_2O-rich CH_3OH ice mixture (1:5 CH_3OH:H_2O), in the fitting procedure results in satisfactory fits of both the 3.53 μm band and the 3.4 μm region (Figure 3.A.9). A similar combination of pure CH_3OH and CH_3OH:H_2O laboratory spectra was used by Dartois et al. (1999) to fit the 3.53 and 3.9 μm features in the spectra observed toward MYSOs W33A and RAFGL 7009s.

Table 2.3: Derived CH_3OH ice column densities and abundances with respect to H_2O ice.

Source	CH_3OH	
	(10^{17} cm^{-2})	(% H_2O)
HOPS 370	7.8±1.6	16±6
IRAS 20126	22±4	27±10

The resulting CH_3OH column densities (reported in Table 2.3) are obtained using the band strength of 4.86×10^{-18} cm molec^{-1} for the C-H stretching mode of pure amorphous CH_3OH at 20 K (Luna et al. 2018). This band strength was chosen because the profile of the 3.53 μm band indicates that the majority of the detected CH_3OH ice along these lines of sight is pure, amorphous, and cold (>60 K). The ratio of pure CH_3OH ice to CH_3OH ice mixed with H_2O that results in the best fits is highly dependent on the dilution factor of the CH_3OH:H_2O mixture used, so separate column densities for each of the two CH_3OH components were not calculated. Any effects of dilution with H_2O on the band strength of this feature are expected to be well within the 20% uncertainty reported for the pure band strength (Kerkhof et al. 1999; Luna et al. 2018). The reported uncertainties are explained in Appendix 2.A.3. The implications of the non-detection of warm or crystalline CH_3OH ice toward these lines of sight are further discussed in Section 2.4.3.

2.3.2 4 μm region: CH_3OH, S-bearing species, and HDO

A local continuum in the 3.7-4.2 μm (2700-2380 cm^{-1}) region was adopted so that the optical depth of the CH_3OH combination modes predicted by the CH_3OH column density derived from the 3.53 μm band did not exceed the optical depth of the continuum-subtracted spectrum, providing a constraint to prevent over-subtraction of features due to continuum choice in this region. The RMS error in optical depth was calculated for this region using data from 3.70-3.77 μm (2700-2650 cm^{-1}). It is important to note that, as can be seen in the right panel of Figure 5.3, the warping of the continuum by the scattering wings of the strong 4.27 μm CO_2 feature is very minimal in both spectra in comparison to some other icy lines of sight (e.g., Dartois et al. 2022, 2024), greatly reducing the uncertainty of the local continuum placement in this region. The adopted local continua, the subtracted spectra in optical depth units, and the 3σ uncertainty levels from the RMS error are presented in Figure 2.5.

Following this procedure, both lines of sight have excess absorption on top of the CH_3OH feature at ∼3.9 μm (∼2550 cm^{-1}). Jiménez-Escobar & Muñoz Caro (2011) noted a similar excess absorption in the spectrum of the MYSO W33A and used it to derive an H_2S ice upper limit. However, Hudson & Gerakines (2018) recently pointed out that many other S-H

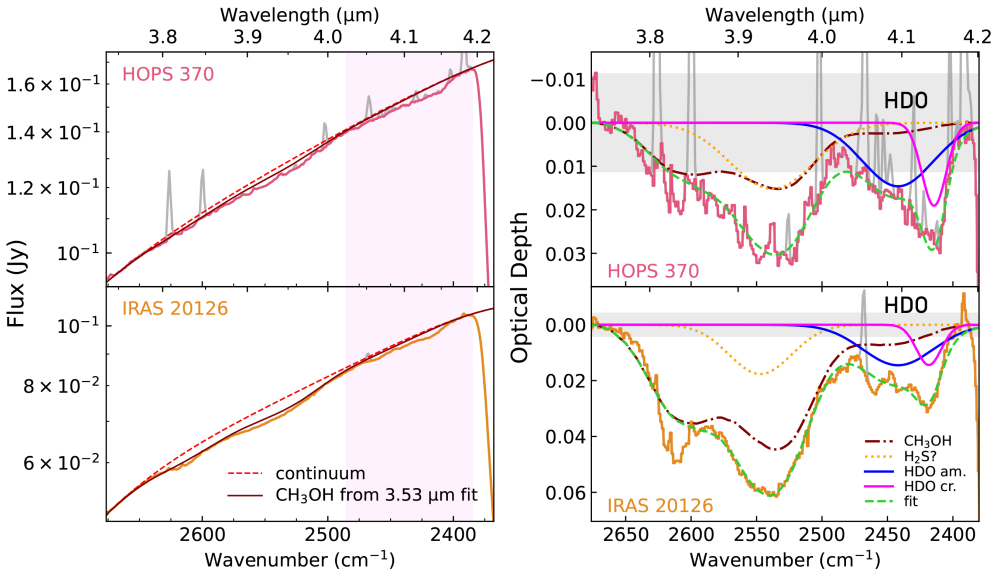


Figure 2.5: Extraction and fitting of the 4 μm region. Left: adopted local continua, along with CH_3OH spectra determined from the 3.53 μm band fitting used to aid the continuum placement. The spectral region of the HDO O-D stretching mode is indicated via magenta shading. Right: fits to the extracted optical depth spectra (am. = amorphous; cr. = crystalline). The shaded gray regions indicate 3σ uncertainty levels. The same combination of pure and H_2O-rich CH_3OH spectra as used to fit the 3.53μm feature is used in this fit. The best-fitting temperatures of the amorphous/crystalline HDO ice components are 132 K/47 K for HOPS 370 and 138 K/90 K for IRAS 20126, respectively (see Sections 2.3.3 and Appendix 2.A.2 for more details).

bond-containing ices, like CH_3SH and CH_3CH_2SH, have strong absorption features in this spectral region with nearly identical peak profiles, making it difficult to conclusively assign the broad excess absorption in this region to a specific molecule. Additionally, there is a lack of publicly available laboratory ice spectra of many of these sulfur-bearing species in astrophysically relevant mixtures. As sulfur-bearing ices are not the focus of this paper and the fitting of this feature has little effect on the analysis of the HDO ice feature, we simply fit this excess with a Gaussian and leave further analysis to a future work.

A small, narrow excess absorption is also present in both lines of sight at $\sim$3.83 μm ($\sim$2611 cm^{-1}), in addition to a sharp peak toward IRAS 20126 at $\sim$4.07 μm ($\sim$2459 cm^{-1}). We initially suspected these features could be attributed to crystalline CH_3OH ice, which has two sharp peaks at 3.83 and 4.07 μm (2612 and 2455 cm^{-1}) in the pure form. However, the entire CH_3OH combination mode complexes over the full 3.7-4.2 μm range could not be satisfactorily fit with any available crystalline CH_3OH ice spectra, pure or mixed. The observed spectra are missing an additional sharp and distinct feature at 3.94 μm (2536 cm^{-1}) that is present in the crystalline CH_3OH laboratory spectra. Annealed crystalline CH_3OH spectra also did not provide a good fit. Furthermore, the 3.53 μm feature lacks any significant spectral contribution from crystalline CH_3OH ice. Because no other ice spectra available to us provided a convincing match, we refrain from assigning these features, although we do not

completely exclude crystalline CH_3OH as a candidate carrier.

Finally, in both lines of sight, excess absorption emerges from the continuum between ~4.04-4.17 μm (~2475-2400 cm^{-1}) which cannot be accounted for by the CH_3OH combination mode without inducing unrealistic inflections in the local continua or overfitting the CH_3OH combination modes between 3.8-3.9 μm. There are no currently known S-H bond-bearing species whose absorptions peak at these wavelengths (Hudson & Gerakines 2018), and the features present in crystalline CH_3OH ice spectra in this spectral region are all too blue-shifted from the observed peak positions at ~4.14 μm. We therefore assign these features to HDO ice in various morphological states.

2.3.3 HDO ice

We performed fits to the local continuum-subtracted 4.04-4.17 μm region using a combination of CH_3OH ice laboratory spectra, a Gaussian representing S-H bond-bearing species, and HDO ice laboratory spectra. Prior to the fitting, the profiles of the HDO O-D stretching features were isolated from the underlying broad H_2O combination modes in the 0.4% HDO:H_2O ice spectra (see Figure 2.A.9) and subsequently smoothed with Gaussian fits to eliminate experimental noise. The optical depths of the CH_3OH combination modes (as constrained by the CH_3OH column density derived from the 3.53 μm band in Section 2.3.1) and the Gaussian fit to the 3.9 μm excess were not varied in the fitting procedure. The same combinations of pure and H_2O-rich CH_3OH ice spectra that were used to fit the 3.53 μm feature were also used here.

Toward both sources, a minimum of two HDO profiles, one amorphous and one crystalline, is needed to fit the HDO feature due to its asymmetric profile. The 3 μm H_2O bands toward both sources also have profiles characteristic of the lines of sight containing both amorphous and crystalline H_2O ice (Section 2.3.4). This correlation between the detected presence of crystalline H_2O and crystalline HDO provides additional confidence in the peak assignment, because if some regions of the observed ice envelopes have been thermally processed enough to crystallize the H_2O ice, then any HDO ice in those regions should have crystallized as well.

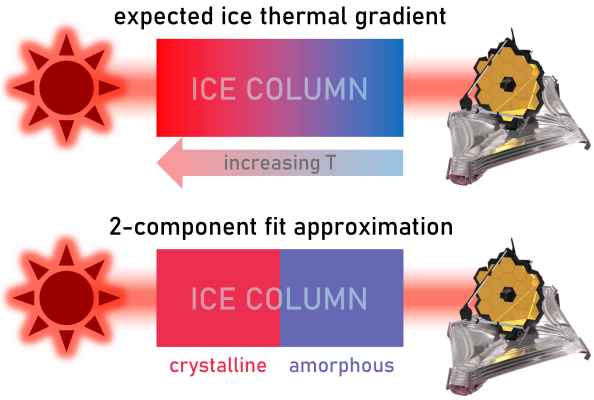


Figure 2.6: A simplified diagram showing the difference between the expected thermal profile of the observed ice columns and the two-component fit approximation used to fit the observations in this work.

In total, 84 amorphous HDO ice spectra between 15-140 K and 22 crystalline HDO ice spectra between 15-150 K were collected. Every possible combination of one amorphous profile and one crystalline profile out of these spectra were fit to the observed spectra using a least-squares fitting procedure. The least-squares fits that result in the lowest χ^2 value for both lines of sight are presented in Figure 2.5. The relationships between the fit χ^2 values and the temperatures of the laboratory spectra are shown in Figure 2.A.13.

It is important to emphasize that the temperatures resulting in the lowest χ^2 values should not be interpreted as the actual temperatures of the observed ices for four reasons. First, laboratory ice temperatures do not correspond directly to interstellar ice temperatures due to the faster heating rates and higher pressures experienced by laboratory ices (Redhead 1962; Minissale et al. 2022). This means that, in the laboratory, ices crystallize and desorb at higher temperatures than in the interstellar medium. Second, these fits are not guaranteed to be unique, especially given that the broad, weak profile of the amorphous HDO could be considered degenerate at a wide range of temperatures when accounting for fitting errors caused by factors such as the observed spectral noise and uncertainties in the local continuum choice. This is particularly clear from Figure 2.A.13, which shows that a wide range of HDO temperatures produce fits that are degenerate within 3σ. Third, it is possible that much of the HDO ice along these lines of sight is located in different chemical environments than just pure H_2O ice, which could further alter the HDO band profile. For example, models from Taquet et al. (2014) and Furuya et al. (2016) suggest that the majority of HDO ice is co-produced with CH_3OH ice after the heavy CO freeze-out stage. Changes in the amorphous HDO feature caused by such chemical environments are difficult to unambiguously characterize in the laboratory due to the spectral overlap between the main HDO band and the CH_3OH combination modes. However, such chemical environments would not be expected to affect the crystalline component because CH_3OH and CO both desorb at temperatures lower than the water ice crystallization temperature, so by the time HDO ice crystallizes, it is expected to have been effectively distilled by heating. And finally, fitting two laboratory spectra at discrete temperatures to the observations is merely an approximation of the expected continuous thermal gradient experienced by the observed ices along each line of sight (Figure 2.6).

Nonetheless, such an approximation is still useful for evaluating the thermal structure of the ice envelope qualitatively (Smith et al. 1989). In particular, the presence of a crystalline HDO component indicates that at least some regions within the ice envelopes must have experienced temperatures high enough to crystallize water ice, while the presence of an amorphous component indicates that other regions of the ice envelopes must have remained colder. Furthermore, the peak position of the crystalline HDO component, which suffers from much less uncertainties due to its sharper profile, matches best with annealed laboratory spectra, hinting at a possibility of heated ices being re-cooled within the ice envelope (see further discussion in Section 2.4.3).

The uncertainty in the temperature of the observed ices translates to an uncertainty in any HDO ice column density calculations because the apparent band strength of the O-D stretching feature in HDO measured in the laboratory varies with temperature, particularly for the amorphous phase (see Figure 2.A.10). Between 15 and 135 K, the amorphous HDO apparent band strength increases by a factor $\sim$1.7 from 4.2×10^{-17} to 7.1×10^{-17} cm molec^{-1}. This uncertainty is much smaller for the crystalline HDO component because its apparent band strength only varies by $\sim$8% between 15-150 K. When calculating the HDO column densities from the fits, we used band strengths of 6.0×10^{-17} and 6.7×10^{-17} cm molec^{-1} for the

amorphous and crystalline HDO ice features, respectively, which correspond to intermediate laboratory ice temperatures of around 80 K for the amorphous component and 90 K for the crystalline component (see Table 2.A.7). The resulting HDO ice column densities are listed in Table 2.4, and the reported uncertainties are explained in Appendix 2.A.3.

Table 2.4: Derived HDO ice column densities and abundances with respect to H_2O ice.

Source	Amorphous HDO (10^{16} cm^{-2})	Crystalline HDO (10^{15} cm^{-2})	Total HDO (10^{16} cm^{-2})	Total HDO (% H_2O)
HOPS 370	1.6±0.8	6.5±0.5	2.3±0.8	0.46±0.22
IRAS 20126	1.6±0.9	5.0±0.9	2.1±0.9	0.26±0.14

Within the uncertainties, the ratio of amorphous:crystalline HDO ice column densities are calculated to be between ∼1.2-4 for HOPS 370 and between ∼1.2-6 for IRAS 20126 (i.e., there is more amorphous than crystalline HDO ice toward both sources). However, it must be emphasized once more that the uncertainties of the assignment, fits, and calculated column densities are greater for the amorphous HDO component because the amorphous profile is significantly weaker and broader and its apparent band strengths vary to a much greater extent with temperature, so more precise ratios of amorphous:crystalline HDO ice cannot be determined.

2.3.4 H_2O ice

To estimate the ice HDO/H_2O ratios along these lines of sight, we quantified the H_2O ice column density from the 3 μm band by defining global continua over the full NIRSpec G395M range and subsequently fitting the 3 μm band with laboratory H_2O ice spectra. The global continua and least-squares fits of the 3 μm feature are presented in Figure 2.7.

An important caveat in the analysis of this feature is the lack of collected continuum data points below 2.9 μm, resulting in greater uncertainties in the slope of the blue wing and optical depth of the 3 μm feature in the global continuum-subtracted spectra. We attempted to mitigate this issue by using spectra of other MYSO ice envelopes as templates to guide our global continuum choice. These spectra contain continuum data points $<$2.9 μm, making their global continuum determinations and subsequent H_2O profile extractions much more reliable, and their H_2O profiles are similar to those in the spectra investigated in this work. The best-matching H_2O profiles found for HOPS 370 and IRAS 20126 were those of Orion from ISO (shown in Dartois & d'Hendecourt 2001) and G034.7123-00.5946 from IRTF (shown in Boogert et al. 2022), respectively. The continuum points on the blue side of the 3 μm band were then defined so that the profile of the 3 μm feature in the JWST spectra replicated the profile in the template spectra as closely as possible (see Figure 2.7).

As done in previous studies (Smith et al. 1989; Dartois & d'Hendecourt 2001), the H_2O band in the optical depth scale was then fit with multiple components as an approximation to the thermal gradient expected along the line of sight. The fitting procedure was analogous to that performed on the 4 μm region in that the best-fitting combination of one amorphous and

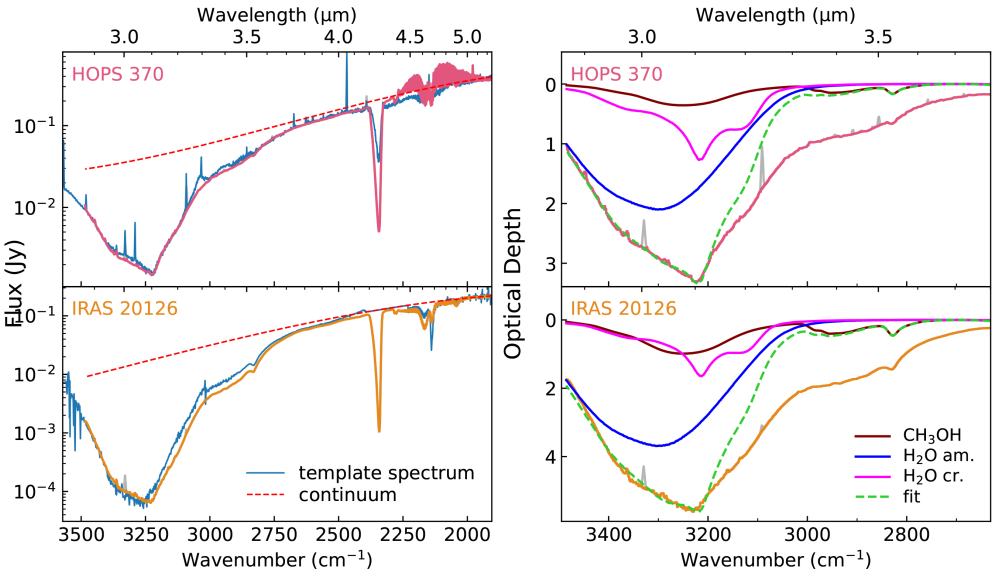


Figure 2.7: Extraction and fitting of the H_2O 3 μm band. Left: adopted global continua and the archival MYSO ice spectra used as templates to guide the continuum choice. Right: fits to the extracted optical depth spectra (am. = amorphous; cr. = crystalline).

one crystalline H_2O lab spectrum was determined by calculating the χ^2 values of the least-squares fits of every possible combination. As stressed in Section 2.3.3, the temperatures of the lab H_2O ices fit to the observations should not be taken as indications of the real physical temperature of the observed ices, as these two-component fits are only simple approximations of the thermal gradient that is expected along these lines of sight, and they are not guaranteed to be unique; however, it is certain that some combination of cold and warm ices is needed to sufficiently fit the feature toward both sources. Furthermore, similarly to the analysis performed by the ICE AGE team in McClure et al. (2023), grain shape effects were not modeled in these fits, as a detailed characterization of the H_2O 3 μm band is outside our primary scope (quantifying H_2O to obtain HDO/H_2O ratios). Indeed, recently published follow-up analyses of grain shape effects in the ICE AGE spectra show that their derived relative ice abundances are largely the same regardless of whether their spectral fitting procedure includes grain shape effects (Dartois et al. 2024).

The contribution of the O-H stretching mode of CH_3OH ice to the observed 3 μm feature was also approximated similarly to the HDO fitting procedure, where the column density of CH_3OH was set as a constant value from the fits to the 3.53 μm band. However, a spectrum of only pure CH_3OH was used to model the contribution of CH_3OH to the 3 μm feature, as it is difficult to accurately deconvolve the overlapping O-H stretching modes of CH_3OH and H_2O in the CH_3OH:H_2O lab spectra. Contributions to the red wing by ammonia hydrates were neglected. For this reason (as well as the neglect of grain shape effects), only the region from 2.88-3.13 μm (3470-3191 cm^{-1}) was considered in the fitting procedure, and the long-wavelength wing of the 3 μm feature remains underfit. This underfitting is taken into account in our reported uncertainties (see Appendix 2.A.3).

Similar to the band strength of the HDO O-D stretch, the band strength of the H_2O O-H stretch varies with temperature. The reported magnitude of this variation differs in the literature (Hagen et al. 1981; Gerakines et al. 1995; Mastrapa et al. 2009). In our experiments, the integrated absorbance of the O-H stretch increases by a factor of up to 1.26 between 15 and 135 K in amorphous H_2O, while there is only a factor of 1.16 difference between the integrated absorbance at 150 and 15 K in crystalline H_2O. These variations are again treated as a source of uncertainty in the reported H_2O column densities (see Appendix 2.A.3).

Table 2.5: Derived H_2O ice column densities.

Source	Amorphous H_2O (10^{18} cm^{-2})	Crystalline H_2O (10^{17} cm^{-2})	Total H_2O (10^{18} cm^{-2})
HOPS 370	4.0±1.7	9.9±3.1	5.0±1.7
IRAS 20126	7.0±2.7	12±4.1	8.3±2.8

To quantify H_2O, all of the fit H_2O components were integrated, and a band strength of 1.9×10^{-16} cm molec^{-1} (Mastrapa et al. 2009) was used for the amorphous component. For the crystalline component, a band strength of 2.5×10^{-16} cm molec^{-1} was used, which is the apparent band strength we calculated for the crystalline H_2O O-H stretch below 120 K in our laboratory spectra. The resulting values are reported in Table 2.5. Within the error margins, the ratios of amorphous:crystalline H_2O ice column densities range from 3.8-5.8 toward HOPS 370 and 5.7-9.1 toward IRAS 20126. These amorphous:crystalline ratios are higher than those of HDO but remain in agreement when considering uncertainties. We refrain from drawing chemical conclusions from the comparison between amorphous and crystalline column densities of HDO and H_2O ice for reasons discussed in Section 2.4.1.

2.4 Discussion

2.4.1 Inferred ice HDO/H_2O ratios

The ice HDO/H_2O ratios measured toward HOPS 370 and IRAS 20126, $4.6\pm2.2\times10^{-3}$ and $2.6\pm1.4\times10^{-3}$, respectively, are both two orders of magnitude greater than what is expected from the cosmic standard D/H abundance. This enhancement far exceeds our reported error margins and is consistent with the deuterated water ice that we detect along these lines of sight having cold, prestellar origins. The ice HDO/H_2O of the IMYSO is higher by almost a factor of 2 compared to the MYSO, but this difference is not significant within the error margins of both values. A larger sample size of ice detections in IMYSOs and MYSOs is needed to draw concrete conclusions regarding any systematic differences between IMYSO and MYSO ice HDO/H_2O ratios.

While the ice HDO/H_2O measured toward these protostars are expected to largely reflect their prestellar conditions and timescales, experimental works have shown that it is also possible for the prestellar D/H ratios of protostellar ices to be altered prior to sublimation via inter-species deuterium exchange reactions during ice thermal processing. Specifically,

deuterium exchange reactions proceed very efficiently in warm ices ($T \gtrsim$70-120 K) between atoms involved in hydrogen bonds in a variety of astrophysically relevant simple molecules (Kawanowa et al. 2004; Ratajczak et al. 2009; Faure et al. 2015; Lamberts et al. 2015) and are particularly promoted between water molecules following the phase transition from amorphous to crystalline (Gálvez et al. 2011).

It may therefore be tempting to compare the ice HDO/H_2O ratios of the separate amorphous and crystalline components to investigate if a difference in deuteration ratio in the unprocessed versus thermally processed ices can be observed. Although the HDO/H_2O ice ratios of the reported crystalline components are higher than those of the amorphous components toward both sources (i.e., the ratios of amorphous:crystalline column densities are lower for HDO than for H_2O), we caution against drawing chemical conclusions from these differences for multiple reasons: 1) the differences are close to the reported error margins and therefore are far from statistically significant; 2) because the two-component fits only approximate the expected thermal gradients, the relative abundances of amorphous to crystalline ices are also only approximate; and 3) grain shape effects were not taken into account when the H_2O bands were fit. This last point is particularly important to remember because, while including grain shape effects in spectral fitting procedures may not greatly affect the derived overall relative molecular abundances of ice species, the warping of the strongest ice bands by grain shape effects do preclude detailed quantitative analysis of ice temperature, morphology, or chemical environment via the profiles of such bands without accounting for grain shape correction (Dartois et al. 2024).

2.4.2 Comparing ice and gas HDO/H_2O ratios

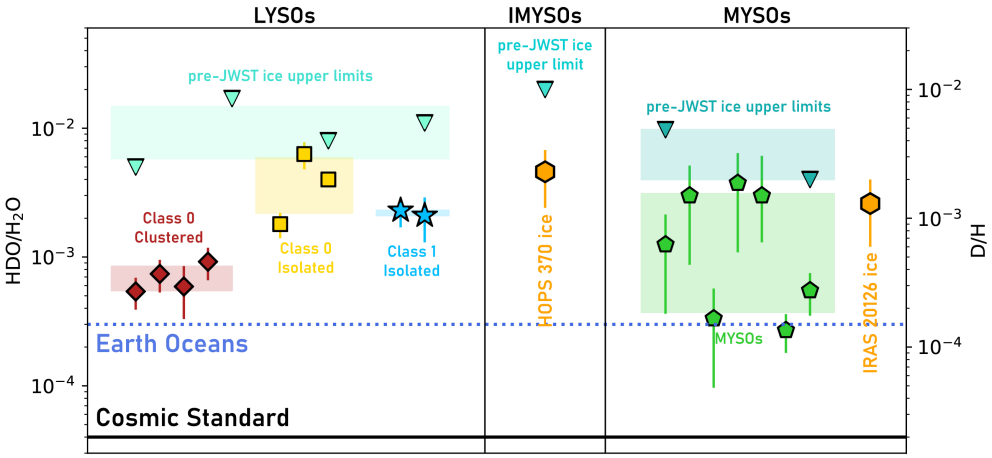


Figure 2.8: Comparison of HDO/H_2O ratios measured in the gas and ice toward protostars of various masses (adapted from Jensen et al. 2019 and Andreu et al. 2023). Ratios measured in the gas phase are plotted with red diamonds for clustered Class 0 LYSOs, yellow squares for isolated Class 0 LYSOs, blue stars for isolated Class 1 LYSOs, and green pentagons for MYSOs. Ice upper limits derived from pre-JWST spectra are plotted with teal triangles. The JWST ice values from this work are plotted with orange hexagons. The literature values used in this figure are provided in Table 2.A.10.

Figure 2.8 provides a comparison of the ice HDO/H_2O ratios measured in this work with previously published protostellar gas phase ratios and ice upper limits from predecessor IR telescopes.

The MYSO gas HDO/H_2O ratios reported in the literature over the past couple decades span an order of magnitude from values as low as 2-3$\times10^{-4}$ (Emprechtinger et al. 2013; Coutens et al. 2014b) to as high as 2-3$\times10^{-3}$ (van der Tak et al. 2006; Neill et al. 2013). The ice HDO/H_2O ratio measured in this work toward the MYSO IRAS 20126 is in agreement with the highest gas-phase MYSO HDO/H_2O ratios. The agreement supports the frequently made assumption that deuterium abundances detected in the hot inner regions of protostars are representative of deuterium abundances in ices.

An ice HDO/H_2O ratio on the order of 10^{-3} toward a MYSO is also consistent with the conclusions drawn by van der Tak et al. (2006), who observed an inverse correlation between the gas HDO/H_2O ratios and the mass-weighted average envelope temperatures of the four MYSOs they studied. They interpreted this as evidence that the HDO/H_2O ratios on the order of 10^{-3} (measured toward the coldest envelopes) were the most representative of ice HDO/H_2O ratios, while the HDO/H_2O ratios on the order of 10^{-4} (measured toward the warmer, more evolved envelopes) had already been partially altered by gas-phase reactions in the hot cores where water ice desorbs. It is interesting to also note that, according to the fits of Boogert et al. (2000), the $^{13}CO_2$ ice features of the two sources studied by van der Tak et al. (2006) with lower HDO/H_2O ratios show a significant degree of CO_2 ice segregation and therefore thermal processing, while the $^{13}CO_2$ ice feature of the van der Tak et al. (2006) source in which the gas HDO/H_2O ratio was the highest, W33A, is indicative of a much lower degree of thermal processing.

However, it is also possible that MYSOs could vary significantly in their prestellar timescales and conditions, and therefore their ice HDO/H_2O ratios may greatly differ. A larger sample size of MYSO ice HDO/H_2O measurements will be needed to ascertain what causes the observed spread in MYSO gas HDO/H_2O values. In any case, the agreement between the IRAS 20126 ice HDO/H_2O ratio and the gas HDO/H_2O ratios of several other MYSOs suggests that the water gas detected toward at least some hot cores has not been substantially processed by gas-phase reactions.

van der Tak et al. (2006) additionally noted that the gas HDO/H_2O ratios measured toward their MYSOs are one to two orders of magnitude lower than those measured in LYSOs, consistent with the theory that LYSOs experience longer prestellar dense stages than MYSOs. An analogous trend is observed in the deuterium ratios of protostellar gas-phase CH_3OH, which are on average more than an order of magnitude lower in MYSOs than LYSOs; such a difference can be explained with models if MYSOs have shorter and/or warmer prestellar stages relative to LYSOs (van Gelder et al. 2022). However, the most recent gas HDO/H_2O LYSO values that utilize interferometric techniques to target only the hot inner regions of these objects and detect multiple high S/N HDO lines indicate that some of the previously measured LYSO gas HDO/H_2O ratios were likely overestimated by one to two orders of magnitude (Persson et al. 2013). In fact, recent gas phase ratios of isolated LYSOs (which are thought to experience long and cold dense stages) ranging from 1.8-6.3$\times10^{-3}$ (Jensen et al. 2019, 2021) are very similar to the highest measured MYSO gas ratios as well as the IMYSO and MYSO ice ratios measured here. The clustered LYSO gas ratios are on average a factor of a few lower, ranging from 5.4-9.2$\times10^{-4}$ (Persson et al. 2014; Jensen et al. 2019), and are more similar to the low-end of measured MYSO ratios.

This similarity in the recently published gas HDO/H_2O ratios of LYSOs and MYSOs could be interpreted in a number of ways. One potential explanation is that the most recently published gas-phase LYSO HDO/H_2O ratios have been altered by gas-phase reactions, meaning that the measured hot inner gas molecular abundances are not fully representative of the molecular abundances of icy species (similar to the interpretation of MYSO gas HDO/H_2O ratios on the order of 10^{-4} made by van der Tak et al. 2006). Measurements of ice HDO/H_2O ratios toward LYSOs may prove useful in resolving if this is the case.

Alternatively, some MYSOs may experience prestellar stages with timescales and temperatures similar to LYSOs. Measuring the gas-phase D_2O/HDO ratios in MYSOs could elucidate the credibility of this latter scenario. This is because D_2O/HDO ratios, especially when compared to HDO/H_2O ratios, are also an excellent diagnostic of formation conditions (Furuya et al. 2017). Multiple studies have measured gas D_2O/HDO ratios in LYSOs that are more than a factor of two higher than their gas HDO/H_2O ratios (Coutens et al. 2014a; Jensen et al. 2021), a result that can only be reproduced by models if the majority of deuterated water ice is produced in the cold dense prestellar stage after the heavy CO freeze-out stage alongside CH_3OH ice (Furuya et al. 2016).

Due to the extremely low abundance of D_2O, few gas D_2O/HDO ratios have been measured in either LYSOs or MYSOs. Currently, one D_2O/HDO ratio has been measured toward the hot core of the Orion KL MYSO (Neill et al. 2013). This value, 1.6×10^{-3}, is an order of magnitude lower than the gas D_2O/HDO ratios that have been measured in LYSOs (Jensen et al. 2021), which may indicate that less of the deuterated water detected toward Orion KL was produced in the cold dense prestellar stages. However, this is again a comparison of very few data points, and more D_2O/HDO measurements in both LYSOs and MYSOs are needed to draw such a conclusion with certainty.

2.4.3 Ice envelope evolution

In addition to the ice HDO/H_2O ratios, the ice fitting performed in this work can also provide information about the thermal and chemical evolution of the ice envelopes surrounding the investigated objects.

Ice thermal cycling

The peak position of the crystalline components observed toward HOPS 370 and IRAS 20126 match best with that of annealed HDO ice (*i.e.*, HDO that has been heated to its crystallization temperature and then cooled back down), as fits using non-annealed crystalline HDO ice at 150 K result in $\Delta\chi^2$ values that lie outside the 3σ confidence intervals (Figure 2.A.13). Such an observed red-shift from the laboratory crystalline HDO ice peak positions at 150 K may be indicative of thermal cycling within the protostellar envelopes, where ice that was heated to high enough temperatures to transition from an amorphous to a crystalline state was either transported back to cooler regions in the cold envelope (e.g., via motions driven by outflows), or the thermal gradient within the cold envelope changed (e.g., due to an accretion burst).

CH_3OH ice formation

The CH_3OH ice abundances of 16% and 27% with respect to H_2O ice toward both sources are on the high end of the values typically measured for both low-mass and massive protostars

(Boogert et al. 2015 and references therein). Although unusual, it is not unprecedented for such high values to be measured toward MYSOs (Dartois et al. 1999). These high CH_3OH ice abundances may be due to particularly long cold dense prestellar stages relative to the length of the warmer and less dense stages when the bulk of the H_2O ice is produced. As models suggest that the majority of HDO ice is produced during the cold dense prestellar stage with CH_3OH ice (Furuya et al. 2016), this would imply that the ice HDO/H_2O ratios measured here could also be on the high end of most protostars, and other protostars with lower CH_3OH ice abundances relative to H_2O ice that had shorter cold dense prestellar stages could then have lower ice HDO/H_2O ratios. However, it is also possible that thermal processing could affect CH_3OH ice abundances. Correlations between ice HDO/H_2O ratios, CH_3OH ice abundances, and the profiles of ice thermal processing tracers like $^{13}CO_2$ may be interesting to investigate once the sample size of measured ice HDO/H_2O ratios is larger.

The fact that the current fitting procedure of the 3.5 μm absorption complex requires a component of CH_3OH in H_2O-rich mixtures also carries astrochemical significance. Although the earliest fits to CH_3OH ice features toward protostars often utilized H_2O-rich CH_3OH ice mixtures (Allamandola et al. 1992; Dartois et al. 1999; Brooke et al. 1999; Pontoppidan et al. 2003), subsequent studies popularized an ice evolution model where most of the observed CH_3OH ice forms after CO freeze-out in a relatively CO-rich and H_2O-poor ice environment. This model is supported by analysis of the profiles of the 9.75 μm CH_3OH ice C-O stretching mode (Bottinelli et al. 2010), the "red component" of the 4.67 μm CO ice C$\equiv$O stretching mode (Cuppen et al. 2011; Penteado et al. 2015), the relationships between CH_3OH ice column densities, CO ice column densities, and visual extinction A_v (Boogert et al. 2015), and the experimentally demonstrated efficiency of solid-state CH_3OH formation via CO hydrogenation (Watanabe & Kouchi 2002; Fuchs et al. 2009)

However, recent experimental works indicate that CH_3OH can also be produced in H_2O-rich ices via a reaction between CH_4 and OH radicals (Qasim et al. 2018), albeit less efficiently than via CO hydrogenation. Recent JWST data toward prestellar cores, where the 9.75 μm CH_3OH ice feature is well-fit with a combination of CO-rich and H_2O-rich CH_3OH ice mixtures, provide observational evidence supporting this pathway as a secondary means of prestellar CH_3OH ice production (McClure et al. 2023). In our fits, the lack of a CO-rich CH_3OH ice component is likely due to the fact that most of the CO ice toward these lines of sight has thermally desorbed, as indicated by the low CO ice column density and presence of CO gas lines toward both lines of sight (**?**Rubinstein et al. 2024), leaving behind a layer of nearly pure CH_3OH ice that likely formed via CO hydrogenation, as well as some CH_3OH ice in a water-rich chemical environment that may have formed during the less dense prestellar stages, perhaps via the CH_4 + OH pathway.

Notably, despite the presence of thermal processing tracers in both spectra, there is a lack of strong spectroscopic evidence of heated or crystalline CH_3OH ice along either line of sight. Perhaps this could be explained by the heated ices having mostly experienced temperatures too hot for CH_3OH to remain in the ice (i.e., a steep thermal gradient along the line of sight). However, both the dominant component of the CH_3OH feature being pure CH_3OH ice as well as the low optical depth of the CO ice feature indicate that the majority of the "cold" ices in the outermost envelope must have also experienced some amount of heating (equivalent to at least 30-40 K in the laboratory).

2.5 Conclusions

Here we present $>3\sigma$ detections of both amorphous and crystalline HDO ice at 4.1 μm in JWST NIRSpec spectra taken toward the IMYSO HOPS 370 and the MYSO IRAS 20126+4104. The HDO ice column densities were quantified in a fitting procedure that accounted for potential spectral contributions from CH_3OH ice. The H_2O ice column densities were quantified via the 3 μm feature to enable comparisons between HDO/H_2O ratios measured in the ice with those measured in the gas toward protostars. Our main findings are summarized as follows:

1. Toward both sources, the detection of a crystalline HDO ice component at 4.1 μm correlates with the detection of a crystalline H_2O ice component at 3 μm as well as other tracers of ice thermal processing, increasing confidence in our assignment of the 4.1 μm feature to HDO ice.

2. We measure ice HDO/H_2O ratios of $4.6\pm2.2\times10^{-3}$ and $2.6\pm1.4\times10^{-3}$ toward HOPS 370 and IRAS 20126, respectively. These ratios are enriched by approximately two orders of magnitude relative to the cosmic standard deuterium abundance, consistent with the water ice toward these objects having cold, prestellar origins.

3. The ice HDO/H_2O ratio measured toward the MYSO IRAS 20126 is consistent with the highest reported gas HDO/H_2O ratios toward MYSOs (a couple $\times10^{-3}$), supporting the assumption that the deuterium abundances of the gas-phase water observed toward these objects are representative of the deuterium abundances of their surrounding water ice.

4. The ice HDO/H_2O ratios toward these objects are remarkably similar to each other as well as to the gas HDO/H_2O ratios measured toward isolated LYSOs. A larger sample of ice HDO/H_2O ratios, both toward LYSOs and MYSOs, as well as more measurements of D_2O/H_2O ratios in the gas phase could help to explain the cause of this similarity.

5. The peak position of the crystalline HDO ice component toward both sources suggests that the thermally processed ice in these lines of sight experienced re-cooling to some degree.

6. The CH_3OH ice requires a water-rich CH_3OH ice mixture to obtain a satisfactory fit to the 3.4 μm region, supporting recent experimental and observational evidence that some CH_3OH ice may form prior to the heavy CO freeze-out stage in an H_2O-rich environment.

7. As part of this work, several new laboratory spectra of HDO, H_2O, CH_3OH, and CO ice mixtures are now available for public use on the Leiden Ice Database (LIDA).

2.6 Acknowledgements

K.S. thanks Brian Ferrari, Adwin Boogert, Jenny Noble, Helen Fraser, Melissa McClure, Sergio Ioppolo, Neal Evans, and Alessio Caratti o Garatti for helpful discussions, Adwin Boogert for providing IRTF spectra, and Julia Santos for experimental support. This work is based on observations made with the NASA/ESA/CSA James Webb Space Telescope. The data were

obtained from the Mikulski Archive for Space Telescopes at the Space Telescope Science Institute, which is operated by the Association of Universities for Research in Astronomy, Inc., under NASA contract NAS 5-03127 for JWST. These observations are associated with program #1802. All the JWST data used in this paper can be found in MAST: 10.17909/3kky-t040. Astrochemistry at Leiden is supported by funding from the European Research Council (ERC) under the European Union's Horizon 2020 research and innovation programme (grant agreement No. 101019751 MOLDISK), the Netherlands Research School for Astronomy (NOVA), and the Danish National Research Foundation through the Center of Excellence "InterCat" (Grant agreement no.: DNRF150). Support for S.F., A.E.R., S.T.M., R.G., J.J.T. and D.W. in program #1802 was provided by NASA through a grant from the Space Telescope Science Institute, which is operated by the Association of Universities for Research in Astronomy, Inc., under NASA contract NAS 5-03127. The National Radio Astronomy Observatory is a facility of the National Science Foundation operated under cooperative agreement by Associated Universities, Inc. Y.-L.Y. acknowledges support from Grant-in-Aid from the Ministry of Education, Culture, Sports, Science, and Technology of Japan (20H05845, 20H05844, 22K20389), and a pioneering project in RIKEN (Evolution of Matter in the Universe).

2.A Appendix

2.A.1 Laboratory data

Here we present the methodologies used to collect and analyze the laboratory data in this work.

Experimental details

In this work, independent dosing lines were used to deposit the CH_3OH-containing binary ice mixtures using the procedure outlined in Yarnall & Hudson (2022), where each leak valve is calibrated so that its position results in the desired deposition rate of each mixture component in its pure form. After this calibration step, shut valves between the gas or vapor reservoirs and the leak valves are opened so that the mixture components deposit simultaneously upon the substrate. As mentioned in Yarnall & Hudson (2022), the leak valve calibration depends on knowing the refractive index and density of each ice component, as well as the measurement of the laser interference pattern as the ice deposits in the calibration step. The benefits of utilizing such a system of independent dosing lines to create mixtures *in situ* on the ice substrate rather than using a single dosing line and mixing gases and vapors prior to their introduction into the chamber have been previously discussed in Gerakines et al. (1995), Yarnall & Hudson (2022), and Slavicinska et al. (2023).

A HeNe laser with a wavelength of 632.8 nm was used for the laser interference measurements. The refractive indexes and densities of the ices used for our calibrations are provided in Table 4.A.8.

Because the physical properties and masses of H_2O and HDO are very similar, their flow rates through the leak valves, pumping speeds, and deposition rates are also expected to be very similar, minimizing the expected error of the HDO:H_2O ice mixing ratio when premixing the components prior to deposition. Therefore, the HDO:H_2O ices were created via

Table 2.A.6: Refractive indexes and densities used for calibration.

Molecule	n	ρ (g cm^{-3})	Ref.
CH_3OH	1.257	0.636	1
H_2O	1.234	0.719	2
CO	1.297	0.870	3

1. Luna et al. 2018; 2. Yarnall & Hudson 2022; 3. Luna et al. 2022.

the traditional pre-mixing method, following the procedure described in Gálvez et al. (2011) to generate HDO via mixing H_2O and D_2O.

During the warm-ups, the ices were heated at a rate of 25 K hr^{-1}, and spectra ranging from 4000-500 cm^{-1} (2.5-20 μm) were continuously collected and averaged every 128 scans, meaning a new spectrum was obtained every 3.5 min. This results in an uncertainty of approximately $\pm$1 K in the reported temperature of each amorphous spectrum. During the re-cooling of the annealed crystalline HDO:H_2O ice mixtures, a cooling rate of -2 K min^{-1} was used so that the experiment could be performed within a single workday, resulting in a higher temperature uncertainty of approximately $\pm$4 K for the annealed crystalline HDO spectra. All spectra were baseline-corrected via cubic spline functions prior to their analysis.

HDO O-D stretch characterization

The peak position, FWHM, and integrated absorbance of the HDO O-D stretching mode was extracted from the thick HDO:H_2O ice spectra (see Table 2.2) using a cubic spline to isolate the feature from the broad 4.5 μm H_2O combination mode followed by a Savitzky-Golay filter to smooth out experimental noise (see Figure 2.A.9).

The apparent band strengths of the HDO O-D stretch at different temperatures, A'_i, were derived by assuming the apparent band strength of the crystalline band at 150 K, A'_{150K}, is equal to 6.4×10^{-17} cm molec^{-1} (Dartois et al. 2003; Gálvez et al. 2011) and using the approximation:

$$A'_i = \frac{\int \mathrm{abs_i}(\nu)\ \mathrm{d}\nu}{\int \mathrm{abs_{150K}}(\nu)\ \mathrm{d}\nu} \times A'_{150K}, \tag{2.A.1}$$

where $\int \mathrm{abs_{150K}}(\nu)\mathrm{d}\nu$ is the integrated absorbance of the crystalline HDO peak at 150 K, and $\int \mathrm{abs_i}(\nu)\mathrm{d}\nu$ is the integrated absorbance of the HDO peak at the phase and temperature of interest.

The resulting peak positions, FWHMs, and apparent band strengths are plotted in Figures 2.A.10 and 2.A.11 and reported in Table 2.A.7. It is evident that the peak extractions are much less reliable for the amorphous ice, where the O-D stretch is very weak and broad (see Figure 2.A.9), resulting in a greater experimental scatter between the amorphous data points in both plots. We smoothed this scatter with fourth-order polynomial fits to the individual amorphous data points, which were used to calculate the final peak positions, FWHMs, and apparent band strengths reported for the amorphous ice. The crystalline data was not treated

in this way because the profile extraction of the crystalline feature from the laboratory spectra was much more straightforward, resulting in much smaller experimental scatter.

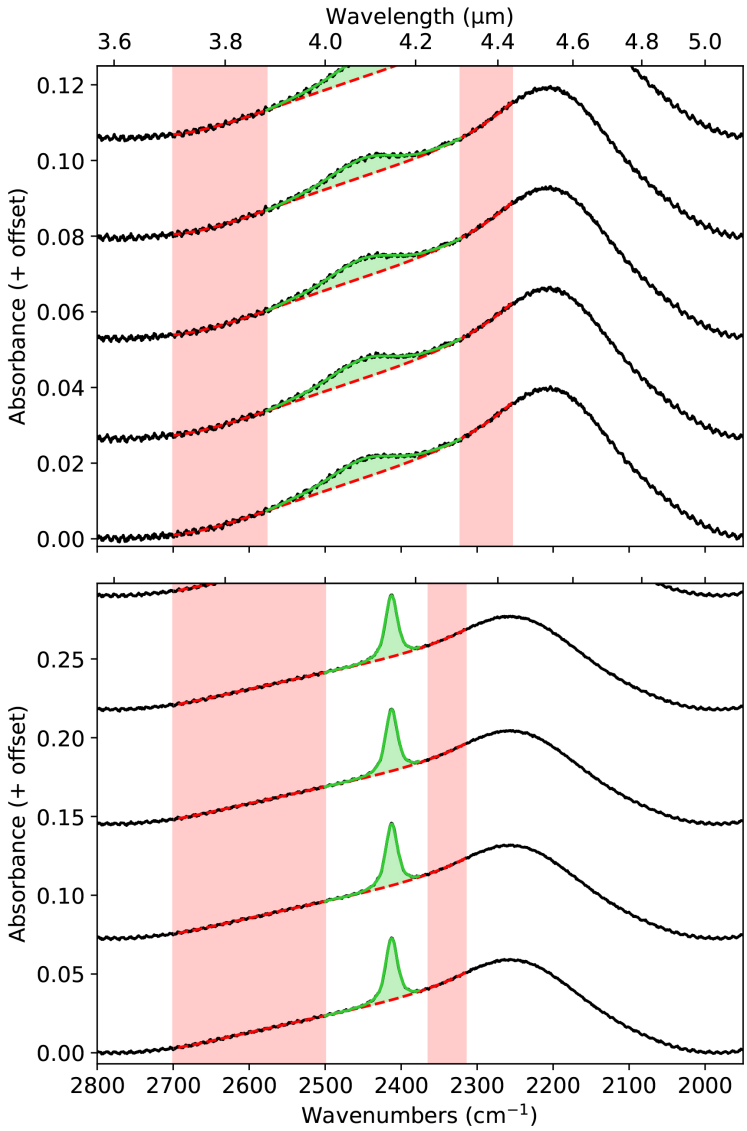


Figure 2.A.9: Example extractions of the profile of the 4.1 μm HDO O-D stretching mode from the H_2O combination mode in 0.4% HDO:H_2O laboratory spectra (top: amorphous; bottom: crystalline). The laboratory data (already baseline corrected) is plotted in black, the local continuum is plotted in dashed red, and the smoothed and extracted profile is plotted in green. The red shading indicates the wavelengths used to define the local continuum, and the green shading indicates the integrated area used to derive apparent band strengths.

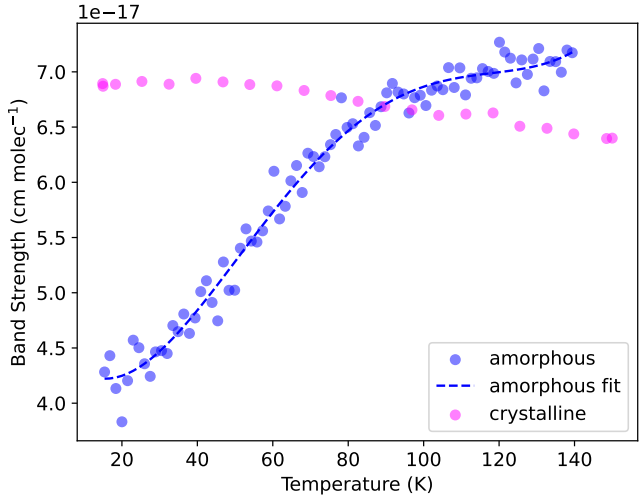


Figure 2.A.10: The temperature-dependent variation of the apparent band strengths of amorphous and crystalline HDO ice. The dashed blue line is a fourth-order polynomial fit to the amorphous band strength data used to extract the final reported apparent band strengths reported in Table 2.A.7.

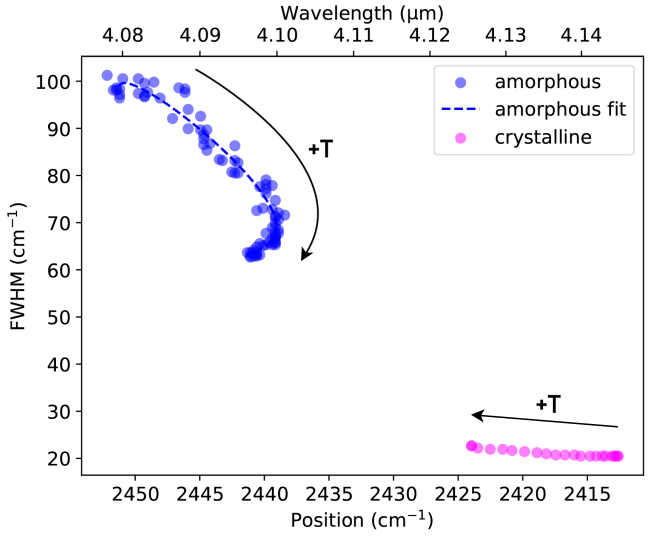


Figure 2.A.11: The range of peak positions and FWHMs of amorphous and crystalline HDO ice in the heating and annealing experiments. The arrows indicate the direction in which the data changes with increasing temperature. The dashed blue line is a fourth-order polynomial fit to the amorphous peak position and FWHM data used to extract the final reported peak positions and FWHMs reported in Table 2.A.7.

Despite the problematic profile of the amorphous HDO ice band, the apparent band strength we derived for amorphous HDO ice at 15 K, 4.2×10^{-17} cm molec^{-1}, is in excellent agreement (within $\sim$2%) with the band strengths reported by Dartois et al. (2003) and Gálvez et al. (2011) for amorphous HDO ice at similar temperatures.

Table 2.A.7: Peak positions, FWHMs, and band strengths of the HDO O-D stretching mode at $\sim$4.1 μm at temperatures from 15-150 K. We estimate uncertainties of 2 cm^{-1} for the peak positions/FWHMs and 20% for the band strengths of the amorphous HDO ice, and 0.5 cm^{-1} for the peak positions/FWHMs and 10% for the band strengths of the crystalline HDO ice.

Ice phase	T (K)	Peak		FWHM		A'_i
		(cm^{-1})	(μm)	(cm^{-1})	(μm)	(10^{-17} cm molec^{-1})
Amorphous	15	2451.3	4.080	98.7	0.164	4.2
	25	2450.5	4.081	99.5	0.166	4.3
	35	2448.8	4.084	97.3	0.162	4.6
	45	2446.5	4.087	93.2	0.156	5.1
	55	2444.3	4.091	88.1	0.147	5.5
	65	2442.2	4.095	82.7	0.139	5.9
	75	2440.6	4.097	77.6	0.130	6.3
	85	2439.5	4.099	73.2	0.123	6.6
	95	2439.1	4.100	69.7	0.117	6.8
	105	2439.2	4.100	67.2	0.113	6.9
	115	2439.7	4.099	65.5	0.110	7.0
	125	2440.4	4.098	64.3	0.108	7.0
	135	2440.9	4.097	63.1	0.106	7.1
Crystalline	15	2412.6	4.145	20.5	0.035	6.9
	25	2412.9	4.144	20.5	0.035	6.9
	47	2413.8	4.143	20.5	0.035	6.9
	68	2415.5	4.140	20.5	0.035	6.8
	90	2417.5	4.137	20.7	0.035	6.7
	111	2419.9	4.132	21.5	0.037	6.6
	133	2422.5	4.128	21.9	0.037	6.5
	150	2424.0	4.125	22.7	0.039	6.4

CH_3OH C-H symmetric stretch characterization

The peak position of the CH_3OH C-H symmetric stretching mode was extracted from the CH_3OH-containing ice spectra using a fourth-order polynomial to isolate the feature from the entire 3.4 μm absorption complex followed by a Savitzky-Golay filter to smooth out experimental noise. These values are given in Tables 2.A.8 and 2.A.9 and are plotted as a function of temperature in Figure 2.A.12, which also shows the observed peak positions of the C-H symmetric stretching mode in the analyzed spectra. Only peak positions are provided here because a full characterization of this peak (i.e., including FWHMs and relative apparent band strengths) is complicated by the fact that this feature is blended with the CH_3OH overtones and C-H asymmetric stretching modes.

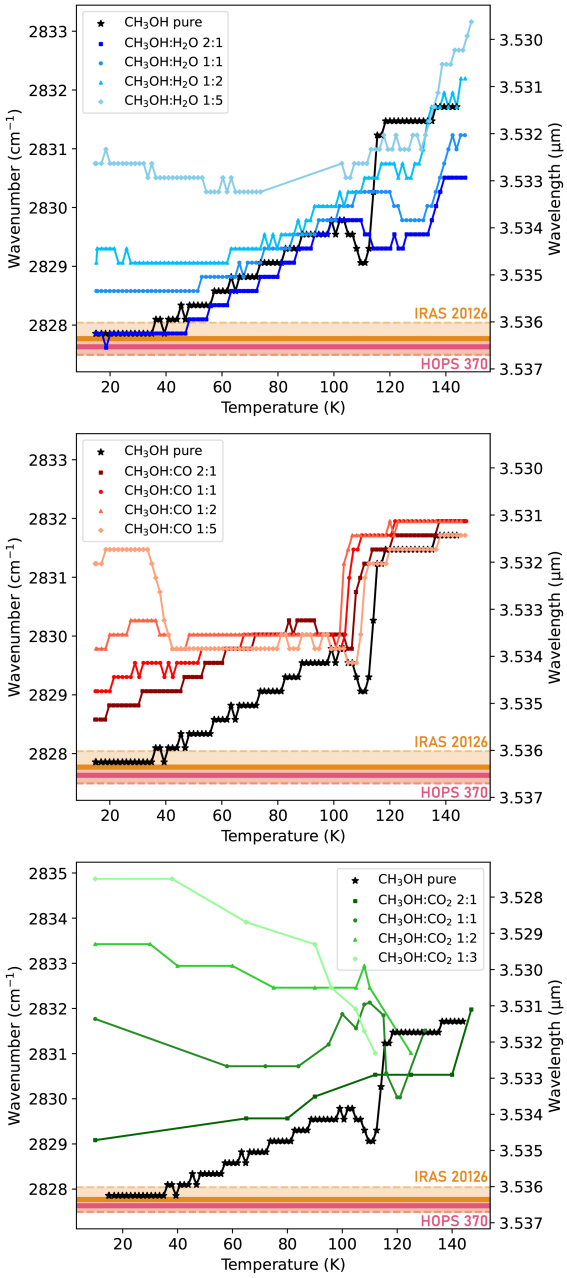


Figure 2.A.12: Peak positions of the 3.53 μm CH_3OH C-H stretching mode in laboratory CH_3OH ices from 15-145 K (points), and peak positions of the 3.53 μm band observed toward HOPS 370 and IRAS 20126 (thick horizontal lines). The observed peak positions were extracted from the observed spectra via Gaussian fits to the local-continuum subtracted 3.53 μm peaks (error margins indicated with shaded areas with dashed borders). The CH_3OH:CO_2 values were extracted from data from Ehrenfreund et al. (1999) available on LIDA.

Table 2.A.8: Peak positions of the CH_3OH C-H symmetric stretching mode at ∼3.53 μm at temperatures from 15-145 K in pure CH_3OH ice and CH_3OH ice mixed with H_2O. We estimate uncertainties of 0.5 cm^{-1} for these peak positions.

T (K)	Pure CH_3OH		CH_3OH:H_2O 2:1		CH_3OH:H_2O 1:1		CH_3OH:H_2O 1:2		CH_3OH:H_2O 1:5	
	(cm^{-1})	(μm)	(cm^{-1})	(μm)	(cm^{-1})	(μm)	(cm^{-1})	(μm)	(cm^{-1})	(μm)
15	2827.9	3.5362	2827.9	3.5362	2828.6	3.5353	2829.1	3.5347	2830.7	3.5326
25	2827.9	3.5362	2827.9	3.5362	2828.6	3.5353	2829.1	3.5347	2830.7	3.5326
35	2827.9	3.5362	2827.9	3.5362	2828.6	3.5353	2829.1	3.5347	2830.7	3.5326
45	2828.3	3.5366	2827.9	3.5362	2828.6	3.5353	2829.1	3.5347	2830.5	3.5329
55	2828.3	3.5366	2828.3	3.5356	2828.8	3.5350	2829.1	3.5347	2830.3	3.5332
65	2828.6	3.5353	2828.6	3.5353	2828.8	3.5350	2829.3	3.5344	2830.3	3.5332
75	2829.1	3.5347	2828.8	3.5350	2829.3	3.5344	2829.5	3.5341	2830.3	3.5332
85	2829.3	3.5344	2829.1	3.5347	2829.5	3.5341	2829.5	3.5341	-	-
95	2829.5	3.5341	2829.5	3.5341	2829.8	3.5338	2830.0	3.5335	-	-
105	2829.5	3.5341	2829.8	3.5338	2830.0	3.5335	2830.3	3.5332	2830.5	3.5329
115	2831.2	3.5320	2829.3	3.5344	2830.3	3.5332	2830.5	3.5329	2831.0	3.5323
125	2831.5	3.5317	2829.3	3.5344	2829.8	3.5338	2830.7	3.5326	2831.0	3.5323
135	2831.5	3.5317	2829.8	3.5338	2830.0	3.5335	2831.7	3.5314	2831.7	3.5314
145	2831.7	3.5314	2830.5	3.5329	2831.2	3.5320	2832.2	3.5308	2832.7	3.5302

Table 2.A.9: Peak positions of the CH_3OH C-H symmetric stretching mode at ∼3.53 μm at temperatures from 15-145 K in CH_3OH ice mixed with CO. We estimate uncertainties of 0.5 cm^{-1} for these peak positions.

T (K)	CH_3OH:CO 2:1		CH_3OH:CO 1:1		CH_3OH:CO 1:2		CH_3OH:CO 1:5	
	(cm^{-1})	(μm)	(cm^{-1})	(μm)	(cm^{-1})	(μm)	(cm^{-1})	(μm)
15	2828.6	3.5353	2829.1	3.5347	2829.8	3.5338	2831.2	3.5320
25	2828.8	3.5350	2829.3	3.5344	2830.0	3.5335	2831.5	3.5317
35	2829.1	3.5347	2829.5	3.5341	2830.3	3.5332	2831.2	3.5320
45	2829.1	3.5347	2829.5	3.5341	2829.8	3.5338	2829.8	3.5338
55	2829.5	3.5341	2829.8	3.5338	2830.0	3.5335	2829.8	3.5338
65	2829.8	3.5338	2829.8	3.5338	2830.0	3.5335	2829.8	3.5338
75	2830.0	3.5335	2830.0	3.5335	2830.0	3.5335	2829.8	3.5338
85	2830.0	3.5335	2830.0	3.5335	2830.0	3.5335	2829.8	3.5338
95	2830.0	3.5335	2830.0	3.5335	2830.0	3.5335	2829.8	3.5338
105	2829.8	3.5338	2831.0	3.5323	2831.5	3.5317	2829.5	3.5341
115	2831.5	3.5317	2831.7	3.5314	2831.7	3.5314	2831.2	3.5320
125	2831.7	3.5314	2832.0	3.5311	2832.0	3.5311	2831.5	3.5317
135	2831.7	3.5314	2832.0	3.5311	2832.0	3.5311	2831.5	3.5317
145	2832.0	3.5311	2832.0	3.5311	2832.0	3.5311	2831.7	3.5314

2.A.2 χ^2 plots

Least-squares fits using every possible combination of one amorphous and one crystalline HDO lab spectra were performed, and the χ^2 values were calculated for all of these possible fits using the following equation:

$$\chi^2 = \frac{\sum(\tau_{obs} - \tau_{fit})^2}{\sigma^2}, \tag{2.A.2}$$

where τ_{obs} is the observed optical depth and τ_{fit} is the optical depth of the fit. The σ value is calculated by propagating the uncertainties in the optical depths that result from the RMS errors and the local continuum placement uncertainties (Figures 2.A.14 and 2.A.15). The 1, 2, and 3σ bounds plotted in Figure 2.A.13 correspond to the critical $\Delta\chi^2$ (χ^2-χ^2_{min}) values at the 68.3, 95.5, and 99.7% confidence intervals, respectively, for fits with four free parameters (in this case, the temperatures and scaling factors of the amorphous and crystalline HDO ice spectra).

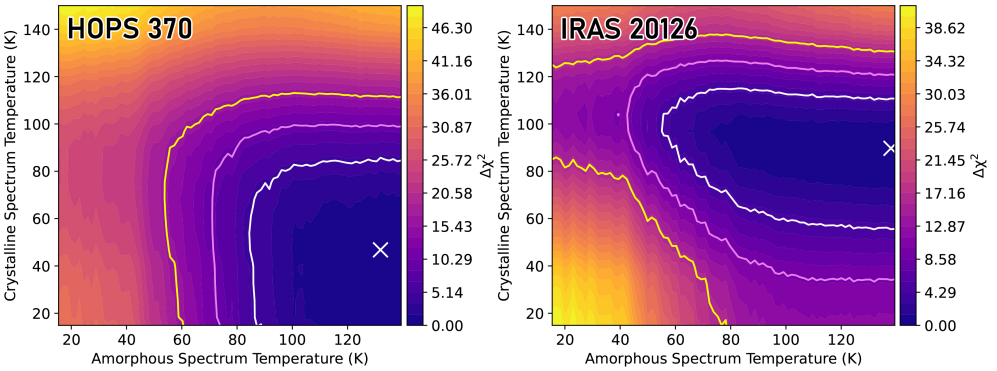


Figure 2.A.13: Contour maps of the $\Delta\chi^2$ values of the least-squares fits with every possible combination of one amorphous and one crystalline HDO component. The white X marks χ^2_{min}, and the white, purple, and yellow contour lines show the $\Delta\chi^2$ values corresponding to 1, 2, and 3σ, respectively.

2.A.3 Estimated continuum errors

CH_3OH ice

The 20% band strength uncertainty (Luna et al. 2018) is propagated to determine the uncertainty in the calculated CH_3OH ice column densities. The implications of these fits and column densities on the thermal and chemical structures of the ice envelopes as well as the physicochemical histories of the sources are discussed in Section 2.4.3.

HDO ice

The reported errors account for two sources of uncertainty: 1) the uncertainty of the HDO O-D stretching mode band strength, and 2) the uncertainty of the local continuum choice. The uncertainty in the band strength accounts for both the aforementioned variation of the band

strength with temperature as well as the reported experimental uncertainties of the amorphous and crystalline HDO band strengths from Gálvez et al. (2011) (∼10% and 5%, respectively), which were used to calculate the band strengths of HDO at higher temperatures presented in Table 2.A.7.

The uncertainty of the local continuum is somewhat subjective, as it depends on what one considers a "reasonable" local continuum. We attempted to quantify this uncertainty by identifying the limits of what we consider a reasonable local continuum for each line of sight and then quantifying the variation in the calculated HDO column density that resulted from these continuum shifts. These lower and upper limit continua are shown in Figure 2.A.14, and the resulting lower and upper limits on the optical depths of the 4 μm region are shown in Figure 2.A.15.

The column density uncertainties were determined by adding in quadrature the band strength uncertainties and the uncertainties caused by the continuum choice, which were estimated by noting the variation in HDO ice column density obtained from repeating the fitting procedure on the spectra that were extracted using the lower and upper limit global continua.

H_2O ice

The uncertainty in the H_2O column density due to the uncertainty of the continuum choice was quantified via a procedure similar to that used for the 4 μm region by exploring the range of artificial short-wavelength continuum points which resulted in continuum shapes and H_2O profiles that appeared reasonable. The lower and upper limit continua are shown in Figure 2.A.16, and the resulting variations in the optical depths and profiles of the 3 μm feature are shown in Figure 2.A.17.

The column density uncertainties were determined by adding in quadrature the uncertainties caused by the variation in band strengths with temperature, a 30% uncertainty accounting for the underfit red wing caused by neglecting ammonia hydrates and grain shape effects (as estimated by Boogert et al. 2008), and the uncertainties caused by the continuum choice, which were estimated by noting the variation in H_2O ice column density obtained from repeating the fitting procedure on the spectra that were extracted using the lower and upper limit global continua.

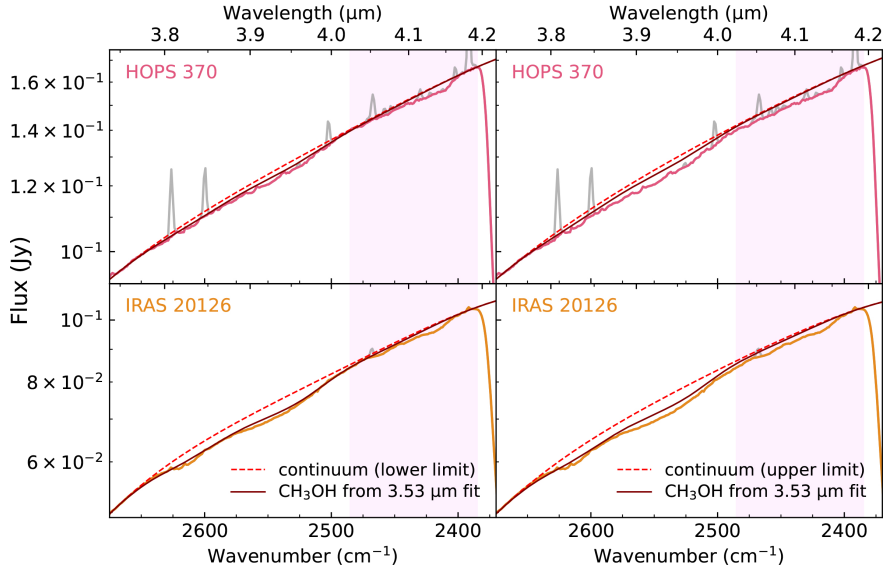


Figure 2.A.14: The alternative local continua used to calculate the uncertainty in HDO column density from local continuum choice. Left: the lower limit continua (i.e., the continua that result in the lowest possible optical depth in the region while remaining reasonable). Right: the upper limit continua (i.e., the continua that result in the highest possible optical depth in the region while remaining reasonable).

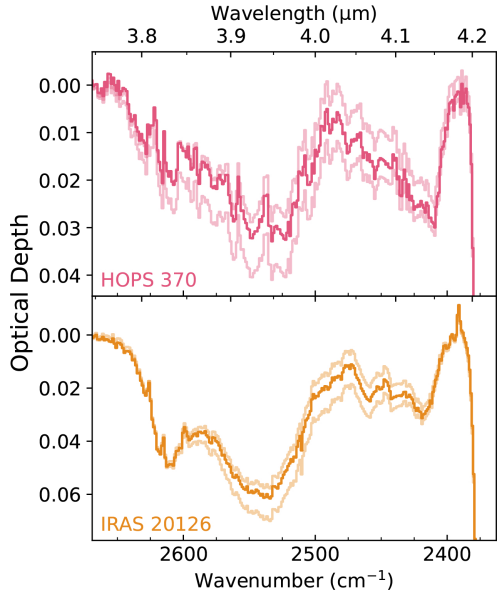


Figure 2.A.15: The change in the optical depth of the features at 4 μm caused by varying the local continua as shown in Figure 2.A.14. The spectra used to calculate the column densities in Table 2.4 are plotted in the dark shades, and the spectra resulting from the lower and upper continuum limits used to estimate the effect of continuum uncertainty are plotted in the light shades.

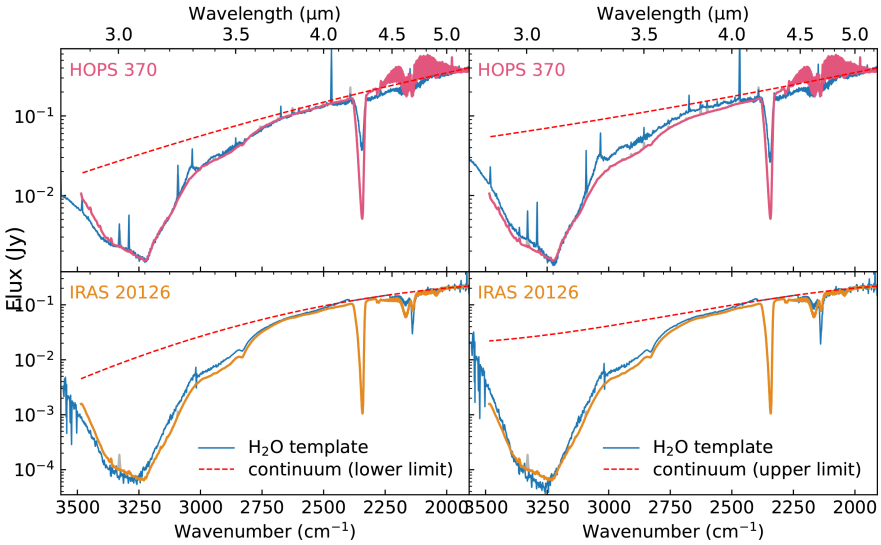


Figure 2.A.16: The alternative global continua used to calculate the uncertainty in H_2O column density from local continuum choice. Left: the lower limit continua (i.e., the continua that result in the lowest possible optical depth in the region while remaining reasonable). Right: the upper limit continua (i.e., the continua that result in the highest possible optical depth in the region while remaining reasonable).

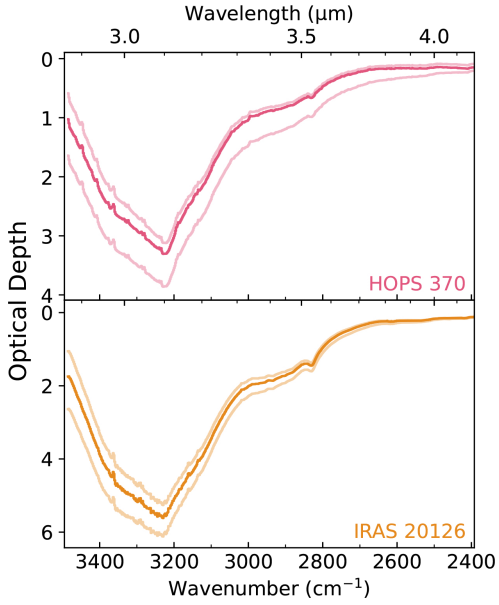


Figure 2.A.17: The change in the optical depth of the 3 μm feature caused by varying the global continua as shown in Figure 2.A.16. The spectra used to calculate the column densities in Table 2.5 are plotted in the dark shades, and the spectra resulting from the lower and upper continuum limits used to estimate the effect of continuum uncertainty are plotted in the light shades.

2.A.4 Literature HDO/H_2O values

Table 2.A.10: Overview of recently published HDO/H_2O values in ices and the gas phase (adapted from Jensen et al. 2019 and Andreu et al. 2023).

Source	Phase	HDO/H_2O 10^{-3}	Ref.
Clustered Class 0 LYSOs			
NGC 1333 IRAS 4A-NW	gas	0.54±0.15	1, 2
NGC 1333 IRAS 2A	gas	0.74±0.21	1
NGC 1333 IRAS 4B	gas	0.59±0.26	1
IRAS 16293-2422	gas	0.92±0.26	1
NGC 1333 SVS 13	ice	≤17	3
Clustered Class I LYSOs			
NGC 1333 SVS 12	ice	≤5	3
Isolated Class 0 LYSOs			
BHR 71-IRS1	gas	1.8±0.4	2
B335	gas	6.3±1.5	4
L483	gas	4.0±0.5	4
Isolated Class I LYSOs			
V883 Ori	gas	2.3±0.6	5
L1551 IRS5	gas	2.1±0.8	6
L1489 IRS	ice	≤8	3
TMR1	ice	≤11	3
IMYSOs			
IRAS 05390-0728	ice	≤10	7
IRAS 08448-4343	ice	≤10	7
HOPS 370	ice	4.6±2.2	8
MYSOs			
W3 IRS5	gas	1.3	9
W33A	gas	3.0	9
AFGL 2591	gas	3.3	9
NGC 7538 IRS1	gas	3.8	9
Orion KL Hot Core	gas	$3.0^{+3.1}_{-1.7}$	10
NGC 6334 I	gas	0.21±0.1	11
G34.26+0.15	gas	0.35-0.75	12
NGC 7538 IRS9	ice	≤8.1-11.4	7
GL 2136	ice	≤4	7
IRAS 20126	ice	2.6±1.4	8

1. Persson et al. 2014; 2. Jensen et al. 2019; 3. Parise et al. 2003; 4. Jensen et al. 2021; 5. Tobin et al. 2023; 6. Andreu et al. 2023; 7. Dartois et al. 2003; 8. this work; 9. van der Tak et al. 2006 (envelope-averaged abundances from radiative transfer models); 10. Neill et al. 2013; 11. Emprechtinger et al. 2013; 12. Coutens et al. 2014b.

2.B Bibliography

Aikawa, Y., Kamuro, D., Sakon, I., et al. 2012, A&A, 538, A57
Allamandola, L., Sandford, S., Tielens, A., & Herbst, T. 1992, ApJ, 399, 134
Andreu, A., Coutens, A., de Miera, F. C.-S., et al. 2023, A&A, 677, L17
Bergin, E. A., Melnick, G. J., & Neufeld, D. A. 1998, ApJ, 499, 777
Boogert, A., Brewer, K., Brittain, A., & Emerson, K. 2022, ApJ, 941, 32
Boogert, A., Chiar, J., Knez, C., et al. 2013, ApJ, 777, 73
Boogert, A., Ehrenfreund, P., Gerakines, P., et al. 2000, A&A, 353, 349
Boogert, A., Huard, T., Cook, A., et al. 2011, ApJ, 729, 92
Boogert, A. A., Gerakines, P. A., & Whittet, D. C. 2015, ARA&A, 53, 541
Boogert, A. C., Pontoppidan, K. M., Knez, C., et al. 2008, ApJ, 678, 985
Bottinelli, S., Boogert, A. A., Bouwman, J., et al. 2010, ApJ, 718, 1100
Brooke, T., Sellgren, K., & Geballe, T. 1999, ApJ, 517, 883
Brunken, N. G., Rocha, W. R., Van Dishoeck, E. F., et al. 2024, A&A, 685, A27
Caratti o Garatti, A., Froebrich, D., Eislöffel, J., Giannini, T., & Nisini, B. 2008, A&A, 485, 137
Caselli, P. & Ceccarelli, C. 2012, AAR, 20, 1
Cazaux, S., Caselli, P., & Spaans, M. 2011, ApJL, 741, L34
Ceccarelli, C., Caselli, P., Bockelée-Morvan, D., et al. 2014, Protostars and Planets VI, 859
Cesaroni, R., Faustini, F., Galli, D., et al. 2023, A&A, 671, A126
Chen, H.-R. V., Keto, E., Zhang, Q., et al. 2016, ApJ, 823, 125
Chen, Y., Van Gelder, M., Nazari, P., et al. 2023, A&A, 678, A137
Coutens, A., Jørgensen, J., Persson, M., et al. 2014a, ApJL, 792, L5
Coutens, A., Vastel, C., Hincelin, U., et al. 2014b, MNRAS, 445, 1299
Cuppen, H., Penteado, E., Isokoski, K., van der Marel, N., & Linnartz, H. 2011, MNRAS, 417, 2809
Dartois, E. & d'Hendecourt, L. 2001, A&A, 365, 144
Dartois, E., Noble, J., Caselli, P., et al. 2024, Nat. Astro., 1
Dartois, E., Noble, J. A., Ysard, N., Demyk, K., & Chabot, M. 2022, A&A, 666, A153
Dartois, E., Schutte, W., Geballe, T., et al. 1999, A&A, 342, L32
Dartois, E., Thi, W.-F., Geballe, T., et al. 2003, A&A, 399, 1009
Ehrenfreund, P., Kerkhof, O., Schutte, W., et al. 1999, A&A, 350, 240
Emprechtinger, M., Lis, D., Rolffs, R., et al. 2013, ApJ, 765, 61
Faure, M., Quirico, E., Faure, A., et al. 2015, Icarus, 261, 14
Federman, S. A., Megeath, S. T., Rubinstein, A. E., et al. 2024, ApJ, 966, 41
Fuchs, G., Cuppen, H., Ioppolo, S., et al. 2009, A&A, 505, 629
Furuya, K., Aikawa, Y., Nomura, H., Hersant, F., & Wakelam, V. 2013, ApJ, 779, 11
Furuya, K., Drozdovskaya, M., Visser, R., et al. 2017, A&A, 599, A40
Furuya, K., van Dishoeck, E., & Aikawa, Y. 2016, A&A, 586, A127
Gálvez, Ó., Maté, B., Herrero, V. J., & Escribano, R. 2011, ApJ, 738, 133
Geiss, J. & Gloeckler, G. 2003, SSRv, 106, 3
Gerakines, P., Schutte, W., Greenberg, J., & van Dishoeck, E. F. 1995, A&A, 296, 810
González-García, B., Manoj, P., Watson, D., et al. 2016, A&A, 596, A26
Hagen, W., Tielens, A., & Greenberg, J. 1981, Chem. Phys., 56, 367
Harada, N., Herbst, E., & Wakelam, V. 2010, ApJ, 721, 1570

Helmich, F., van Dishoeck, E., & Jansen, D. 1996, A&A, 313, 657
Herbst, E. & van Dishoeck, E. F. 2009, ARA&A, 47, 427
Hudson, R. L. & Gerakines, P. A. 2018, ApJ, 867, 138
Jensen, S., Jørgensen, J., Kristensen, L., et al. 2021, A&A, 650, A172
Jensen, S., Jørgensen, J., Kristensen, L., et al. 2019, A&A, 631, A25
Jiménez-Escobar, A. & Muñoz Caro, G. 2011, A&A, 536, A91
Jørgensen, J. K., Belloche, A., & Garrod, R. T. 2020, ARA&A, 58, 727
Kawanowa, H., Kondo, M., Gotoh, Y., & Souda, R. 2004, Surf. Sci., 566, 1190
Kerkhof, O., Schutte, W., & Ehrenfreund, P. 1999, A&A, 346, 990
Knez, C., Boogert, A. A., Pontoppidan, K. M., et al. 2005, ApJ, 635, L145
Lamberts, T., Ioppolo, S., Cuppen, H., Fedoseev, G., & Linnartz, H. 2015, MNRAS, 448, 3820
Luna, R., Millán, C., Domingo, M., Santonja, C., & Satorre, M. Á. 2022, ApJ, 935, 134
Luna, R., Molpeceres, G., Ortigoso, J., et al. 2018, A&A, 617, A116
Mastrapa, R., Sandford, S., Roush, T., Cruikshank, D., & Dalle Ore, C. 2009, ApJ, 701, 1347
McClure, M. K., Rocha, W., Pontoppidan, K., et al. 2023, Nat. Astro., 1
Megeath, T., Anglada, G., Atnagulov, P., et al. 2021, JWST Proposal. Cycle 1, 1802
Minissale, M., Aikawa, Y., Bergin, E., et al. 2022, ACS Earth Space Chem., 6, 597
Montes, V. A., Hofner, P., Anderson, C., & Rosero, V. 2015, ApJS, 219, 41
Narang, M., Manoj, P., Tyagi, H., et al. 2024, ApJL, 962, L16
Nazari, P., Meijerhof, J., van Gelder, M., et al. 2022, A&A, 668, A109
Nazari, P., Rocha, W., Rubinstein, A., et al. 2024, A&A, 686, A71
Neill, J. L., Wang, S., Bergin, E. A., et al. 2013, ApJ, 770, 142
Öberg, K. I. & Bergin, E. A. 2021, Phys. Rep., 893, 1
Osorio, M., Díaz-Rodríguez, A. K., Anglada, G., et al. 2017, ApJ, 840, 36
Owen, J. E. & Jacquet, E. 2015, MNRAS, 446, 3285
Parise, B., Simon, T., Caux, E., et al. 2003, A&A, 410, 897
Penteado, E., Boogert, A., Pontoppidan, K., et al. 2015, MNRAS, 454, 531
Persson, M., Jørgensen, J., van Dishoeck, E., & Harsono, D. 2014, A&A, 563, A74
Persson, M. V., Jørgensen, J. K., & van Dishoeck, E. F. 2013, A&A, 549, L3
Pontoppidan, K. M., Dartois, E., van Dishoeck, E. F., Thi, W.-F., & d'Hendecourt, L. 2003, A&A, 404, L17
Prodanović, T., Steigman, G., & Fields, B. D. 2010, MNRAS, 406, 1108
Qasim, D., Chuang, K.-J., Fedoseev, G., et al. 2018, A&A, 612, A83
Qiu, K., Zhang, Q., Megeath, S. T., et al. 2008, ApJ, 685, 1005
Rachid, M., Brunken, N., De Boe, D., et al. 2021, A&A, 653, A116
Ratajczak, A., Quirico, E., Faure, A., Schmitt, B., & Ceccarelli, C. 2009, A&A, 496, L21
Redhead, P. A. 1962, Vacuum, 12, 203
Reid, M., Menten, K., Brunthaler, A., et al. 2019, ApJ, 885, 131
Roberts, H., Herbst, E., & Millar, T. 2003, ApJ, 591, L41
Rocha, W., Rachid, M., Olsthoorn, B., et al. 2022, A&A, 668, A63
Rocha, W., Van Dishoeck, E., Ressler, M., et al. 2024, A&A, 683, A124
Rubinstein, A. E., Evans, N. J., Tyagi, H., et al. 2024, ApJ, 974, 112
Sato, A., Takahashi, S., Ishii, S., et al. 2023, ApJ, 944, 92
Shimajiri, Y., Takahashi, S., Takakuwa, S., Saito, M., & Kawabe, R. 2008, ApJ, 683, 255
Slavicinska, K., Rachid, M. G., Rocha, W. R. M., et al. 2023, A&A, 677, A13

Smith, R. G., Sellgren, K., & Tokunaga, A. T. 1989, ApJ, 344, 413
Tanaka, M., Sato, S., Nagata, T., & Yamamoto, T. 1990, ApJ, 352, 724
Taquet, V., Ceccarelli, C., & Kahane, C. 2012, ApJL, 748, L3
Taquet, V., Charnley, S. B., & Sipilä, O. 2014, ApJ, 791, 1
Teixeira, T., Devlin, J., Buch, V., & Emerson, J. 1999, A&A, 347, L19
Tielens, A. 1983, A&A, 119, 177
Tobin, J. J., Sheehan, P. D., Megeath, S. T., et al. 2020a, ApJ, 890, 130
Tobin, J. J., Sheehan, P. D., Reynolds, N., et al. 2020b, ApJ, 905, 162
Tobin, J. J., van't Hoff, M. L., Leemker, M., et al. 2023, Nature, 615, 227
Turner, B., Zuckerman, B., Fourikis, N., Morris, M., & Palmer, P. 1975, ApJ, 198, L125
van der Tak, F., Walmsley, C., Herpin, F., & Ceccarelli, C. 2006, A&A, 447, 1011
van Dishoeck, E. F. 2017, Proc. Int. Astron. Union., 13, 3
van Dishoeck, E. F., Bergin, E. A., Lis, D. C., & Lunine, J. I. 2014, arXiv preprint arXiv:1401.8103
van Dishoeck, E. F., Herbst, E., & Neufeld, D. A. 2013, Chem. Rev., 113, 9043
van Dishoeck, E. F., Kristensen, L. E., Mottram, J. C., et al. 2021, A&A, 648, A24
van Gelder, M., Jaspers, J., Nazari, P., et al. 2022, A&A, 667, A136
Visser, R., Doty, S., & van Dishoeck, E. 2011, A&A, 534, A132
Watanabe, N. & Kouchi, A. 2002, ApJ, 571, L173
Yarnall, Y. Y. & Hudson, R. L. 2022, ApJL, 931, L4

3

HDO ice detected toward an isolated low-mass protostar with JWST

Katerina Slavicinska, Łukasz Tychoniec, María Gabriela Navarro, Ewine F. van Dishoeck, John J. Tobin, Martijn L. van Gelder, Yuan Chen, A. C. Adwin Boogert, W. Blake Drechsler, Henrik Beuther, Alessio Caratti o Garatti, S. Thomas Megeath, Pamela Klaassen, Leslie W. Looney, Patrick J. Kavanagh, Nashanty G. C. Brunken, Patrick Sheehan, William J. Fischer

The Astrophysical Journal Letters (2025), 986(2), L19

Abstract

Water is detected in environments representing every stage of star and solar system formation, but its chemical evolution throughout these stages remains poorly constrained. Deuterium ratios offer a means of probing chemical links between water in different cosmic regions because of their sensitivity to physicochemical conditions. Here, we present the first detection of the 4.1 μm HDO ice feature with JWST toward a low-mass protostar, L1527 IRS, which may eventually grow to a sun-like mass. We measure an ice HDO/H_2O ratio of $4.4^{+3.7}_{-1.7}\times10^{-3}$, where the reported error is dominated by uncertainties in continuum definition and ice band strengths. This fraction is similar to the gas HDO/H_2O ratios measured in the warm (>100 K) inner cores of other low-mass protostellar envelopes and protoplanetary disks found in comparably isolated star-forming regions. Such a similarity tentatively supports the assumption that water vapor detected in these regions is not significantly altered by gas-phase reactions following ice sublimation. It also supports the hypothesis that pre- and protostellar water ice is largely inherited in a chemically unaltered state by outer protoplanetary disks. However, the fraction is a factor of ∼4-10 times higher than the gas HDO/H_2O ratios measured toward comets and low-mass protostars in clustered star-forming regions. This difference may be due to either gas-phase water reprocessing in protostellar envelopes and protoplanetary disks, or differences between prestellar conditions of isolated dense cores and the clustered star-forming regions that are more analogous to the environment in which our Sun formed.

3.1 Introduction

Water is a highly influential molecule that is essential to the formation and evolution of stars, planetary bodies, and life as we know it. It is also one of the most abundantly detected molecules in star-forming regions and has been observed at every evolutionary stage of star formation, from prestellar clouds to protostellar envelopes, protoplanetary disks, and solar system bodies such as our Earth, icy moons, and comets (Encrenaz 2008; van Dishoeck et al. 2014, 2021).

In recent years, numerous works have investigated whether the water found in these various environments is chemically linked. Many of these studies examined water deuterium ratios because the sensitivity of deuterium isotopic exchange reactions to physicochemical conditions makes D/H ratios excellent tracers of the origins and evolutionary histories of molecules. In particular, much of the water detected in our solar system is D-enriched (e.g., Lécuyer et al. 1998; Waite et al. 2009; Alexander et al. 2012; Altwegg et al. 2015), in some cases by almost two orders of magnitude, with respect to the D/H observed in the diffuse interstellar medium ($\sim2\times10^{-5}$, Prodanović et al. 2010). Because deuterium enrichment is efficient in low-temperature environments, these high water D/H ratios may be a remnant signature of water's origins in the primitive ices of extremely cold and dense prestellar clouds from which stars and solar systems eventually form.

To confirm such a link between the water in our solar system and interstellar water ice, the water deuterium ratios (HDO/H_2O) of ices in young star-forming regions must be measured. In theory, this value can be obtained by calculating HDO ice column densities via the 4.1 μm O-D stretching mode of HDO. However, prior to the launch of the *James Webb* Space Telescope (JWST), reported detections of this feature (e.g., Teixeira et al. 1999) remained

controversial due to the low sensitivity of previous IR telescopes (Dartois et al. 2003; Parise et al. 2003), hindering the direct quantification of reliable ice HDO/H_2O ratios.

Interferometric (sub)millimeter gas-phase studies thus attempted to quantify interstellar ice HDO/H_2O ratios indirectly instead by targeting the warm (>100 K) inner regions of protostellar envelopes ("hot corinos"). Because it is often argued that the majority of the gas species detected in these environments originate from the thermal desorption of ices with little subsequent gas-phase chemical alteration (e.g., Requena-Torres et al. 2006; Coletta et al. 2020; Van Gelder et al. 2020; Nazari et al. 2021; Chen et al. 2023), their measured gas HDO/H_2O ratios are assumed by some to reflect the ratios of their ice envelopes. Toward four protostars located in the clustered cloud complexes NGC 1333 and Ophiuchus, the measured gas HDO/H_2O ratios range between 5-9$\times10^{-4}$ (Persson et al. 2014), very similar to the ratios measured in several comets in our solar system (e.g., Eberhardt et al. 1995; Villanueva et al. 2008; Altwegg et al. 2015). Because our solar system likely formed in a clustered star-forming region (Adams 2010; Desch & Miret-Roig 2024), this similarity has been used to assert the claim that cometary water ice was directly inherited from the prestellar cloud or protostellar envelope with minimal chemical processing in the protoplanetary disk in which comets formed (Cleeves et al. 2014). In contrast, the gas HDO/H_2O ratios measured toward five distributed hot corinos found in isolated environments (i.e., they are not associated with star-forming cloud complexes) tend to be a factor of 2-10 higher (Jensen et al. 2019, 2021; Andreu et al. 2023; Tobin et al. 2023). Some of these studies suggested that such a difference in gas HDO/H_2O ratios could be due to the lower radiation experienced by more isolated star-forming regions, which implies colder and/or longer prestellar stages than those in more clustered star-forming regions. It must be emphasized, however, that this reported dependence of the protostellar gas HDO/H_2O on the local environment is based on a very limited sample size of sources, as discussed further in Section 3.3.3.

Nevertheless, it is possible that the gas-phase water detected toward hot corinos has experienced some degree of chemical processing in the gas phase (e.g., isotopic exchange with H_2 gas), which would mean that the water accreted by bodies forming in protoplanetary disks could be substantially altered from its prestellar state. To ascertain that these gas HDO/H_2O ratios are in fact not significantly altered by gas-phase processing and therefore are representative of ice HDO/H_2O ratios, HDO ice must be quantified directly.

The advent of JWST, with its unprecedented sensitivity, offers an opportunity to revisit the search for HDO ice toward such star-forming regions. Recently, Slavicinska et al. (2024) demonstrated the capability of JWST to unambiguously detect HDO ice toward two massive protostars and subsequently calculated the ice HDO/H_2O ratios of their envelopes. Here, we focus on the source L1527 IRS (also IRAS 04368+2557, hereafter L1527), an isolated low-mass class 0/I protostar (Tobin et al. 2013) found in the Taurus molecular cloud (d = 140 pc) that is deeply embedded within a dense 0.9 $M_\odot$ envelope and has a 0.0075 $M_\odot$, 75-125 AU-sized disk observed in the edge-on configuration (Aso et al. 2017; Kristensen et al. 2012; Tobin et al. 2013). The protostar currently has a mass around ∼0.3-0.5 $M_\odot$ (Aso et al. 2017; van't Hoff et al. 2023) but may eventually accrete enough material from its envelope to grow to a sun-like mass (Tobin et al. 2012).

A low-resolution (R=$\lambda/\Delta\lambda$∼100) IR spectrum of the ices toward L1527 from 2.5-5.0 μm was previously collected with the AKARI telescope. Aikawa et al. (2012) analyzed the ice features in this spectrum and tentatively assigned a weak feature observed close to the noise level at ∼4.13 μm to HDO ice. While the 3 μm H_2O feature was saturated in this spectrum,

an ice HDO/H_2O ratio was calculated by estimating the H_2O ice column density via fitting the wings of the 3 μm feature. The resulting ratio, 2.0×10^{-2}, is notably higher than the subsequently derived hot inner gas HDO/H_2O ratios of other low-mass protostars (Persson et al. 2014; Jensen et al. 2019, 2021).

Here, we revisit the 4.1 μm spectral region of L1527 with the JWST Near-InfraRed Spectrograph (NIRSpec), whose sensitivity, spatial resolution, and spectral resolution far exceed those of the AKARI facility. Furthermore, we use the JWST Mid-InfraRed Instrument (MIRI) to expand the observed spectrum of L1527 to 27.9 μm, enabling the detection of the 12 μm H_2O ice libration feature. These new high-quality data allow us to determine a robust ice HDO/H_2O ratio within an ice envelope of a low-mass protostar and compare this value with gas HDO/H_2O ratios measured toward hot corinos. Such comparisons can serve to evaluate whether water in protostellar envelopes undergoes significant gas-phase reprocessing once it sublimates from ices, and whether such reprocessing affects the water that is eventually accreted by volatile-rich bodies formed in outer protoplanetary disks.

3.2 Methods

3.2.1 Observations

Medium-resolution ($R=\lambda/\Delta\lambda\sim$700-1300) IR spectra of L1527 covering the 4.1 μm HDO ice band were collected with the NIRSpec Integral Field Unit (IFU) using the G395M grating as part of the cycle 1 GO program #1798 (PI John Tobin). NIRSpec IFU spectra collected with this grating provide continuous spectral coverage from 2.87-5.27 μm, unlike spectra collected with the G395H grating, which have a detector gap that overlaps with the 4.1 μm HDO ice feature. Additional low-resolution NIRSpec IFU PRISM ($R=\lambda/\Delta\lambda\sim$100) spectra from 0.6-5.3 μm collected as part of the cycle 1 GO program #1960 ("JOYS+", PI Ewine van Dishoeck), and MIRI Medium Resolution Spectrometer (MRS, $R=\lambda/\Delta\lambda\sim$1500-3500) spectra from 4.90-27.90 μm collected as part of the cycle 1 GTO program #1290 ("JOYS", PI Ewine van Dishoeck) gave continuous spectral coverage of L1527 from 0.6-27.9 μm. These JWST data can be accessed in the Mikulski Archive for Space Telescopes (MAST) via doi: 10.17909/jhkb-w045.

The one-dimensional continuous 0.6-27.9 μm spectrum analyzed in this work was extracted using 1" and 1.3" diameter apertures for the NIRSpec and MIRI datacubes, respectively (Figure 3.1). The aperture sizes differ to account for the PSF difference between NIRSpec and MIRI at the wavelength where their spectral coverages overlap (MIRI PSF at 5 μm = $\sim$1.3$\times$ NIRSpec PSF at 5 μm, Law et al. 2023; Federman et al. 2024). The spectra did not require scaling for the NIRSpec and MIRI fluxes to align in the overlapping 4.90-5.27 μm wavelength range. The apertures were centered on positions that maximized the flux at 5 μm (α_{J2000}=4:39:53.929, δ_{J2000}=+26:03:09.617 in NIRSpec and α_{J2000}=4:39:53.879, δ_{J2000}=+26:03:10.119 in MIRI) to correct for small ($\sim$0.5") differences in coordinate calibration between NIRSpec and MIRI. Further details regarding the extraction position and data reduction can be found in Appendix 3.A.1.

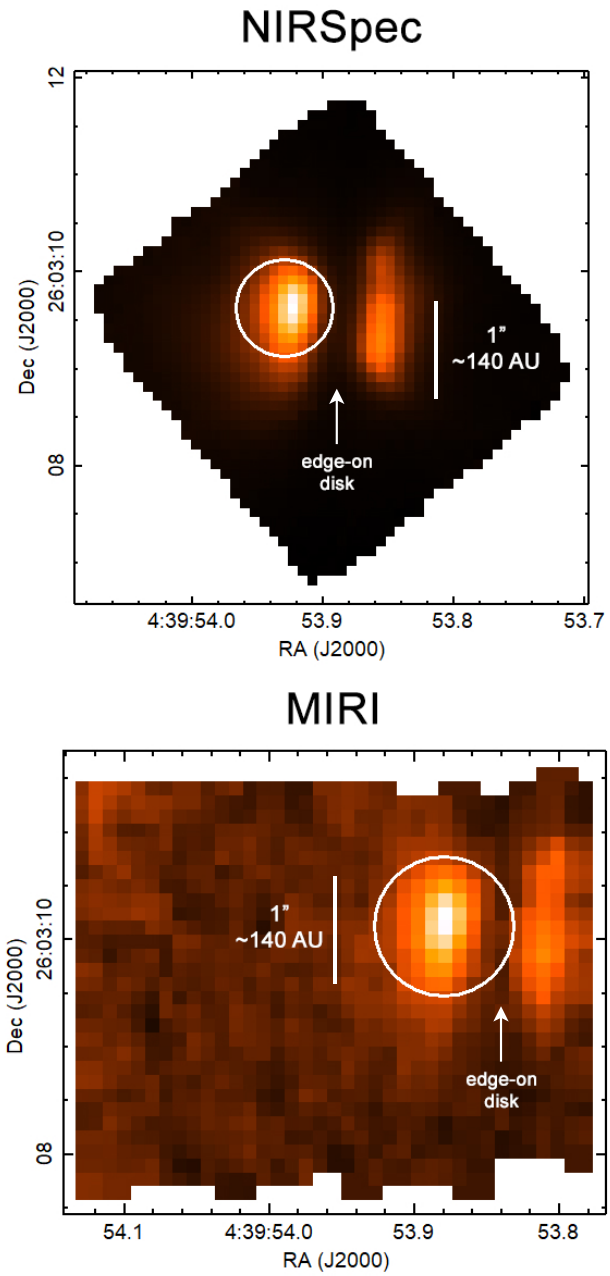


Figure 3.1: 5 μm continuum maps from the L1527 datacubes collected via NIRSpec IFU G395M (top) and MIRI-MRS (bottom) with the positions of the respective 1" and 1.30" diameter apertures used to extract the analyzed spectra shown in white.

3.2.2 Ice fitting

Although L1527 has a disk, its disk mass is $\gtrapprox$100 times less than the mass of its envelope – i.e., the source is still relatively young and very deeply embedded. Therefore, unlike in class II sources where the ice envelopes have largely dissipated and most of any observed ice absorptions are expected to originate from disks, we expect ices in the envelope to dominate the observed ice absorption toward L1527, and that the ice absorptions observed at short (NIRSpec) and long (MIRI) wavelengths probe similar spatial regions of the protostellar system. To confirm that this assumption is reasonable, we used the diagnostic technique of comparing ice bands of the same species at different wavelengths suggested by Pontoppidan et al. (2005). Specifically, we compared the profiles and optical depths of the 4.39 μm $^{13}CO_2$ and 3.53 μm CH_3OH bands in the NIRSpec data with those of the 15.2 μm $^{12}CO_2$ and 9.7 μm CH_3OH bands in the MIRI data and found that the degrees of thermal processing and column densities indicated by these bands were consistent with each other (see Appendix 3.A.3). Thus, we opted to analyze the L1527 spectrum via classical techniques used to fit ice absorptions toward other class 0 and I sources (e.g., Gibb et al. 2004; Boogert et al. 2008) rather than the complex radiative transfer modeling employed to analyze ice absorptions toward class II sources (e.g, Sturm et al. 2023a; Bergner et al. 2024).

HDO and CH_3OH ice fitting

The 4 μm spectral region where the strongest HDO ice feature is found can also include contributions from CH_3OH and S-bearing ice species. This work used the procedures and laboratory data described in Slavicinska et al. (2024) to deconvolve these blended features and quantify the HDO and CH_3OH ice observed toward L1527 via the NIRSpec G395M data.

To briefly summarize this procedure, the CH_3OH ice column density was first obtained by fitting the 3.53 μm feature (isolated via a third-order polynomial local continuum subtraction, see Figure 3.A.8) with CH_3OH ice laboratory spectra and a Gaussian representing NH_3 hydrates, although NH_4^+ salts can also have similar broad absorption feature around the same wavelength (Schutte & Khanna 2003). More details on the CH_3OH ice fitting at 3.53 μm can be found in Appendix 3.A.2. The resulting CH_3OH ice column density, calculated using a band strength of 4.86×10^{-18} cm molec^{-1} for the 3.53 μm band from Luna et al. (2018), was then used to constrain the expected contribution of the CH_3OH combination modes to the 3.7-4.2 μm spectral region (isolated via a fourth-order polynomial local continuum subtraction, see Figure 3.A.5). The remaining spectral excess between 3.7-4.2 μm was subsequently fit with a combination of a Gaussian representing SH-bearing species and smoothed laboratory spectra of both amorphous and crystalline HDO ice. Band strengths of 6.9×10^{-17} and 6.8×10^{-17} cm molec^{-1} from Table A2 in Slavicinska et al. (2024) corresponding to the temperatures of the best-fitting amorphous and crystalline HDO profiles, respectively, were used to calculate the total HDO ice column density. These corresponding temperatures should not be interpreted as directly representative of the ice temperatures, as this two-component fit is only a first-order approximation of the continuous thermal gradient that is expected along the line of sight. Details on the uncertainty calculations for the HDO and CH_3OH ice column density can be found in Appendix 3.A.4.

H_2O ice fitting

H_2O ice, the most abundant observable ice toward most protostars, has mid-IR absorption features at approximately 3, 4.5, 6, and 12 μm that vary significantly in strength (Mastrapa et al. 2009). The 3 μm stretching feature is preferentially used to quantify H_2O ice whenever possible because out of the four main H_2O mid-IR features, it is the strongest and the least blended with other ice or dust bands. However, as a result of its strength and the relatively high abundance of water ice, it is frequently saturated toward the most embedded protostellar sight-lines, as is the case for L1527. Two alternative methods can be used to derive H_2O ice column densities when this is the case: 1) fitting one or both of the wings of the 3 μm feature (e.g., Aikawa et al. 2012), or 2) fitting the 12 μm libration feature (e.g., Boogert et al. 2008; Chen et al. 2024). The first method is complicated by the fact that the wings of the 3 μm band shift with temperature, grain size, and chemical environment (Smith et al. 1989; Dartois & d'Hendecourt 2001), so H_2O ice column densities derived from this method are highly dependent on the physical and chemical parameters of the template H_2O ice spectra used in the fit, as discussed further in Appendix 3.A.5. The second method requires full mid-IR spectral coverage due to the broad profile of the 12 μm feature as well as its blending with similarly broad neighboring silicate features at 10 and 18 μm.

In this work, we derived the H_2O ice column density by fitting the 12 μm band. We used the observed optical depths at 2.8, 4.5, and 6 μm as additional constraints (i.e., the blue wing of the 3 μm band and the 4.5 and 6 μm features should not be vastly overfit with the model). Details on the continuum fitting used to extract the spectrum into the optical depth scale and the silicate subtraction used to isolate the 12 μm band can be found in Appendix 3.A.2. A set of H_2O ice spectral models with a range of temperatures and grain sizes were generated via the DHS model for irregular grains (Min et al. 2005) with the `OPTOOL` code (Dominik et al. 2021), using water ice optical constants from (Mastrapa et al. 2009). The full continuum- and silicate-subtracted spectrum was then fit with various combinations of these models until a combination that met all of the fitting criteria (sufficiently fits the 12 μm band without vastly overfitting the blue wing of the 3 μm band and the 4.5 and 6 μm bands) was found. The final model used a power-law size distribution $N(a) \propto a^{-3.5}$ with grain sizes ranging from 0.1-1.0 μm and included amorphous H_2O ice at 40 K, amorphous H_2O ice at 80 K, and crystalline H_2O ice at 80 K. Band strengths from Mastrapa et al. (2009) corresponding to these respective ice temperatures and phases (2.3×10^{-17}, 3.0×10^{-17}, and 3.3×10^{-17} cm molec^{-1}) were then used to calculate the total H_2O ice column density by summing the contribution to the full 12 μm band from each of these fit components. As with the HDO, the temperatures used in this model should not be interpreted as extracted temperatures of the H_2O ice, as they are only a rough approximation of the expected continuous thermal gradient along the line of sight. Additionally, these fits use only pure H_2O ice laboratory data and thus do not account for possible changes in the peak profiles due to chemical effects (e.g., mixing with other ice species like CO_2, NH_3/NH_4^+, CH_3OH, etc.), which can be degenerate with temperature effects. Details on the uncertainty calculations for the H_2O ice column density can be found in Appendix 3.A.4.

3.3 Results and discussion

3.3.1 HDO ice

Figure 3.2 presents the 3.7-4.2 μm region of the L1527 spectrum in optical depth units after the local continuum subtraction (see Appendix 3.A.2). The CH_3OH column density from the 3.53 μm fit (see Appendix 3.A.2) applied to fit this spectral region leaves small ($\sim$0.01-0.02 τ) and large ($\sim$0.14 τ) excess absorptions between 3.9-4.0 and 4.0-4.2 μm, respectively. The large excess between 4.0-4.2 μm is observed throughout the entire datacube, including areas both with and without scattering wings around the 4.27 μm CO_2 band (see Figure 3.A.5).

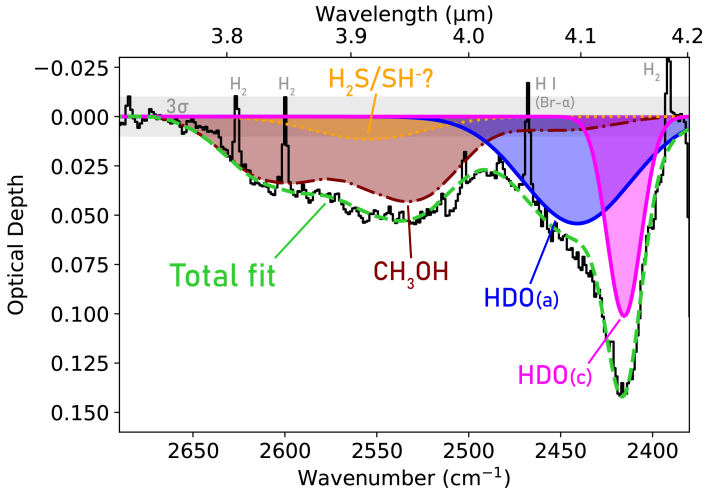


Figure 3.2: NIRSpec spectrum of L1527 on the optical depth scale from 3.7-4.2 μm (solid black trace) along with the ice fit components CH_3OH (dash-dotted brown trace), a Gaussian representing SH-bearing ices (dotted yellow trace), amorphous HDO (solid blue trace), crystalline HDO (solid magenta trace), and the total combined ice fit (dashed green trace). The gray horizontal shaded region indicates the 3σ noise level. See Figure 3.A.5 for the local continuum used to extract this spectrum.

The absorption excess between 4.0-4.2 μm presents an asymmetric feature with a profile very similar to that observed by Slavicinska et al. (2024) toward higher mass sources, although with much higher optical depth and improved S/N. Given an RMS σ value of $\sim$0.004 determined from the relatively featureless 3.71-3.77 μm range, the feature is detected at almost 40σ, far exceeding the S/N of the L1527 HDO ice detection reported by Aikawa et al. (2012). As with the massive protostellar spectra presented in Slavicinska et al. (2024), the feature is fit well using a combination of amorphous and crystalline HDO ice profiles that correspond to temperatures of $\sim$100 and 70 K, respectively, in laboratory 0.4% HDO:H_2O ice mixtures. Such a combination of amorphous and crystalline components approximates to a low degree a thermal gradient within the ice envelope, which is expected along the line of sight, and thus should not be interpreted as the extracted physical ice temperatures. The presence of both amorphous and crystalline HDO is consistent with additional spectral evidence for thermal processing toward this source, such as the double-peaked 4.39 μm $^{13}CO_2$ stretching and 15.2 μm $^{12}CO_2$ bending features (Pontoppidan et al. 2008; Brunken et al. 2024b), and indicates that

the most heated regions have experienced high enough temperatures to crystallize water ice. The HDO ice column density calculated from these fits, $9.2^{+7.3}_{-1.7}\times10^{16}$ cm^{-2} (see Table 3.1), is consistent with the L1527 HDO ice column density of 9.6×10^{16} cm^{-2} reported from AKARI data by Aikawa et al. (2012) despite the differences in the data quality and fitting methods (further discussion in Appendix 3.A.5).

The excess absorption between 3.9-4.0 μm is fit well with a Gaussian with a peak position of $\sim$3.9 μm and FWHM of $\sim$0.1 μm, which is similar to the profile of the S-H stretching mode of SH-bearing species like H_2S and NH_4SH in water-rich ices (Yarnall & Hudson 2022; Slavicinska et al. 2025). The fit presented in Figure 3.2 results in column density upper limits of $\sim$0.3% with respect to H_2O if assuming the only species contributing to the excess is H_2S and $\sim$13% with respect to H_2O if assuming the only species contributing to the excess is NH_4SH, but these upper limits are extremely dependent on the continuum choice, resulting in estimated uncertainties on the order of $\sim$300% and $\sim$70%, respectively (see Appendix 3.A.4).

Table 3.1: Ice column densities and abundances toward L1527 and the optical depths of the features used to calculate them.

Ice	Feature μm	Optical depth τ	Column density 10^{17} cm^{-2}	Abundance w.r.t. H_2O
H_2O	12	$2.0^{+0.7}_{-0.4}$	209^{+102}_{-51}	$\equiv1$
HDO	4.1	$0.14^{+0.03}_{-0.01}$ [a]	$0.92^{+0.73}_{-0.17}$	$4.4^{+3.7}_{-1.7}\times10^{-3}$
CH_3OH	3.53	$0.58^{+0.05}_{-0.06}$ [b]	22^{+9}_{-11}	$0.11^{+0.05}_{-0.06}$

[a] Optical depth of the entire amorphous and crystalline HDO absorption complex at 4.14 μm. The optical depths of the individual fitted amorphous and crystalline components are $0.05^{+0.03}_{-0.01}$ and $0.101^{+0.002}_{+0.005}$, respectively, with the asymmetric errors reflecting the differences in the optical depth of the fit components when using the "upper and lower limit" local continua shown in Appendix 3.A.4. [b] Optical depth of the entire CH_3OH+NH_3 absorption complex at 3.53 μm.

3.3.2 H_2O ice

The profile of the isolated 12 μm H_2O libration band is fit with a combination of grain-shape corrected models of amorphous H_2O ice at 40 K, amorphous H_2O ice at 80 K, and crystalline H_2O ice at 80 K (Figure 3.3). Such a combination of amorphous and crystalline components again approximates a thermal gradient within the ice envelope. This fit at 12 μm is consistent with the optical depth of the 4.5 μm combination mode and does not result in any overfitting of the 6 μm feature (which consists of the H_2O ice bending mode blended with other ice features, Boogert et al. 2008). However, the blue wing of the 3 μm band is slightly overfit, while the red wings of the 3 and 12 μm bands are underfit. It was not possible to obtain a satisfactory fit to these wings while still sufficiently fitting the 12 μm feature using only grain shape-corrected pure H_2O models. Including laboratory spectra of H_2O mixed with other major ice components (e.g., CO_2, NH_3, ammonium salts) may result in improvements to the fits in these wings, but we did not include such components in our fit for simplicity's sake, as deducing the chemical environment of H_2O ice is outside the scope of this work, and the inclusion of such components likely would not affect the final calculated H_2O ice column

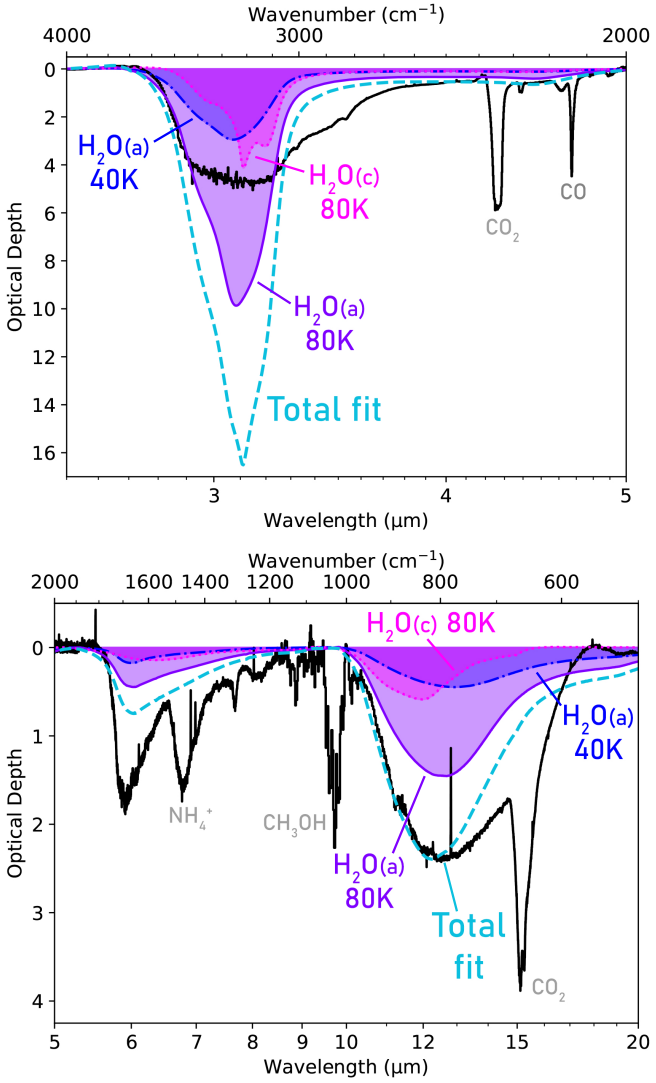


Figure 3.3: Silicate-subtracted NIRSpec (top) and MIRI (bottom) spectra of L1527 on the optical depth scale (solid black trace) along with the fit components for H_2O ice: amorphous H_2O at 40 K (dash-dotted blue trace), amorphous H_2O at 80 K (solid purple trace), crystalline H_2O at 80 K (dotted magenta trace), and the total combined ice fit (dashed light blue trace). The observational data between 8.7-11.7 μm has been smoothed with a 10-point boxcar average to ameliorate the higher noise level due to the deep silicate feature at these wavelengths. Peaks of other major species (e.g., CO_2, CO) are labeled in gray but not fit. The temperatures indicated in this figure should not be interpreted as the extracted physical temperatures of the observed H_2O ice (see Sections 3.2.2 and 3.3.2). See Figure 3.A.6 for the global continuum fit and Figure 3.A.7 for the silicate subtraction.

density outside of the reported uncertainties (see Appendix 3.A.4) given that the band strength of the H_2O libration mode is not strongly affected by mixing with other common interstellar ice constituents (Kitta & Krätschmer 1983).

The H_2O ice column density obtained from the fit, $2.09^{+1.02}_{-0.51}\times10^{19}$ cm^{-2} (see Table 3.1), is a factor of 4 greater than the H_2O ice column density measured from the AKARI spectra (Aikawa et al. 2012), which was likely underestimated due to the availability of only the wings of the 3 μm band for fitting and a single template H_2O ice spectrum at a very cold temperature (10 K) being used in the fit (see Appendix 3.A.5). A higher H_2O ice column density, on the order of 10^{19} molec cm^{-2}, is expected toward this source given its massive envelope and very deep silicate feature (Figure 3.A.14). In fact, the high water column density and optical depth of the 9.7 μm silicate feature ($\tau\sim4.2$) of L1527 are typical of other deeply embedded low-mass Class 0 protostars now being probed by JWST (e.g., Chen et al. 2024).

While the 12 μm H_2O feature serves as a satisfactory means of measuring the total H_2O ice column density, it cannot reliably indicate ice physical properties in the way that the sharp, asymmetric profile of the 4.1 μm HDO band indicates crystallinity (Section 3.3.1) due to the degenerate effects of temperature, grain shape and size, chemical environment, and the choices in continuum and subtracted silicate template on its broad profile (e.g., Boogert et al. 2008; Mastrapa et al. 2009). This means that the temperatures of the H_2O ice data used in the H_2O fit should not be interpreted as representative of the actual temperature of the observed H_2O ice, as possible effects of different chemical environments on the profile of the 12 μm band were not considered here (see Section 3.2.2). The profile change of the 12 μm feature upon crystallization is also not as dramatic compared to the very evident sharpening of the 3 μm H_2O stretching mode, which is saturated toward this source. As mentioned in Section 3.2.2, physicochemical effects on the wings of the 3 μm feature can be degenerate as well, so these wings are also unreliable tracers of physical properties when the 3 μm feature is saturated. For this reason, no secure conclusions can be drawn about the temperature or morphology of H_2O ice toward this source from this fit.

However, the total L1527 water ice abundance with respect to the hydrogen column density can provide other valuable information regarding the thermal processing history of the ice envelope. This value can be approximated using the relation between silicate optical depth and N_H in the dense cores of Lupus (Boogert et al. 2013). The resulting inferred H_2O ice abundance of L1527 is $\sim4\times10^{-5}$, on par with the higher end of H_2O ice abundance values measured toward other low-mass protostars (Figure 3.A.14). Such an abundance demonstrates that, although temperatures high enough to crystallize water ice must have been reached in at least some parts of the envelope of L1527 based on the 4.1 μm HDO ice band profile, a large portion of the envelope was likely not heated to high enough temperatures to desorb a significant portion of the H_2O ice (>100 K). The relatively blue peak position of the L1527 6.85 μm NH_4^+ feature, which is more redshifted toward sources that have lost most of their H_2O ice, is also consistent with this moderate processing scenario (Slavicinska et al. 2025).

3.3.3 HDO/H_2O ratio

The column densities of HDO and H_2O ice found here result in an ice HDO/H_2O ratio of $4.4^{+3.7}_{-1.7}\times10^{-3}$. A comparison of this ratio with HDO/H_2O values and upper limits previously measured in protostellar envelopes as well as volatile-rich solar system objects is presented in Figure 5.4.

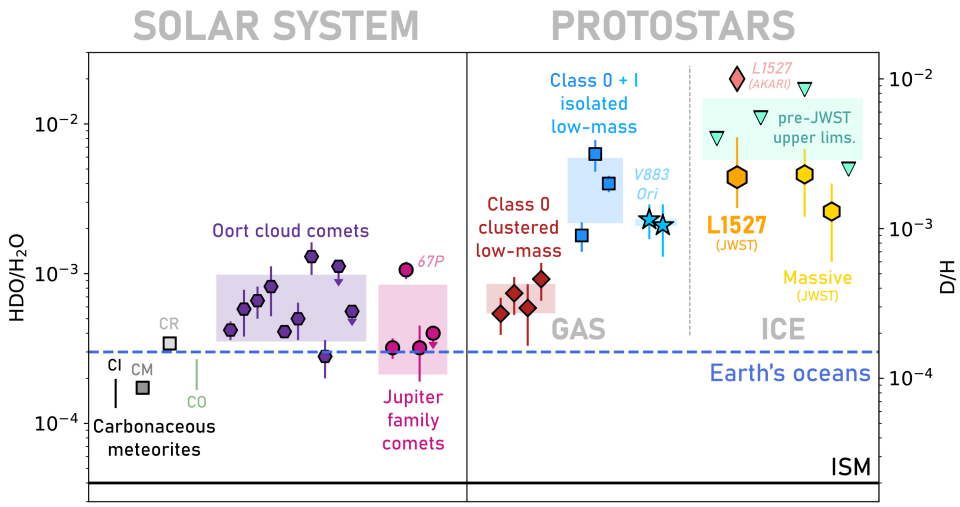


Figure 3.4: Comparison of HDO/H_2O ratios measured in various primitive solar system objects and toward protostars in both ices and the gas phase. The ice HDO/H_2O ratio of L1527 measured in this work using JWST data is indicated with the large orange hexagon. The data and their sources can be found in Tables 3.A.2 and 3.A.3.

Within the reported uncertainties, our value is consistent with the range of HDO/H_2O gas values that have been observed toward isolated low-mass protostars (1.8 ± 0.4-$6.3\pm1.5\times10^{-3}$) in the hot inner regions of Class 0 and I protostellar envelopes (Jensen et al. 2019, 2021; Andreu et al. 2023). This similarity supports the assumption that the gas HDO/H_2O ratios measured in the hot regions of protostars with sun-like masses are indeed representative of their ice HDO/H_2O ratios. Nevertheless, given the nearly half order of magnitude scatter observed in the gas HDO/H_2O ratios of isolated low-mass protostars, it is clear that parameters such as specific local conditions and evolutionary timescales may affect these ratios as well, so future work comparing gas and ice HDO/H_2O ratios toward the same protostar will be crucial for constraining the exact extent of gas-phase water reprocessing upon the sublimation of water ice in the envelopes of these objects.

Tobin et al. (2023) recently showed that the gas HDO/H_2O ratio of $2.26\pm0.63\times10^{-3}$ measured within the extended snowline of a disk of an isolated Class I protostar that recently experienced an accretion burst, V883 Ori, is generally consistent with the gas ratios measured in the hot inner regions of isolated Class 0 low-mass protostars. Such a consistency serves as evidence that the ices formed early in the star formation process, in prestellar clouds and protostellar envelopes, may be largely inherited by the outer regions of protoplanetary disks (and, by extension, the planetary bodies that form within them) of sun-like protostars without substantial chemical alteration via gas-phase reactions. Given that L1527 is an isolated low-mass protostar classified somewhere between the Class 0 and I stages (Tobin et al. 2013), the similarity of its ice HDO/H_2O ratio to gas HDO/H_2O ratios measured toward both Class 0 and Class I isolated sources, including V883 Ori, further corroborates this scenario.

The ice HDO/H_2O ratio of L1527 being consistent with the gas HDO/H_2O ratios of other

isolated low-mass protostars means that it is also higher by a factor of ∼4-7 than the gas HDO/H_2O ratios measured in the hot inner regions of clustered Class 0 protostars and up to an order of magnitude higher than the HDO/H_2O ratios measured in comets (see Tables 3.A.2 and 3.A.3). As mentioned previously, it has been suggested that water formed in isolated star-forming regions has higher D/H ratios than that formed in clustered regions because of either longer or colder prestellar stages, during which the majority of the ices in protostellar envelopes form (Jensen et al. 2019, 2021). If this hypothesis is correct and local conditions greatly influence deuterium ratios, then our L1527 ice HDO/H_2O ratio is not fully comparable to cometary HDO/H_2O ratios because our Sun likely formed in a highly clustered and irradiated (and thus warmer) star-forming region (Adams 2010; Desch & Miret-Roig 2024). However, more samples are needed to ensure that this trend of higher HDO/H_2O ratios in more isolated protostars is statistically robust, as the current sample of protostellar gas HDO/H_2O values is still relatively small and consists of sources scattered throughout multiple molecular clouds in different galactic locations. The four currently published clustered protostellar gas HDO/H_2O values were measured toward the Ophiuchus and Perseus NGC 1333 molecular clouds, while the five isolated gas values were measured toward less populated regions in Orion and Taurus and three different isolated Bok globules. This means that any comparison of their values does not control for differences that could arise due to sampling from different star-forming regions. For this reason, larger sample sizes of both gas and ice HDO/H_2O measurements, particularly of protostars in the same molecular cloud but with different proximities to other stars, are crucial.

Furthermore, the ice HDO/H_2O ratio of L1527 is very similar to the ice HDO/H_2O ratios measured recently with NIRSpec IFU G395M toward more massive protostars (2.6 ± 1.4 and $4.6\pm2.2 \times10^{-3}$, Slavicinska et al. 2024). HOPS 370 in particular is located north of the extended Orion Nebula Cluster, a highly active star-forming region, so its similar ice HDO/H_2O ratio to L1527 is inconsistent with the above hypothesis. It is also inconsistent with the trend observed in the deuterium ratio of CH_3OH gas in protostars, which correlates negatively with stellar mass (i.e., more massive protostars tend to have lower CH_2DOH/CH_3OH ratios, van Gelder et al. 2022). If isotopic ratios of species that formed primarily in the solid state do in fact reflect prestellar cloud conditions as has been previously suggested (Jensen et al. 2019; van Gelder et al. 2022), the similarity between HDO/H_2O ratios in low- and high-mass protostars, both in the ice as noted here and in some gas measurements as discussed previously in Slavicinska et al. (2024), would imply similar prestellar conditions between isolated low-mass protostars and some massive protostars. However, the large scatter in the massive protostellar gas HDO/H_2O ratios and the small ice HDO/H_2O sample size in both isolated low-mass and massive protostars precludes drawing more general statements regarding the prestellar conditions of low-mass and massive protostars as a whole.

3.4 Conclusions

We report the first JWST detection and quantification of HDO ice toward a low-mass protostar, L1527 IRS. The detection and quantification were performed using the 4.1 μm O-D stretching mode observed with the NIRSpec IFU instrument. Due to JWST's unprecedented sensitivity and spectral resolution, the detection exceeds the noise level by almost 40σ, and the feature is spectrally resolved enough to reveal an asymmetric profile characteristic of both

amorphous and crystalline HDO ice in the envelope of L1527. We subsequently quantified the ice HDO/H_2O ratio toward this source using the 12 μm H_2O ice libration mode in the MIRI range. Our main conclusions can be summarized as follows:

1. We measured an ice HDO/H_2O ratio toward L1527 of $4.4^{+3.7}_{-1.7}\times10^{-3}$, where the reported uncertainties are dominated by uncertainties in continuum definition and laboratory ice band strengths rather than observational uncertainties.

2. The L1527 ice HDO/H_2O ratio is similar to the gas HDO/H_2O ratios measured interferometrically toward the hot inner regions of other isolated low-mass protostars and within the snowline of the young protoplanetary disk V883 Ori. This similarity is in general agreement with the assumption that gas-phase molecular abundances in hot corinos and young disks are representative of those in protostellar ices, with minimal alteration caused by chemical processing by gas-phase reactions following ice sublimation.

3. The ice HDO/H_2O ratio of L1527 is a factor of 4-7 times greater than the gas HDO/H_2O ratios measured toward Class 0 clustered low-mass protostars and up to an order of magnitude greater than those measured in comets. This difference may be due to the water in these objects having undergone gas-phase reprocessing at some stage, or because of differences in the local star-forming environments being reflected in the HDO/H_2O ratio of ices formed during the prestellar stages. If the latter scenario is the case, then the ice HDO/H_2O ratio measured toward an isolated object like L1527 would be expected to exceed the ratios measured in comets in our solar system because our Sun likely formed in a more clustered environment.

Moving forward, a comparison of the gas and ice HDO/H_2O ratios measured toward the same source will be essential to conclusively determine the extent of gas-phase chemical alteration of water in protostellar envelopes and protoplanetary disks given the large scatter in gas HDO/H_2O values measured in low-mass protostars. Additionally, measurements of HDO ice toward a larger sample of low-mass protostars in both clustered and isolated star-forming regions are needed to fully characterize the effects of local environmental conditions on ice HDO/H_2O ratios in protostellar envelopes and to conclusively evaluate the plausible link between protostellar and cometary water ice. The unprecedented sensitivity and spectral resolution of JWST opens the door for such measurements in the future.

3.5 Acknowedgments

K.S. thanks Brian Ferrari and Gary Huss for helpful scientific discussions. The authors thank an anonymous reviewer for their insightful comments that helped to improve this paper. This work is based on observations made with the NASA/ESA/CSA *James Webb* Space Telescope. The data were obtained from the Mikulski Archive for Space Telescopes at the Space Telescope Science Institute, which is operated by the Association of Universities for Research in Astronomy, Inc., under NASA contract NAS 5-03127 for JWST. These observations are associated with programs #1798, #1290, and #1960. All the data used in this paper can be found in MAST: doi: 10.17909/jhkb-w045. The following National and International

Funding Agencies funded and supported the MIRI development: NASA; ESA; Belgian Science Policy Office (BELSPO); Centre Nationale d'Etudes Spatiales (CNES); Danish National Space Centre; Deutsches Zentrum fur Luft- und Raumfahrt (DLR); Enterprise Ireland; Ministerio De Economiá y Competividad; Netherlands Research School for Astronomy (NOVA); Netherlands Organisation for Scientific Research (NWO); Science and Technology Facilities Council; Swiss Space Office; Swedish National Space Agency; and UK Space Agency. Astrochemistry at Leiden is supported by funding from the European Research Council (ERC) under the European Union's Horizon 2020 research and innovation programme (grant agreement No. 101019751 MOLDISK), the Netherlands Research School for Astronomy (NOVA), and the Danish National Research Foundation through the Center of Excellence "InterCat" (Grant agreement no.: DNRF150). A.C.G. acknowledges support from PRIN-MUR 2022 20228JPA3A "The path to star and planet formation in the JWST era (PATH)" funded by NextGeneration EU and by INAF-GoG 2022 "NIR-dark Accretion Outbursts in Massive Young stellar objects (NAOMY)" and Large Grant INAF 2022 "YSOs Outflows, Disks and Accretion: towards a global framework for the evolution of planet forming systems (YODA)".

3.A Appendix

3.A.1 Observations

The extraction coordinates are centered on the upper layer of the L1527 disk seen in scattered light, slightly off the source (which lies in the dark area between the two scattered light lobes visible in Figure 3.1) to maximize S/N of the ice features. However, besides S/N differences, there is little variation in the profiles and relative optical depths of the ice features in the spectrum extracted from these coordinates and the spectrum extracted from the source center, and in fact, there are no noticeable spatial variations in the ice band profiles throughout most of the datacube.

The NIRSpec data were reduced via the JWST pipeline v1.16.0 using the Calibration Reference Data System 154 (CRDS) context file `jwst_1298.pmap`. A wavelength offset of -0.004 μm was applied to the PRISM data to correct for what appears to be a discrepancy in wavelength calibration between PRISM and the G395M/H gratings observed in peak positions of both gas and ice lines. The MIRI data reduction is described in Devaraj et al. (2026).

3.A.2 Continuum, silicate, and CH_3OH ice fitting

Local continuum at 3.7-4.2 μm

The top panel of Figure 3.A.5 shows the continuum applied to extract the optical depth spectrum of the 3.7-4.2 μm region that was used to calculate the HDO ice column density (Figure 3.2). The local continuum fitting of this region is not trivial in this spectrum because the continuum is distorted by light scattering at the wings of the 4.27 μm CO_2 ice band, resulting in a break between the respective continua on the blue and red sides of the feature (e.g., Dartois et al. 2022).

However, in other spatial regions within the datacube, data can be extracted where the CO_2 scattering wings are minimal, and such a break in the continuum around the feature does not occur. The middle panel of Figure 3.A.5 shows a spectrum extracted from such a region

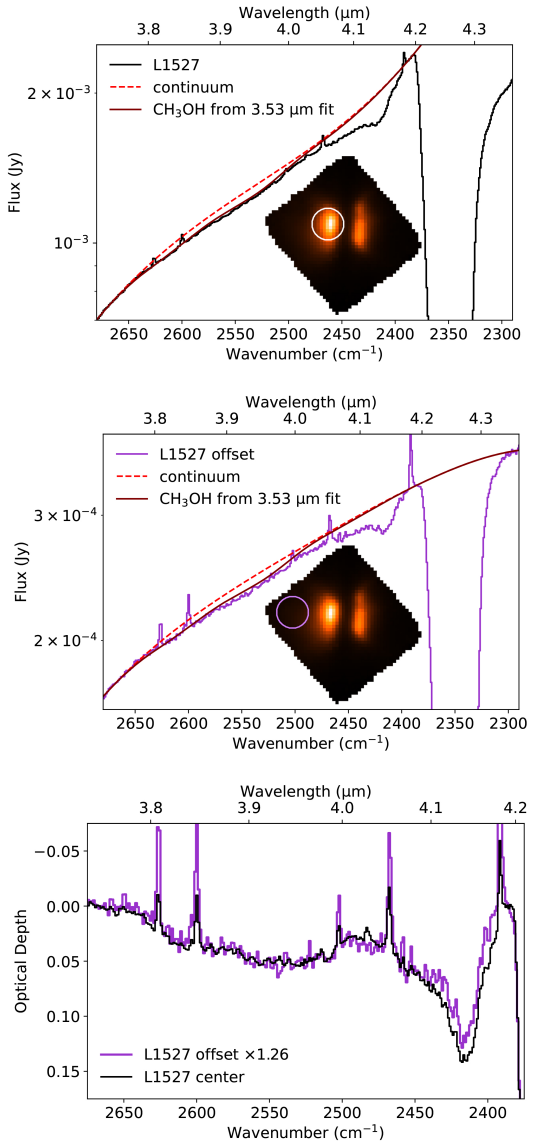


Figure 3.A.5: NIRSpec spectra of L1527 from 3.7-4.2 μm extracted with 1" apertures from the region where the flux at 5 μm is maximized (top panel, black trace) and the region where ice absorption features are still present, but the CO_2 scattering wing is minimized (middle panel, purple trace). The dashed red traces indicate the local continua fit to these spectral regions, and the insets show the respective extracted regions in the NIRSpec datacube. The bottom panel compares the extracted optical depth spectra resulting from these local continuum fits to the two spectra. The local continuum in the top panel was used to calculate the optical depth spectrum presented in Figure 3.2.

located east of the source. For this spectrum, the local continuum fitting at 3.7-4.2 μm is more straightforward as it can be defined so that it follows the flux on both sides of the 4.27 μm CO_2 band. This off-source spectrum can therefore be used to guide the local continuum fit to the higher S/N spectrum extracted from the region closer to the center of the source, where the continuum around the 4.27 μm band is disrupted by scattering.

The extracted spectra in optical depth resulting from these two local continuum fittings are shown in the bottom plot in Figure 3.A.5. Although the local continua of the two spectra differ in shape, the profiles and relative optical depths of the extracted ice features are consistent with each other. The profiles and relative optical depths of ice features in spectral regions where local continuum fitting is more trivial because there are no spectrally adjacent strong features distorting the continuum (e.g., CH_3OH at $\sim$3.5 μm, $^{13}CO_2$ at $\sim$4.4 μm, and OCN^- and CO at $\sim$4.6-4.7 μm) are also consistent, which shows that the ices observed along these two lines of sight have similar chemical compositions and have experienced similar degrees of thermal processing. However, the absolute optical depths of the ice features observed near the source center are on average a factor of $\sim$1.26 higher than those of the features in the offset position, which may be due to the ice envelope toward the offset position being thinner. For this reason, the offset spectrum in the bottom panel of Figure 3.A.5 is scaled by a factor of 1.26. The consistency between the extracted HDO absorption profiles provides confidence that the local continuum fit to the flux extracted from the central position sufficiently models the continuum distortion caused by the scattering wings of the 4.27 μm CO_2 ice band.

Global continuum and silicate subtraction

To extract the full combined NIRSpec+MIRI spectrum into the optical depth scale, we defined two separate but connecting global continua in the near-IR (2.5-5 μm) and mid-IR (5-28 μm) ranges by fitting low-order polynomials to the data on a $\log(\lambda F_\lambda)$ versus $\log(\lambda)$ scale, similar to the procedure described in Boogert et al. (2008). The resulting global continuum fit to the 2.5-27.9 μm spectral range is shown in Figure 3.A.6. Similarly curved SEDs have been used to subtract the global continuum from other protostellar spectra (e.g., see the CrA IRAS 32, IRAS 03235+3004, and CRBR 2422.8-3423 global continua in Figure 1 of Boogert et al. 2008) and can be reproduced by radiative transfer models of protostellar systems (Crapsi et al. 2008). In the case of our global continuum for L1527, the polynomial continuum fit can also be reproduced well with two blackbody curves, one at $\sim$450 K and another at $\sim$100 K, roughly simulating scattered light and thermal emission from different regions of the L1527 system.

We then isolated the 12 μm feature by subtracting a synthetic silicate spectrum generated for small spherical grains via the optical constants of amorphous olivine ($MgFeSiO_4$) and pyroxene ($Mg_{0.5}Fe_{0.5}SiO_3$) from Dorschner et al. (1995), as done previously for other dense and icy sightlines (Boogert et al. 2011). The fit used for the silicate subtraction is shown in Figure 3.A.7.

Local continuum at 3.3-3.7 μm and CH_3OH ice fit

The fit to the 3.3-3.7 μm region used to calculate the CH_3OH ice column density is shown in Figure 3.A.9. Despite the obvious presence of thermally processed ices along the line of sight, the CH_3OH feature at 3.53 μm is best fit only with laboratory spectra of cold (<40 K) CH_3OH.

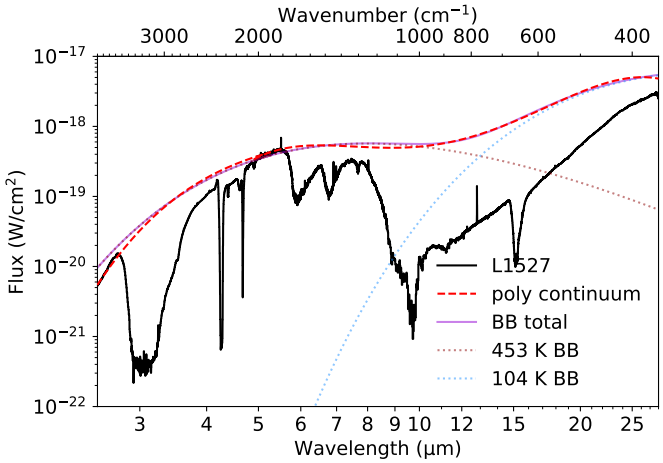


Figure 3.A.6: Global continuum fit to the combined NIRSpec and MIRI spectrum of L1527 across the 2.5-27.9 μm spectral range. The observational data between 8.7-11.7 μm has been smoothed with a 10-point boxcar average to ameliorate the higher noise level due to the deep silicate feature at these wavelengths. The dashed red trace shows the polynomial continuum used to perform the global continuum subtraction, while the translucent purple trace shows how the profile of this polynomial can be reproduced with two blackbody emission profiles, one at 453 K (dotted red trace) and another at 104 K (dotted blue trace).

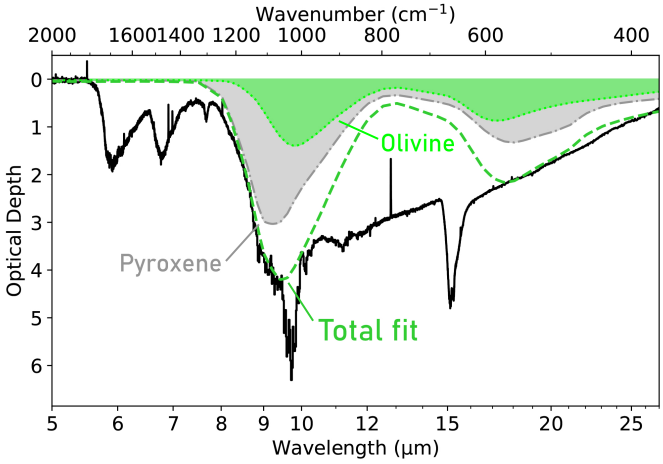


Figure 3.A.7: MIRI spectrum of L1527 on the optical depth scale following global continuum subtraction (solid black trace) along with the silicate fit components pyroxene (dash-dotted gray trace) and olivine (dotted lime trace) and the total combined silicate fit (dashed green trace). This silicate fit was used to isolate the 12 μm H_2O ice libration feature shown in Figure 3.3. The observational data between 8.7-11.7 μm has been smoothed with a 10-point boxcar average to ameliorate the higher noise level due to the deep silicate feature at these wavelengths.

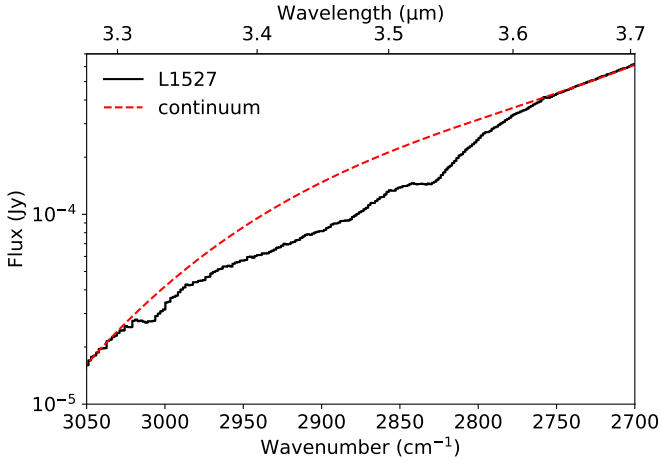


Figure 3.A.8: Local continuum fit to the 3.3-3.7 μm spectral region used to extract the optical depth spectra in Figure 3.A.9.

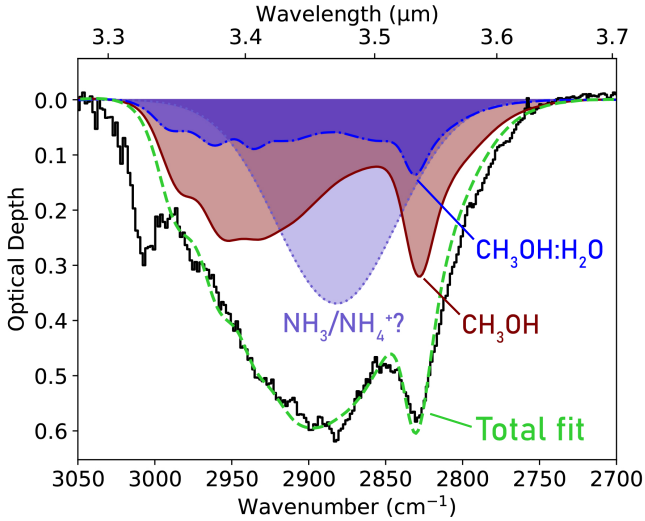


Figure 3.A.9: NIRSpec spectrum of L1527 on the optical depth scale from 3.3-3.7 μm (solid black trace) along with the ice fit components pure CH_3OH (solid brown trace), a 1:5 CH_3OH:H_2O ice mixture (dash-dotted blue trace), a Gaussian representing NH_3 hydrates or NH_4^+ salts (dotted lavender trace), and the total combined ice fit (dashed green trace). This CH_3OH fit was used to constrain the contribution of CH_3OH to the 3.7-4.2 μm region shown in Figure 3.2. See Figure 3.A.8 for the local continuum used to extract this spectrum.

Additionally, a combination of pure CH_3OH and CH_3OH in a water-dominated ice (in this case CH_3OH:H_2O 1:5) is needed to fit the feature. These fitting parameters are very

similar to those used in Slavicinska et al. (2024) toward two massive protostars with thermally processed lines of sight. The resulting CH_3OH ice column density is $2.2^{+0.8}_{-0.9}\times10^{18}$ cm^{-2}. The abundance of CH_3OH ice with respect to H_2O ice, $\sim$11%, is close to the upper quartile value of CH_3OH ice abundances toward the sample of mostly Class I low-mass protostars observed before JWST (Boogert et al. 2015).

3.A.3 Comparing NIRSpec and MIRI bands of the same ice species

Comparing the profiles and optical depths of bands found at different wavelengths but belonging to the same ice species can serve as a tool to evaluate whether disk radiative transfer effects need to be considered toward a source, as the ice column densities and chemical environments extracted from such bands of common species can differ in the same line of sight due to differences in photon paths through the disk at different wavelengths (Pontoppidan et al. 2005; Sturm et al. 2023b). Such differences can indicate that the observed ice absorptions originate from ices located in different regions of the protostellar system (i.e., the short and long wavelengths do not probe the same spatial regions). Here we compare the $^{13}CO_2$ stretching mode at 4.39 μm and the $^{12}CO_2$ bending mode at 15.2 μm as well as the CH_3OH C-H stretching mode at 3.53 μm and the CH_3OH C-O stretching mode at 9.7 μm to investigate if the ice column densities and physicochemical environments extracted from these profiles at different wavelengths are consistent with each other, as would be expected for ice absorptions that originate from an isotropic envelope made up of small ($\lesssim$1 μm) grains, where the same complex radiative transfer effects are not at play.

Figure 3.A.10 shows the comparison of these bands. First, both the 4.39 μm $^{13}CO_2$ feature and the 15.2 μm $^{12}CO_2$ feature have double-peaked profiles indicative of ice thermal processing (see Boogert et al. 2000; Pontoppidan et al. 2008; Brunken et al. 2024b). This consistency demonstrates that the degrees of thermal processing experienced by the ices probed at short and long wavelengths are similar. Furthermore, the $^{12}C/^{13}C$ ratio derived from these two bands by Brunken et al. (2024a) for L1527, 105, is consistent with the range of $^{12}C/^{13}C$ ratios derived for less evolved class 0 sources with split CO_2 features ($\sim$100-120). Although the 4.27 μm $^{12}CO_2$ stretching feature is saturated toward L1527 and the narrow 2.70 μm $^{12}CO_2$ combination mode is not resolved well enough in the low-resolution PRISM spectrum to derive a $^{12}CO_2$ column density from the shorter wavelengths, Brunken et al. (2024a) found that for similar sources with similar $^{12}C/^{13}C$ ratios and coherent 2.70, 4.27, and 15.2 μm bands, the $^{12}CO_2$ column densities derived from NIRSpec and MIRI data are remarkably consistent (typically within $\sim$5-20% error).

The CH_3OH ice column density derived from fitting the 9.7 μm band using the same combination of pure CH_3OH and CH_3OH:H_2O spectra used to fit the 3.5 μm absorption complex results in a CH_3OH column density of $3.1\pm0.6\times10^{18}$ molec cm^{-2} using a band strength of 1.56×10^{-17} cm molec^{-1} from Luna et al. (2018). This CH_3OH column density is consistent with the CH_3OH column density derived from the 3.53 μm band within the reported uncertainties that take into account both uncertainties in the continuum subtraction and band strengths. The difference between the two values, $\sim$33%, is similar to the difference between CH_3OH column densities from the 3.53 and 9.7 μm bands reported for observations of dense clouds (McClure et al. 2023).

These consistencies in the ice morphologies and column densities between ice bands of the same species probed at different wavelengths support the notion that the short and long

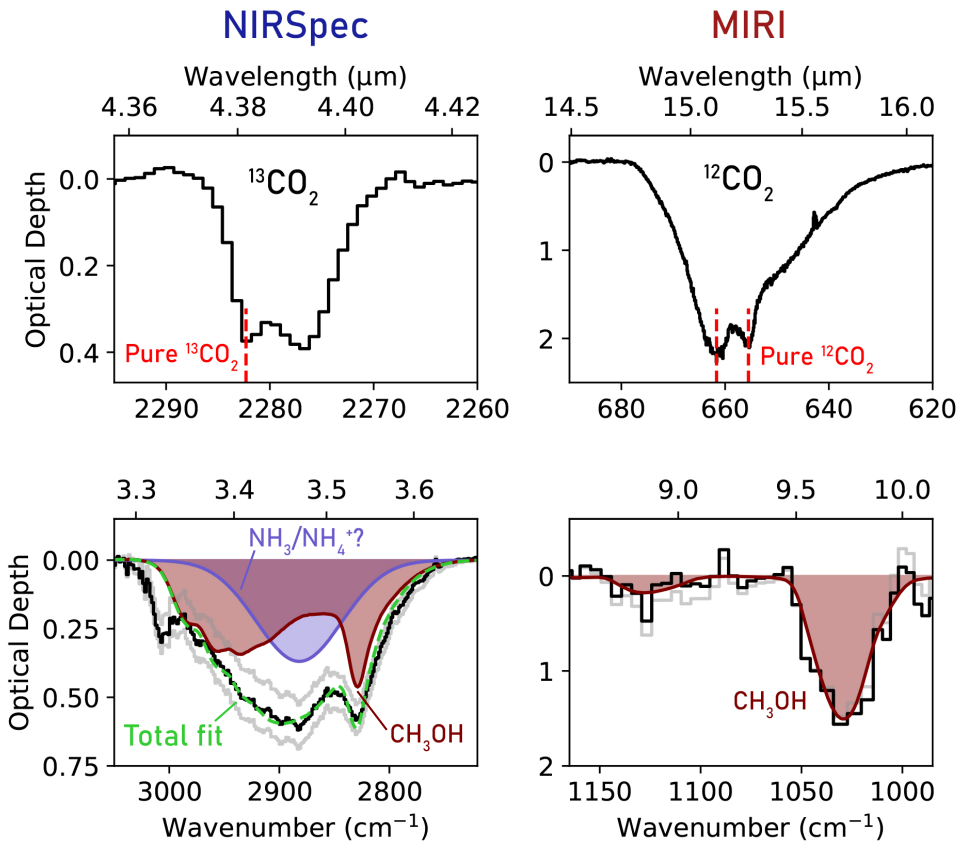


Figure 3.A.10: Comparison of absorption bands from the same ice species at NIRSpec and MIRI wavelengths. Top left: the 4.39 μm $^{13}CO_2$ stretching mode (NIRSpec). Top right: the 15.2 μm $^{12}CO_2$ bending mode (MIRI). In both top plots, the red dashed lines mark peak positions indicating the presence of pure CO_2 ice that segregated from other ice species during thermal processing. Bottom left: fit to the 3.53 μm CH_3OH C-H stretching mode (NIRSpec). The gray traces indicate the optical depth of this spectral region extracted with the upper and lower limit continua shown in Figure 3.A.13. Bottom right: fit to the 9.7 μm CH_3OH C-O stretching mode (MIRI) using the same combination of CH_3OH laboratory data used to fit the 3.5 μm complex in the bottom left panel. The data was binned using a binning factor of 30 to reduce the noise levels due to the CH_3OH band being located at the tip of the nearly saturated silicate feature. The black trace indicates the optical depth of this spectral region after the silicate subtraction shown in Figure 3.A.7. The gray trace indicates the optical depth of this spectral region extracted using the local continuum fitting procedure described in Section 2.1 of Bottinelli et al. (2010).

wavelengths probe similar spatial regions in the L1527 protostellar system and provide confidence that the ice absorptions observed toward L1527 can be analyzed using classical ice fitting techniques.

3.A.4 Ice fitting uncertainties

The reported uncertainties on the HDO, H_2O, and CH_3OH ice column densities were determined here using methods similar to those described in Slavicinska et al. (2024). Two main sources of uncertainty were considered: uncertainty of the local/global continuum choice, and uncertainty of the laboratory band strengths used to calculate the ice column densities. Compared to these two sources of uncertainty, other sources of uncertainty like observational noise and fitting covariances are small and are therefore treated here as negligible.

We quantified the uncertainties on the column densities from continuum uncertainty by defining the lower and upper limits of what we consider to be a "reasonable" continuum (top panels of Figures 3.A.11, 3.A.12, and 3.A.13) and then using the same methods described in Section 3.2 to derive lower and upper limits of HDO, H_2O, and CH_3OH column densities by fitting the optical depth spectra extracted via these continua (bottom panels of Figures 3.A.11, 3.A.12, and 3.A.13). In the case of HDO, we also ensured that a similar extracted spectral profile could be achieved with a "reasonable" local continuum fit to the spectrum extracted from the off-center position discussed in Section 3.A.2 (second and third rows in Figure 3.A.11). These column density lower and upper limits serve as estimates of the column density uncertainties from uncertainties in continuum fitting. They are asymmetric and, to an extent, subjective depending on what one considers to be a "reasonable" continuum.

The reported laboratory band strengths of the HDO and H_2O bands used here to calculate the ice column densities can vary significantly with temperature, particularly for the amorphous ices. Because we do not attempt to model the temperature gradient with our fits, we treat this variation of band strength with temperature as an additional source of uncertainty in the ice column densities. We again calculate lower and upper limits of HDO and H_2O ice column densities, this time by using the respective highest and lowest band strength measured for a given phase of the ice. The resulting uncertainties are again asymmetric. For CH_3OH, temperature and chemical environment changes can change the band strength of the 3.53 μm feature by a maximum of $\sim$20% (Kerkhof et al. 1999; Luna et al. 2018), and Luna et al. (2018) report experimental uncertainties of 20%. For all three ice species, the band strength and continuum uncertainties are both considered systematic and are thus added linearly to provide the total ice column density uncertainties.

Although SH-bearing ice species are not the focus of this work, we report in Section 3.3.1 H_2S and NH_4SH upper limits ($\sim$0.3 and 13% w.r.t. H_2O, respectively) calculated from the Gaussian fit to the excess at 3.9 μm, in the case that these upper limits may be useful for other studies of sulfur in star-forming regions or interstellar ices. However, it is evident from Figure 3.A.11 that the optical depth of this Gaussian can vary dramatically with the continuum choice, resulting in high uncertainties in these reported upper limits. Depending on the continuum, the H_2S upper limits can range from 0.07-2%. For NH_4SH, the upper limit is $\sim$4% in the case of the lower limit continuum choice shown in the bottom left panel of Figure 3.A.11. In the case of the upper limit continuum choice in the bottom right panel, the 3.9 μm Gaussian profile is too broad to be attributed exclusively with NH_4SH. Furthermore, the L1527 NH_4^+ column density derived from the 6.85 μm feature (Slavicinska et al. 2025) provides an additional constraint that the NH_4SH upper limit cannot exceed that derived from the fit presented in Figure 3.2 ($\sim$13%).

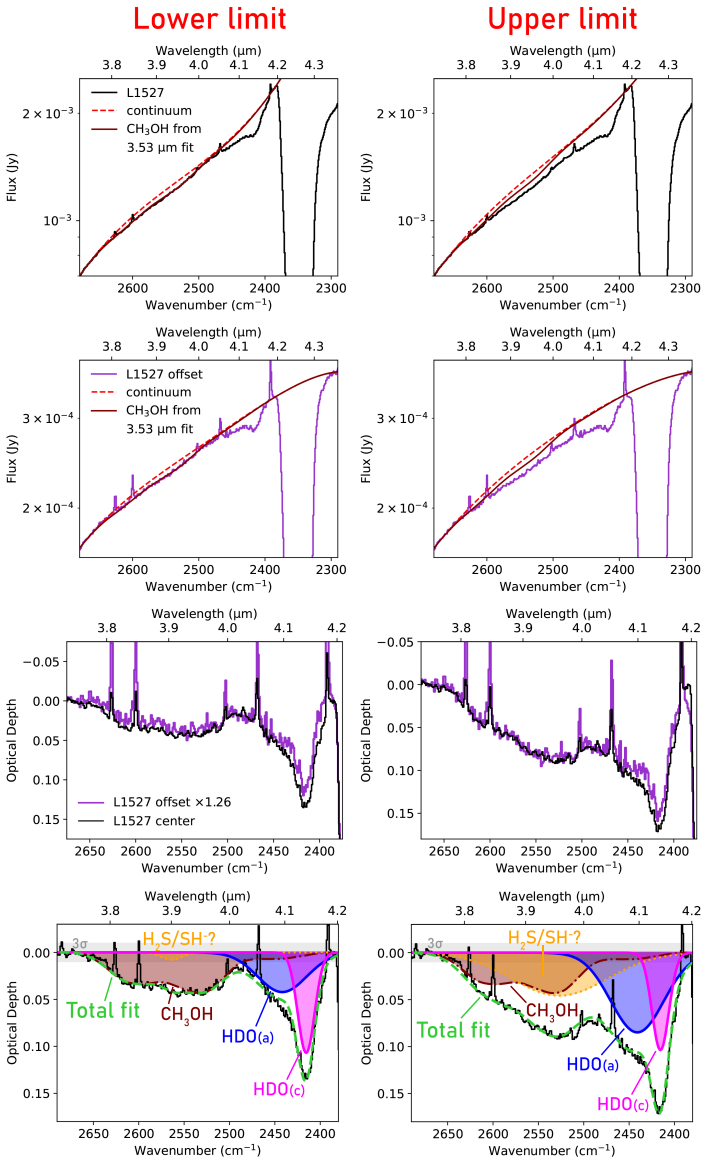


Figure 3.A.11: The local continua and subsequent fits to the 3.7-4.2 μm region used to define continuum uncertainties on the HDO column densities. First row: the lower (left) and upper (right) limits on the local continua in the central spectrum. Second row: the corresponding lower (left) and upper (right) limits on the local continua in the off-source spectrum. Third row: comparisons of the extracted spectra resulting from the lower (left) and upper (right) limit continua between the two positions. Fourth row: ice fits to the spectra extracted using the continua in the top row. The resulting HDO column densities were used to define the HDO column density uncertainty from the continuum choice.

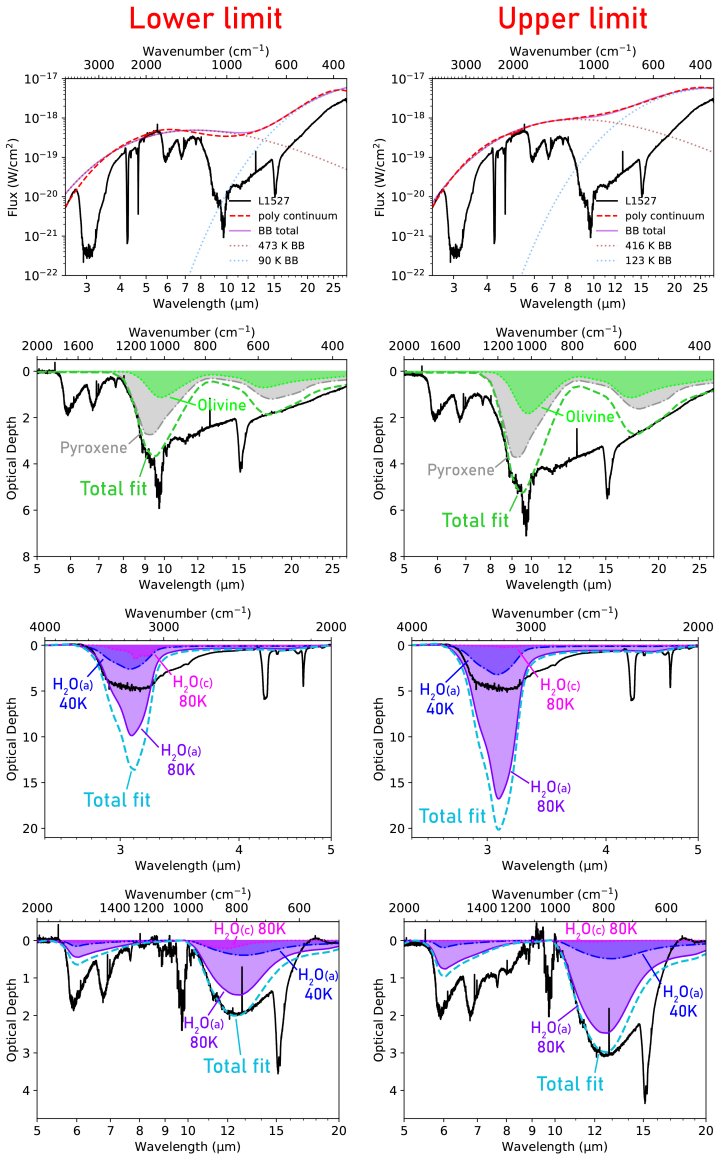


Figure 3.A.12: The global continua and subsequent silicate subtractions and H_2O ice fits used to define continuum uncertainties on the H_2O column densities. First row: the lower (left) and upper (right) limits on the global continua in the central spectrum. Second row: the silicate subtraction performed on the optical depth-scale spectra extracted using the continua in the top row. Third and fourth row: H_2O ice fits to the NIRSpec and silicate-subtracted MIRI spectra. The resulting H_2O column densities were used to define the H_2O column density uncertainty from the continuum choice.

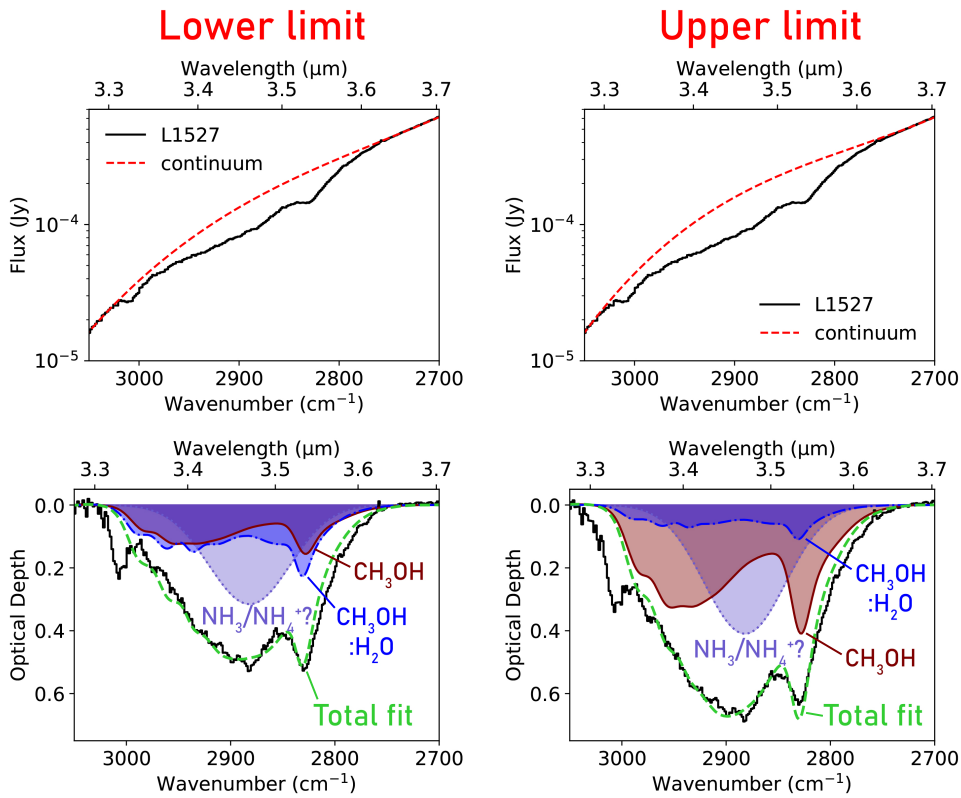


Figure 3.A.13: The local continua and subsequent fits to the 3.3-3.7 μm region used to define continuum uncertainties on the CH_3OH column densities. Top row: the lower (left) and upper (right) limits on the local continua in the central spectrum. Bottom row: ice fits to the spectra extracted using the continua in the top row. The resulting CH_3OH column densities were used to define the CH_3OH column density uncertainty from the continuum choice.

3.A.5 Comparison with AKARI results

HDO ice

While Aikawa et al. (2012) cautioned that their HDO column densities obtained from AKARI data toward L1527 "should be interpreted with caution" given the low signal-to-noise ("small bumps and hollows that deviate from the HDO feature"), the HDO ice column density measured here is similar to their value. Although the AKARI data were not spectrally resolved enough to reveal the asymmetric profile of the 4.1 μm band and were thus only fit with a single Gaussian, Aikawa et al. (2012) noted that the profile of their best-fitting Gaussian was narrower and peaked at longer wavelengths than expected for cold and amorphous HDO ice and thus stated that the feature resembles HDO ice that has been annealed. While this is in contradiction with their fitting of 10 K amorphous H_2O ice to the 3 μm band wings, it is in agreement with our analysis that includes a prominent crystalline component of the HDO

band.

H_2O ice

Our H_2O ice column density, $2.09^{+1.02}_{-0.51}\times10^{19}$ cm^{-2}, is over a factor of 4 greater than the H_2O ice column density measured toward L1527 using AKARI spectra by Aikawa et al. (2012), $4.7\pm1.3\times10^{18}$ cm^{-2}. This is because Aikawa et al. (2012) derived their H_2O ice column densities by fitting the wings of the 3 μm feature with pure, 10 K H_2O ice spectra. Because the wings of this feature can redshift significantly with grain effects and higher temperatures, it is easy to over- or underfit this feature when fitting only its wings. Aikawa et al. (2012) state that "the H_2O ice column density cannot be significantly larger than we estimated" because their fit to the 3 μm band wings is also consistent with their extracted optical depth of the 4.5 μm combination mode, but the optical depth of this extremely broad feature can change significantly with even small changes in the fitted global continuum. In past literature, the continuum from 2-5 μm has frequently been defined using datapoints around 4 μm (e.g., Gibb et al. 2004) despite the fact that numerous weak ice features, including the broad blue wing of the H_2O combination mode, have absorptions in this spectral region. Such fitting can result in an underestimation of the H_2O ice combination mode optical depth.

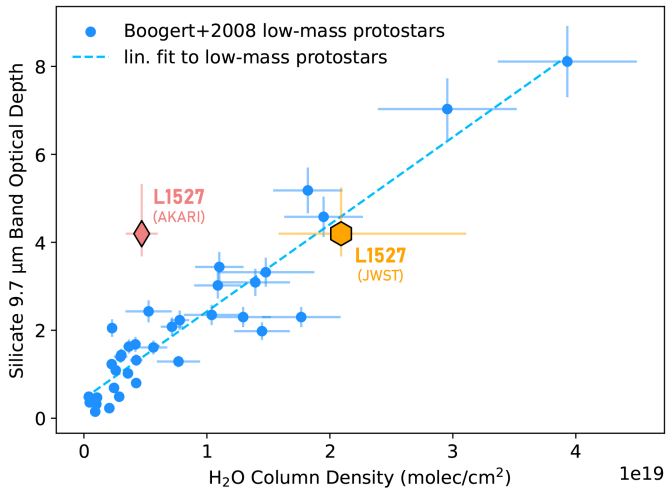


Figure 3.A.14: Optical depth of the 9.7 μm silicate feature plotted as a function of H_2O ice column density toward low-mass protostars. The blue data points were obtained from Spitzer data (Boogert et al. 2008), and the blue dashed line shows the best linear fit to the data. The red diamond represents L1527 using the H_2O ice column density from Aikawa et al. (2012), while the golden hexagon represents L1527 using the H_2O ice column density from this work. Both L1527 data points use the silicate optical depth obtained from the MIRI spectrum in this paper.

Further supporting our significantly larger L1527 H_2O ice column density is a comparison of the 9.7 μm silicate feature optical depth and the H_2O ice column density observed toward L1527 versus those of other low-mass protostars (Figure 3.A.14). In general, the optical depth

of the 9.7 μm feature strongly correlates with the observed H_2O column density toward these objects, and based on the high 9.7 μm feature optical depth observed toward L1527 ($\tau \sim$4.2), its H_2O ice column density is indeed expected to be $\gtrsim 2\times10^{19}$ cm^{-2}.

3.A.6 Literature HDO/H_2O values

Table 3.A.2: Overview of HDO/H_2O values of various solar system objects.

Object	Phase	HDO/H_2O 10^{-3}	Ref.
Carbonaceous Chondrites			
CI chondrites	-	0.129-0.195	1
CM chondrites	-	0.173±0.0072	1
CR chondrites	-	$0.342^{+0.034}_{-0.02}$	1
CO chondrites	-	0.170-0.264	1
Oort Cloud Comets			
1P/Halley	gas	0.42±0.06	2
C/1996 B2 Hyatuake	gas	0.58±0.20	3
C/1995 O1 Hale-Bopp	gas	0.66±0.16	4
8P/Tuttle	gas	0.82±0.29	5
C/2009 P1 Garradd	gas	0.41±0.04	6
C/2002 T7 LINEAR	gas	0.50±0.14	7
C/2012 F6 Lemmon	gas	1.30±0.32	8
C/2014 Q2 Lovejoy	gas	0.28±0.08	8
C/2007 B3 Lulin	gas	<1.12	9
153P/Ikeya-Zhang	gas	<0.56±0.06	10
Jupiter Family Comets			
103P/Hartley 2	gas	0.32±0.05	11
67P/Churyumov-Gerasimenko	gas	1.06±0.14	12
46P/Wirtanen	gas	0.32±0.13	13
45P/Honda-Mrkos-Pajdušáková	gas	<0.40	14

Refs: 1. Alexander et al. (2012); 2. Brown et al. (2012); 3. Bockelée-Morvan et al. (1998); 4. Meier et al. (1998); 5. Villanueva et al. (2008); 6. Bockelée-Morvan et al. (2012); 7. Hutsemekers et al. (2008); 8. Biver et al. (2016); 9. Gibb et al. (2012); 10. Biver et al. (2006); 11. Hartogh et al. (2011); 12. Altwegg et al. (2015); 13. Lis et al. (2019); 14. Lis et al. (2013).

Table 3.A.3: Overview of HDO/H_2O values of various protostars.

Source	Phase	HDO/H_2O 10^{-3}	Ref.
Clustered Class 0 LYSOs			
NGC 1333 IRAS 4A-NW	gas	0.54±0.15	1, 2
NGC 1333 IRAS 2A	gas	0.74±0.21	1
NGC 1333 IRAS 4B	gas	0.59±0.26	1
IRAS 16293-2422	gas	0.92±0.26	1
NGC 1333 SVS 13	ice	≤17	3
Clustered Class I LYSOs			
NGC 1333 SVS 12	ice	≤5	3
Isolated Class 0 LYSOs			
BHR 71-IRS1	gas	1.8±0.4	2
B335	gas	6.3±1.5	4
L483	gas	4.0±0.5	4
Isolated Class 0/I LYSOs			
L1527 IRS	ice	$4.4^{+3.7}_{-1.7}$	5
Isolated Class I LYSOs			
V883 Ori	gas	2.3±0.6	6
L1551 IRS5	gas	2.1±0.8	7
L1489 IRS	ice	≤8	3
TMR1	ice	≤11	3
IMYSOs			
IRAS 05390-0728	ice	≤10	8
IRAS 08448-4343	ice	≤10	8
HOPS 370	ice	4.6±2.2	9
MYSOs			
W3 IRS5	gas	1.3	10
W33A	gas	3.0	10
AFGL 2591	gas	3.3	10
NGC 7538 IRS1	gas	3.8	10
Orion KL Hot Core	gas	$3.0^{+3.1}_{-1.7}$	11
NGC 6334 I	gas	0.21±0.1	12
G34.26+0.15	gas	0.35-0.75	13
NGC 7538 IRS9	ice	≤8.1-11.4	8
GL 2136	ice	≤4	8
IRAS 20126	ice	2.6±1.4	9

Refs: 1. Persson et al. (2014); 2. Jensen et al. (2019); 3. Parise et al. (2003); 4. Jensen et al. (2021); 5. this work; 6. Tobin et al. (2023); 7. Andreu et al. (2023); 8. Dartois et al. (2003); 9. Slavicinska et al. (2024); 10. van der Tak et al. (2006) (envelope-averaged abundances from radiative transfer models); 11. Neill et al. (2013); 12. Emprechtinger et al. (2013); 13. Coutens et al. (2014).

3.B Bibliography

Adams, F. C. 2010, ARA&A, 48, 47
Aikawa, Y., Kamuro, D., Sakon, I., et al. 2012, A&A, 538, A57
Alexander, C. O., Bowden, R., Fogel, M., et al. 2012, Science, 337, 721
Altwegg, K., Balsiger, H., Bar-Nun, A., et al. 2015, Science, 347, 1261952
Andreu, A., Coutens, A., de Miera, F. C.-S., et al. 2023, A&A, 677, L17
Aso, Y., Ohashi, N., Aikawa, Y., et al. 2017, ApJ, 849, 56
Bergner, J. B., Sturm, J., Piacentino, E. L., et al. 2024, ApJ, 975, 166
Biver, N., Bockelée-Morvan, D., Crovisier, J., et al. 2006, A&A, 449, 1255
Biver, N., Moreno, R., Bockelée-Morvan, D., et al. 2016, A&A, 589, A78
Bockelée-Morvan, D., Biver, N., Swinyard, B., et al. 2012, A&A, 544, L15
Bockelée-Morvan, D., Gautier, D., Lis, D., et al. 1998, Icarus, 133, 147
Boogert, A., Chiar, J., Knez, C., et al. 2013, ApJ, 777, 73
Boogert, A., Ehrenfreund, P., Gerakines, P. A., et al. 2000, A&A, 353, 349
Boogert, A., Huard, T., Cook, A., et al. 2011, ApJ, 729, 92
Boogert, A. A., Gerakines, P. A., & Whittet, D. C. 2015, ARA&A, 53, 541
Boogert, A. C., Pontoppidan, K. M., Knez, C., et al. 2008, ApJ, 678, 985
Bottinelli, S., Boogert, A. A., Bouwman, J., et al. 2010, ApJ, 718, 1100
Brown, R. H., Lauretta, D. S., Schmidt, B., & Moores, J. 2012, Planet. Space Sci., 60, 166
Brunken, N., van Dishoeck, E., Slavicinska, K., et al. 2024a, A&A, 692, A163
Brunken, N. G., Rocha, W. R., Van Dishoeck, E. F., et al. 2024b, A&A, 685, A27
Chen, Y., Rocha, W. R. M., van Dishoeck, E. F., et al. 2024, A&A, 690, A205
Chen, Y., Van Gelder, M., Nazari, P., et al. 2023, A&A, 678, A137
Cleeves, L. I., Bergin, E. A., Alexander, C. M. O., et al. 2014, Science, 345, 1590
Coletta, A., Fontani, F., Rivilla, V., et al. 2020, A&A, 641, A54
Coutens, A., Vastel, C., Hincelin, U., et al. 2014, MNRAS, 445, 1299
Crapsi, A., Van Dishoeck, E., Hogerheijde, M., Pontoppidan, K., & Dullemond, C. 2008, A&A, 486, 245
Dartois, E. & d'Hendecourt, L. 2001, A&A, 365, 144
Dartois, E., Noble, J. A., Ysard, N., Demyk, K., & Chabot, M. 2022, A&A, 666, A153
Dartois, E., Thi, W.-F., Geballe, T., et al. 2003, A&A, 399, 1009
Desch, S. & Miret-Roig, N. 2024, SSRv, 220, 76
Devaraj, R., van Dishoeck, E. F., Ray, T. P., et al. 2026, A&A, 708, A29
Dominik, C., Min, M., & Tazaki, R. 2021, OpTool: Command-line driven tool for creating complex dust opacities, Astrophysics Source Code Library, record ascl:2104.010
Dorschner, J., Begemann, B., Henning, T., Jaeger, C., & Mutschke, H. 1995, A&A, 300, 503
Eberhardt, P., Reber, M., Krankowsky, D., & Hodges, R. 1995, A&A, 302, 301
Emprechtinger, M., Lis, D., Rolffs, R., et al. 2013, ApJ, 765, 61
Encrenaz, T. 2008, ARA&A, 46, 57
Federman, S. A., Megeath, S. T., Rubinstein, A. E., et al. 2024, ApJ, 966, 41
Gibb, E., Whittet, D., Boogert, A., & Tielens, A. 2004, ApJS, 151, 35
Gibb, E. L., Bonev, B. P., Villanueva, G., et al. 2012, ApJ, 750, 102
Hartogh, P., Lis, D. C., Bockelée-Morvan, D., et al. 2011, Nature, 478, 218
Hutsemekers, D., Manfroid, J., Jehin, E., Zucconi, J.-M., & Arpigny, C. 2008, A&A, 490, L31

Jensen, S., Jørgensen, J., Kristensen, L., et al. 2021, A&A, 650, A172
Jensen, S., Jørgensen, J., Kristensen, L., et al. 2019, A&A, 631, A25
Kerkhof, O., Schutte, W., & Ehrenfreund, P. 1999, A&A, 346, 990
Kitta, K. & Krätschmer, W. 1983, A&A, 122, 105
Kristensen, L., van Dishoeck, E. F., Bergin, E., et al. 2012, A&A, 542, A8
Law, D. D., Morrison, J. E., Argyriou, I., et al. 2023, AJ, 166, 45
Lécuyer, C., Gillet, P., & Robert, F. 1998, Chem. Geol., 145, 249
Lis, D., Biver, N., Bockelée-Morvan, D., et al. 2013, ApJL, 774, L3
Lis, D. C., Bockelée-Morvan, D., Güsten, R., et al. 2019, A&A, 625, L5
Luna, R., Molpeceres, G., Ortigoso, J., et al. 2018, A&A, 617, A116
Mastrapa, R., Sandford, S., Roush, T., Cruikshank, D., & Dalle Ore, C. 2009, ApJ, 701, 1347
McClure, M. K., Rocha, W., Pontoppidan, K., et al. 2023, Nat. Astro., 7, 431
Meier, R., Owen, T. C., Matthews, H. E., et al. 1998, Science, 279, 842
Min, M., Hovenier, J., & De Koter, A. 2005, A&A, 432, 909
Nazari, P., Van Gelder, M., Van Dishoeck, E., et al. 2021, A&A, 650, A150
Neill, J. L., Wang, S., Bergin, E. A., et al. 2013, ApJ, 770, 142
Parise, B., Simon, T., Caux, E., et al. 2003, A&A, 410, 897
Persson, M., Jørgensen, J., Van Dishoeck, E., & Harsono, D. 2014, A&A, 563, A74
Pontoppidan, K. M., Boogert, A. C., Fraser, H. J., et al. 2008, ApJ, 678, 1005
Pontoppidan, K. M., Dullemond, C. P., van Dishoeck, E. F., et al. 2005, ApJ, 622, 463
Prodanović, T., Steigman, G., & Fields, B. D. 2010, MNRAS, 406, 1108
Requena-Torres, M. A., Martín-Pintado, J., Rodríguez-Franco, A., et al. 2006, A&A, 455, 971
Schutte, W. & Khanna, R. 2003, A&A, 398, 1049
Slavicinska, K., Boogert, A., van Dishoeck, E., et al. 2025, A&A, 693, A146
Slavicinska, K., van Dishoeck, E. F., Tychoniec, Ł., et al. 2024, A&A, 688, A29
Smith, R. G., Sellgren, K., & Tokunaga, A. T. 1989, ApJ, 344, 413
Sturm, J., McClure, M., Beck, T., et al. 2023a, A&A, 679, A138
Sturm, J., McClure, M., Bergner, J., et al. 2023b, A&A, 677, A18
Teixeira, T., Devlin, J., Buch, V., & Emerson, J. 1999, A&A, 347, L19
Tobin, J. J., Hartmann, L., Chiang, H.-F., et al. 2013, ApJ, 771, 48
Tobin, J. J., Hartmann, L., Chiang, H.-F., et al. 2012, Nature, 492, 83
Tobin, J. J., van't Hoff, M. L., Leemker, M., et al. 2023, Nature, 615, 227
van der Tak, F., Walmsley, C., Herpin, F., & Ceccarelli, C. 2006, A&A, 447, 1011
van Dishoeck, E. F., Bergin, E. A., Lis, D. C., & Lunine, J. I. 2014, Protostars and Planets VI, 835
van Dishoeck, E. F., Kristensen, L. E., Mottram, J. C., et al. 2021, A&A, 648, A24
van Gelder, M., Jaspers, J., Nazari, P., et al. 2022, A&A, 667, A136
Van Gelder, M., Tabone, B., van Dishoeck, E., et al. 2020, A&A, 639, A87
van't Hoff, M. L., Tobin, J. J., Li, Z.-Y., et al. 2023, ApJ, 951, 10
Villanueva, G., Mumma, M., Bonev, B., et al. 2008, ApJ, 690, L5
Waite, J. H., Lewis, W., Magee, B., et al. 2009, Nature, 460, 487
Yarnall, Y. Y. & Hudson, R. L. 2022, ApJL, 931, L4

4

Ammonium hydrosulfide (NH_4SH) as a potentially significant sulfur sink in interstellar ices

Katerina Slavicinska, A. C. Adwin Boogert, Łukasz Tychoniec, Ewine F. van Dishoeck, Martijn L. van Gelder, María Gabriela Navarro, Julia C. Santos, Pamela D. Klaassen, Patrick J. Kavanagh, Ko-Ju Chuang

Astronomy & Astrophysics (2025), 693, A146

Abstract

Context. Sulfur is depleted with respect to its cosmic standard abundance in dense star-forming regions. It has been suggested that this depletion is caused by the freeze-out of sulfur on interstellar dust grains, but the observed abundances and upper limits of sulfur-bearing ices remain too low to account for all of the missing sulfur. Toward the same environments, a strong absorption feature at ∼6.85 μm is observed, but its long-standing assignment to the NH_4^+ cation remains tentative.

Aims. We aim to spectroscopically investigate the plausibility of NH_4SH salt serving as a sulfur reservoir and a carrier of the 6.85 μm band in interstellar ices by characterizing its IR signatures and apparent band strengths in water-rich laboratory ice mixtures. We then use this laboratory data to constrain NH_4SH abundances in observations of interstellar ices.

Methods. Laboratory transmission IR spectra of NH_3:H_2S ice mixtures both with and without H_2O were collected. The apparent band strengths of the NH_4^+ asymmetric bending (ν_4) mode and the SH^- stretching mode in H_2O-containing mixtures were calculated with Beer's law plots. The IR features of the laboratory salts were compared to those observed toward a sample of four protostars (two low-mass, two high-mass) and two cold dense clouds without star formation.

Results. Apparent band strengths ranging from 3.2(±0.3)-3.6(±0.4)×10^{-17} cm molec^{-1} and 3.1(±0.4)-3.7(±0.5)×10^{-19} cm molec^{-1} are calculated for the NH_4^+ ν_4 mode at ∼6.8 μm/1470 cm^{-1} and the SH^- stretching mode at ∼3.9 μm/2560 cm^{-1}, respectively, in NH_4SH:H_2O mixtures. The peak position of the NH_4^+ ν_4 mode redshifts with increasing temperature but also with increasing salt concentration with respect to matrix species H_2O and NH_3. The observed 6.85 μm feature is fit well with the laboratory NH_4SH:H_2O ice spectra. NH_4^+ column densities obtained from the 6.85 μm band range from 8-23% with respect to H_2O toward the sample of protostars and dense clouds. These column densities are consistent with the optical depths observed at 3.9 μm (the SH^- stretching mode spectral region). A weak and broad feature observed at ∼5.3 μm/1890 cm^{-1} is tentatively assigned to the combination mode of the NH_4^+ ν_4 mode and the SH^- libration. The combined upper limits of four other counter-anion candidates, OCN^-, CN^-, $HCOO^-$, and Cl^-, are determined to be $\lesssim$15-20% of the total NH_4^+ column densities toward three of the protostars.

Conclusions. The redshift of the 6.85 μm feature correlates with higher abundances of NH_4^+ with respect to H_2O in both the laboratory data presented here and observational data of dense clouds and protostars. The apparent band strength of the SH^- feature is likely too low for the feature to be detectable in the spectrally busy 3.9 μm region, but the 5.3 μm NH_4^+ ν_4 + SH^- R combination mode may be an alternative means of detection. Its tentative assignment adds to mounting evidence supporting the presence of NH_4^+ salts in ices and is the first tentative observation of the SH^- anion toward interstellar ices. If the majority ($\gtrsim$80-85%) of the NH_4^+ cations quantified toward the investigated sources in this work are bound to SH^- anions, then NH_4SH salts could account for up to 17-18% of their sulfur budgets.

4.1 Introduction

The observed depletion of sulfur toward star-forming regions is a persistent topic of debate in the field of astrochemistry. In the diffuse interstellar medium, sulfur is mostly present

in its singly ionized form (S^+) with an observed abundance of $\sim 1.7 \times 10^{-5}$ with respect to hydrogen (Esteban et al. 2004), similar to its observed solar abundance as well as the abundance measured in CI chondrite meteorites (Lodders 2003; Asplund et al. 2009). However, in the higher-density cold interstellar environments like dense clouds, prestellar cores, and protostellar envelopes from which stellar systems eventually form, the abundance of observed gas-phase sulfur species can be two or three orders of magnitude lower (Joseph et al. 1986; Tieftrunk et al. 1994).

Many chemical models suggest that in such cold and dense environments, most of the sulfur should freeze out and form H_2S ice via hydrogenation on the surfaces of interstellar grains (Garrod et al. 2007; Druard & Wakelam 2012; Vidal et al. 2017; Vidal & Wakelam 2018), but to date, no convincing detection of this ice in the interstellar medium exists. This is in part due to the fact that the strongest IR absorption of H_2S ice, its stretching mode at 3.93 μm (2547 cm^{-1}), has a broad profile that overlaps with combination modes of CH_3OH ice, a major constituent of interstellar ices, in the same spectral region. Additionally, several other species with S-H bonds have been shown to have absorption profiles similar to H_2S that peak between 3.93-3.96 μm, making a secure assignment of any absorption detected in this spectral region specifically to H_2S ice difficult (Hudson & Gerakines 2018). Nevertheless, H_2S ice upper limits measured toward prestellar cores and protostars are typically $\lesssim$1% with respect to H_2O, indicating that H_2S ice cannot be the major sulfur carrier in these dense environments (Smith 1991; Jiménez-Escobar & Caro 2011; McClure et al. 2023). Two other sulfur-bearing ice species, OCS and SO_2, have been detected more securely but at very low abundances ($<$1% with respect to H_2O, Boogert et al. 1997; Öberg et al. 2008; Boogert et al. 2022; McClure et al. 2023; Rocha et al. 2024); therefore, these ices can also only account for at maximum a couple of percent of the cosmic sulfur budget.

This observed sulfur depletion, sometimes dubbed "the missing sulfur problem," has spurred a variety of questions in the astrochemical community over the past couple of decades. These include why H_2S ice is not detected despite what models predict, whether H_2S reacts on the ice grain surfaces and forms other icy species that are not easily detected (e.g., Garozzo et al. 2010; Jiménez-Escobar & Caro 2011; Jiménez-Escobar et al. 2014; Chen et al. 2014; Woods et al. 2015; Martín-Doménech et al. 2016; Laas & Caselli 2019), whether H_2S ice is just quick to chemisorb into the gas phase from the grain surface following its formation (Oba et al. 2018; Furuya et al. 2022; Santos et al. 2023), or if most of the sulfur is actually hidden in minerals like sulfides (e.g., Keller et al. 2002; Kama et al. 2019; Perrero et al. 2024).

An essential clue may lie in the recently published analysis of in situ mass spectrometric data of the dust grains of comet 67P collected by the ROSINA Double Focusing Mass Spectrometer (Altwegg et al. 2022). This work shows that the cometary grains contain NH_4SH salt ($NH_4^+SH^-$) in exceptionally high abundance. In fact, it is estimated that approximately 90% of the ammonium (NH_4^+) cations in the analyzed dust grains could be bound to SH^- anions. As it is thought that comets may be chemically linked to pre- and protostellar environments (Bockelée-Morvan et al. 2000; Drozdovskaya et al. 2019; Altwegg et al. 2019), it is no stretch to hypothesize that NH_4SH salts could be similarly abundant in primitive interstellar ices.

Experiments show that at the cold temperatures expected in the environments where sulfur depletion is observed, NH_4SH forms readily via an acid-base reaction between NH_3 and H_2S (Loeffler et al. 2015; Hudson et al. 2015; Vitorino et al. 2024). Both molecules are expected to accumulate on interstellar grains around the same time, during the prestellar epoch in which most of the H_2O ice forms, based on their deuterium ratios measured in the gas phase (Vastel

et al. 2003; Caselli & Ceccarelli 2012). Indeed, NH_3 ice has been securely detected toward both dense clouds and protostellar ice envelopes via its 9 μm umbrella mode, with abundances ranging from 3-10% with respect to H_2O (Boogert et al. 2015), and its peak profile and narrow abundance distribution with respect to H_2O indicate that it likely exists in a water-rich environment (Bottinelli et al. 2010; Öberg et al. 2011).

Furthermore, the NH_4^+ cation has long been suspected to be the primary carrier of the ubiquitous 6.85 μm feature that is present in the majority of ice-containing lines of sight (Knacke et al. 1982; Grim et al. 1989a,b). The peak position of this feature has also been proposed as a tracer of thermal processing due to its correlation with dust and ice temperatures in protostellar envelopes (Keane et al. 2001; Boogert et al. 2008), a trend that is experimentally corroborated by a redshift in the NH_4^+ ν_4 feature observed during the warm-up of laboratory ammonium salt ices (Schutte & Khanna 2003). NH_4^+ pre- and protostellar ice abundances calculated from the 6.85 μm feature (using a band strength of 4.4×10^{-17} cm molec^{-1} measured for the asymmetric bending mode ν_4 of NH_4^+ in laboratory mixtures of $NH_4^+HCOO^-$ salts diluted in H_2O, Schutte & Khanna 2003) range from 4-34% with respect to H_2O, on par with abundances of the major ice constituents CO, CO_2, and CH_3OH (Boogert et al. 2015).

However, the assignment remains controversial for multiple reasons. First, no laboratory data of NH_4^+-containing ices have provided a "convincing" fit to the observed feature (Boogert et al. 2015). In particular, currently available laboratory spectra of ammonium salts diluted in H_2O-rich ice matrices are too broad and weak to fit the observed feature (Maté et al. 2009; Galvez et al. 2010) despite column density correlations indicating that the primary carrier of the 6.85 μm feature is chemically linked to H_2O ice (Tielens & Allamandola 1987; Pontoppidan 2006; Boogert et al. 2011). Additionally, the combined abundances with respect to H_2O ice of anionic species identified so far in interstellar ices, OCN^- and $HCOO^-$, are usually over an order of magnitude lower than those calculated for NH_4^+ (e.g., Schutte et al. 1999; van Broekhuizen et al. 2004, 2005; Boogert et al. 2022; McClure et al. 2023; Rocha et al. 2024), so if the 6.85 μm band indeed consists primarily of the ν_4 mode of NH_4^+, other anionic species must be identified to fully counterbalance its net positive charge. Furthermore, no other bands have been unambiguously assigned to NH_4^+; although the 3.26 and 3.48 μm features observed toward some sources on the red wing of the 3 μm H_2O feature have been proposed to be NH_4^+ combination modes (Schutte & Khanna 2003), absorptions at these wavelengths could also be attributed to PAHs (Sellgren et al. 1995) and NH_3 hydrates (Dartois & d'Hendecourt 2001), respectively.

With this work, we seek to investigate whether NH_4SH salts formed in H_2O-rich ices could serve, metaphorically, as a "stone" that simultaneously kills two astrochemical "birds": the sink of the missing sulfur and the identity of the 6.85 μm band. Band strengths of polycrystalline NH_4SH ice at 160 K were previously derived by Ferraro et al. (1980), who reported a band strength of $\sim1.2\times10^{-19}$ cm molec^{-1} for the SH^- anion stretching mode at 3.89 μm (2570 cm^{-1}). In comparison, Yarnall & Hudson (2022) reported a band strength that is over two orders of magnitude higher, 1.66×10^{-17} cm molec^{-1}, for the 3.93 μm stretching mode of neutral H_2S in a water-rich ice at 10 K . Such a dramatic difference in the reported band strengths of the H_2S and SH^- stretching features at nearly the same wavelengths highlights the possibility that the abundance of sulfur in interstellar ices may be significantly higher than what the current ice abundances and upper limits predict if some H_2S ice has been converted into its anionic form. Ferraro et al. (1980) also reported a band strength of $\sim2.6\times10^{-17}$ cm molec^{-1} for the NH_4^+ asymmetric bending mode (ν_4) at 7.05 μm, almost a factor of 2 lower

than the NH_4^+ band strength of 4.4×10^{-17} measured by Schutte & Khanna (2003) that is used the most frequently in astronomical literature to quantify NH_4^+ cations in interstellar ices (e.g., Boogert et al. 2008, 2011; McClure et al. 2023). Therefore, if NH_4SH is the main carrier of the 6.85 μm band, its abundance could be almost a factor of 2 higher than indicated by the current NH_4^+ column density calculations. However, it is important to note that these band strengths were calculated for pure polycrystalline NH_4SH at a relatively high temperature (160 K), and the band strengths of NH_4SH may differ significantly if the salt is primarily amorphous and in H_2O-dominated ice mixtures, as would be expected in most icy lines of sight. To our knowledge, the present literature lacks laboratory spectra and band strengths of NH_4SH salts in such astrophysically relevant conditions as well as comparisons of NH_4SH laboratory spectra to observed spectra of interstellar ices.

To that end, we have measured infrared spectra of NH_4SH formed via the acid-base reaction of co-deposited NH_3 and H_2S ice, both with and without H_2O ice, at temperatures relevant to pre- and protostellar ices. These spectra are made publicly available to the community via the Leiden Ice Database (LIDA, Rocha et al. 2022) for use in fitting to observed ice spectra. We characterize how the peak profiles of the salt change as functions of temperature and dilution with H_2O. We then derive apparent band strengths of the NH_4^+ ν_4 mode and SH^- stretch in H_2O-rich NH_4SH ices for use in deriving column densities and upper limits from IR observations. Finally, we compare our laboratory spectra to IR spectra of pre- and protostellar ices to qualitatively evaluate whether NH_4SH is a feasible candidate carrier of the 6.85 μm band and quantify plausible column densities of NH_4SH ice in the dense star-forming environments where sulfur is depleted.

4.2 Methodology

4.2.1 Experimental

All experiments were performed on the InfraRed Absorption Setup for Ice Spectroscopy (IRASIS) in the Laboratory for Astrophysics in the Leiden Observatory. A schematic of the setup is presented in Rachid et al. (2021), and recent upgrades are described in Slavicinska et al. (2023). Briefly, the setup consists of a KBr substrate cooled to a minimum temperature of 15 K via a closed-cycle helium cryostat within an ultrahigh vacuum chamber (base pressure $<1\times10^{-9}$ mbar). Ices are grown on the substrate via background deposition through three independent leak valves, and each leak valve is connected to an independent reservoir on a gas manifold. Ice thickness throughout deposition is monitored via the interference patterns of a 633 nm laser that reflects off both sides of the substrate at 45° incidence, and transmission infrared spectra of the ice on the substrate are collected continuously during deposition and warm-up with a Varian 670 Fourier-transform infrared spectrometer (FTIR). The IR spectra here are collected with a resolution of 0.5 cm^{-1} using 128 scans per spectrum. A Spectra Microvision Plus quadrupole mass spectrometer (QMS) is used to calibrate each leak valve to specific deposition rates for pure molecules, monitor the ice deposition, and, in some experiments, collect temperature-programmed desorption (TPD) mass spectra during warm-up. Following deposition, the substrate can be warmed until all ices have desorbed from the substrate using a LakeShore Model 335 Temperature Controller to heat the substrate at a specific rate. Most of the experiments in this paper utilized a 1 K min^{-1} heating rate, resulting in a

temperature difference of ∼3.6 K between each spectrum collected during the warm-up and corresponding to a temperature uncertainty of ∼±2 K for each warm-up spectrum.

The liquids and gases used in this work were ammonia (PraxAir, ≥99.96%), hydrogen sulfide (Linde Gas, ≥99.5%), and water (Milli-Q, Type I).

Ice growth rate calibration

The three independent reservoirs of NH_3 gas, H_2S gas, and H_2O vapor each have their own leak valve and inlet into the main chamber. Each leak valve position is calibrated to a specific ice growth rate of a given molecule via dosing the molecule into the chamber at a constant rate and monitoring the ice growth rate with laser interference. More details on the calibration procedure can be found in Appendix 4.A.1. The benefits of using independent dosing lines compared to dosing a gas mixture from a single dosing line to create an ice mixture have been previously described in Yarnall & Hudson (2022) and Slavicinska et al. (2023).

NH_3:H_2S experiments

Table 4.1: Summary of NH_3:H_2S experiments performed.

Dosing ratios		Final ratios[a]			Lim.	Dep. time
NH_3	H_2S	NH_4SH	NH_3	H_2S	react.	(min)
10	11	10	0	1	NH_3	20, 40, 60
3	2	2	1	0	H_2S	20, 40, 60
2	3	2	0	1	NH_3	20, 40, 60

[a] once 100% of the limiting reactant is consumed in the acid-base reaction.

Previously, Loeffler et al. (2015) formed NH_4SH ice in situ on a cryo-cooled substrate via the acid-base reaction of co-deposited NH_3 and H_2S at 10 K. Here, we partially replicated the methodology for the sake of having pure NH_4SH spectra to compare to those of NH_4SH mixed with H_2O ice. In our experiments, NH_3 and H_2S were co-deposited at 15 K in a solid-state ratio of 1:1.1. After deposition, the samples were held at 15 K for ∼1 hr and then heated at a rate of 1 K min^{-1} until the salt desorbed. We repeated this methodology with 3:2 and 2:3 NH_3:H_2S mixtures to aid feature assignment in the 15 K pure salt spectrum, which consists of a complex blend of NH_3, H_2S, and NH_4SH features (Figure 4.1). Three experiments were performed for each ratio: a short deposition (20 min) for simultaneous TPD collection, a long deposition (60 min) for accurate characterization of weak features, and a medium-length deposition (40 min) for the sake of collecting spectra with high S/N whose strongest peaks did not eventually saturate during warm-up. These experiments are summarized in Table 4.1.

H_2O:NH_3:H_2S experiments

Table 4.2 provides an overview of the NH_4SH:H_2O mixtures we characterized in our experiments. In these experiments, H_2O, NH_3, and H_2S were co-deposited at 15 K in the ratios specified in the table. As with the pure mixtures, the samples were held at 15 K for ∼1 hr and then heated at a rate of 1 K min^{-1} until all ice species desorbed. For three mixtures, we

Table 4.2: Summary of H_2O:NH_3:H_2S experiments performed.

Dosing ratios			Final ratios[a]				% NH_4SH[a] wrt H_2O	Lim. react.	Dep. time (min)
H_2O	NH_3	H_2S	H_2O	NH_4SH	NH_3	H_2S			
10	2	1	10	1	1	0	10	H_2S	10, 20, 30, 40, 50
8	2	1	10	8	1	0	12.5	H_2S	20
6	2	1	10	6	1	0	16.7	H_2S	20
5	2	1	5	1	1	0	20	H_2S	20
12	3	2	12	2	1	0	16.7	H_2S	30
10	3	2	10	2	1	0	20	H_2S	10, 20, 30, 40, 50
6	3	2	6	2	1	0	33.3	H_2S	30
4	3	2	4	2	1	0	50	H_2S	30
3	3	2	3	2	1	0	66.7	H_2S	30
8	5	4	8	4	1	0	50	H_2S	10, 20, 30, 40, 50
5	1	1	5	1	0	0	20	-	30
2	1	1	2	1	0	0	50	-	40
1	1	1	1	1	0	0	100	-	40
10	2	3	10	2	0	1	20	NH_3	40

[a] once 100% of the limiting reactant is consumed by the acid-base reaction.

deposited 5 samples of different thicknesses to calculate the band strengths of the NH_4^+ ν_4 mode and the SH^- stretching mode. In these experiments, we interrupted the warm-up ramp with a 40 min hold at 120 K (further details are provided in Section 4.2.1). For the remainder of the mixtures, we deposited one sample with the goal of achieving a thickness that provided sufficient S/N for most of the ice features of interest without any of the major peaks saturating upon warm-up. Because the stretching modes of H_2S and SH^- overlap, we aimed to mini-

mize the unreacted H_2S present at the end of warm-up by setting H_2S as the limiting reactant in most of the mixtures.

Band strength calculations

Measuring band strengths of species that form via reactions in ices can be a complicated endeavor because it is oftentimes only possible to quantify them indirectly. Previous works that reported band strengths of salt species in ices often performed such an indirect measurement by quantifying the loss of acid or base precursor (Schutte et al. 1999; Schutte & Khanna 2003; van Broekhuizen et al. 2004; Bergner et al. 2016). However, this approach usually relies on the use of literature band strengths of the precursors that were measured in physical and chemical conditions that differ (sometimes significantly) from the ices in which the salt formation was performed, leading to inaccuracies stemming from the assumption that the precursor band strengths are identical in the two different experiments.

Recently, Gerakines et al. (2024) directly measured the refractive index, density, and apparent band strengths of a pure ammonium salt, NH_4CN, by dosing NH_3 and HCN vapor onto substrates at 125 K and monitoring the ice growth with laser interferometry, a quartz crystal microbalance, and transmission IR. The authors claim that 125 K is too high for the neutral species to stick to their substrates, resulting in in situ formation of pure NH_4CN salt absent of unreacted neutrals. Unfortunately, this method cannot be reliably used to find the band strengths of salts in mixtures with other ice species because calculating band strengths of species in mixtures requires knowledge of the deposition rate or deposited column density of the species of interest (Yarnall & Hudson 2022), and the deposition rate of a salt on a substrate may change substantially if another ice species is simultaneously accumulating on the substrate and changing the quantity of acid and base that react with each other on the substrate before they can desorb (relative to the amount that react with each other in a pure salt deposition).

With our method, we aim to eliminate the inaccuracies associated with utilizing previously published band strengths of precursors when deriving the apparent band strengths of our salts. Instead, we have relied on previously determined refractive index and density measurements of the pure limiting reactant in the acid-base reaction, H_2S, to calibrate our leak valves to a specific ice growth rate and subsequently have made two assumptions: 1) the deposition rate of H_2S on the substrate is the same when it is pure and when it is co-deposited with other species; and 2) 100% of the deposited H_2S is converted to its ionic form at the point in the experiment when the integrals of the bands of interest are taken (135 K). We estimate from the IR and TPD spectra of our salt mixtures that the consumption of H_2S in our H_2O mixture experiments is likely $\geq$96% at 135 K (see Section 4.3.2). This would result in a liberal estimate of $\sim$4% error in our derived band strengths caused by the uncertainty in the reaction completion fraction. To remain conservative in our reported uncertainties, we opt to use a reaction completion uncertainty of twice this value, 8%, in our apparent band strength error calculations (see Appendix 4.A.2).

The column density of our limiting reactant, H_2S, deposited in each experiment was calculated using a deposition rate obtained via a series of control experiments. In this series, we deposited pure H_2S ices with the same leak valve position and substrate temperature used during deposition in the mixture experiments. We then derived a deposition rate from the laser interference measured during the deposition using the previously published H_2S refractive in-

dex of 1.407 and density of 0.944 g cm^{-3} (Yarnall & Hudson 2022). We repeated this control measurement five times to obtain an average deposition rate and a standard deviation, and we multiplied the average control deposition rate by the deposition time to obtain the total deposited H_2S column density for each mixture experiment. The standard deviation of the five control experiments yields an experimental error of 0.36%, which represents the day-to-day variations between depositions performed in different experiments as well as noise and fitting errors in the laser interference data.

We then formed our salt-H_2O ice mixtures by depositing H_2S with the same experimental parameters as those used in the control experiments, except that we also simultaneously co-deposited NH_3 and H_2O via their independent leak valves calibrated to deposition rates that corresponded to our desired H_2O:NH_3:H_2S ratios. Following the deposition and a brief hold period at 15 K, we warmed the mixtures at 1 K min^{-1} until reaching 120 K, where we held them for 40 min to maximize products formed by the beginning of ice desorption. After this second hold, we resumed the 1 K min^{-1} warm-up until all ice species desorbed. Finally, we created Beer's law plots for each IR feature of interest by plotting its optical depth at 135 K as a function of total deposited H_2S column density for five different deposition times and obtained apparent band strengths from the slopes of the linear least-square fits to the data. The data at 135 K were used to simultaneously maximize the quantity of salt formed (which is greatest at high temperatures) and minimize the loss of salt, matrix, or unreacted precursor via desorption from the analyzed ice (which becomes significant >135 K in the TPD spectra, Figure 4.A.25). The linear fits were obtained using the York method for fitting data with errors on both X and Y variables (York 1966), and the apparent band strengths uncertainties calculated via this procedure range from ∼9-14%. Details regarding the uncertainties of the integrated optical depths and ice column densities used in the Beer's law plots can be found in Appendix 4.A.2.

It should be noted that the band strengths calculated in this paper are referred to as "apparent band strengths" and denoted as A' because they are derived from the infrared spectra of the ices of interest rather than their optical constants. A more detailed explanation of the difference between apparent band strengths and absolute band strengths (typically denoted as A) can be found in Section 3 in Hudson et al. (2014).

4.2.2 Observational

The selected observed sources for comparison to our laboratory data in this work are presented in Table 4.3. These sources span a range of masses, environments, and degrees of thermal processing. The spectra of the investigated low-mass young stellar objects (LYSOs) were collected by the Near Infrared Spectrograph Integral Field Unit (NIRSpec IFU, Jakobsen et al. 2022; Böker et al. 2022) and Mid-Infrared Instrument Medium-Resolution Spectrometer (MIRI-MRS, Wright et al. 2023; Argyriou et al. 2023) on the *James Webb* Space Telescope (JWST, Gardner et al. 2023) as part of the JWST Observations of Young protoStars (JOYS+) collaboration (Program IDs 1290 and 1960, PI Ewine van Dishoeck).[1] The massive young stellar objects (MYSOs) W33A and S140 IRS1 were observed by the Short Wavelength Spectrometer on the Infrared Space Observatory (ISO/SWS) (Gibb et al. 2004). The dense cloud spectra were observed by the InfraRed Spectrograph (IRS) on the *Spitzer* Space Telescope

[1] https://miri.strw.leidenuniv.nl

Table 4.3: Summary of sources whose ice spectra are compared to laboratory NH_4SH spectra in this work.

Source	Telescope	Source Type	Environment	Thermal processing[(a)]
Elias 16	*Spitzer*	dense cloud	-	no processing
CK2	*Spitzer*	dense cloud	-	no processing
B1c	JWST	LYSO	clustered	little/no processing
L1527	JWST	LYSO	isolated	highly processed
W33A	ISO	MYSO	-	little/no processing
S140 IRS 1	ISO	MYSO	-	highly processed

[(a)] as is indicated by presence of a pure CO_2 component in the 4.39 μm $^{13}CO_2$ ice feature, a crystalline 3 μm H_2O ice feature, and/or a low optical depth of the 4.67 μm CO ice feature relative to the optical depth of the 4.27 μm CO_2 feature.

(Knez et al. 2005).

The NIRSpec IFU data of B1c was collected with the G395M grating, resulting in continuous medium-resolution (R=$\lambda/\Delta\lambda\sim$700-1300) spectral coverage from 2.85-5.29 μm. The NRSIRS2RAPID readout pattern and a 4-point dither were used, with a total integration time of 1342 s. The instrument parameters used for the B1c MIRI data are described in Chen et al. (2024).

Spectra were extracted from the B1c NIRSpec and MIRI datacubes with apertures centered on the central brightest pixel over the full wavelength range (NIRSpec: RA 3:33:17.885, Dec +31:09:31.952; MIRI: RA 3:33:17.898, Dec +31:09:31.852). Differences in coordinates of the extraction apertures are a result of a known issue with WCS calibration in JWST pipeline.[2] A wavelength-dependent aperture of seven times the diffraction-limited radius was used to extract 1D spectra from both datacubes, resulting in two spectra with overlapping data points between 4.90-5.29 μm. A scaling factor of 0.856 was used to scale the NIRSpec data to the MIRI data in the spectral overlap region.

The NIRSpec IFU data of L1527 was collected with the PRISM and G395H grating, resulting in low-resolution (R=$\lambda/\Delta\lambda\sim$30-200) spectral coverage from 0.60-2.87 and 4.06-4.18 μm and high-resolution (R=$\lambda/\Delta\lambda\sim$1900-3700) spectral coverage from 2.87-4.06 and 4.18-5.27 μm. The NRSIRS2RAPID readout pattern and a 4-point dither were used for both observations, with a total integration time of 2451 s for the G395H grating and 700 s for the PRISM. The MIRI data of L1527 spans the full MIRI range of 4.90-27.90 μm (R=$\lambda/\Delta\lambda\sim$1300-3700) and was collected using the FASTR1 readout pattern, a 2-point dither, and a total integration time of 2997 s divided equally between the three MIRI-MRS gratings.

Spectra were extracted from the L1527 NIRSpec and MIRI datacubes with apertures centered on the pixel providing the highest average signal over the full wavelength range (NIRSpec: RA 4:39:53.916, Dec +26:03:09.639; MIRI: RA 4:39:53.886, Dec +26:03:10.1248). A constant aperture with a 1" diameter was used to extract 1D spectra from both datacubes due to the source being extended and the majority of the detected flux being scattered light. The extraction resulted in two spectra with overlapping data points between 4.90-5.27 μm. A

[2]https://jwst-docs.stsci.edu/known-issues-with-jwst-data

scaling factor of 0.783 was used to scale the NIRSpec data to the MIRI data in the spectral overlap region.

4.3 Spectroscopic characterization

4.3.1 NH_3:H_2S

Spectra of the NH_3:H_2S 1:1 mixture at various temperatures, along with spectra of pure NH_3 and H_2S at 15 K, are plotted with band assignments labeled in Figure 4.1. The peak positions for each assignment are listed in Table 4.A.9. Assignments were made based on the work of Bragin et al. (1977), Ferraro et al. (1980) and, in the case of the NH_3:H_2S mixture at 15 K, changes in the relative intensities of features between the 3:2, 1:1, and 2:3 NH_3:H_2S mixtures (Figure 4.A.15). For example, the relative intensity of the broad feature at 2417 cm^{-1} (middle panel) increases with increasing fraction of H_2S with respect to NH_3 and decreases during warm-up as the neutral ices are consumed by the acid-base reaction, leading to a tentative assignment of the feature to H_2S in a matrix with NH_3 or NH_4SH. Some features are too blended to assign to one specific mode (e.g., the broad feature $\sim$2900 cm^{-1} in the NH_3:H_2S mixture at 15 K tentatively assigned to two blended NH_4^+ modes).

Reaction at 15 K

It is clear from the prominent NH_4^+ ν_4 feature at $\sim$6.85 μm/1460 cm^{-1} in the NH_3:H_2S mixtures that a significant amount of NH_4SH already forms upon co-deposition at 15 K. The quantity of reactants consumed at 15 K can be estimated via two methods: 1) by calculating the ratio between the peak area of the NH_3 umbrella mode in the mixture (with the contribution of the H_2S bending mode subtracted out via a two-Gaussian deconvolution) and the peak area in a pure NH_3 control sample deposited with identical experimental parameters, or 2) by calculating the ratio between the peak area of the NH_4^+ ν_4 mode at 15 K and the maximum peak area achieved during warm-up. Both methods result in similar estimates of $\sim$50-60% of the deposited NH_3 being consumed immediately upon deposition in all three of the mixing ratios investigated here. However, it is important to note that this is only a rough estimate of the reaction progression as these methods do not account for band strength variations caused by changes in temperature or chemical environment.

The in situ formation of ammonium salts below 20 K has been observed in previous works investigating the acid-base reaction between ammonia and H_2S (Loeffler et al. 2015) and other acids such as HNCO (van Broekhuizen et al. 2004), HCN (Gerakines et al. 2004; Noble et al. 2013), and HCOOH (Galvez et al. 2010; Bergner et al. 2016). van Broekhuizen et al. (2004) and Gerakines et al. (2004) suggested that the reaction may be driven at such low temperatures by the freed kinetic energy or the heat of condensation, respectively, of the room-temperature gas-phase molecules when they deposit on the cold substrate. In our experiments, we held the ice samples at 15 K for approximately 1 hr after deposition finished before beginning warm-up to monitor the reaction process at cold temperatures without energy input from the warm gas deposition. During this time, the integrated peak area of the NH_4^+ ν_4 mode continued to increase while the integrated peak area of the blended NH_3 umbrella mode and H_2S bending mode decreased (Figure 4.2), demonstrating that the NH_3 and H_2S ice continue to react with

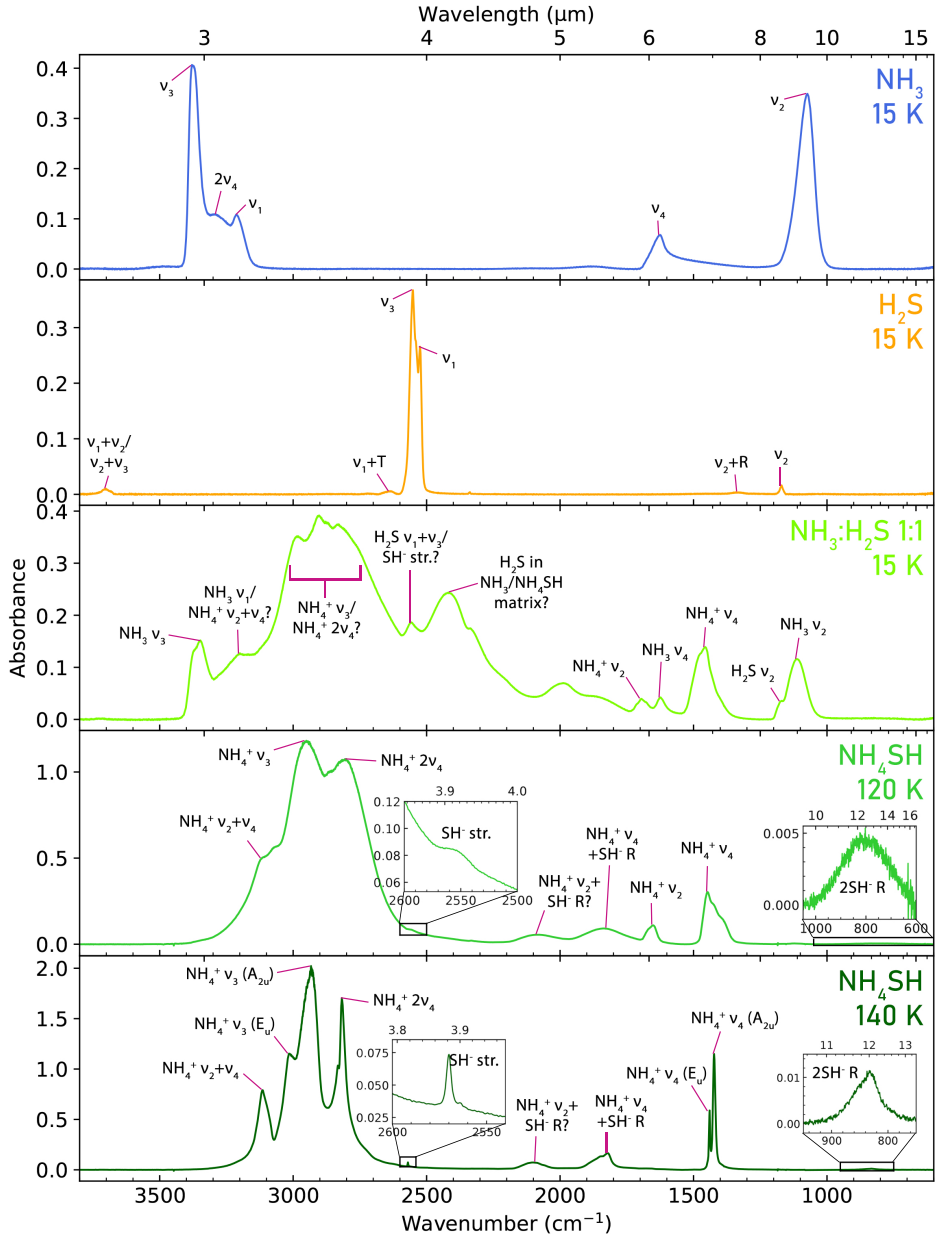


Figure 4.1: Comparison of the infrared spectra of pure and mixed NH_3 and H_2S ices with peak assignments labeled (see Table 4.A.9). Libration modes are indicated with an R. Several features in the spectrum of mixed NH_3 and H_2S ices at 15 K indicate the formation of NH_4SH salt, although peaks of nonreacted NH_3 and H_2S are still present. By 120 K, only signatures of the salt remain. The narrowing of the salt features by 140 K is characteristic of the salt undergoing a phase change (i.e., crystallization).

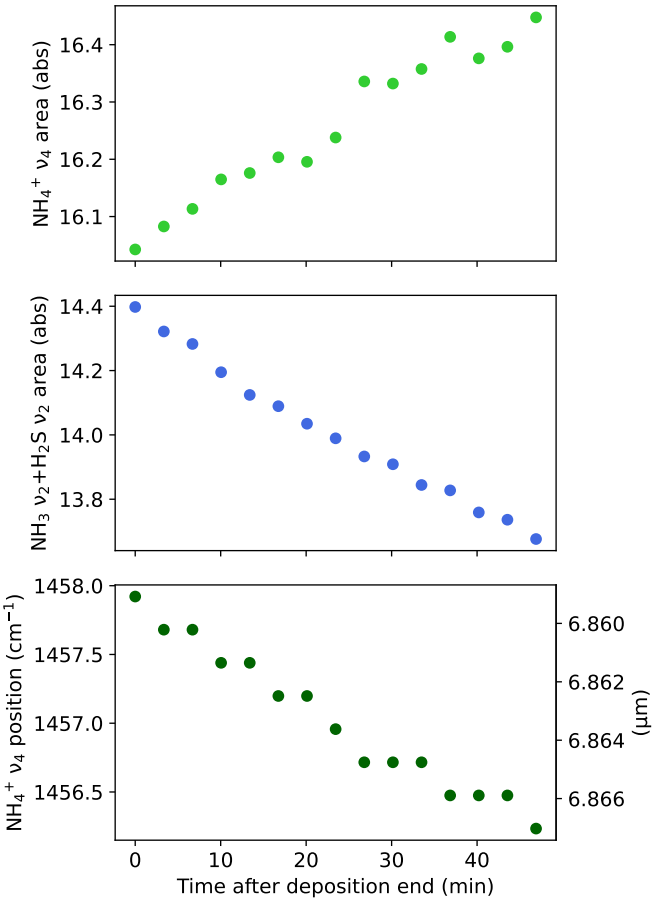


Figure 4.2: Characterization of selected features in the NH_3:H_2S 1:1 spectra during the isothermal hold at 15 K after deposition finished. Top: peak area of the NH_4^+ ν_4 feature. Middle: peak area of the blended NH_3 umbrella bending and H_2S bending features. Bottom: peak position of the NH_4^+ ν_4 feature.

each other even after the deposition is complete and the reactants are completely thermalized by the actively cryo-cooled substrate.

Reaction during warm-up, crystallization, and desorption

As the ice mixtures are heated, their NH_4^+ ν_4 features grow at a much faster rate than during the isothermal hold at 15 K, indicating an increase in the reaction rate. In the 1:1 mixture, the NH_4^+ ν_4 feature reaches its maximum peak area at ∼131 K. At this temperature, the integrated peak area of the NH_3 umbrella mode is 3% relative to its integrated peak area at the beginning of the warm-up (at which point ∼50% of the NH_3 had already reacted). Moreover, the TPD spectra show that thermal desorption of NH_3 between 15-131 K only accounts for

0.4% of the total 17 m/z mass signal (which traces the desorption of both neutral ammonia and the ammonium cation) integrated from 15-250 K. This leads us to estimate that ∼98% of the deposited NH_3 is converted to NH_4SH by 131 K, with very little of the originally deposited NH_3 remaining neutral or desorbing by this temperature.

During the warm-up from 15 to 131 K, the broadness of the NH_4SH IR features and the presence of the NH_4^+ symmetric bending mode (ν_2) at 5.90 μm/1696 cm^{-1}, which is IR inactive in crystalline NH_4SH (Hudson et al. 2015), shows that the ice remains amorphous at these temperatures. Peak sharpening and/or splitting of all of the NH_4SH IR features (except the NH_4^+ ν_2 feature, which disappears), are observed at ∼135 K, indicative of the salt crystallizing. This event also coincides with an increase in the desorption of both NH_3 and H_2S in the TPD spectrum (Figure 4.A.16) and the beginning of the gradual decrease in the peak area of the NH_4^+ ν_4 feature, demonstrating that the crystallization and desorption temperatures of this salt are very close to each other. Peak desorption is observed at 164 K in the TPD, and all of the salt features disappear from the IR spectrum by ∼174 K. In the NH_3:H_2S 2:3 and 3:2 mixtures, the maximum NH_4^+ ν_4 peak area (i.e., maximum reaction completion assuming the band strength does not change significantly with temperature) is achieved at lower temperatures, and the samples crystallize at higher temperatures (see Figure 4.A.17).

NH_4^+ ν_4 feature

The growth of the NH_4^+ ν_4 feature during warm-up from 15 to 131 K is accompanied by a change in the feature's profile, which becomes more asymmetric, and a redshift in the feature's peak position. Such a redshift of this feature with increasing temperature has been observed in other laboratory ammonium salts (Grim et al. 1989a; Schutte & Khanna 2003; Raunier et al. 2003). These spectral changes during the warm-up are likely a consequence of the change in the chemical environment between 15 K (when the ice matrix is still dominated by a relatively high quantity of unreacted neutral NH_3 and H_2S) and 131 K (when very little NH_3 and H_2S remain in the ice matrix, resulting in a matrix that now contains nearly exclusively ionic species). Thermal effects may also play a role in the redshift of the feature during warm-up, but the fact that we also observe a redshift in the feature during the isothermal holds at 15 K, during which the concentration of NH_4SH with respect to NH_3 and H_2S in the ice matrix is increasing (see Figure 4.2), demonstrates that increasing salt concentration in the ice matrix must play a role in the redshift as well. The redshift of this feature has significant astronomical ramifications that are further discussed in Section 4.4. The peak positions, FWHMs, and relative areas of this feature during warm-up are presented in Table 4.A.10 and Figure 4.A.17.

SH^- stretching feature

It is difficult to similarly characterize the SH^- stretching mode at ∼2555 cm^{-1} throughout sample warm-up because the feature directly overlaps with the H_2S asymmetric and symmetric stretching modes (Figure 4.1). At 15 K, when salt concentrations are the lowest in the sample, the feature sits at 2560 cm^{-1}, its peak area is at its maximum, and it is blended with neighboring strong, broad features. As the sample is warmed and the acid-base reaction is facilitated, the combined H_2S and SH^- peak redshifts and decreases in area, demonstrating that the band strength of the SH^- stretching mode is considerably lower than that of the the H_2S stretching modes. At this point in the warm-up, the contribution of unreacted H_2S to this

feature may not be negligible in the mixtures where H_2S is in excess, so the feature is only characterized further in the NH_3:H_2S 3:2 mixture. During crystallization, the feature sharpens and blueshifts to 2570 cm^{-1}, but its area remains small. The peak positions, FWHMs, and relative areas of the SH^- feature at temperatures at and above 102 K (the temperature at which the reaction is complete) in the 3:2 mixture are reported in Table 4.A.11.

4.3.2 H_2O:NH_3:H_2S

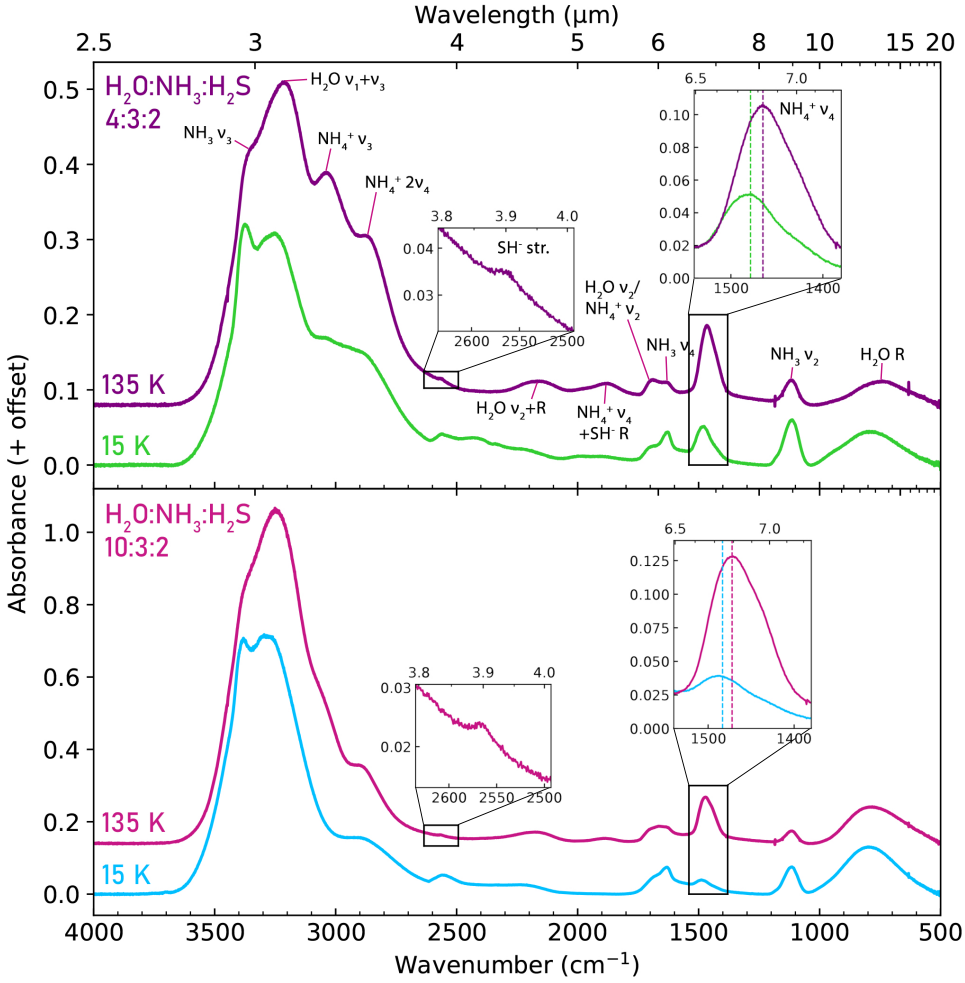


Figure 4.3: Spectra of two H_2O:NH_3:H_2S mixtures at 15 and 135 K. The plot insets zoom in on two features of interest in this work, the SH^- stretching mode and the NH_4^+ asymmetric bending (ν_4) mode. The dashed vertical lines within the right inset indicate the peak positions of the NH_4^+ ν_4 mode at the two plotted temperatures, showing how the feature redshifts as the ice is heated. Vibrational mode assignments are provided for the H_2O:NH_3:H_2S mixture at 135 K.

Spectra of two selected H_2O:NH_3:H_2S mixtures at 15 and 135 K are presented in Figure 4.3. Several of the features that are clear in the NH_3:H_2S mixtures are much less prominent once H_2O is added to the mixtures, in particular the various NH_4^+ peaks between ∼3.2-3.6 μm/3100-2800 cm^{-1}, which present as broad shoulders on the red wing of the H_2O OH stretching mode, the NH_4^+ scissor (symmetric) bending mode at ∼5.9 μm/1690 cm^{-1}, which blends with the H_2O bending mode, and the weak feature we tentatively assign to the combination of the NH_4^+ symmetric bend and the SH^- libration at ∼4.8/2090 cm^{-1}, which blends with the broad H_2O combination mode. However, the NH_4^+ ν_4 mode at 6.80 μm/1470 cm^{-1} and its combination band with the SH^- libration at 5.3 μm/1880 cm^{-1} remain distinct from the water ice bands. The SH^- stretching mode at 3.9 μm/2560 cm^{-1} is also clearly distinguishable from its local continuum but remains extremely small relative to the other salt features.

Reaction at 15 K

The presence of the NH_4^+ ν_4 mode already at 15 K in all of the water-containing mixtures demonstrates that NH_4SH can form at such low temperatures even when NH_3 and H_2S are diluted in water. Furthermore, just as in the water-free mixtures, acid-base reaction progression during an isothermal hold at 15 K after deposition has ended can be observed via the simultaneous increase in the peak area of the NH_4^+ ν_4 mode and decrease in the peak area of the blended NH_3 umbrella bending mode and H_2S bending mode (Figure 4.4). This reaction progression is again accompanied by a redshift in the peak position of the NH_4^+ ν_4 mode. However, the more dilute the initial concentrations of NH_3 and H_2S with respect to H_2O, the lower the integrated absorbance of the NH_4^+ ν_4 mode at 15 K with respect to the final integrated absorbance of the NH_4^+ ν_4 mode at 135 K – that is, the reaction at 15 K is slowed, but not completely prevented, by the presence of water at the investigated concentrations. The ratio of the integrated absorbance of the NH_4^+ ν_4 mode at 15 K versus 135 K is plotted as a function of final NH_4^+ abundance with respect to H_2O for all the investigated mixtures in Figure 4.5 to demonstrate this point.

Reaction during warm-up, crystallization, and desorption

During warm-up of the water-rich mixtures, the NH_4^+ ν_4 mode grows until reaching a maximum between 135-140 K while the area of the blended NH_3 umbrella bending mode and H_2S bending mode decreases, similar to what is observed in the water-free mixtures. The sharpening of the NH_4SH features characteristic of crystallization does not occur until ∼150-155 K, so dilution with H_2O delays the salt crystallization just as the presence of excess unreacted NH_3 and H_2S do in the water-free mixtures. As the warm-up continues after crystallization, the salt features begin to rapidly diminish and are completely absent from the spectrum between ∼175-180 K, around the same temperature range in which H_2O desorbs. The TPD peaks of NH_3, H_2S, and H_2O occur around the same temperatures, ∼171-172 K (e.g., Figure 4.A.25). Such an increase (∼10 K) in the peak desorption temperature of NH_4SH when it is mixed with water rather than pure was also recently observed by Vitorino et al. (2024). The consequences of the similar desorption temperatures of NH_4SH and H_2O on the detection of the NH_4SH desorption products in the gas phase are discussed in Section 4.5.2.

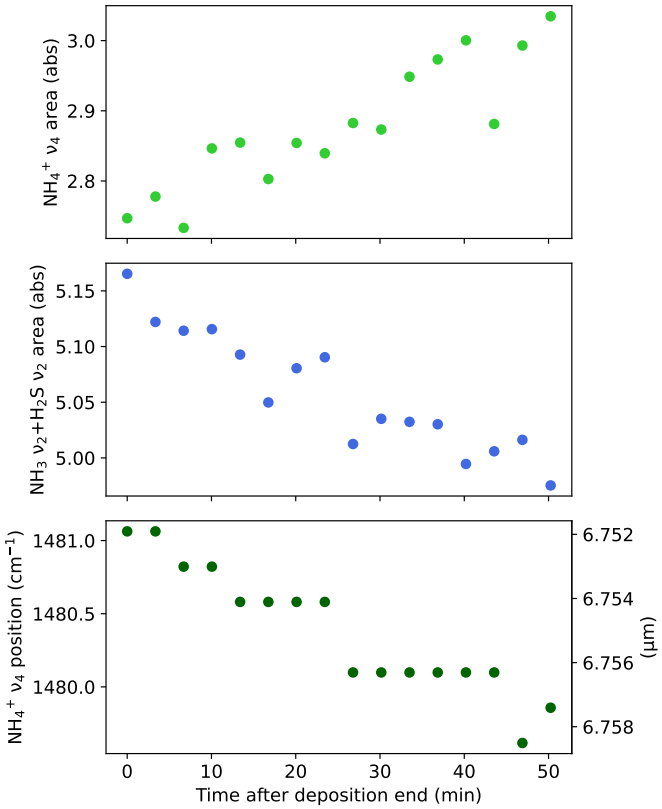


Figure 4.4: Characterization of selected features in the H_2O:NH_3:H_2S 4:3:2 spectra in the period between the end of the ice deposition and the start of the ice warm-up. During this time, the sample was held at 15 K. Top: peak area of the NH_4^+ ν_4 feature. Middle: peak area of the blended NH_3 umbrella bending and H_2S bending features. Bottom: peak position of the NH_4^+ ν_4 feature.

NH_4^+ ν_4 feature

As in the water-free spectra, the NH_4^+ ν_4 mode redshifts during warm-up. However, the feature also redshifts with increasing salt concentration with respect to H_2O when comparing the spectra of ices at the same temperature. Figure 4.6 visualizes this trend at 135 K. Comparison of the NH_4^+ ν_4 mode peak position at 135 K between the H_2O:NH_3:H_2S 5:2:1, 10:3:2, 5:1:1, and 10:2:3 mixtures (where the salt concentrations with respect to H_2O are identical at 20%, assuming reaction completion in all of the mixtures) also reveals that increasing the excess of unreacted NH_3 in the matrix causes the NH_4^+ ν_4 mode to blueshift, while increasing the excess of unreacted H_2S in the matrix causes it to redshift.

This led us to postulate that the redshifts of this feature observed during the isothermal holds at 15 K and the warm-up are caused primarily by the increase in salt concentration with respect to the hydrogen-bonded matrix. During warm-up, the salt concentrations increase at a higher rate due to the acid and base molecules mobilizing with increasing temperature, which

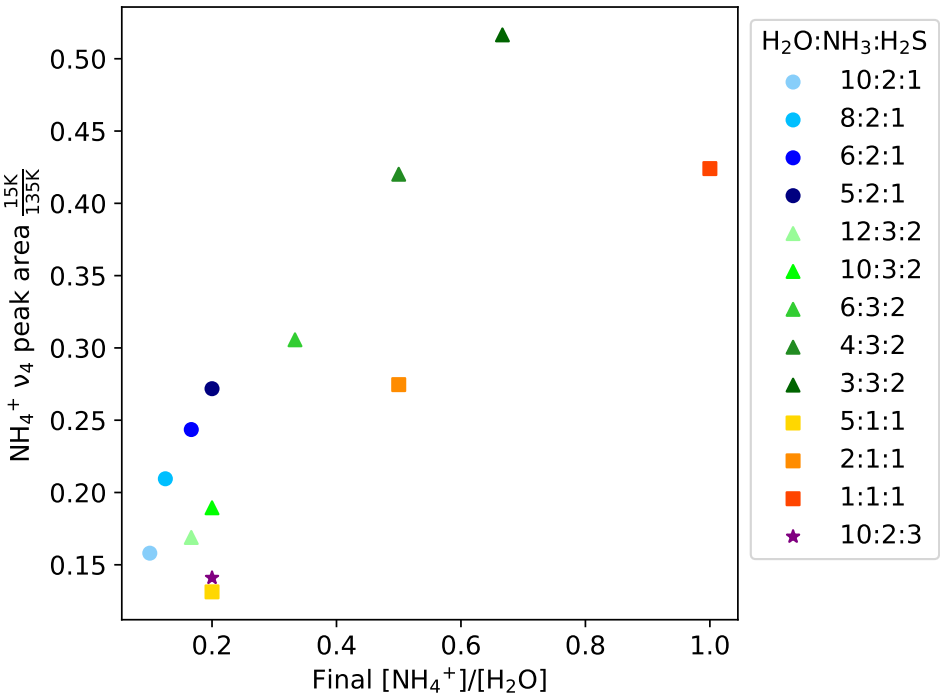


Figure 4.5: The ratio of the integrated absorbance of the NH_4^+ ν_4 peak at 15 K versus 135 K plotted as a function of the concentration of NH_4^+ with respect to H_2O (assuming 100% reaction completion) for various H_2O:NH_3:H_2S mixtures.

allows them to diffuse more easily within the ice matrix and react with each other.

In an effort to characterize the potential degeneracy between redshifts caused by increasing temperature and concentration, we conducted an annealing experiment where we deposited a H_2O:NH_3:H_2S 10:3:2 mixture, warmed it to 135 K at 1 K min^{-1}, and recooled it to 15 K at -5 K min^{-1}. Upon recooling (during which the salt concentration in the ice is not expected to change), the NH_4^+ ν_4 mode blueshifted from 1472 cm^{-1} to 1475.5 cm^{-1} (Figure 4.A.26). This peak shift of 3.5 cm^{-1} is significantly smaller than the redshift of over 11 cm^{-1} (1483 to 1472 cm^{-1}) that occurred over the initial warm-up from 15 to 135 K during which the majority of the salt formed. This suggests that thermal changes are not the main driver of most of the feature's redshift observed during warm-up, leaving changes in the chemical environment (e.g., salt concentration) as well as irreversible thermally-driven changes in the ice morphology (e.g., ice compaction) as the remaining possible contributors to the majority of the observed redshift during warm-up.

We therefore conclude that, although some of the redshifts in the NH_4^+ ν_4 mode associated with warm-up in our experiments as well as in some previous works may be caused by thermal effects, one of the primary physical causes of the redshift is the increase in salt concentration with respect to hydrogen-bonded matrix species as the deposited ice is warmed. We

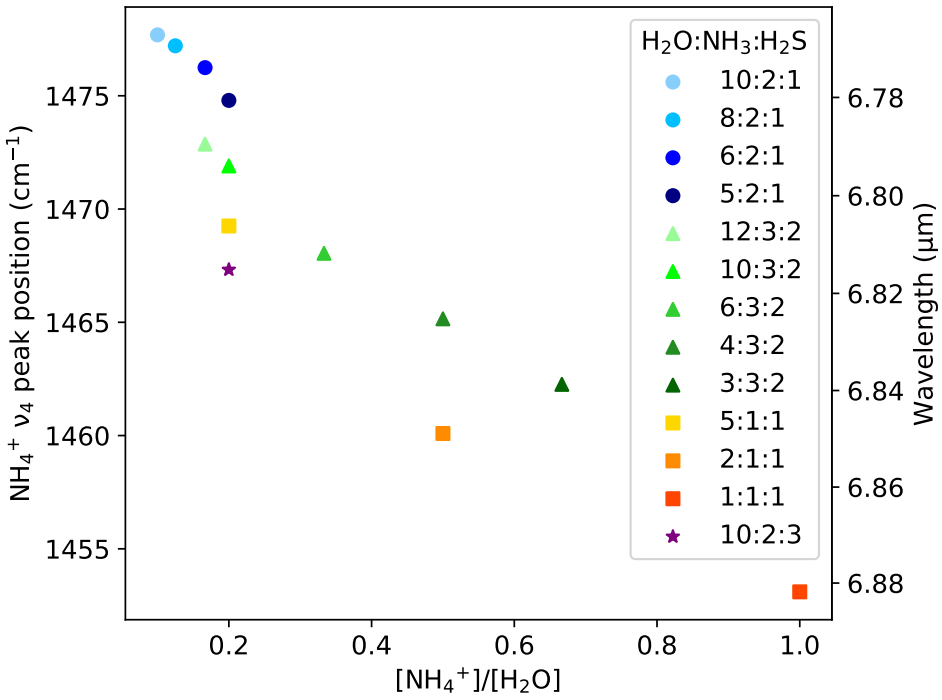


Figure 4.6: The peak position of the NH_4^+ ν_4 mode at 135 K as a function of the concentration of NH_4^+ with respect to H_2O plotted for various H_2O:NH_3H_2S mixtures.

specify that the concentration increase is with respect to hydrogen-bonded matrix species because we do not observe the same trend when the salt is diluted with excess H_2S (Figure 4.6). Our conclusion is consistent with that drawn by Maté et al. (2009), who stated that the redshift in the NH_4^+ ν_4 mode observed by Schutte & Khanna (2003) upon ice warm-up was likely due to "varying interactions among all the different species in the matrix." Also, the NH_4^+ ν_4 mode does not appear to vary significantly between 14 and 150 K in the NH_4HCOO:H_2O spectra formed via hyperquenching in Galvez et al. (2010), in which the salt concentration does not change during heating. The astronomical ramifications of this concentration dependence of the NH_4^+ ν_4 mode peak position are further discussed in Section 4.4.1. The peak positions, FWHMs, and relative areas of this feature during warm-up in all of the investigated mixtures are reported in Appendix 4.A.4.

SH^- stretching feature

As in the pure NH_4SH spectra, the blended H_2S and SH^- stretching peak becomes smaller as the ice is heated and the NH_4^+ ν_4 mode grows. The peak positions and FWHMs of the feature at 135 K range from 2567-2559 cm^- and 25-32 cm^-, respectively, in the mixtures investigated here, with the highest salt concentration mixtures having the most redshifted and

broadest features (see Appendix 4.A.4).

Band strengths

Table 4.4: Apparent band strengths of the NH_4^+ ν_4 mode and the SH^- stretching mode in H_2O:NH_3H_2S mixtures of three different concentrations.

Ratio H_2O:NH_3H_2S	A' NH_4^+ ν_4[(a)] 10^{-17} cm molec^{-1}	A' SH^- str.[(b)] 10^{-19} cm molec^{-1}
10:2:1	3.6±0.4	3.7±0.5
10:3:2	3.6±0.4	3.1±0.4
8:5:4	3.2±0.3	3.2±0.4

[(a)] Integration range: 1560-1340 cm^{-1}.
[(b)] Integration range: 2611-2520 cm^{-1}.

The Beer's law plots used to calculate the apparent band strengths of the NH_4^+ ν_4 mode and the SH^- stretching mode in the 10:3:2 H_2O:NH_3:H_2S mixture are shown in Figures 4.7 and 4.8 (the 10:2:1 and 8:5:4 mixture plots can be found in Appendix 4.A.4). The derived values from the slopes of the linear fits in all of these plots are provided in Table 5.3.

Despite previous theoretical and experimental works raising concerns regarding the NH_4^+ ν_4 mode band strength decreasing significantly with dilution in H_2O (Maté et al. 2009; Galvez et al. 2010), we do not find statistically significant differences between the NH_4^+ apparent band strengths of NH_4SH:H_2O mixtures with different salt concentrations ranging from 10-50% with respect to H_2O. Our apparent band strengths are very close to the apparent band strength of the NH_4^+ ν_4 mode in pure NH_4CN derived recently by Gerakines et al. (2024), 3.58(±0.07)×10^{-17} cm molec^{-1}. They are also a factor of∼1.22-1.38 lower than the band strength of the NH_4^+ ν_4 mode in NH_4HCOO:H_2O ice from Schutte & Khanna (2003), 4.4×10^{-17} cm molec^{-1}, which is often utilized to quantify NH_4^+ ice column densities in observational works. The band strength of the SH^- stretching mode is almost two orders of magnitude lower than the band strength of the H_2S stretching mode at the same wavelength (Yarnall & Hudson 2022).

As was mentioned previously, these band strengths assume that the limiting reactant, H_2S, was fully consumed in the reaction by 135 K. The quantity of H_2S consumed in the experiments used to calculate these band strengths cannot be estimated from the IR spectra because its strongest band, the stretching mode, overlaps closely with the strongest band of the reaction product SH^-. For this reason, we estimate instead the quantity of limiting reactant consumed by 135 K in the H_2O:NH_3:H_2S 10:2:3 mixture, where an estimate of the final abundance of the limiting reactant, NH_3, can be obtained via its umbrella mode. At 135 K, the peak area of the NH_3 umbrella mode is ∼4% relative to its peak area at the beginning of the warm-up (at which point we estimate ∼14% of the deposited NH_3 has already reacted based on Figure 4.5). Assuming negligible desorption of unreacted NH_3 by 135 K due to entrapment based on QMS data, we estimate that ∼96% of the deposited NH_3 has reacted with H_2S by 135 K in this experiment. Given that, in the NH_3:H_2S mixtures, the acid-base reaction appears to proceed more readily in NH_3 excess than in H_2S excess (Figure 4.A.17), we extrapolate that

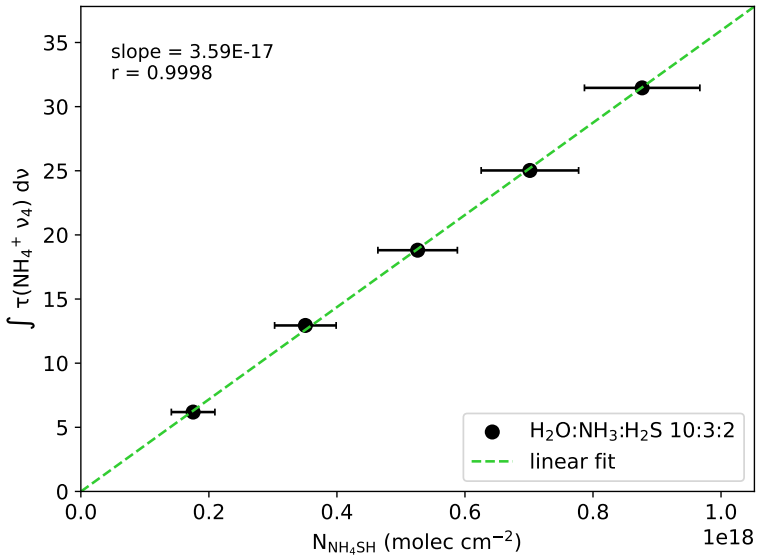


Figure 4.7: Beer's law plot used to derive the apparent band strength of the NH_4^+ ν_4 feature formed in the H_2O:NH_3:H_2S 10:3:2 mixture.

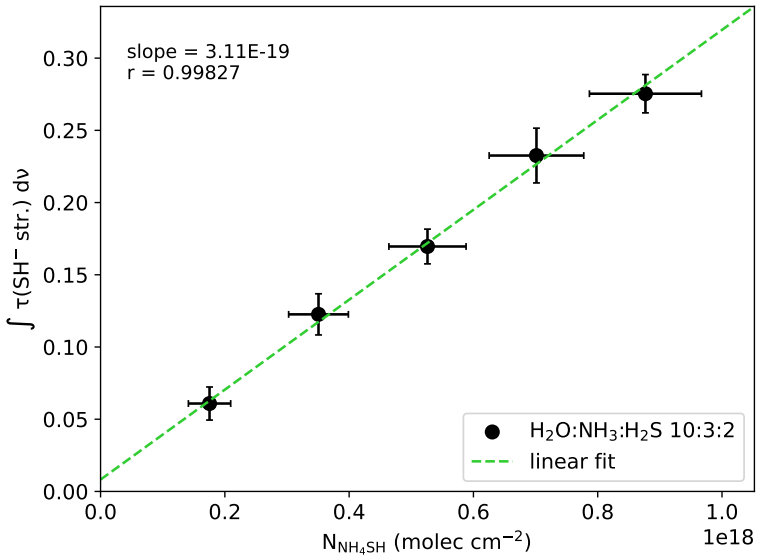


Figure 4.8: Beer's law plot used to derive the apparent band strength of the SH^- stretching feature formed in the H_2O:NH_3:H_2S 10:3:2 mixture.

in our H_2O-containing mixtures where H_2S is the limiting reactant, an equivalent or higher percentage of H_2S will have been consumed in the acid-base reaction by 135 K.

4.4 Comparing NH_4SH:H_2O laboratory spectra to observations

The assignment of the 6.85 μm band observed toward icy sightlines to the NH_4^+ cation was first suggested over 40 years ago (Knacke et al. 1982). Since then, despite rigorous investigations in numerous observational, experimental, and theoretical works, the assignment remains tentative. As mentioned in Section 4.1, previous works provided three primary arguments against a secure assignment: 1) the NH_4^+ ν_4 mode is too broad in laboratory data of ammonium salts in water-rich matrices to match observations and, at the expected NH_4^+ concentrations, the band strength of the feature is likely so low that it may render the salt undetectable (Maté et al. 2009; Galvez et al. 2010); 2) the calculated column densities of anions identified in interstellar ices are insufficient (by about an order of magnitude) to fully counterbalance the expected positive charge from the NH_4^+ cation (Schutte et al. 1999; van Broekhuizen et al. 2004, 2005; Boogert et al. 2022; McClure et al. 2023; Rocha et al. 2024); and 3) no other features that can be unambiguously assigned to NH_4^+ have been detected (Boogert et al. 2015). In the subsequent analysis, we will address each of these points using the new laboratory data collected in this work.

4.4.1 NH_4^+ ν_4 mode

Our apparent band strength measurements of the NH_4^+ ν_4 mode in NH_4SH diluted in H_2O ice at concentrations between 10 and 50% with respect to H_2O range from 3.2($\pm$0.3) - 3.6($\pm$0.4) $\times$ 10^{-17} cm molec^{-1}. Such band strengths are comparable in order of magnitude to the band strength of the NH_3 umbrella bending mode at 9.35 μm (Kerkhof et al. 1999; Hudson et al. 2022), which is typically detected at concentrations on the order of $\sim$5% with respect to H_2O toward pre- and protostellar ices (Bottinelli et al. 2010; Boogert et al. 2015; McClure et al. 2023).

Previous laboratory experiments where ammonium salts were grown via the hyperquenching method (i.e., droplets of salts dissolved in liquid water at the desired concentration are directly dripped onto a cold IR substrate) at concentrations between 7-25% with respect to H_2O did not formally report band strengths of the NH_4^+ ν_4 mode, but it was noted that the feature was so weakened and broadened by the presence of water that it became implausible to securely detect assuming similar local salt concentrations with respect to H_2O in interstellar ices (Maté et al. 2009; Galvez et al. 2010). Galvez et al. (2010) pointed out that such dramatic weakening did not occur in salt:H_2O ice mixtures formed via vapor co-deposition, the same method used in this work, and ascribed the difference in band strengths to the fact that, in hyperquenched ice samples, the ions are expected to be densely surrounded by "solvation spheres" of H_2O molecules, which disturbs their ionic character and decreases their band strengths. They further argued that the water-rich ices forming in the interstellar medium via atom-addition reactions on grain surfaces are expected to be compact, mimicking more closely the morphology of their hyperquenched samples rather than the open, porous structures of water ices formed via vapor deposition in the lab.

We argue that this may not necessarily be the case, because if the salts in interstellar ice mantles form via in situ acid-base reactions, the acid and base molecules must be adjacent to each other in the ice matrix, which will result in the cations and anions formed via the reaction to be adjacent to each other as well, rather than separated and fully surrounded by solvation spheres of water. Such cation-anion pairs within the ice matrix are expected to have higher ionic character and, therefore, higher band strengths.

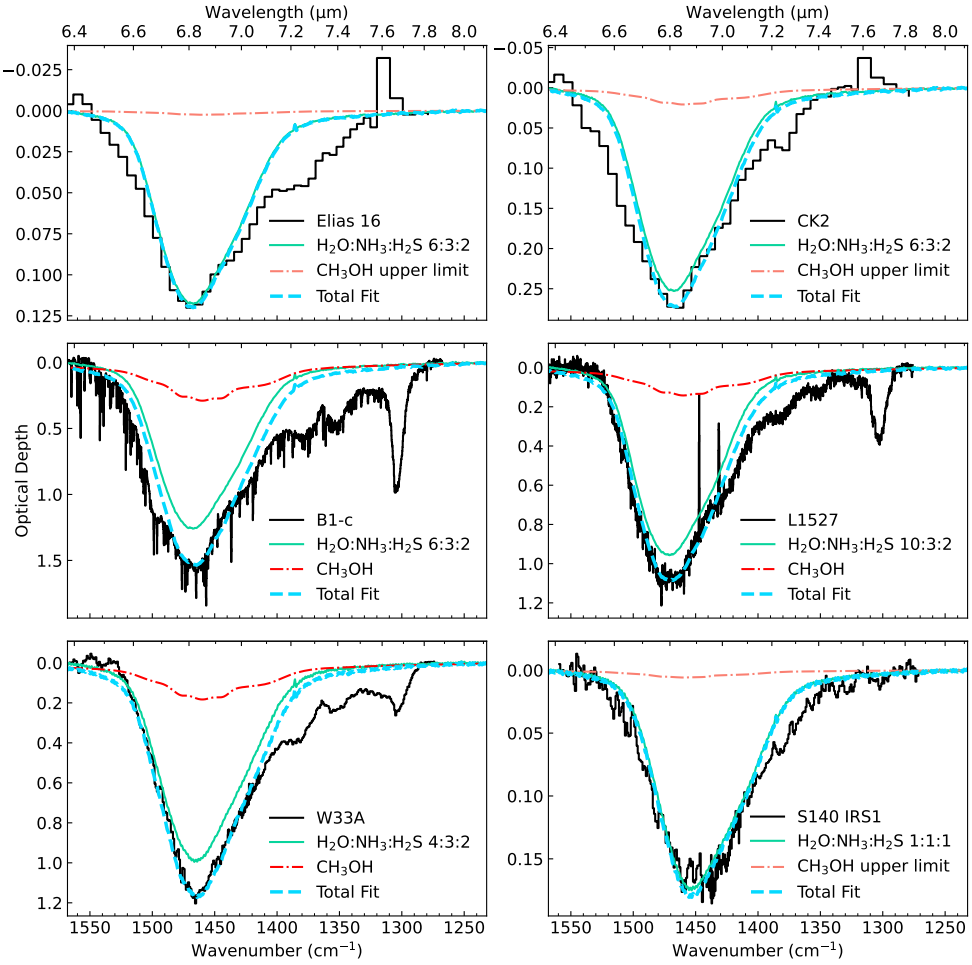


Figure 4.9: Fits of laboratory IR spectra of NH_4SH:H_2O ice mixtures at 135 K (sea green solid trace) and pure CH_3OH ice at 15 K (dash-dotted red or pink trace) to the 6.85 μm feature observed toward four protostars and two dense clouds (see Table 4.3). The total combined fits of both NH_4SH and CH_3OH are indicated with the dashed light blue trace. The best fitting mixture used in each fit is listed inside each panel. Note that many of the sharp spikes present in the JWST LYSO spectra are gas-phase lines in absorption (e.g., B1-c) or emission (e.g., L1527) rather than noise. Local continua used to extract the feature from the observational spectra can be found in Figure 4.A.28.

Table 4.5: H_2O and NH_4^+ ice column densities calculated toward the investigated sources using laboratory IR spectra and apparent band strengths of NH_4SH in H_2O-rich ices.

Source	H_2O	NH_4^+	
	10^{19} cm^{-2}	10^{18} cm^{-2}	% H_2O
Elias 16	0.24 (0.03)$^{(a)}$	0.26 (0.05)	11 (2)
CK2	0.30 (0.03)$^{(a)}$	0.57 (0.11)	19 (4)
B1c	2.5 (0.2)$^{(b)}$	2.8 (0.5)	11 (2)
L1527	2.6 (0.6)$^{(c)}$	2.1 (0.4)	8 (3)
W33A	1.25 (0.3)$^{(a)}$	2.5 (0.5)	20 (7)
S140 IRS1	0.20 (0.03)$^{(a)}$	0.45 (0.08)	23 (5)

Uncertainties are indicated in parentheses (). $^{(a)}$ from Boogert et al. (2013). $^{(b)}$ from Chen et al. (2024). $^{(c)}$ from the 12 μm H_2O libration using a band strength of 3.2×10^{-17} cm molec^{-1} (Mastrapa et al. 2009; Bouilloud et al. 2015); see Figure 4.A.27.

In Figure 4.9, we fit the 6.85 μm feature in our selected observed spectra toward dense clouds and protostars with the NH_4^+ ν_4 mode in our NH_4SH:H_2O laboratory spectra at 135 K and use these fits to derive NH_4^+ cation column densities and abundances with respect to H_2O ice (Table 4.5). We use only the laboratory spectra at 135 K because this is the temperature at which the salt concentrations are expected to be the closest to the target salt concentrations, and our annealing experiment shows that recooling the salt mixture from 135 K to 15 K has little effect on the NH_4^+ ν_4 mode profile and position compared to the changes in the feature due to increasing NH_4SH concentration that occur during the initial warm-up. As CH_3OH ice has a weak absorption complex of O-H and C-H bending modes at 6.85 μm as well, we account for the approximate expected contribution of CH_3OH ice to our fits by scaling a laboratory spectrum of pure CH_3OH ice at 15 K using literature CH_3OH ice column densities calculated from the 3.53 or 9.74 μm features (Boogert et al. 2008, 2011; Chen et al. 2024; Slavicinska et al. in prep.).

The observed 6.85 μm features toward these sources are fit very well by the NH_4SH:H_2O laboratory data. Specifically, the investigated dense clouds and LYSOs are best fit with laboratory spectra of more dilute NH_4SH ices ($NH_4SH/H_2O \sim$ 20-33%) compared to the MYSOs, which require laboratory spectra of more concentrated NH_4SH ices ($NH_4SH/H_2O \sim$ 50-100%) to fit their more redshifted features. This is consistent with previously reported trends of MYSOs, particularly thermally processed ones, generally having more redshifted 6.85 μm features than LYSOs (Keane et al. 2001; Boogert et al. 2008). Given these salt concentrations of the best-fitting laboratory spectra, we used the apparent band strength calculated from the lower concentration NH_4SH:H_2O mixtures (3.6×10^{-17} cm molec^{-1}) to calculate NH_4^+ column densities in the cloud and LYSO sources, while using the apparent band strength calculated from the higher concentration NH_4SH:H_2O mixtures (3.2×10^{-17} cm molec^{-1}) to calculate NH_4^+ column densities in the MYSO sources. Figure 4.10 shows the 6.85 μm feature of one of the sources, L1527, overplotted with the NH_4^+ ν_4 feature in five selected laboratory spectra with NH_4SH/H_2O concentrations ranging from 10-100% to help the reader visualize how NH_4SH concentration with respect to H_2O (and excess NH_3) affects the fitting of this feature.

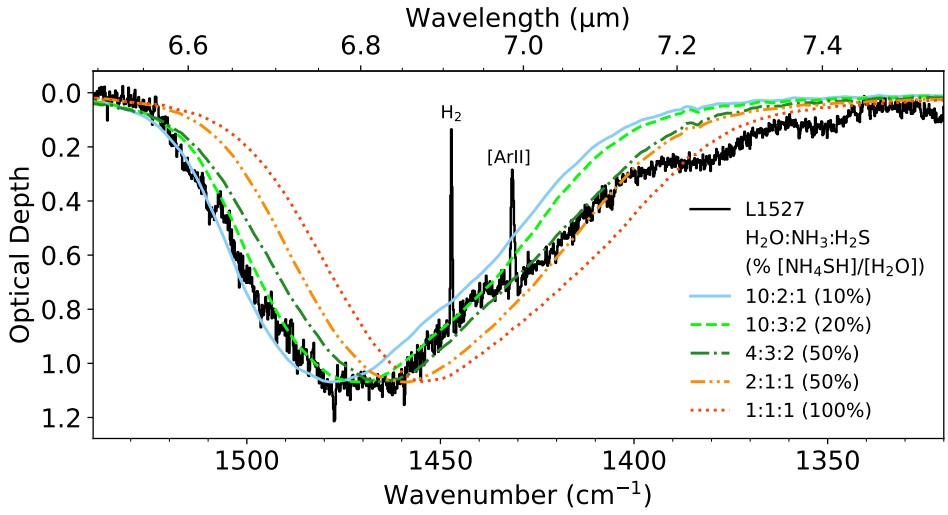


Figure 4.10: Selected laboratory spectra of H_2O:NH_3:H_2S ice mixtures of various concentration plotted with the 6.85 μm feature observed toward L1527 with JWST.

The resulting calculated NH_4^+ ice column densities presented in Table 4.5 range between 8-23% with respect to H_2O, within the previously reported ranges of NH_4^+ ice abundances with respect to H_2O toward dense clouds and protostars (Boogert et al. 2011, 2015). Considering the typical NH_3 ice abundances in such objects (3-10% with respect to H_2O, Boogert et al. 2015) results in combined NH_3+NH_4^+ abundances on the order of 10^{-6}-10^{-5} with respect to H_2 (see Section 4.5.1 for H column densities). Such values are in line with the typical gas-phase NH_3 abundances with respect to H_2 derived from small-beam radio/cm measurements targeting highly excited rotational lines in the most inner regions of hot cores, where temperatures are high enough that most NH_3 and NH_4^+ are expected to have desorbed into the gas phase (Pauls et al. 1983; Wilson et al. 1983; Mauersberger et al. 1986; Henkel et al. 1987; Brown et al. 1988; Walmsley 1994). However, the uncertainties of these gas NH_3 abundances are very high (up to an order of magnitude, due primarily to the poorly constrained warm H_2 column densities in their denominators), so the total abundance of NH_3 in dense star-forming regions remains an open question.

Our reported bulk NH_4^+ abundances with respect to H_2O are also approximately a factor of 2 lower than the NH_4^+ abundances of the laboratory ices whose spectra best fit the observed 6.85 μm features ($\geq$20%). One explanation for such a discrepancy could be an addition to the current layered ice model described in Boogert et al. (2015) and references therein. This model explains why, despite H_2O being the most abundantly detected icy species, the peak profiles of molecules like CO, CH_3OH, and OCS indicate that a significant fraction of these ices are in water-poor chemical environments: there is a difference in the timescale/cloud density at which H_2O formation and CO freeze-out occur, leading to distinct ice layers rather than a homogeneous ice mixture. Although H_2S is expected to form on ice grains at timescales closer to H_2O formation than CO freeze-out, models predict that H_2S formation should be

slightly delayed (by $\sim$1.4 A_v) relative to H_2O formation due to S atoms' lower abundance and heavier mass with respect to O atoms (Goicoechea et al. 2021). Such a delay could result in a gradient within the polar ice layer where the outer layer of polar ice that formed at later times in the dense cloud has a higher NH_4SH salt concentration than the inner layer of polar ice formed at earlier times. In such a scenario, high local salt concentrations in the salt-rich layer could still be consistent with overall lower bulk salt concentrations.

However, it is also possible that the discrepancies in NH_4^+ peak positions and calculated concentrations are caused by the presence of other species in the ice matrix (e.g., CO_2), overlap with other ice features in this region, or differences in temperature between the laboratory ices and the observed ices. Furthermore, the NH_4^+ abundances reported here are calculated only using laboratory data of NH_4SH, and although contributions from other ammonium salts like NH_4OCN, NH_4CN, NH_4HCOO, and NH_4Cl cannot dominate the 6.85 μm feature given their low abundances and upper limits with respect to the total NH_4^+ column densities (see Section 4.4.5), they could still cause some redshift of the 6.85 μm feature if their NH_4^+ ν_4 peak positions are redder than that of NH_4SH. A systematic characterization and comparison of multiple ammonium salts with carefully controlled concentrations in astrophysically relevant ice mixtures is needed to constrain and differentiate potential contributions from other ammonium salts to this feature.

4.4.2 Redshift of the 6.85 μm feature

In the past, observational studies empirically decomposed the observed 6.85 μm feature into two components, a blue component centered at $\sim$6.75 μm and a red component centered at $\sim$6.95 μm (referred to respectively as "component 1" and "component 2" in Keane et al. 2001 and "C3" and "C4" in Boogert et al. 2008, 2011, 2015). A combination of both components was needed to fit the 6.85 μm feature toward most observed icy lines of sight, but sight-lines with unprocessed ices typically had low τ_{int}C4/τ_{int}C3 ratios (i.e., a very blueshifted 6.85 μm feature, Boogert et al. 2011) while high τ_{int}C4/τ_{int}C3 ratios (i.e., a very redshifted 6.85 μm feature) were associated with thermally processed sources with low H_2O column densities (with respect to the depth of the 9.7 μm silicate band, Boogert et al. 2008). The association of redshift in the 6.85 μm feature with thermal processing was also supported by the previously available laboratory data of NH_4^+ salts in astrophysically relevant ice mixtures, in which only ices at very high temperatures (>200 K, Schutte & Khanna 2003) could reproduce the redshifted peak position of the C4 component.

Our experiments show clearly that the NH_4^+ ν_4 mode redshifts with increasing salt concentration with respect to hydrogen-bonding matrix species. Moreover, the redshift observed when salt concentration with respect to H_2O increases from 10 to 50% is approximately a factor of 3 larger (on the wavenumber scale) than the redshift observed when the ice temperature increases from 15 to 135 K in an annealed ice, where the salt concentration does not change upon warm-up (Figure 4.A.26).

Toward dense clouds without star formation, thermal processing cannot explain any variation in the peak position of the 6.85 μm feature. Thus, the small variations in the 6.85 μm feature peak position toward different prestellar sight-lines should be due purely to differences in the ice chemical composition. Indeed, we find that the published τ_{int}C4/τ_{int}C3 ratios of ices in the isolated dense clouds from Boogert et al. (2011) correlate very strongly with the reported NH_4^+ abundances with respect to H_2O (Figure 4.11, left plot). The Spearman's

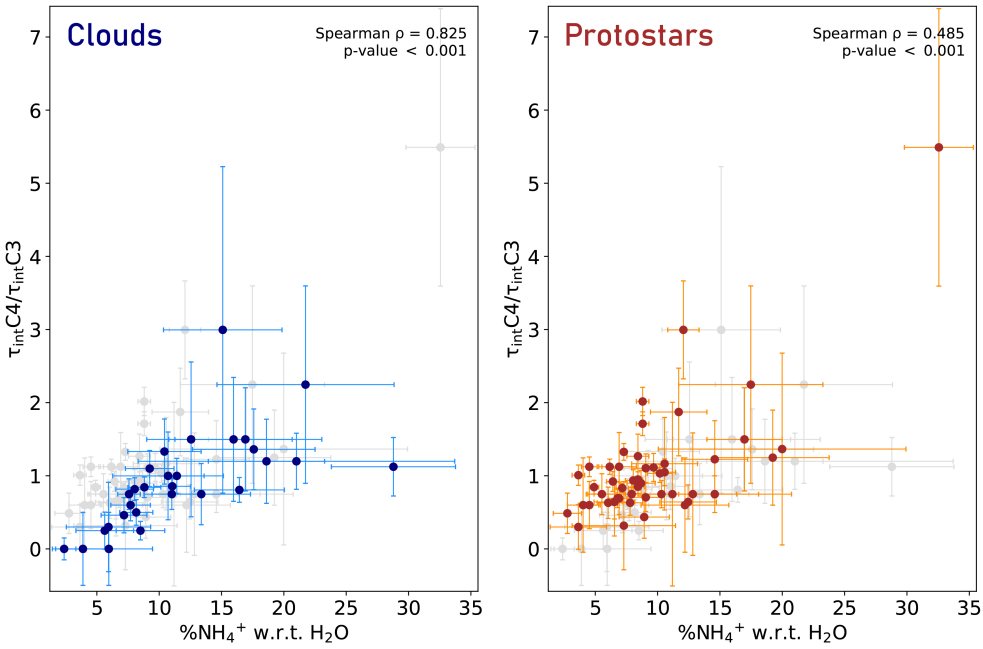


Figure 4.11: Abundances of the ammonium cation with respect to H_2O ice plotted against the $\tau_{int}C4/\tau_{int}C3$ ratios of ices toward isolated dense clouds (left, blue) and protostars (right, red). To facilitate comparison, the protostellar and cloud values are also plotted in the left and right plots, respectively, in light gray. A higher $\tau_{int}C4/\tau_{int}C3$ is indicative of a greater redshift in the peak position of the 6.85 μm feature. The plotted values are taken from Boogert et al. (2011) (clouds) and Boogert et al. (2008) (protostars). The Spearman's rank correlation coefficient ρ and the p-value indicating probability of noncorrelation are provided in the top right corner. The plotted NH_4^+ abundances have been multiplied by a correction factor of 4.4/3.6 to account for the difference between NH_4^+ ν_4 mode band strength used by Boogert et al. (2008) and Boogert et al. (2011) (4.4×10^{-17} cm molec^{-1} from Schutte & Khanna 2003) and the band strengths calculated in this work to enable a direct comparison to our NH_4^+ ice upper limits in Table 4.5. Upper limits have been excluded from this plot, as well as data from the sources 2MASS J19214480+1121203 (due to the high error of its $\tau_{int}C4/\tau_{int}C3$ ratio) and IRAS 03301+3111 (due to its $\tau_{int}C4/\tau_{int}C3$ ratio being undefined because its $\tau_{int}C3 = 0$).

rank correlation coefficient, which expresses the probability of two variables being related by a monotonically increasing function on a scale of 0 to 1, is very high at ρ=0.825. Such a correlation is consistent with the trend noted in our laboratory data. However, it is important to once again keep in mind that the redshift of the NH_4^+ ν_4 feature with increasing concentration could also be degenerate with other chemical effects that are not investigated here (e.g., presence of CO_2 in the ice matrix, ionic bonds with other anions, etc.).

Toward protostars, the correlation between the NH_4^+ abundances and the peak position is more moderate with a Spearman's rank of ρ=0.485 (Figure 4.11, right plot). The redshift of the 6.85 μm band observed toward thermally processed protostellar sources could be due in part to the formation of more NH_4^+ ions from leftover unreacted neutrals driven by diffusion at warm temperatures, but it is also possible that increases in local concentrations of NH_4^+

ions caused by thermally-driven ice restructuring, such as that which occurs during the heating of CO_2:H_2O ice mixtures (Ehrenfreund et al. 1997; Boogert et al. 2000), also contribute to the observed redshifts. Such structural changes would not change the overall line-of-sight averaged NH_4^+ abundance with respect to H_2O and would therefore result in a lesser correlation between the two variables.

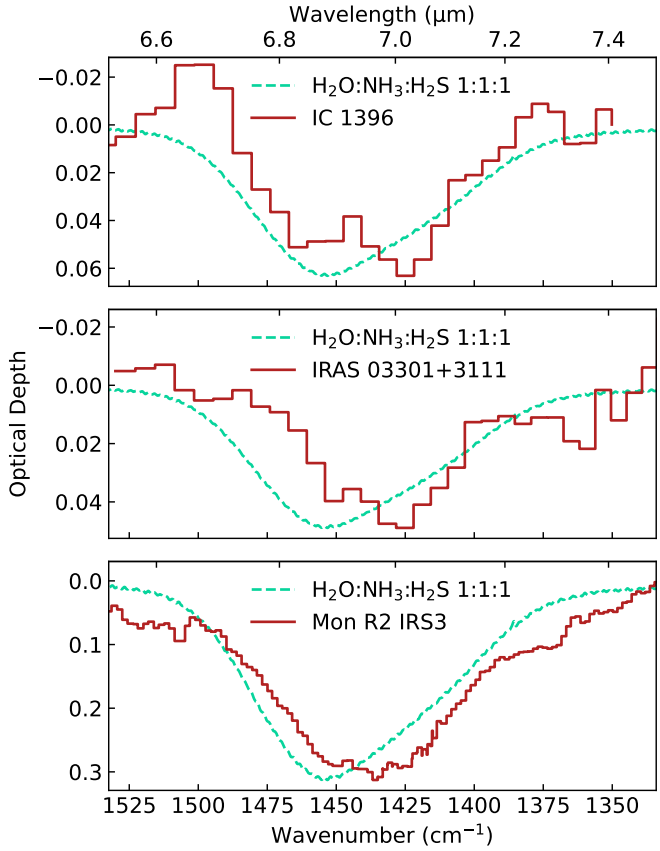


Figure 4.12: The highly redshifted 6.85 μm band of three unusual protostellar sources (red solid traces) which are not sufficiently fit with any of our laboratory NH_4SH:H_2O mixtures. The laboratory spectrum with the greatest redshift out of our full lab sample, the H_2O:NH_3:H_2S 1:1:1 ice heated to 135 K, is overplotted in dotted sea green traces for comparison.

Finally, comparisons of our laboratory spectra to unique, highly redshifted sources with extreme conditions reveal a third possible driver of the 6.85 μm feature's redshift in thermally processed sources. While our set of NH_4SH data is able to fit well the majority of the 6.85 μm features observed toward icy lines of sight, which have τ_{int}C4/τ_{int}C3 ratios below 3, a few exceptional sources exist whose 6.85 μm bands are too redshifted to be covered by even our most concentrated NH_4SH:H_2O $\sim$1:1 ice mixture (Figure 4.12). These sources are the LYSO IC 1396α (Reach et al. 2008), the LYSO IRAS 03301+3111 (Boogert et al. 2008), and the

MYSO Mon R2 IRS3 (Keane et al. 2001). The 6.85 μm bands of these features can be fit almost exclusively with the empirical C4 component.

IRAS 03301+3111 and Mon R2 IRS3 are unusual in that they have exceptionally low H_2O ice abundances with respect to H (a factor of 3-7 lower than typical protostellar sources like B1c, L1527, and W33A, Boogert et al. 2013), indicating that the thermal processing of their ice envelopes has been extensive enough to sublimate a significant fraction of their water ice. IC 1395α also has a low water ice column and additionally exists in a harsh, highly clustered and irradiated environment (Reach et al. 2008).

We find in our experiments that NH_4SH salts have similar desorption temperatures as H_2O, so if these sources' envelopes have lost a significant fraction of their water ice to thermal desorption, we would expect them to have lost a significant fraction of their NH_4SH salts, if present, as well. This would imply that NH_4SH cannot be the sole carrier of the empirically derived C4 component (although it may still contribute to the component because some water ice remains in these lines of sight). A significant part of the C4 component must therefore spectrally consist of either a more refractory ammonium salt with a more redshifted 6.85 μm feature or an entirely different species.

The next most abundant ammonium salt after NH_4SH detected in the dust grains of comet 67P, NH_4CN, has laboratory desorption temperatures similar to NH_4SH (Gerakines et al. 2024), so it is not a suitable C4 candidate. The third-, fourth-, and fifth-most abundant ammonium salts, NH_4Cl, NH_4OCN, and NH_4HCOO, are significantly more refractory with laboratory desorption temperatures above at least 200 K (Maté et al. 2009; Jiménez-Escobar et al. 2014; Ligterink et al. 2018; Bergner et al. 2016; Kruczkiewicz et al. 2021). Perhaps one or a combination of these salts (or other refractory ammonium salts) are major contributors to the C4 component. The highly redshifted reported peak positions of NH_4Cl:H_2O ice formed via hyperquenching in Galvez et al. (2010) and ammonium salts formed by photolysis experiments in Schutte & Khanna (2003) point to a promising future direction for elucidating the carriers of these highly redshifted features.

4.4.3 SH^- stretching mode

Following the fits of the NH_4^+ ν_4 mode to the 6.85 μm band, we aimed to investigate if the optical depths of the fit NH_4^+ features were consistent with SH^- column densities or upper limits that could be calculated using the SH^- stretching mode at 3.9 μm. We performed local continuum subtractions on the 3.7-4.2 μm region toward the sources in our sample whose spectra in this range are available to us (Figure 4.A.29) and compared the subtracted spectra to the local continuum-subtracted SH^- feature in the laboratory spectra, scaled with the same factor as was used to fit the NH_4^+ feature in each source in Figure 4.9. Similarly to the 6.85 μm band fits, the expected contribution of CH_3OH ice to this spectral region was approximated by scaling a laboratory spectrum of CH_3OH ice at 15 K using literature CH_3OH ice column densities calculated from the 3.53 or 9.74 μm features (Boogert et al. 2008, 2011; Chen et al. 2024; Slavicinska et al. in prep.).

The excess absorptions left over toward each source after accounting for the CH_3OH and SH^- ice features were fit with Gaussians, whose peak positions and FWHMs range from 2716-2728 cm^{-1} and 20-40 cm^{-1}, respectively. Such profiles hint at the possible presence of thiol ices like methanethiol and ethanethiol toward these lines of sight, but secure assignment to a specific species is precluded by the broad, overlapping profiles of such molecules (Hud-

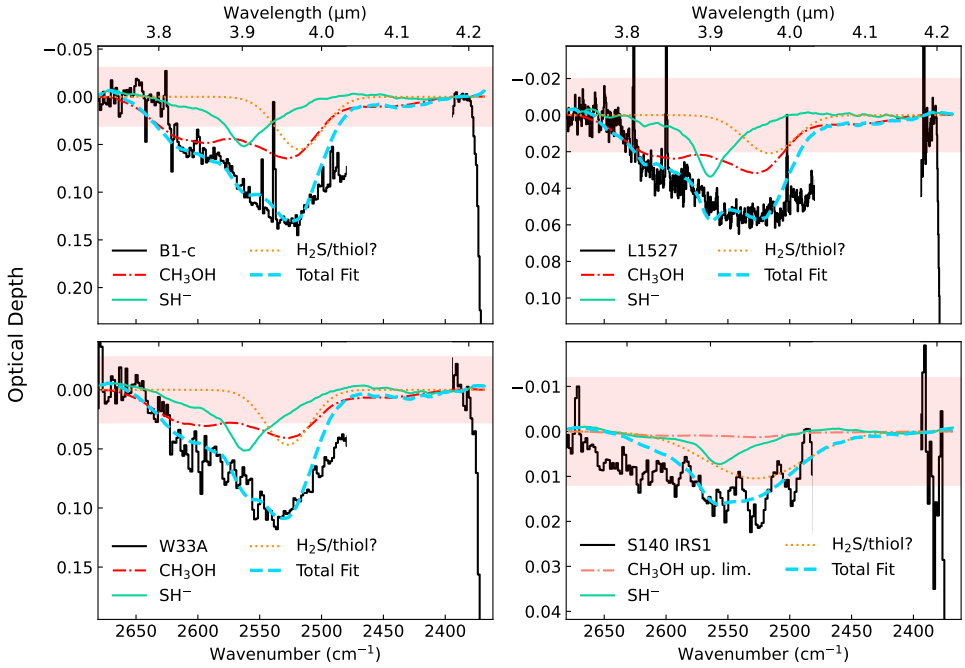


Figure 4.13: Fits of the SH^- stretching mode from laboratory NH_4SH:H_2O spectra (dark green solid trace) and the combination modes from laboratory CH_3OH spectra (dash-dotted red or pink trace) to the absorption complex between 3.8-4.2 μm observed toward four protostars. The fit SH^- features are isolated from the laboratory spectra via a local continuum subtraction and scaled with the same factors as those used to fit the 6.85 μm bands in Figure 4.9. The CH_3OH features are similarly scaled using literature CH_3OH ice column densities or upper limits calculated from the 3.53 or 9.74 μm features. As the SH^- stretching mode and CH_3OH combination modes are some of the weakest spectral features of the investigated ices, both the NH_4SH and CH_3OH laboratory spectra are smoothed with a Savgol filter prior to fitting to remove experimental noise. Excess absorptions that is not fit with SH^- and CH_3OH features are fit with Gaussians (dotted orange trace) that could be attributed to a combination of H_2S and thiol ices. The full fit is indicated with a dashed light green trace, and the horizontal shaded red bars indicate 3σ levels calculated from RMS errors in the 3.72-3.77 μm range. Data from 4.03-4.18 μm (G395H gap in JWST data, low S/N region in ISO data) is excluded from the plot. Plots of the local continua applied to the observed spectra can be found in Appendix 4.A.5.

son & Gerakines 2018). Furthermore, the fitting of a single Gaussian to this excess is merely a first-order approximation to what could be a complex of multiple Gaussian-like absorptions attributable to several different species containing S-H bonds. The upper limits obtained from assigning these Gaussians to either H_2S or thiols are on the order of $\lesssim$1% and $\lesssim$5% with respect to H_2O, respectively (using the band strengths of 1.66×10^{-17} cm molec^{-1} for H_2S, Yarnall & Hudson 2022, and 3.40×10^{-18} cm molec^{-1} for 1-propanethiol, Hudson & Gerakines 2018). The underfit red shoulder of the absorption complex >4 μm may be the blue wing of an HDO ice absorption (Slavicinska et al. 2024).

The resulting fits are presented in Figure 4.13, where the green solid trace indicates the

maximum possible SH^- contribution (assuming $[NH_4^+] = [SH^-]$). Given the blending of multiple overlapping ice features in this spectral region as well as the extremely weak band strength of the SH^- stretching mode, we cannot claim tentative or secure detection of the SH^- anion in this spectral region toward these sources, and it is unlikely that this feature could serve as a reliable tracer of NH_4SH ice in other interstellar ice spectra. However, these fits by no means preclude the presence of SH^- column densities comparable to the NH_4^+ column densities calculated from the 6.85 μm features of these sources. In fact, these fits show that sizable column densities of SH^- anions can be masked very effectively by the absorptions of CH_3OH ice, H_2S or thiol ices, and observational noise at the wavelengths where the SH^- stretching mode is found.

4.4.4 NH_4^+ ν_4 and SH^- libration combination mode

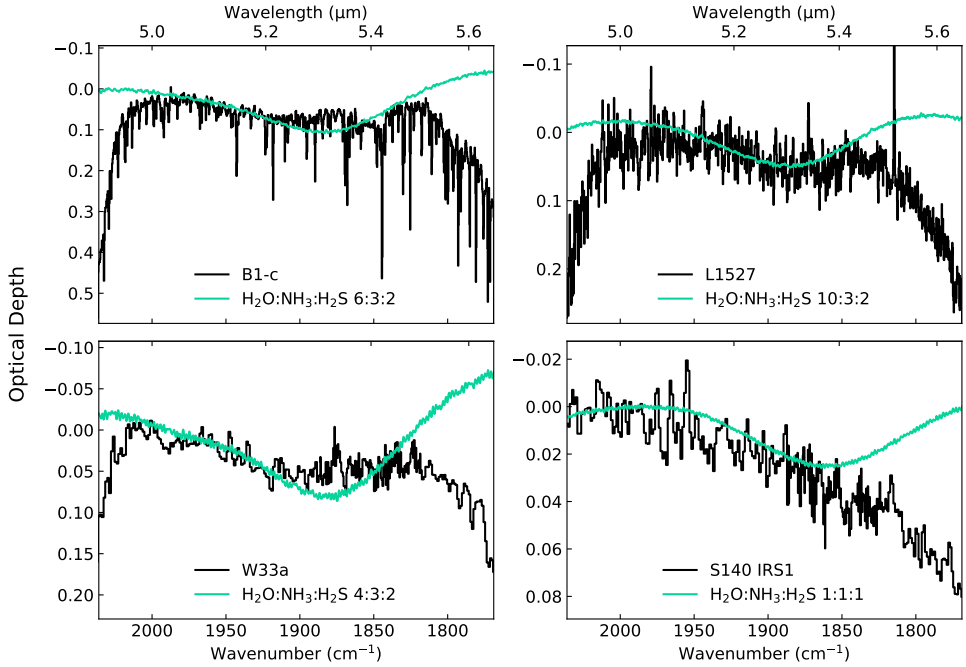


Figure 4.14: Laboratory NH_4SH:H_2O data scaled with the same factor as that used to fit the 6.85 μm band in Figure 4.9 plotted with the global continuum-subtracted spectra of four protostars, zoomed in on the 4.8-5.6 μm region where a weak and broad absorption is observed. The profile of the observed absorption matches well the NH_4^+ ν_4 + SH^- libration combination mode in the laboratory spectra. Plots of the global continua applied to the observed spectra can be found in Appendix 4.A.5.

Boogert et al. (2022) first reported the presence of a weak, broad absorption centered at approximately 5.25 μm in the IRTF spectra of W33A and a "number" of other MYSOs. This feature has not been assigned to any species and, prior to JWST, was not reported toward any dense clouds or LYSOs, likely due to the limited spectral coverage of the full width of this

band by both ground-based NIR data and *Spitzer* Space Telescope MIR data. Here, we report the presence of a similar feature centered around ∼5.3 μm/1890 cm^{-1} with a FWHM of ∼0.26 μm/92 cm^{-1} toward both of the LYSOs observed with JWST in our sample of sources and tentatively assign it to the combination mode of the NH_4^+ ν_4 mode and the SH^- libration. The tentative assignment has two-fold significance: it reinforces the presence of NH_4^+ in interstellar ices, and it is a tentative detection of a SH^- signature in a spectral region that is less busy than the 3.9 μm region where the SH^- stretching mode is found. The only other major ice bands present in this region are the OCS feature at 4.9 μm and the 6.0 µm band, whose wings overlap slightly with the blue and red edges, respectively, of the very broad 5.3 µm band.

In Figure 4.14, the observed feature is fit with the same NH_4SH laboratory spectra and scaling factors as those used to fit the 6.85 μm band to each source in Figure 4.9. The profile of the features in the laboratory spectra match the profile of the observed features quite well, and the observed depths are similar to the depths of the laboratory features when they are scaled with the same factor that is used to fit the 6.85 μm band. However, it must be stressed that, due to the weak and broad profile of the feature as well as its overlap with the blue wing of the large 6.0 μm ice feature, it is difficult to accurately extract its profile and depth from the source continuum, and even slight inflections in the continuum choice can significantly affect its calculated depth. Therefore, we do not consider this feature to be a reliable means of quantifying the SH^- anion column density. Nevertheless, we conclude that the observed depth of this feature is not inconsistent with the observed depth of the NH_4^+ band, and its presence shows that SH^- is an excellent candidate anion to counterbalance the majority of the NH_4^+ cations quantified via the 6.85 μm band.

4.4.5 Other anions (OCN^-, CN^-, $HCOO^-$, Cl^-)

Table 4.6: Estimated abundances and upper limits of four other counterion candidates, reported in percentages (%) with respect to NH_4^+ column densities.

Source	OCN^- [a]	CN^- [b]	$HCOO^-$ [c]	Cl^- [d]	Total anion budget	
					w/o Cl^-	incl. Cl^-
B1c	6.7 (1.3)	≤0.9	≤6.4	≤8.5	≤14	≤22
L1527	4.5 (0.9)	≤0.1	≤2.9	≤8.2	≤7.5	≤16
W33A	10.8 (2.2)	n.d.	≤2.4	≤8.1	≤13	≤21

Uncertainties are indicated in parentheses (). [a] calculated using a band strength of 1.3×10^{-16} cm molec^{-1} (van Broekhuizen et al. 2004). [b] calculated using a band strength of 5.74×10^{-18} cm molec^{-1} (Gerakines et al. 2024). [c] calculated using a band strength of 2.1×10^{-17} cm molec^{-1} (Bergner et al. 2016). [d] calculated using the diffuse ISM Cl/H of 2.88×10^{-7} (Esteban et al. 2004).

After the SH^- fitting attempt at 3.9 μm, we estimated abundances and upper limits of four other NH_4^+ counterion candidates identified in prior studies of interstellar ices and 67P dust grains to constrain how much NH_4^+ with unbalanced positive charge remains after accounting for these counterions, leaving room for other anions like SH^-.

Table 4.6 presents the estimated abundances of OCN^- and the upper limits of CN^-,

$HCOO^-$, and Cl^- in percentages with respect to the NH_4^+ column densities (Table 4.5) toward three of the four selected protostellar sources. The spectrum of S 140 IRS1 was not included in this analysis due to its relatively low S/N that prevented the detection of any known anionic features.

The OCN^-, CN^-, and $HCOO^-$ values were calculated via fitting their IR features at $\sim$4.62 μm/2165 cm^{-1}, $\sim$4.78 μm/2093 cm^{-1}, and $\sim$7.39 μm/1352 cm^{-1} with Gaussians (Figure 4.A.31). The calculated column densities of CN^- and $HCOO^-$ are only considered upper limits due to the possible contribution of other ice species to their observed bands (e.g., ^{13}CO for CN^- (McClure et al. 2023; **?**); CH_3CHO for $HCOO^-$, Rocha et al. 2024; Chen et al. 2024). Because the column density of Cl^- cannot be similarly constrained from IR spectra, its upper limit was constrained using the cosmic standard abundance of chlorine (i.e., assuming all Cl atoms are in the form of NH_4Cl toward these objects using Cl/H = 2.88×10^{-7} from Esteban et al. 2004).

The alternative anion candidates can only counterbalance up to $\sim$15-20% of the ammonium cations toward these lines of sight. This upper limit is similar to the total combined abundance of the neutral acid counterparts of these anions with respect to NH_3 quantified from the 67P dust grain impact event #4 in Altwegg et al. (2022).

Therefore, a minimum of $\sim$80-85% of the ammonium cations observed toward these lines of sight must be counterbalanced by other anions. It has been previously suggested that this counterbalance could come from a "variety" of multiple other anions, perhaps formed by energetic processing, whose weak and blended spectral signatures could create an undetectable "pseudo-continuum" (Schutte & Khanna 2003). Here, we show that SH^- column densities as high as the total measured NH_4^+ column densities can be effectively hidden in the 3.9 μm spectral region via blending with CH_3OH, H_2S, and thiol features (Section 4.4.3). Furthermore, SH^- can form purely via low-temperature acid-base chemistry without needing to invoke energetic processing (Section 4.3.2).

4.5 Astronomical implications

4.5.1 Sulfur budgets

Estimates of the total sulfur budgets that could be accounted for by solid NH_4SH toward all of the investigated sources are provided in Table 4.7. The ranges in this table are calculated with the assumption that 80-85% of the NH_4^+ cations quantified via the 6.85 μm band (see Table 4.5) are bound to SH^- anions (as the relative abundance of H_2S with respect to the combined abundances of all acids in the comet 67P dust grain impact event #4 was $\sim$82% in Altwegg et al. 2022, and the total NH_4^+ column density left without corresponding counterions after accounting for OCN^-, CN^-, $HCOO^-$, and Cl^- abundances and upper limits is $\gtrsim$80-85%). The hydrogen column densities (N_H) used to determine S/H were taken from Boogert et al. (2013) except in the case of L1527, whose N_H was similarly calculated from the optical depth of the 9.7 μm silicate feature in the L1527 MIRI spectrum (see Appendix 4.A.5).

Our observationally constrained estimates indicate that 10-18% of the sulfur expected toward the investigated lines of sight could be in the form of NH_4SH ice. The estimated sulfur abundance in NH_4SH is lowest toward S140 IRS1, the source whose ices have experienced the most thermal processing and which also has a very low H_2O ice abundance with respect

Table 4.7: Estimated contribution of NH_4SH salt to the total S budgets of each of the investigated sources, assuming 80-85% of the NH_4^+ cations quantified via the 6.85 μm band are bound to SH^- anions.

Source	N_H 10^{23} cm^{-2}	S in NH_4SH % S cosmic std.$^{(a)}$
Elias 16	0.89 (0.27)$^{(b)}$	14-15
CK2	1.9 (0.6)$^{(b)}$	14-15
B1c	8.3 (2.5)$^{(b)}$	17-18
L1527	5.9 (1.8)$^{(c)}$	17-18
W33A	7.1 (2.1)$^{(b)}$	17-18
S140 IRS1	2.2 (0.7)$^{(b)}$	10

Uncertainties are indicated in parentheses (). $^{(a)}$ relative to the diffuse ISM S/H of 1.66×10^{-5} from Esteban et al. (2004). $^{(b)}$ from Boogert et al. (2013). $^{(c)}$ from the 9.7 μm silicate feature; see Appendix 4.A.5.

to H (Boogert et al. 2013). Therefore, its envelope may have already lost a significant portion of its ices, including NH_4SH, to thermal desorption. In the case of the rest of the protostars in our sample, almost a fifth of the expected sulfur column may be locked in NH_4SH salt, much more than the previously constrained $\lesssim$5% S locked in ices calculated from OCS column densities and H_2S, thiol, and SO_2 upper limits (Palumbo et al. 1997; Boogert et al. 1997; Jiménez-Escobar & Caro 2011; Boogert et al. 2015, 2022; McClure et al. 2023; Rocha et al. 2024).

These estimates demonstrate that NH_4SH is a potentially significant sulfur sink in pre- and protostellar environments. They also show that NH_4SH alone cannot solve the sulfur problem, leaving the field open to other potential sulfur sinks whose abundances in dense star-forming regions are still not spectroscopically well-constrained (e.g., sulfur allotropes and minerals). Notably, the $\sim$82-83% of the sulfur that remains missing after accounting for the plausible abundance of NH_4SH is close to the proposed S/H abundance of highly refractory sulfur-bearing species (e.g., FeS) in protoplanetary disks quantified indirectly via the accretion-contaminated photospheres of young stars (89$\pm$8%, Kama et al. 2019).

4.5.2 NH_4SH ice desorption front

In protostellar envelopes and protoplanetary disks, molecules in ices warm up via heating by the growing central source and, at high enough temperatures, thermally desorb into the gas phase, where they can be detected via their rotational transitions by millimeter and submillimeter spectroscopy. The temperature at which desorption of a given ice molecule occurs is dictated by its binding energy to its surrounding molecules (i.e., other ices or grain materials like silicates). A molecule's thermal desorption can also occur at lower or higher temperatures if it is deeply trapped in a matrix of molecules that desorb at lower or higher temperatures.

Although we do not derive binding energies of NH_4SH in this work, the TPD experiments here indicate that NH_4SH desorbs at nearly the same temperature as H_2O, both when it is pure and when it is in H_2O-rich mixtures. As ionic salts desorb as their neutral counterparts, this means that any gas-phase NH_3 or H_2S that has thermally desorbed from NH_4SH ices should

have a sublimation front very similar to H_2O. While pure neutral NH_3 and H_2S ices desorb at much lower temperatures ($\sim$110 K and $\sim$90 K, respectively, in our experiments), neutral NH_3 and H_2S in interstellar ices may have sublimation fronts at temperatures closer to the sublimation front of H_2O ($\sim$170 K in our experiments) due to entrapment by a surrounding H_2O ice matrix. Whether the sublimation fronts of neutral NH_3 and H_2S mixed in H_2O ices would be different enough to distinguish them from NH_3 and H_2S originating from thermally desorbed NH_4SH salts must be determined with studies measuring the entrapment of NH_3 and H_2S in H_2O ices.

4.6 Conclusions

In this work, we present a systematic characterization of the laboratory IR spectra of NH_4SH ices, both pure and mixed with H_2O. From this characterization and a subsequent comparison of the laboratory spectra to spectra observed toward dense clouds and protostellar ice envelopes, we draw the following conclusions:

1. NH_4SH salts form via the in situ reaction of NH_3 and H_2S ices already at 15 K even when diluted in H_2O ice in mixing ratios relevant to interstellar ices.

2. The apparent band strength of the NH_4^+ ν_4 feature ($\sim$6.8 μm/1470 cm^{-1}) in 10-50% NH_4SH:H_2O mixtures ranges from 3.2($\pm$0.3)-3.6($\pm$0.4)$\times10^{-17}$, which does not preclude the detection of ammonium cations at similar concentrations with respect to H_2O in interstellar ice spectra. These apparent band strengths are a factor of $\sim$1.22-1.38 lower than the NH_4^+ ν_4 band strength in NH_4HCOO:H_2O ice from Schutte & Khanna (2003) that is frequently used to quantify NH_4^+ ice column densities in interstellar ice spectra.

3. The apparent band strength of the SH^- stretching mode ($\sim$3.9 μm/2560 cm^{-1}) in 10-50% NH_4SH:H_2O mixturesranges from 3.1($\pm$0.4)-3.7($\pm$0.5)$\times10^{-19}$ cm molec^{-1}. This is nearly two orders of magnitude lower than the apparent band strength of the H_2S stretching mode in the same spectral region. Therefore, it is significantly more challenging to detect H_2S if it is anionic.

4. The peak profile of the NH_4^+ ν_4 feature in the laboratory NH_4SH:H_2O spectra matches well with the profile of the observed 6.85 μm feature in the pre- and protostellar sources investigated here. From these fits, we derive NH_4^+ column densities ranging from $\sim$8-23% with respect to H_2O.

5. The NH_4^+ ν_4 feature in laboratory NH_4SH ices redshifts not only when heated, but also when the salt's concentration increases with respect to hydrogen-bonding matrix species like H_2O and NH_3. This could explain why the ammonium ion abundance with respect to H_2O is very strongly correlated with the peak position of the 6.85 μm feature toward cold dense clouds and moderately correlated toward protostars. The redshifts in the 6.85 μm feature toward thermally processed protostars could be driven by multiple physicochemical effects, such as an increase in the local concentration of ammonium salts with respect to H_2O caused by the reaction of leftover neutrals in the ice promoted by diffusion or thermally-driven ice restructuring. In ices found toward protostars with

extreme environments and exceptionally redshifted features, the thermal desorption of NH_4SH with water ice may also contribute to the observed redshift.

6. While the extremely low apparent band strength of the SH^- stretching mode makes it very difficult to reliably detect in the spectrally busy region at 3.9 μm, the weak and broad NH_4^+ ν_4 + SH^- libration combination mode at 5.3 μm is an alternative means of SH^- detection due to a lack of other major ice features at this wavelength. Here, we tentatively assign the weak and broad feature observed at 5.3 μm in the JWST spectra of our two investigated LYSOs to this combination band of NH_4SH.

7. The maximum possible combined contributions of the salts NH_4OCN, NH_4CN, NH_4HCOO, and NH_4Cl to the total ammonium salt abundance range between 15-20% toward the three investigated protostars with clearly detected 4.62 and 7.39 μm features.

8. If the SH^- anion is indeed the primary counterion to the observed column density of NH_4^+ cations in these spectra (as it is in the dust grains of comet 67P), then NH_4SH could account for up to 17-18% of the S budget toward our investigated sources, making it a potentially significant sulfur sink in dense star-forming regions.

4.7 Acknowledgements

This work is based on observations made with the NASA/ESA/CSA *James Webb* Space Telescope. The data were obtained from the Mikulski Archive for Space Telescopes at the Space Telescope Science Institute, which is operated by the Association of Universities for Research in Astronomy, Inc., under NASA contract NAS 5-03127 for JWST. These observations are associated with programs #1290 and #1960. All the JWST data used in this paper can be found in MAST: 10.17909/3kky-t040. The following National and International Funding Agencies funded and supported the MIRI development: NASA; ESA; Belgian Science Policy Office (BELSPO); Centre Nationale d'Etudes Spatiales (CNES); Danish National Space Centre; Deutsches Zentrum fur Luft- und Raumfahrt (DLR); Enterprise Ireland; Ministerio De Economiá y Competividad; Netherlands Research School for Astronomy (NOVA); Netherlands Organisation for Scientific Research (NWO); Science and Technology Facilities Council; Swiss Space Office; Swedish National Space Agency; and UK Space Agency. Astrochemistry at Leiden is supported by funding from the European Research Council (ERC) under the European Union's Horizon 2020 research and innovation programme (grant agreement No. 101019751 MOLDISK), the Netherlands Research School for Astronomy (NOVA), and the Danish National Research Foundation through the Center of Excellence "InterCat" (Grant agreement no.: DNRF150). We thank an anomymous reviewer for their constructive and insightful comments that we believe improved this paper.

4.A Appendix

4.A.1 Calibration procedure supplementary information

The thickness of a pure ice, d, can be calculated from its laser interference pattern during its deposition if its refractive index is known via the following equation:

$$d = \frac{m\lambda}{2\sqrt{n^2 - sin^2\theta}}, \tag{4.A.1}$$

where m is an integer number of constructive fringes, λ is the laser wavelength, n is the ice refractive index, and θ is the angle of incidence (45° on IRASIS). The ice thickness can be converted into an ice column density using a measured ice density value, ρ, allowing for the calculation of an ice deposition rate in units of column density per unit of time when the period of the laser interference oscillation is determined using a curve fitting procedure.

The refractive index and density values used to calibrate the deposition rates of our three ices of interest, H_2O, NH_3, H_2S, in our experiments are presented in Table 4.A.8.

Table 4.A.8: Refractive indexes and densities used for calibration.

Molecule	n	ρ (g cm^{-3})	Ref.
H_2O	1.234	0.719	Yarnall & Hudson 2022
NH_3	1.33	0.68	Hudson et al. 2022
H_2S	1.407	0.944	Yarnall & Hudson 2022

4.A.2 Beer's law plot errors

Errors of the integrated optical depths of the features used in the Beer's law plots are estimated by smoothing the integrated optical depth data throughout the entire warm-up in each individual experiment with a Savgol filter and then taking the standard deviation of five raw integrated optical depth data points collected at the end of the 120 K hold from the smoothed data (used here as expected values). This provides an individual error for each data point in the Beer's law plots.

Three sources of error contribute to the uncertainty of the ice column densities in the Beer's law plots. First, there is the experimental error caused by day-to-day fluctuations in the calibrated deposition rate, which we estimate to be 0.36% from our repeat measurements of the laser interference patterns during pure ice depositions (Section 4.2.1). Then there is the error caused by the uncertainty of laser incidence angle in our optical alignment that we estimate to be ±5°, resulting in an error of ∼4% in the ice thickness values calculated from the laser interference patterns. The largest source of uncertainty in the ice column density is the uncertainty associated with reaction completion, for which we use a conservative estimate of 8%. Propagating these errors results in a final error of 9% on the ice column densities.

4.A.3 Pure NH_4SH supplementary laboratory data

This appendix contains supplementary figures and tables of the laboratory data from the pure NH_4SH experiments.

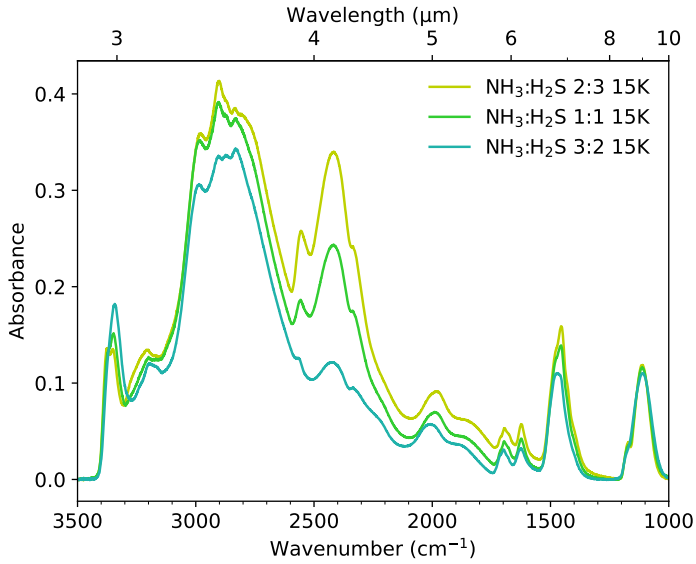


Figure 4.A.15: Spectra of NH_3:H_2S mixtures with various mixing ratios at 15 K. In all ices, the same quantity of NH_3 was deposited.

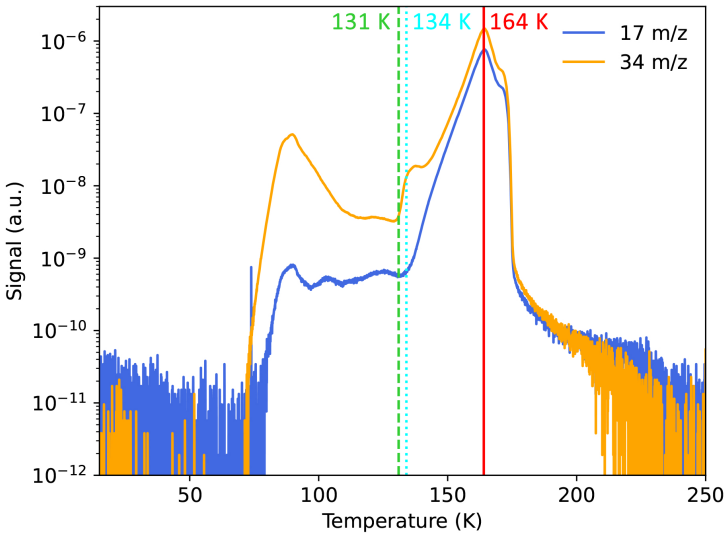


Figure 4.A.16: TPD curve of 17 m/z (NH_3^+) and 34 m/z (H_2S^+) from the NH_3:H_2S 1:1 mixture. The temperature at the maximum area of the NH_4^+ ν_4 mode (131 K) is marked with a green dashed line, the temperature when crystallization begins (134 K) is marked with a cyan dotted line, and the temperature of peak desorption (164 K) is marked with a red solid line.

Table 4.A.9: Vibrational mode assignments of the peaks observed in the IR spectra of pure NH_3 ice at 15 K, pure H_2S ice at 15 K, NH_3:H_2S ice at 15 K, NH_4SH ice at 120 K, and NH_4SH ice at 140 K.

Ice	Temp. (K)	Phase	Mode	Peak position ($cm^{-1}/\mu m$)
NH_3	15	Amorphous	ν_3 (asymm. stretch)	3375/2.963
			$2\nu_4$	3291/3.039
			ν_1 (symm. stretch)	3213/3.112
			ν_4 (sciss. bend)	1625/6.154
			ν_2 (umb. bend)	1074/9.311
H_2S	15	Amorphous	$\nu_1+\nu_2/\nu_2+\nu_3$	3702/2.701
			ν_1+T	2636/3.794
			ν_3 (asymm. stretch)	2251/4.442
			ν_1 (symm. stretch)	2525/3.960
			ν_2+R	1334/7.496
			ν_2 (bend)	1170/8.547
NH_3:H_2S 1:1	15	Amorphous	NH_3 ν_3	3348/2.987
			NH_3 ν_1/NH_4^+ $\nu_2+\nu_4$	3202/3.123
			NH_4^+ ν_3/NH_4^+ $2\nu_4$	2905/3.442
			H_2S $\nu_1+\nu_3$/SH^- str.	2559/3.908
			H_2S in NH_3/NH_4SH matrix?	2418/4.136
			NH_4^+ ν_2	1696/5.896
			NH_3 ν_4	1624/6.158
			NH_4^+ ν_4	1455/6.873
			H_2S ν_2	1177/8.496
			NH_3 ν_2	1112/8.993
NH_4SH	120 K	Amorphous	NH_4^+ $\nu_2+\nu_4$	3121/3.204
			NH_4^+ ν_3 (asymm. stretch)	2953/3.386
			NH_4^+ $2\nu_4$	2804/3.566
			SH^- str.	2553/3.917
			NH_4^+ ν_2+SH^- R?	2089/4.787
			NH_4^+ ν_4+SH^- R	1837/5.444
			NH_4^+ ν_2 (sciss. bend)	1651/6.057
			NH_4^+ ν_4 (umb. bend)	1448/6.906
			2 SH^- R	803/12.453
NH_4SH	140 K	Crystalline	NH_4^+ $\nu_2+\nu_4$	3115/3.210
			NH_4^+ ν_3 E_u	3017/3.315
			NH_4^+ ν_3 A_{2u}	2930/3.413
			NH_4^+ $2\nu_4$	2817/3.550
			SH^- str.	2570/3.891
			NH_4^+ ν_2+SH^- R?	2099/4.764
			NH_4^+ ν_4+SH^- R	1821/5.491
			NH_4^+ ν_4 E_u	1440/6.944
			NH_4^+ ν_4 A_{2u}	1423/7.027
			2 SH^- R	832/12.019

T = translation; R = libration

Table 4.A.10: Peak positions, FWHMs, and integrated band areas of the NH_4^+ ν_4 mode in NH_3:H_2S ices with various mixing ratios at temperatures ∼15-159 K. The uncertainties of the peak positions and FWHMs are 0.5 cm^{-1}. Reported band areas are provided relative to the maximum amorphous value recorded during the warm-up. The reported band areas at different temperatures should not be used to calculate relative band strengths, as the salt abundance in the laboratory ice varies during warm-up as the acid-base reaction proceeds, and the salt begins desorbing at temperatures >135 K.

NH_3:H_2S mixing ratio	T (K)	Peak (cm^{-1})	Peak (μm)	FWHM (cm^{-1})	FWHM (μm)	Rel. band area
1:1	15	1455.5	6.870	76.7	0.358	0.53
	34	1455.0	6.873	74.0	0.346	0.53
	56	1451.4	6.890	65.3	0.308	0.59
	77	1449.0	6.901	49.9	0.240	0.76
	99	1448.5	6.904	55.4	0.268	0.93
	120	1448.0	6.906	63.9	0.311	0.99
	132	1447.6	6.906	63.9	0.311	1
	138	1422.7	7.029	12.1	0.060	0.99
	156	1423.2	7.026	10.8	0.054	0.91
3:2	15	1463.5	6.833	78.8	0.366	0.80
	37	1459.1	6.853	77.4	0.359	0.81
	59	1455.3	6.872	70.1	0.328	0.87
	80	1453.6	6.880	66.8	0.314	0.96
	102	1452.9	6.883	66.8	0.315	1
	123	1452.4	6.885	67.0	0.317	0.99
	145	1451.4	6.890	65.8	0.313	0.97
	159	1420.8	7.038	11.6	0.057	0.85
2:3	15	1454.5	6.875	76.7	0.359	0.58
	34	1454.3	6.876	74.0	0.347	0.59
	56	1450.4	6.894	65.6	0.310	0.65
	77	1446.6	6.913	47.7	0.230	0.85
	99	1445.9	6.916	49.2	0.238	0.99
	120	1445.4	6.919	50.6	0.245	1
	142	1444.9	6.921	51.8	0.251	0.98
	152	1422.5	7.030	11.6	0.057	0.16

Table 4.A.11: Peak positions, FWHMs, and integrated band areas of the SH^- stretching mode in NH_3:H_2S 3:2 ice at temperatures 102-159 K. The uncertainties of the peak positions and FWHMs are 0.5 cm^{-1}. Reported band areas are provided relative to the SH^- band area at 102 K, the temperature when the band area of the NH_4^+ ν_4 mode reaches its maximum amorphous peak area in the NH_3:H_2S 3:2 ice mixture. The reported band areas at different temperatures should not be used to calculate relative band strengths, as the salt begins desorbing at temperatures >135 K.

T	Peak		FWHM		Rel. band area
(K)	(cm^{-1})	(μm)	(cm^{-1})	(μm)	
102	2557.9	3.910	24.8	0.038	1
123	2556.9	3.911	25.3	0.039	1.00
145	2557.4	3.910	24.1	0.037	0.88
159	2569.9	3.891	4.1	0.006	0.63

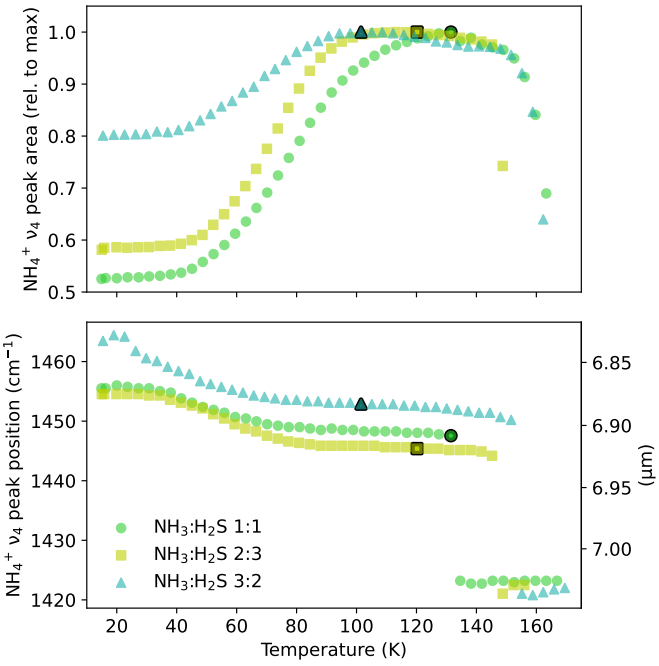


Figure 4.A.17: Areas (relative to the maximum peak area for each experiment) and positions of the NH_4^+ ν_4 mode during warm-up of the NH_3:H_2S ice mixtures. The points at the temperatures when the peak areas are at their maximum for each experiment are indicated with a black outline.

4.A.4 NH_4SH:H_2O supplementary laboratory data

This appendix contains supplementary data for the laboratory NH_4SH:H_2O ice mixture experiments.

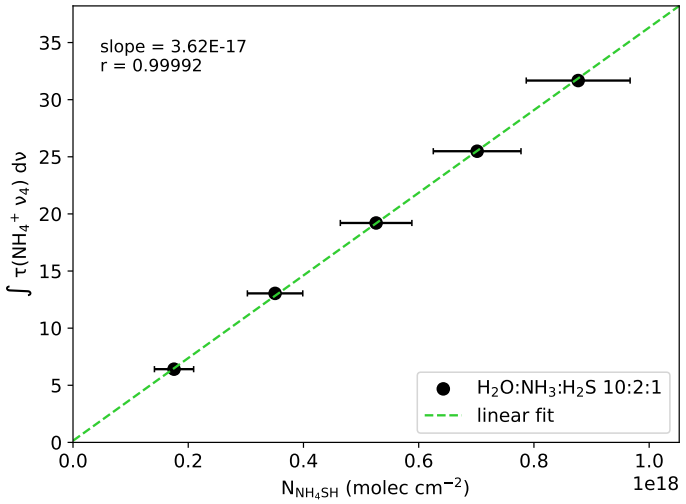


Figure 4.A.18: Beer's law plot used to derive the apparent band strength of the NH_4^+ ν_4 feature formed in the H_2O:NH_3:H_2S 10:2:1 mixture.

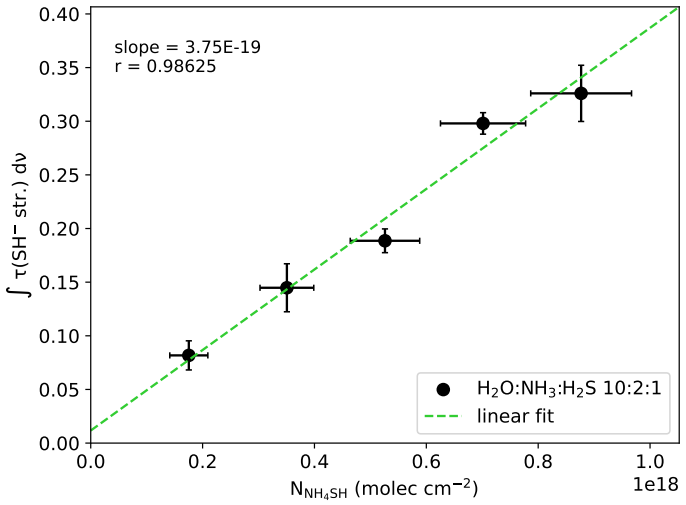


Figure 4.A.19: Beer's law plot used to derive the apparent band strength of the SH^- stretching feature formed in the H_2O:NH_3:H_2S 10:2:1 mixture.

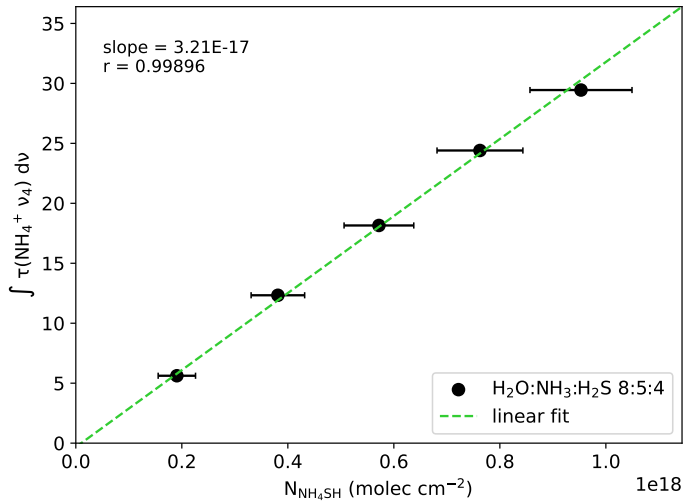


Figure 4.A.20: Beer's law plot used to derive the apparent band strength of the NH_4^+ ν_4 feature formed in the H_2O:NH_3:H_2S 8:5:4 mixture.

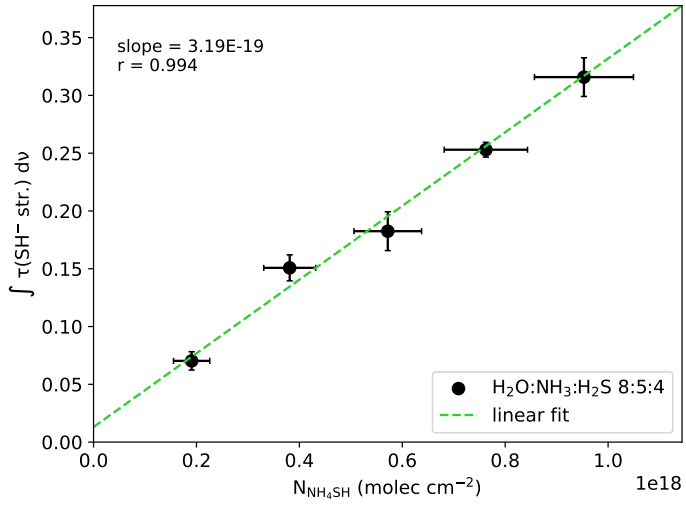


Figure 4.A.21: Beer's law plot used to derive the apparent band strength of the SH^- stretching feature formed in the H_2O:NH_3:H_2S 8:5:4 mixture.

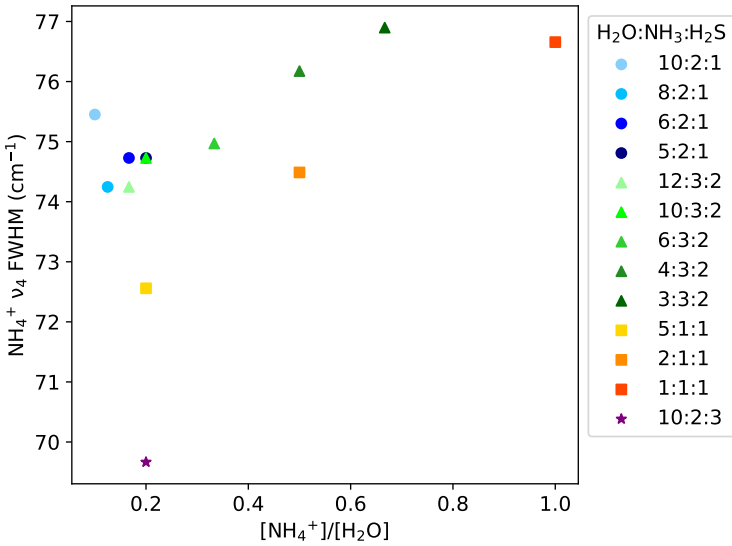


Figure 4.A.22: The FWHM of the NH_4^+ ν_4 mode at 135 K plotted as a function of the concentration of NH_4^+ with respect to H_2O (assuming 100% reaction completion) for various H_2O:NH_3:H_2S mixtures.

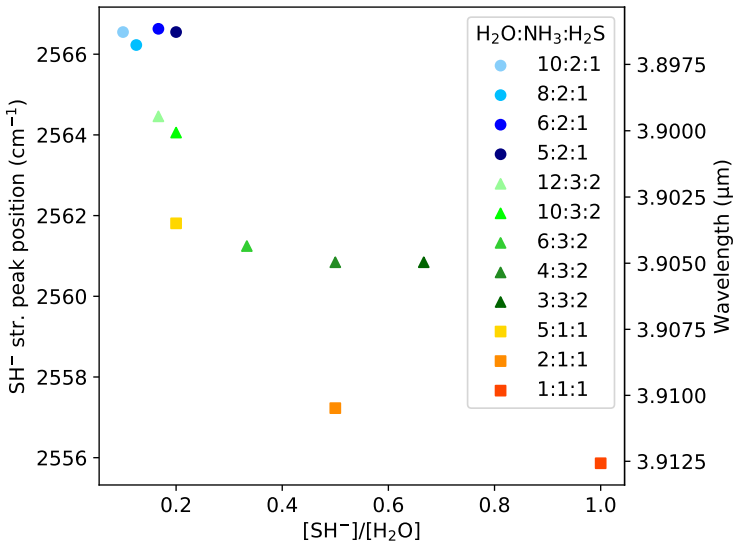


Figure 4.A.23: The peak position of the SH^- stretching mode at 135 K plotted as a function of the concentration of SH^- with respect to H_2O (assuming 100% reaction completion) for various H_2O:NH_3:H_2S mixtures.

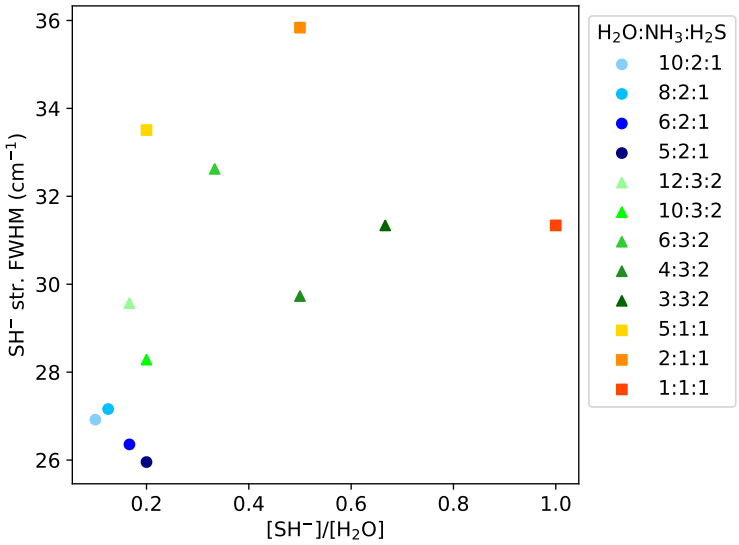


Figure 4.A.24: The FWHM of the SH^- stretching mode at 135 K plotted as a function of the concentration of SH^- with respect to H_2O (assuming 100% reaction completion) for various H_2O:NH_3:H_2S mixtures.

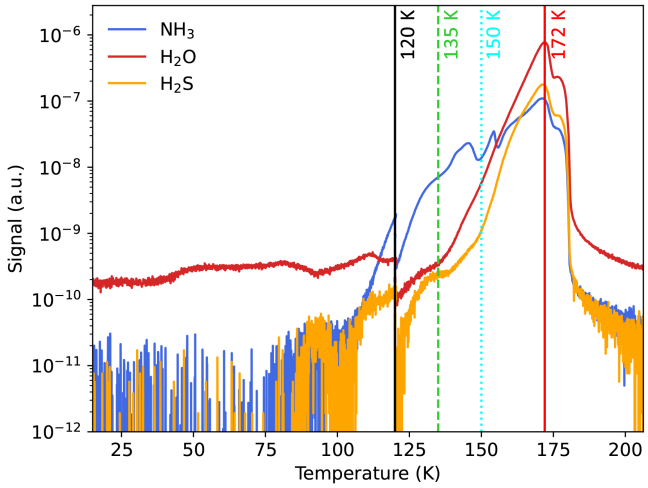


Figure 4.A.25: TPD curve of NH_3, H_2O, and H_2S from the H_2O:NH_3:H_2S 10:3:2 mixture. The temperature of the 40 min hold (120 K) is marked with a solid black line, the temperature at the maximum area of the NH_4^+ ν_4 mode (135 K) is marked with a green dashed line, the temperature when crystallization begins (150 K) is marked with a cyan dotted line, and the temperature of peak desorption is marked with a red solid line (172 K). The H_2S signal consists of the 34 m/z peak (H_2S^+). The NH_3 and H_2O signals are derived by deconvolving the 17 m/z (NH_3^+ and OH^+) and 18 m/z (H_2O^+ and $^{15}NH_3^+$) signals using systems of equations and scaling factors obtained from QMS data from pure depositions.

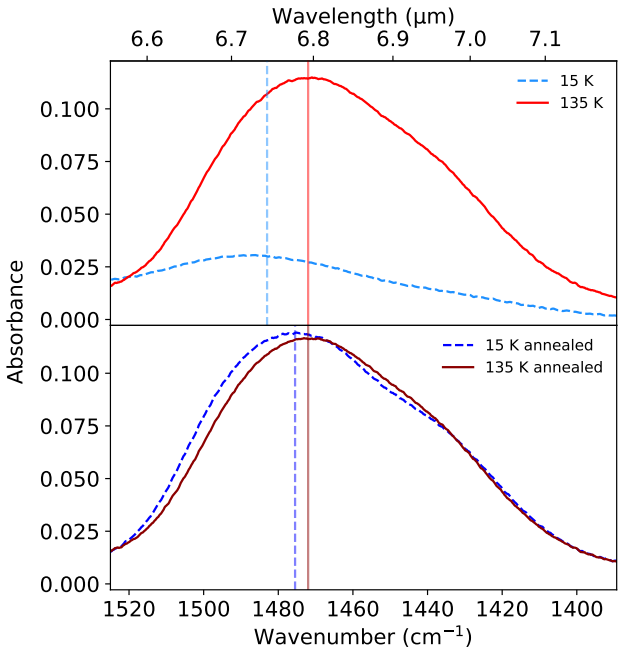


Figure 4.A.26: Comparison of the NH_4^+ ν_4 features in the spectra of the H_2O:NH_3:H_2S 10:3:2 ice mixtures before and after annealing. Top: NH_4^+ ν_4 mode after deposition at 15 K (light blue dashed trace) and after heating to 135 K (solid red trace). Bottom: NH_4^+ ν_4 mode after re-cooling from 135 K to 15 K (blue dashed trace) and after re-heating the annealed ice from 15 K to 135 K (solid dark red trace). Peak positions are marked with translucent vertical lines.

Table 4.A.12: Peak positions, FWHMs, and integrated band areas of the NH_4^+ ν_4 mode in H_2O:NH_3:H_2S ice with a mixing ratio of 8:5:4 at temperatures ∼15-170 K. The uncertainties of the peak positions and FWHMs are 0.5 cm^{-1}. Reported band areas are provided relative to the maximum amorphous value recorded during the warm-up. The reported band areas at different temperatures should not be used to calculate relative band strengths, as the salt abundance in the laboratory ice varies during warm-up as the acid-base reaction proceeds, and the salt begins desorbing at temperatures >135 K.

H_2O:NH_3:H_2S mixing ratio	T (K)	Peak (cm^{-1})	Peak (μm)	FWHM (cm^{-1})	FWHM (μm)	Rel. band area
8:5:4	15	1478.2	6.765	73.0	0.337	0.36
	33	1477.4	6.768	73.3	0.338	0.40
	55	1474.3	6.783	73.0	0.339	0.49
	76	1467.8	6.813	75.0	0.351	0.69
	98	1463.5	6.833	75.7	0.356	0.84
	120	1460.6	6.847	76.4	0.362	0.96
	135	1459.6	6.851	75.9	0.360	1
	156	1421.0	7.037	11.1	0.055	0.97
	174	1419.8	7.043	8.9	0.044	0.21

Table 4.A.13: Peak positions, FWHMs, and integrated band areas of the NH_4^+ ν_4 mode in H_2O:NH_3:H_2S ices with NH_3:H_2S mixing ratios of 2:1 at temperatures ∼15-170 K. The uncertainties of the peak positions and FWHMs are 0.5 cm^{-1}. Reported band areas are provided relative to the maximum amorphous value recorded during the warm-up. The reported band areas at different temperatures should not be used to calculate relative band strengths, as the salt abundance in the laboratory ice varies during warm-up as the acid-base reaction proceeds, and the salt begins desorbing at temperatures >135 K.

H_2O:NH_3:H_2S mixing ratio	T (K)	Peak (cm^{-1})	Peak (μm)	FWHM (cm^{-1})	FWHM (μm)	Rel. band area
10:2:1	15	1484.9	6.734	69.9	0.320	0.15
	34	1485.2	6.733	69.9	0.320	0.17
	56	1483.5	6.741	69.4	0.319	0.27
	77	1480.3	6.755	70.9	0.327	0.46
	99	1478.9	6.762	73.3	0.339	0.71
	120	1478.4	6.764	75.2	0.348	0.94
	133	1477.9	6.766	74.0	0.343	1
	144	1475.5	6.777	74.7	0.347	0.84
	154	1422.5	7.030	11.1	0.055	0.65
	176	1422.7	7.029	7.7	0.038	0.18
8:2:1	15	1484.4	6.737	71.4	0.327	0.21
	34	1484.7	6.735	68.9	0.315	0.22
	56	1483.2	6.742	67.5	0.310	0.30
	77	1480.1	6.756	71.1	0.328	0.51
	99	1478.2	6.765	74.5	0.345	0.74
	120	1477.0	6.771	75.7	0.351	0.92
	134	1477.2	6.770	74.2	0.344	1
	142	1474.1	6.784	75.5	0.351	0.89
	156	1422.5	7.030	11.1	0.055	0.65
	170	1422.7	7.029	9.2	0.045	0.22
6:2:1	15	1485.2	6.733	68.5	0.313	0.24
	34	1484.4	6.737	68.5	0.313	0.26
	56	1482.8	6.744	69.7	0.320	0.37
	77	1479.4	6.760	71.8	0.331	0.54
	99	1477.2	6.770	75.5	0.350	0.76
	120	1476.2	6.774	76.2	0.353	0.89
	135	1476.2	6.774	74.7	0.347	1
	142	1473.1	6.788	76.7	0.357	0.96
	156	1422.0	7.032	10.4	0.051	0.68
	170	1421.8	7.034	8.9	0.044	0.26
5:2:1	15	1484.4	6.737	68.5	0.313	0.25
	34	1483.7	6.740	68.7	0.315	0.28
	55	1482.0	6.748	70.1	0.322	0.38
	77	1478.4	6.764	72.6	0.335	0.55
	98	1475.8	6.776	75.7	0.351	0.73
	120	1475.0	6.779	76.7	0.356	0.85
	134	1474.8	6.781	74.7	0.347	0.91
	141	1471.9	9.794	76.4	0.356	1
	156	1421.5	7.035	10.6	0.052	0.73
	170	1421.3	7.036	8.9	0.044	0.33

Table 4.A.14: Peak positions, FWHMs, and integrated band areas of the NH_4^+ ν_4 mode in H_2O:NH_3:H_2S ices with NH_3:H_2S mixing ratios of 3:2 at temperatures ∼15-170 K (part 1). The uncertainties of the peak positions and FWHMs are 0.5 cm^{-1}. Reported band areas are provided relative to the maximum amorphous value recorded during the warm-up. The reported band areas at different temperatures should not be used to calculate relative band strengths, as the salt abundance in the laboratory ice varies during warm-up as the acid-base reaction proceeds, and the salt begins desorbing at temperatures >135 K.

H_2O:NH_3:H_2S mixing ratio	T (K)	Peak (cm^{-1})	Peak (μm)	FWHM (cm^{-1})	FWHM (μm)	Rel. band area
12:3:2	15	1483.2	6.742	69.9	0.321	0.17
	34	1483.0	6.743	72.1	0.331	0.20
	56	1482.0	6.748	69.4	0.319	0.28
	77	1477.4	6.768	72.6	0.336	0.47
	99	1475.5	6.777	74.2	0.345	0.68
	120	1473.6	6.786	75.5	0.351	0.88
	135	1472.9	6.789	74.2	0.346	0.99
	142	1471.2	6.797	74.7	0.349	0.95
	156	1422.7	7.029	11.1	0.055	0.63
	170	1422.7	7.029	8.7	0.043	0.30
10:3:2	15	1482.5	6.745	71.1	0.327	0.21
	34	1482.5	6.745	71.4	0.328	0.23
	56	1480.6	6.754	70.4	0.324	0.32
	77	1477.0	6.771	72.6	0.336	0.51
	99	1474.3	6.783	74.7	0.348	0.72
	120	1472.4	6.792	75.7	0.353	0.91
	136	1472.1	6.793	73.5	0.343	1
	154	1422.5	7.030	11.3	0.056	0.66
	172	1422.2	7.031	8.9	0.044	0.31
6:3:2	15	1482.0	6.748	69.9	0.321	0.27
	34	1481.1	6.752	68.9	0.317	0.28
	56	1478.7	6.763	70.6	0.326	0.38
	77	1473.8	6.785	73.5	0.341	0.55
	99	1470.2	6.802	75.2	0.351	0.70
	120	1468.5	6.810	76.7	0.359	0.83
	134	1468.0	6.812	75.0	0.351	0.90
	145	1465.4	6.824	75.0	0.352	0.96
	156	1421.5	7.035	11.1	0.055	0.77
	170	1420.3	7.041	8.9	0.044	0.47

Table 4.A.15: Peak positions, FWHMs, and integrated band areas of the NH_4^+ ν_4 mode in H_2O:NH_3:H_2S ices with NH_3:H_2S mixing ratios of 3:2 at temperatures ∼15-170 K (part 2). The uncertainties of the peak positions and FWHMs are 0.5 cm^{-1}. Reported band areas are provided relative to the maximum amorphous value recorded during the warm-up. The reported band areas at different temperatures should not be used to calculate relative band strengths, as the salt abundance in the laboratory ice varies during warm-up as the acid-base reaction proceeds, and the salt begins desorbing at temperatures >135 K.

H_2O:NH_3:H_2S mixing ratio	T (K)	Peak (cm^{-1})	Peak (μm)	FWHM (cm^{-1})	FWHM (μm)	Rel. band area
4:3:2	15	1478.7	6.763	71.1	0.327	0.41
	34	1478.7	6.763	71.8	0.330	0.44
	56	1476.5	6.773	71.8	0.332	0.52
	77	1471.4	6.796	75.0	0.349	0.69
	99	1467.1	6.816	76.4	0.358	0.83
	120	1465.4	6.824	77.4	0.363	0.92
	135	1465.2	6.825	76.2	0.358	0.97
	145	1463.2	6.834	75.9	0.358	1
	160	1421.0	7.037	10.1	0.050	0.98
	170	1419.8	7.043	8.4	0.042	0.60
3:3:2	15	1477.4	6.768	72.3	0.333	0.51
	33	1476.7	6.772	73.3	0.338	0.55
	54	1474.6	6.782	74.0	0.342	0.63
	76	1468.8	6.808	74.5	0.347	0.75
	97	1464.4	6.829	76.4	0.358	0.89
	119	1463.0	6.835	77.4	0.364	0.95
	140	1461.5	6.842	76.7	0.362	1
	158	1420.8	7.038	10.1	0.050	1.03
	169	1420.3	7.041	9.4	0.047	0.67

Table 4.A.16: Peak positions, FWHMs, and integrated band areas of the NH_4^+ ν_4 mode in H_2O:NH_3:H_2S ices with NH_3:H_2S mixing ratios of 1:1 at temperatures ∼15-170 K. The uncertainties of the peak positions and FWHMs are 0.5 cm^{-1}. Reported band areas are provided relative to the maximum amorphous value recorded during the warm-up. The reported band areas at different temperatures should not be used to calculate relative band strengths, as the salt abundance in the laboratory ice varies during warm-up as the acid-base reaction proceeds, and the salt begins desorbing at temperatures >135 K.

H_2O:NH_3:H_2S mixing ratio	T (K)	Peak (cm^{-1})	Peak (μm)	FWHM (cm^{-1})	FWHM (μm)	Rel. band area
5:1:1	15	1482.8	6.744	71.4	0.328	0.12
	34	1482.0	6.748	71.1	0.328	0.14
	56	1480.6	6.754	70.9	0.327	0.22
	77	1475.8	6.776	72.3	0.336	0.39
	99	1473.8	6.785	72.6	0.338	0.59
	120	1471.9	6.794	73.3	0.342	0.80
	131	1470.0	6.803	73.3	0.343	0.92
	142	1467.8	6.813	71.6	0.335	1
	160	1422.7	7.029	11.6	0.057	0.62
	170	1422.7	7.029	8.7	0.043	0.27
2:1:1	15	1478.9	6.762	72.6	0.335	0.27
	34	1478.4	6.764	72.1	0.333	0.29
	56	1475.5	6.777	72.8	0.337	0.39
	77	1470.0	6.803	73.5	0.343	0.57
	99	1465.2	6.825	74.5	0.350	0.75
	120	1462.3	6.839	74.7	0.353	0.89
	131	1460.6	6.847	74.7	0.353	0.96
	142	1458.9	6.855	74.2	0.352	1
	160	1421.5	7.035	11.6	0.057	0.97
	170	1420.6	7.039	9.6	0.048	0.70
1:1:1	15	1473.8	6.785	73.3	0.339	0.41
	34	1473.1	6.788	74.5	0.345	0.46
	56	1470.2	6.802	73.3	0.341	0.53
	77	1462.5	6.838	73.0	0.343	0.68
	99	1457.7	6.860	73.8	0.350	0.84
	120	1455.0	6.873	75.7	0.361	0.93
	135	1453.1	6.882	76.7	0.367	0.98
	145	1451.7	6.889	76.7	0.368	1
	160	1421.5	7.035	11.1	0.055	0.90
	170	1421.5	7.035	10.4	0.051	0.36

Table 4.A.17: Peak positions, FWHMs, and integrated band areas of the NH_4^+ ν_4 mode in H_2O:NH_3:H_2S ice with a mixing ratio of 10:2:3 at temperatures ∼15-170 K. The uncertainties of the peak positions and FWHMs are 0.5 cm^{-1}. Reported band areas are provided relative to the maximum amorphous value recorded during the warm-up. The reported band areas at different temperatures should not be used to calculate relative band strengths, as the salt abundance in the laboratory ice varies during warm-up as the acid-base reaction proceeds, and the salt begins desorbing at temperatures >135 K.

H_2O:NH_3:H_2S mixing ratio	T (K)	Peak (cm^{-1})	Peak (μm)	FWHM (cm^{-1})	FWHM (μm)	Rel. band area
10:2:3	15	1479.4	6.760	69.9	0.322	0.14
	34	1478.4	6.764	72.6	0.336	0.17
	56	1477.4	6.768	70.4	0.326	0.26
	77	1473.1	6.788	70.9	0.330	0.45
	99	1470.9	6.798	70.9	0.331	0.67
	120	1469.0	6.807	70.4	0.329	0.85
	135	1467.3	6.815	69.7	0.326	0.97
	142	1466.8	6.817	68.9	0.323	1
	160	1422.2	7.031	11.6	0.057	0.68
	170	1422.2	7.031	9.9	0.049	0.34

Table 4.A.18: Peak positions and FWHMs of the SH^- stretching mode in H_2O:NH_3:H_2S ices at 135 K. The uncertainties of the peak positions and FWHMs are 0.5 cm^{-1}.

H_2O:NH_3:H_2S mixing ratio	Peak (cm^{-1})	Peak (μm)	FWHM (cm^{-1})	FWHM (μm)
10:2:1	2565.7	3.898	22.4	0.034
8:2:1	2566.1	3.897	27.2	0.041
6:2:1	2566.5	3.896	26.2	0.040
5:2:1	2566.6	3.896	25.8	0.039
12:3:2	2564.2	3.900	29.3	0.045
10:3:2	2564.5	3.899	27.3	0.042
6:3:2	2561.2	3.904	32.2	0.049
4:3:2	2560.8	3.905	29.2	0.045
3:3:2	2559.8	3.907	31.1	0.047
8:5:4	2558.2	3.909	34.6	0.053
5:1:1	2561.3	3.904	32.3	0.049
2:1:1	2557.2	3.910	35.9	0.055
1:1:1	2555.9	3.913	30.4	0.047

4.A.5 Observational supplementary data

Continua

This appendix contains figures showing the local and global continua used to extract the observed features of interest for further analysis as well as fits to the anion features in B1-c, L1527, and W33A and the silicate and H_2O libration features in L1527.

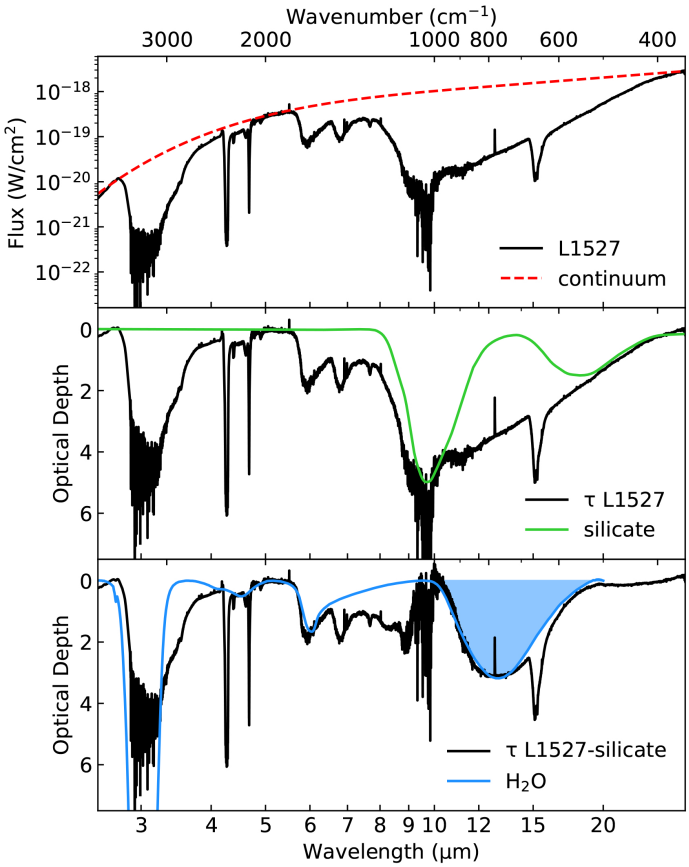


Figure 4.A.27: Fits used to extract the optical depth of the silicate feature and H_2O ice column density from the spectrum of L1527. The fitting procedure is analogous to that described in Boogert et al. (2008). Top: global continuum used to derive the spectrum of L1527 on the optical depth scale. Middle: subtraction of the silicate template spectrum GCS 3 (Kemper et al. 2004) from the spectrum of L1527 on the optical depth scale. Bottom: fit of a laboratory 15 K H_2O ice spectrum to the 12 μm H_2O libration mode in the silicate subtracted spectrum of L1527 on the optical depth scale.

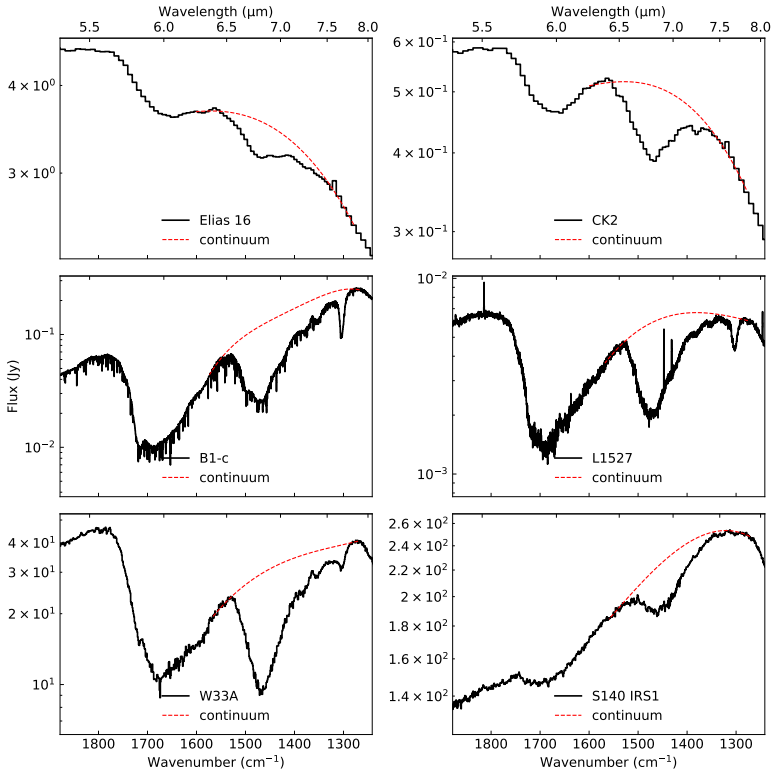


Figure 4.A.28: Local continua used to extract the 6.85 μm feature for fitting with laboratory data.

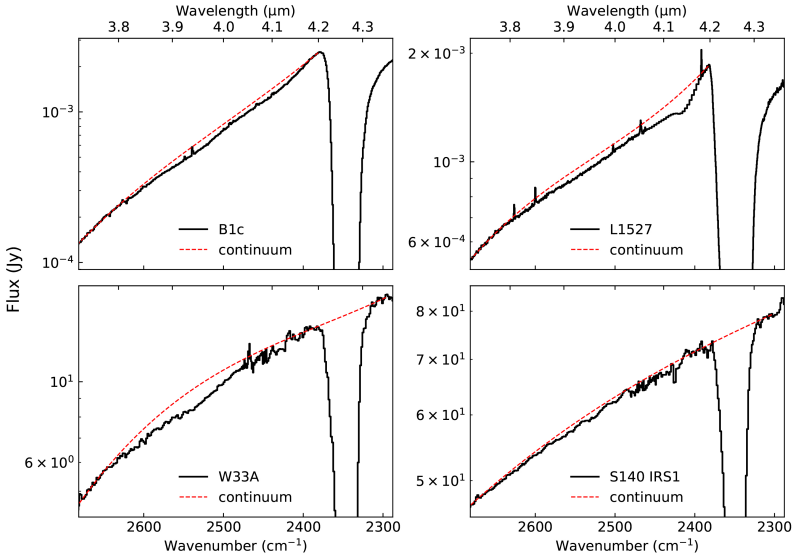


Figure 4.A.29: Local continua used to extract the 3.7-4.2 μm spectral region for fitting with laboratory data.

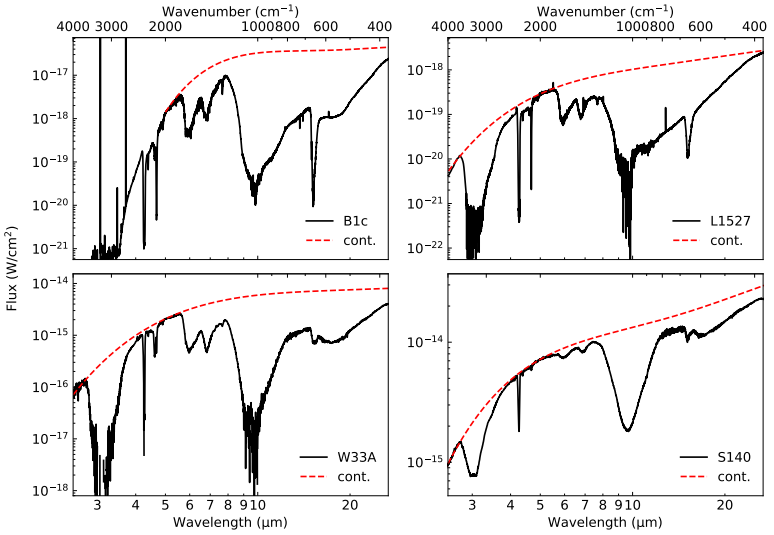


Figure 4.A.30: Global continua used to extract the 5.3 μm feature for fitting with laboratory data.

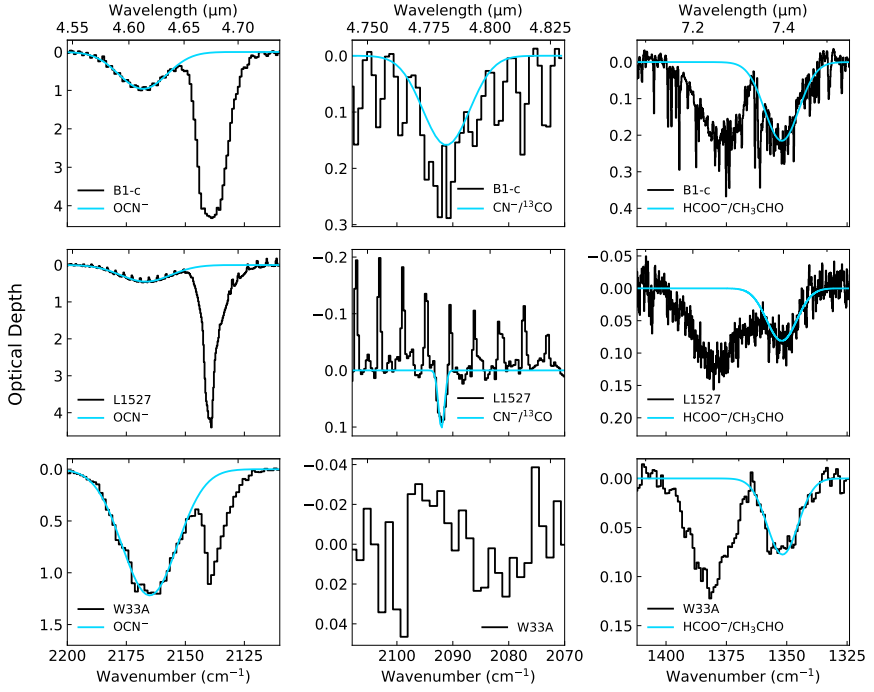


Figure 4.A.31: Gaussian fits used to estimate abundances and upper limits of the OCN^-, CN^-, and $HCOO^-$ anions toward three protostellar sources. The selected IR features of CN^- and $HCOO^-$ overlap with those of ^{13}CO and CH_3CHO, respectively, so their column densities resulting from these fits are only considered upper limits. No feature is detected in the $CN^-/^{13}CO$ spectral region in the W33A spectrum.

N_H from $\tau_{9.7}$

The hydrogen column densities of the investigated sources were estimated in all of the investigated sources except L1527 by Boogert et al. (2013) using the relation:

$$N_H = 3.08 \times 10^{22} \times A_K(cm^{-2}), \tag{4.A.2}$$

where A_K was estimated using the fitting parameters derived from the optical depths of the silicate features ($\tau_{9.7}$) and measured A_K values in the dense cores of Lupus:

$$\tau_{9.7} = 0.26 \times A_K. \tag{4.A.3}$$

Assuming that the relationships between $\tau_{9.7}$ and A_K in the clouds and protostellar envelopes investigated here are consistent with those observed in the dense cores of Lupus, an uncertainty of $\sim$30% applies to the derived N_H values (Boogert et al. 2013). Using fitting parameters derived from measurements of the diffuse medium would provide N_H values up to a factor of 2-4 lower (Bohlin et al. 1978; Boogert et al. 2013; Whittet 2018), resulting in total % S budgets that are a factor of 2-4 higher than our reported values, but the environments of the sources investigated here are more likely to be analogous to the dense clouds of Lupus rather than the diffuse medium.

4.B Bibliography

Altwegg, K., Balsiger, H., & Fuselier, S. A. 2019, ARA&A, 57, 113
Altwegg, K., Combi, M., Fuselier, S., et al. 2022, MNRAS, 516, 3900
Argyriou, I., Glasse, A., Law, D. R., et al. 2023, A&A, 675, A111
Asplund, M., Grevesse, N., Sauval, A. J., & Scott, P. 2009, ARA&A, 47, 481
Bergner, J. B., Öberg, K. I., Rajappan, M., & Fayolle, E. C. 2016, ApJ, 829, 85
Bockelée-Morvan, D., Lis, D., Wink, J., et al. 2000, A&A, 353, 1101
Bohlin, R. C., Savage, B. D., & Drake, J. 1978, ApJ, 224, 132
Böker, T., Arribas, S., Lützgendorf, N., et al. 2022, A&A, 661, A82
Boogert, A., Brewer, K., Brittain, A., & Emerson, K. 2022, ApJ, 941, 32
Boogert, A., Chiar, J., Knez, C., et al. 2013, ApJ, 777, 73
Boogert, A., Ehrenfreund, P., Gerakines, P. A., et al. 2000, A&A, 353, 349
Boogert, A., Huard, T., Cook, A., et al. 2011, ApJ, 729, 92
Boogert, A., Schutte, W., Helmich, F., Tielens, A., & Wooden, D. 1997, A&A, 317, 929
Boogert, A. A., Gerakines, P. A., & Whittet, D. C. 2015, ARA&A, 53, 541
Boogert, A. C., Pontoppidan, K. M., Knez, C., et al. 2008, ApJ, 678, 985
Bottinelli, S., Boogert, A. A., Bouwman, J., et al. 2010, ApJ, 718, 1100
Bouilloud, M., Fray, N., Bénilan, Y., et al. 2015, MNRAS, 451, 2145
Bragin, J., Diem, M., Guthals, D., & Chang, S. 1977, J. Chem. Phys., 67, 1247
Brown, P., Charnley, S., & Millar, T. 1988, MNRAS, 231, 409
Caselli, P. & Ceccarelli, C. 2012, A&AR, 20, 1
Chen, Y., Rocha, W. R. M., van Dishoeck, E. F., et al. 2024, A&A
Chen, Y.-J., Juang, K.-J., Nuevo, M., et al. 2014, ApJ, 798, 80
Dartois, E. & d'Hendecourt, L. 2001, A&A, 365, 144
Drozdovskaya, M. N., van Dishoeck, E. F., Rubin, M., Jørgensen, J. K., & Altwegg, K. 2019, MNRAS, 490, 50
Druard, C. & Wakelam, V. 2012, MNRAS, 426, 354
Ehrenfreund, P., Boogert, A., Gerakines, P., Tielens, A., & Van Dishoeck, E. 1997, A&A, 328, 649
Esteban, C., Peimbert, M., García-Rojas, J., et al. 2004, MNRAS, 355, 229
Ferraro, J. R., Sill, G., & Fink, U. 1980, Appl. Spectrosc., 34, 525
Furuya, K., Oba, Y., & Shimonishi, T. 2022, ApJ, 926, 171
Galvez, O., Maté, B., Herrero, V. J., & Escribano, R. 2010, ApJ, 724, 539
Gardner, J. P., Mather, J. C., Abbott, R., et al. 2023, PASP, 135, 068001
Garozzo, M., Fulvio, D., Kanuchova, Z., Palumbo, M., & Strazzulla, G. 2010, A&A, 509, A67
Garrod, R. T., Wakelam, V., & Herbst, E. 2007, A&A, 467, 1103
Gerakines, P., Moore, M., & Hudson, R. 2004, Icarus, 170, 202
Gerakines, P. A., Yarnall, Y. Y., & Hudson, R. L. 2024, Icarus, 116007
Gibb, E., Whittet, D., Boogert, A., & Tielens, A. 2004, ApJS, 151, 35
Goicoechea, J. R., Aguado, A., Cuadrado, S., et al. 2021, A&A, 647, A10
Grim, R., Greenberg, J., De Groot, M., et al. 1989a, A&AS, 78, 161
Grim, R. J., Greenberg, J. M., Schutte, W. A., & Schmitt, B. 1989b, ApJL, 341, L87
Henkel, C., Wilson, T., & Mauersberger, R. 1987, A&A, 182, 137
Hudson, R., Ferrante, R., & Moore, M. 2014, Icarus, 228, 276

Hudson, R., Gerakines, P., & Loeffler, M. 2015, PCCP, 17, 12545
Hudson, R. L. & Gerakines, P. A. 2018, ApJ, 867, 138
Hudson, R. L., Gerakines, P. A., & Yarnall, Y. Y. 2022, ApJ, 925, 156
Jakobsen, P., Ferruit, P., de Oliveira, C. A., et al. 2022, A&A, 661, A80
Jiménez-Escobar, A. & Caro, G. M. 2011, A&A, 536, A91
Jiménez-Escobar, A., Muñoz Caro, G., & Chen, Y.-J. 2014, MNRAS, 443, 343
Joseph, C. L., Snow Jr, T. P., Seab, C. G., & Crutcher, R. M. 1986, ApJ, 309, 771
Kama, M., Shorttle, O., Jermyn, A. S., et al. 2019, ApJ, 885, 114
Keane, J., Tielens, A., Boogert, A., Schutte, W., & Whittet, D. 2001, A&A, 376, 254
Keller, L., Hony, S., Bradley, J., et al. 2002, Nature, 417, 148
Kemper, F., Vriend, W., & Tielens, A. 2004, ApJ, 609, 826
Kerkhof, O., Schutte, W., & Ehrenfreund, P. 1999, A&A, 346, 990
Knacke, R., McCorkle, S., Puetter, R., Erickson, E., & Krätschmer, W. 1982, ApJ, 260, 141
Knez, C., Boogert, A. A., Pontoppidan, K. M., et al. 2005, ApJ, 635, L145
Kruczkiewicz, F., Vitorino, J., Congiu, E., Theulé, P., & Dulieu, F. 2021, A&A, 652, A29
Laas, J. C. & Caselli, P. 2019, A&A, 624, A108
Ligterink, N., Terwisscha van Scheltinga, J., Taquet, V., et al. 2018, MNRAS, 480, 3628
Lodders, K. 2003, ApJ, 591, 1220
Loeffler, M. J., Hudson, R. L., Chanover, N. J., & Simon, A. A. 2015, Icarus, 258, 181
Martín-Doménech, R., Jiménez-Serra, I., Caro, G. M., et al. 2016, A&A, 585, A112
Mastrapa, R., Sandford, S., Roush, T., Cruikshank, D., & Dalle Ore, C. 2009, ApJ, 701, 1347
Maté, B., Gálvez, O., Herrero, V., et al. 2009, ApJ, 703, L178
Mauersberger, R., Henkel, C., Wilson, T., & Walmsley, C. 1986, A&A, 162, 199
McClure, M. K., Rocha, W., Pontoppidan, K., et al. 2023, Nat. Astron., 7, 431
Noble, J. A., Theule, P., Borget, F., et al. 2013, MNRAS, 428, 3262
Oba, Y., Tomaru, T., Lamberts, T., Kouchi, A., & Watanabe, N. 2018, Nat. Astron., 2, 228
Öberg, K. I., Boogert, A. A., Pontoppidan, K. M., et al. 2008, ApJ, 678, 1032
Öberg, K. I., Boogert, A. A., Pontoppidan, K. M., et al. 2011, ApJ, 740, 109
Palumbo, M., Geballe, T., & Tielens, A. G. 1997, ApJ, 479, 839
Pauls, A., Wilson, T., Bieging, J., & Martin, R. 1983, A&A, 124, 23
Perrero, J., Beitia-Antero, L., Fuente, A., Ugliengo, P., & Rimola, A. 2024, MNRAS, 527, 10697
Pontoppidan, K. M. 2006, A&A, 453, L47
Rachid, M., Brunken, N., De Boe, D., et al. 2021, A&A, 653, A116
Raunier, S., Chiavassa, T., Marinelli, F., Allouche, A., & Aycard, J. 2003, Chem. Phys. Lett., 368, 594
Reach, W. T., Faied, D., Rho, J., et al. 2008, ApJ, 690, 683
Rocha, W., Rachid, M., Olsthoorn, B., et al. 2022, A&A, 668, A63
Rocha, W., van Dishoeck, E., Ressler, M., et al. 2024, A&A, 683, A124
Santos, J. C., Linnartz, H., & Chuang, K.-J. 2023, A&A, 678, A112
Schutte, W., Boogert, A., Tielens, A., et al. 1999, A&A, 343, 966
Schutte, W. & Khanna, R. 2003, A&A, 398, 1049
Sellgren, K., Brooke, T., Smith, R., & Geballe, T. 1995, ApJ, 449, L69
Slavicinska, K., Rachid, M. G., Rocha, W. R. M., et al. 2023, A&A, 677, A13
Slavicinska, K., van Dishoeck, E. F., Tychoniec, Ł., et al. 2024, A&A, 688, A29
Smith, R. G. 1991, MNRAS, 249, 172

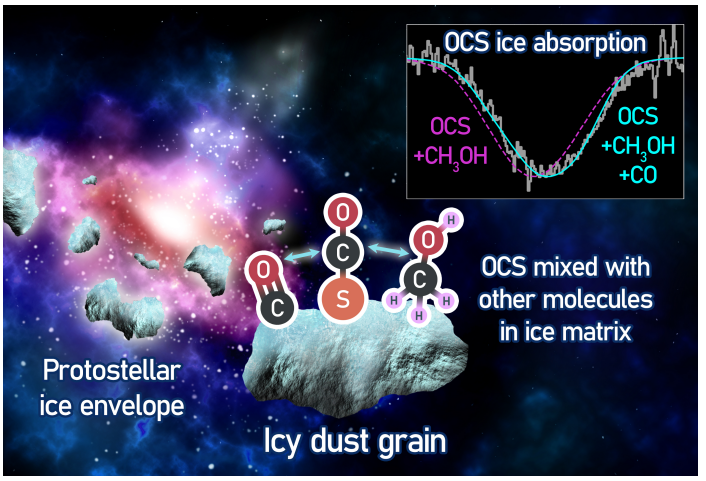
Tieftrunk, A., Pineau des Forets, G., Schilke, P., & Walmsley, C. 1994, A&A, 289, 579
Tielens, A. & Allamandola, L. 1987, Physical processes in interstellar clouds, 333
van Broekhuizen, F., Keane, J., & Schutte, W. 2004, A&A, 415, 425
van Broekhuizen, F. A., Pontoppidan, K., Fraser, H., & Van Dishoeck, E. 2005, A&A, 441, 249
Vastel, C., Phillips, T., Ceccarelli, C., & Pearson, J. 2003, ApJ, 593, L97
Vidal, T. H., Loison, J.-C., Jaziri, A. Y., et al. 2017, MNRAS, 469, 435
Vidal, T. H. & Wakelam, V. 2018, MNRAS, 474, 5575
Vitorino, J., Loison, J.-C., Wakelam, V., Congiu, E., & Dulieu, F. 2024, MNRAS, 533, 52
Walmsley, C. 1994, in AIP Conference Proceedings, American Institute of Physics, 463–475
Whittet, D. C. 2018, Dust in the galactic environment (CRC press)
Wilson, T., Mauersberger, R., Walmsley, C., & Batrla, W. 1983, A&A, 127, L19
Woods, P. M., Occhiogrosso, A., Viti, S., et al. 2015, MNRAS, 450, 1256
Wright, G. S., Rieke, G. H., Glasse, A., et al. 2023, PASP, 135, 048003
Yarnall, Y. Y. & Hudson, R. L. 2022, ApJL, 931, L4
York, D. 1966, Can. J. Phys., 44, 1079

5

Laboratory infrared spectra and band strengths of carbonyl sulfide (OCS) in CH_3OH- and CO-rich ice mixtures for analyzing interstellar ice observations

Katerina Slavicinska, Charlotte Coone, Bryce Benz, Harold Linnartz, A. C. Adwin Boogert, Ko-Ju Chuang

ACS Earth & Space Chemistry (2025), 9(8), 2148-2158



Abstract

Carbonyl sulfide (OCS) is currently the only securely detected sulfur-bearing species in interstellar ices, making it an ideal window into the solid-state sulfur chemistry in dense star-forming regions. Previous astronomical observations of the OCS asymmetric stretching mode (ν_3) at $\sim$2040 cm^{-1} ($\sim$4.9 μm) demonstrate that interstellar OCS may be embedded in CH_3OH-rich ices, indicating that OCS likely forms in the coldest, densest parts of star-forming regions where catastrophic CO freezeout occurs. However, a significant portion of OCS ice observations cannot be fit with binary OCS:CH_3OH laboratory ice mixtures alone, suggesting a greater degree of chemical complexity in the local ice environment. With this work, we aim to aid future studies of the abundance, physicochemical environment, and evolutionary history of interstellar OCS ice, now enabled for many more interstellar environments by the *James Webb* Space Telescope. We provide a library of new laboratory IR transmission spectra of OCS in CH_3OH- and CO-rich ice mixtures, some of which also include H_2S and H_2O. Of these new spectra, the tertiary OCS:CO:CH_3OH ice mixtures provide the best fits to observations of high-mass protostars, providing further support for the hypothesis that OCS forms with CH_3OH, possibly via chemical pathways involving frozen-out CO. We calculate apparent band strengths of the OCS ν_3 mode in OCS:CH_3OH and OCS:CO:CH_3OH ice mixtures. The derived values are consistent (within uncertainties) with the apparent band strength of the feature in pure OCS ice, 1.2×10^{-16} cm molec^{-1}. We therefore recommend using this value when quantifying interstellar OCS ice column densities.

5.1 Introduction

In the past two decades, sulfur-bearing ices have been a major focus of astrochemical research due to the observed gas-phase sulfur depletion in dense star-forming regions (Jiménez-Escobar & Muñoz Caro 2011; Chen et al. 2014; Hudson & Gerakines 2018; Vidal & Wakelam 2018; Laas & Caselli 2019). However, of the many sulfur-bearing molecules proposed by such

works to exist in interstellar ices, carbonyl sulfide (OCS) remains the only secure detection despite its low abundance (∼0.05-0.5% with respect to H_2O, Boogert et al. 2022; McClure et al. 2023). This is due to the high band strength (on the order of 10^{-16} cm molec^{-1}, Yarnall & Hudson 2022) and the relatively isolated peak position (4.9 μm) of its strongest IR vibrational feature, the asymmetric stretching mode (ν_3). These spectral properties aided its early first detection (Geballe et al. 1985) and subsequent identification as OCS (Palumbo et al. 1995) in ground-based IR spectra of the ice envelope surrounding the massive protostar W33A. Since then, OCS has been detected toward the ice envelopes of over 20 massive protostars (Palumbo et al. 1997; Gibb et al. 2004; Boogert et al. 2022; Tyagi et al. 2025), as well as the ice envelope of one low-mass protostar (Aikawa et al. 2012) and two background stars behind a dense molecular cloud (McClure et al. 2023).

Although OCS is decidedly not a major sulfur carrier in dense star-forming regions, its strong ν_3 absorption feature offers a unique window into the solid-state sulfur chemistry of such environments. Experiments presented in Palumbo et al. 1995 demonstrated that the profile of this band is highly dependent on the chemical composition of the surrounding ice matrix, and out of all the laboratory ice mixtures compared to the observations, the ices rich in CH_3OH provided the best fit to many of the observed absorptions (Palumbo et al. 1997; Boogert et al. 2022). Additionally, in a survey of 23 massive protostars, Boogert et al. 2022 found that OCS ice column densities correlate well with the ice column densities of CH_3OH, OCN^-, and the polar CO component, while they correlate poorly with the ice column densities of H_2O and the apolar CO component. A correlation between OCS and CH_3OH column densities (i.e., small scatter in the OCS/CH_3OH ratio) is also observed toward massive protostars in the gas phase (Santos et al. 2024b). These results indicate that most OCS ice likely formed alongside CH_3OH after the heavy CO freezeout stage, in the densest regions of the clouds and envelopes, possibly via routes such as the sulfurization of CO (Shingledecker et al. 2020) or the addition of SH radicals to CO (Santos et al. 2024a).

Despite these indications that interstellar OCS ice may be embedded in a CH_3OH-rich environment, the band strength of the OCS ν_3 feature in CH_3OH-rich ices has not been measured. So far, most currently reported interstellar OCS ice column densities (Palumbo et al. 1997; Boogert et al. 2022) were calculated using an OCS ν_3 band strength of 1.5×10^{-16} cm molec^{-1}, derived for pure OCS ice using a refractive index measured for liquid OCS and a simply assumed ice density of 1 g cm^{-3} (Hudgins et al. 1993). Recently, Yarnall & Hudson 2022 published an improved OCS ν_3 band strength of 1.2×10^{-16} cm molec^{-1} for both pure OCS ice and OCS in a 1:20 binary mixture with H_2O ice using new refractive index and density values that were measured directly for amorphous OCS ice. Nevertheless, existing OCS observations indicate that neither pure nor H_2O-dominated OCS ices are relevant to the interstellar medium.

Furthermore, the large sample of OCS ice observations in Boogert et al. 2022 revealed that in a significant portion of the investigated sources, the observed OCS ν_3 peak position is slightly redshifted (by up to ∼0.01 μm) relative to the peak positions of OCS in binary laboratory ice mixtures with CH_3OH. In contrast, comparably redshifted peak positions of the OCS feature are observed in laboratory spectra of CO- and H_2S-containing ices that were irradiated and then heated (Ferrante et al. 2008; Garozzo et al. 2010). Thus, the observed redshifts may indicate a higher degree of chemical complexity in the ice matrix in which OCS is embedded and could be interpreted as tentative, indirect evidence for OCS formation via energetic processing of other sulfur-bearing ices. However, a lack of publicly available laboratory IR

spectra of OCS in more chemically complex ice matrices with carefully controlled ice mixing ratios precludes drawing more specific conclusions about the chemical environment of OCS toward these sources with redshifted OCS features.

The present work aims to fill several gaps in experimental OCS ice studies. First, we present the transmission IR spectrum from 4000-500 cm^{-1} (2.5-20 μm) of both amorphous and crystalline OCS ice and calculate the band strengths of all of its fundamental vibrational modes using the most recently measured refractive index and density of amorphous OCS ice (Yarnall & Hudson 2022). Then, we aim to aid deeper investigations into the chemical environment of interstellar OCS ice molecules by providing laboratory IR spectra of OCS in more chemically complex, tertiary ice mixtures with a focus on mixtures rich in CH_3OH and CO, given their aforementioned plausible physicochemical links to OCS, and because interstellar CH_3OH ice is thought to form primarily via CO hydrogenation after catastrophic CO freezeout (Watanabe & Kouchi 2002; Fuchs et al. 2009), so it is expected and observationally supported (Cuppen et al. 2011; Penteado et al. 2015) that CO and CH_3OH will be mixed in interstellar ices to some degree. Some of the investigated mixtures also include H_2S, a suggested chemical precursor of OCS (Ferrante et al. 2008; Santos et al. 2024a), and H_2O, the most abundant observable interstellar ice (Boogert et al. 2015). We also provide updated IR spectra of binary OCS ice mixtures using modern ice co-deposition methodologies that result in more accurate and controlled ice mixing ratios (Yarnall & Hudson 2022). We report the peak positions, FWHMs, and relative integrated absorbances of the OCS ν_3 modes observed in these mixtures at temperatures spanning from 15-100 K to facilitate future analyses of astronomically observed OCS ice profiles. The spectral data are made publicly available on the Leiden Ice Database (LIDA, Rocha et al. 2022). Finally, we compare our updated database of OCS ice data to previous OCS ice observations to determine which of our mixtures are most likely to be analogous to the chemical environment of OCS in interstellar ices and calculate the apparent band strengths of the OCS ν_3 mode in these mixtures. This set of experimental data can be used by the community to improve the understanding of the abundance, physicochemical environment, and evolutionary history of interstellar OCS ice in an era of copious new ice observations in environments like cold dark clouds, the faintest and youngest low-mass protostars, and extragalactic star-forming regions that have been enabled by the recently launched *James Webb* Space Telescope.

5.2 Methods

5.2.1 Experimental setup

All of the data presented in this work were collected using the Infrared Absorption Setup for Ice Spectroscopy (IRASIS) at the Leiden Laboratory for Astrophysics. A schematic of the setup is presented by Rachid et al. 2021, and subsequent upgrades are described by Slavicinska et al. 2023. To briefly summarize, the setup consists of an ultrahigh vacuum chamber (ultimate pressure $<1\times10^{-9}$ mbar) containing a KBr substrate that can be cooled down to 15 K with a closed-cycle He cryostat. Three independent dosing lines with independent gas reservoirs, leak valves, and chamber inlets located at the bottom of the chamber enable background vapor deposition of ices on the cryo-cooled substrate. The deposition of these ices can be monitored on both sides of the substrate via laser interferometry with two 633 nm HeNe

laser beams positioned at 45° relative to the substrate normal, as well as via transmission IR spectroscopy with an FTIR beam positioned at 0° relative to the substrate normal. Ices are typically deposited to thicknesses on the order of hundreds to thousands of monolayers (depending on what thickness is needed to achieve satisfactory S/N of the ice feature of interest). The sample temperature can be kept constant or changed at a set rate via proportional-integral-derivative control. Gaseous species present in the chamber during deposition or warm-up are monitored with a quadrupole mass spectrometer (QMS).

In the experiments presented in this work, deposition pressures ranged from the order of 10^{-8} mbar in the case of the pure OCS ices to the order of 10^{-6} mbar in the case of the most diluted OCS ice mixtures. Deposition timescales ranged from ∼20-50 min. The IR spectra presented in this work were collected from 4000-500 cm^{-1} (2.5-20 μm) with a spectral resolution of 0.5 cm^{-1}. Each spectrum consists of 128 averaged scans collected over a period of ∼3.5 min. During the warm-ups, the substrate was heated at a rate of 25 K h^{-1}, resulting in ∼1.5 K intervals between the spectra collected during warm-up.

The liquids and gases used in this work include carbonyl sulfide (Linde Gas, ≥99.9%), methanol (Sigma Aldrich, ≥99.9%), carbon monoxide (Linde Gas, ≥99.997%), water (Milli-Q, Type I), and hydrogen sulfide (Linde Gas, ≥99.5%).

5.2.2 Mixing ratio calibration

This work uses similar methods to those described by Yarnall & Hudson 2022 and Slavicinska et al. 2023 to create binary and tertiary ice mixtures with specific ice component ratios. The position of each leak valve is independently calibrated to output the desired deposition rate of each ice component. This is achieved by first depositing each species of interest in pure form at 15 K and simultaneously monitoring the laser interference pattern and the QMS signal of a selected mass peak of the species of interest throughout the deposition. The period of the laser interference pattern T during deposition can be converted to an ice column density growth rate dN/dt via the following equation:

$$\frac{dN}{dt} = \frac{\lambda}{2\sqrt{n^2 sin^2\theta}} \times \frac{\rho N_A}{MT} \tag{5.1}$$

where λ is the wavelength of the laser, n is the ice refractive index, θ is the laser angle of incidence, ρ is the ice density, N_A is Avogadro's number, and M is the ice molar mass. The literature n and ρ values used to obtain the ice column density growth rates of the species investigated in this work are presented in Table 5.1. The total errors on these growth rates stem from the uncertainties of the literature n and ρ values used, estimated here to be on the order of ∼5 and 15%, respectively, based on typical variations seen in these values between measurements made in different laboratories and with different setup configurations (Bouilloud et al. 2015; Loeffler et al. 2016; Luna et al. 2022). The variations in ice densities measured in different laboratories are often primarily due to different deposition methods resulting in different ice porosities in the case of amorphous ices (Loeffler et al. 2016), where background deposition (the method employed in this work) typically produces more porous ice than directional deposition (the method employed by, e.g., Yarnall & Hudson 2022), although the magnitude of variation depends on the particular species. Additionally, there is a ±5° uncertainty of the laser angle of incidence, which corresponds to an error of ∼4% in the ice growth rates. This propagates to a total uncertainty on the ice growth rate of 16%.

Table 5.1: Literature ice refractive index and density values of pure ices used to calculate ice column density growth rates in this work.

Species	n	ρ (g cm^{-3})	ref.
OCS	1.436	1.248	36
CH_3OH	1.257	0.636	20
CO	1.297	0.870	19
H_2O	1.234	0.719	36
H_2S	1.407	0.944	36

A calibration curve is then generated by repeating a pure ice deposition with at least five different growth rates and finding the best-fit correlation between the calculated ice column density growth rates and the average QMS signal of a selected mass peak throughout the deposition. For all of the investigated molecules, the correlation was well fit using a linear equation, with R^2 values ranging from 0.995-0.9998. Each leak valve can then be calibrated to a desired deposition rate of a specific species by filling the gas reservoir connected to that leak valve with a specific pressure of the gas or vapor of the species and then adjusting the leak valve until the QMS signal that corresponds to the desired ice column density growth rate in the calibration curve is reached. The exact deposition rate is ascertained by performing multiple laser interference control measurements of pure ice deposition rates using the calibrated leak valve position. Five of such measurements typically have a standard deviation of 0.3-3%, and their average varies by 2-5% from the desired growth rate used to calculate the corresponding QMS signal on the calibration curve. However, these experimental errors are negligible when compared to the uncertainty on the calculated ice growth rate caused by the estimated uncertainty of the literature ρ value.

After this calibration is complete for all of the desired ice components, an ice mixture with specific component ratios can be deposited. First, each gas reservoir is filled with the same pressure of the pure gas or vapor used during the leak valve calibration. During this step, deposition of the gases or vapors into the chamber via the opened leak valves is prevented via shut valves preceding the leak valves. Once all of the gas reservoirs have been filled, all of the shut valves are opened to begin simultaneous deposition. As mentioned by Yarnall & Hudson 2022, this method assumes that the ice column density growth rates during co-deposition remain the same as during the deposition of each component individually.

5.2.3 Apparent band strengths

For pure OCS ice, apparent band strengths were calculated by depositing six pure OCS ices at five different deposition rates (one deposition rate was repeated to check for consistency), with rates ranging from ∼0.2-2 μm h^{-1}. Throughout each deposition, transmission IR spectra of the growing ice sample were continuously collected. The changes in the integrated optical depths of the OCS features of interest over time $d\int \tau\, d\nu/dt$ were determined by finding the best linear fits to the integrated optical depths over time. High R^2 values of these fits in the case of the ν_3 feature (≥0.9996) indicate very uniform ice growth rates throughout all of the

depositions. The corresponding ice column density growth rate for each of these measurements was then determined using Equation 5.1 to convert the period of the laser interference pattern generated during each deposition to dN/dt.

The best linear fits to the six independent $d\int\tau\,d\nu/dt$ versus dN/dt measurements, plotted in time-derivative Beer's law plots, were then determined via the York method for fitting data with errors on both X and Y variables (York 1966). The slopes of these fits are reported as the apparent band strengths, A', of the pure OCS bands. Using the time derivatives of the ice column densities and integrated optical depths rather than the absolute values of these variables ensures that any residues from previous experiments present on the substrate do not contribute to the calculated ice column densities. It also eliminates errors caused by human imprecision in stopping deposition at a specific time or ice thickness. The error of the slope calculated by the York method yields A' uncertainties $\sim$10%, with the dominant source of uncertainty being the uncertainty of the ρ value used in Equation 5.1.

For OCS ice mixtures, apparent band strengths were only determined for the ν_3 mode, and they were calculated via a different method than the pure apparent band strengths, as the ice column density growth rates could not be determined from the laser intereference patterns since the n and ρ values of the ice mixtures are not known. Instead, the leak valve used to deposit OCS was calibrated to correspond to a specific OCS ice growth rate, and five pure OCS ice depositions were performed using this leak valve position. The same leak valve position was then used to dose OCS during the deposition of the ice mixture of interest. The apparent band strength of the OCS feature in each mixture was subsequently calculated using the equation:

$$A'_{mix} = A'_{pure} \times \frac{d\int\tau_{mix}\,d\nu/dt}{d\int\tau_{pure,avg}\,d\nu/dt} \tag{5.2}$$

where $d\int\tau_{mix}\,d\nu/dt$ is the change in integrated optical depth of the OCS ν_3 feature during the deposition of each mixture of interest, $d\int\tau_{pure,avg}\,d\nu/dt$ is the average change in integrated optical depth of the OCS ν_3 feature during the five pure OCS depositions (standard deviation = 0.8%), and A'_{pure} is the apparent band strength of the ν_3 mode of pure OCS.

5.3 Results

5.3.1 Pure OCS ice

The IR spectrum of pure OCS ice in both amorphous and crystalline forms is presented in Figure 5.1. The ν_3 (asymmetric stretching) mode around 5 μm is by far the strongest feature. Its profile in both the amorphous and crystalline forms is highly asymmetric and distinctly broad, which has been suggested to be caused by the isotopic shifts of and disruption of molecular coupling in the matrix by $OC^{33}S$ and $OC^{34}S$ (Verderame & Nixon 1966). The other fundamental features, the ν_1 (symmetric stretching) and ν_2 (bending) modes, are significantly weaker than the ν_3 mode in both the amorphous and crystalline ices. Several very weak combination and overtone bands are also present in the investigated spectral range. The peak positions of all of the assigned modes are provided in Table 5.2. A small peak at 2340 cm^{-1}, assigned to CO_2, indicates a minor degree of atmospheric contamination. Using the band strength of the asymmetric stretching mode of pure amorphous CO_2 (Gerakines & Hudson

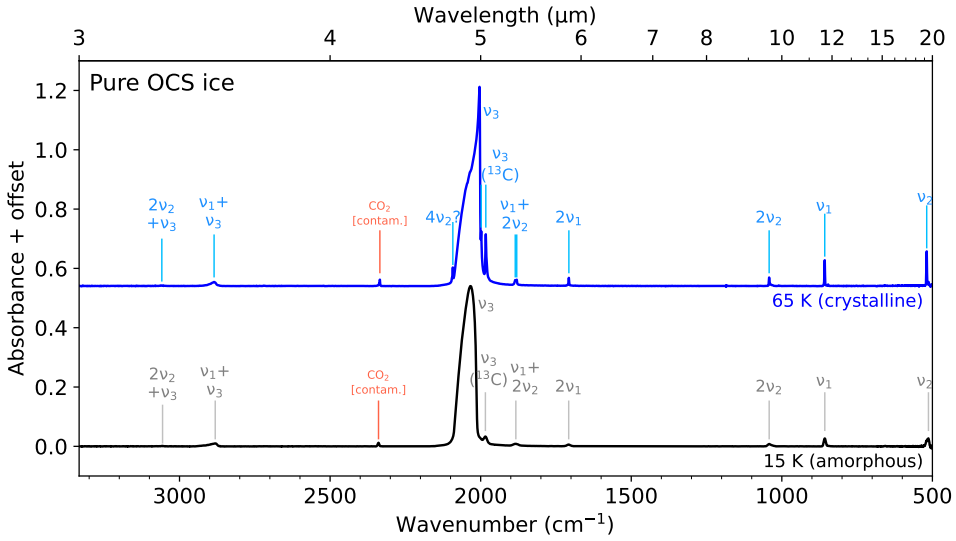


Figure 5.1: Infrared spectra of amorphous (black trace) and crystalline (blue trace) pure OCS ice measured at 15 and 65 K, respectively. Both ices were deposited at 15 K; the crystalline ice was heated from 15 K to 65 K at a rate of 25 K hr^{-1}. Assignments to the absorption features are labeled, and peak positions of these features are provided in Table 5.2. A small feature ∼2340 cm^{-1} assigned to CO_2 ice indicates minor atmospheric contamination.

Table 5.2: Positions and assignments of IR absorption features in pure OCS ice spectra measured at 15 K (amorphous) and 65 K (crystalline).

Assignment[a]	Peak position 15 K		Peak position 65 K	
	(cm^{-1})	(μm)	(cm^{-1})	(μm)
$2\nu_2$+ν_3	3056.3	3.272	3058.7	3.269
ν_1+ν_3	2881.4	3.471	2885.2	3.466
CO_2 contam.	2339.2	4.275	2334.7	4.283
$4\nu_2$?	-	-	2092.4	4.779
ν_3 (asymm. str.)	2033.7	4.917	2003.7	4.991
ν_3 ^{18}OCS	-	-	1998.1	5.005
ν_3 O^{13}CS	1984.3	5.040	1982.9	5.043
ν_1+$2\nu_2$[b]	1883.2	5.310	1885.2 1880.2	5.304 5.319
$2\nu_1$	1707.7	5.856	1707.1	5.858
$2\nu_2$	1042.0	9.597	1042.1	9.596
ν_1 (symm. str.)	857.3	11.665	857.5	11.662
ν_2 (bend)	513.1	19.489	518.9	19.272

[a] Based on assignments from Verderame & Nixon (1966).
[b] Feature is split in crystalline spectrum.

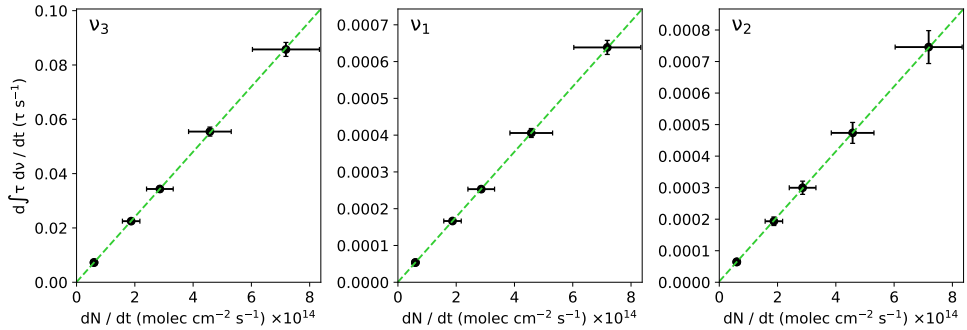


Figure 5.2: Time-derivative Beer's Law plots used to derive the apparent band strengths of the fundamental IR modes of amorphous OCS ice at 15 K. The black points denote the experimental data, with each point representing an individual ice deposition with a given deposition rate in units of column density growth per second, and the dashed green lines denote the best linear fit to the data calculated using the York method.

2015), this contamination is estimated to be on the order of ∼0.2% with respect to OCS. A table containing the peak position, FWHM, and relative integrated absorbance of the ν_3 mode in pure OCS ice throughout its warm-up from 15 to 83 K is provided in the Supporting Information.

The apparent band strengths A' of the three fundamental OCS modes in pure amorphous OCS ice at 15 K were calculated using the method outlined in the Methods section. The resulting A' values are presented in Table 5.3, and the time-derivative Beer's Law plots used to calculate these values are shown in Figure 5.2. Our A' value for the ν_3 mode, 1.20×10^{-16} cm molec^{-1}, is exactly consistent with that reported for pure amorphous OCS ice at 10 K by Yarnall & Hudson 2022. However, we note that our chosen integration range for this peak differs from that listed in Table 2 in Yarnall & Hudson 2022, 2154-2070 cm^{-1}, because their range excludes a majority of the absorption of this feature, leading us to conclude it likely includes a typo.

Our measured A' values of the OCS ν_1 and ν_2 modes are both over two orders of magnitude lower than that of the ν_3 mode. Given such low A' values in combination with the relatively low abundance of OCS in interstellar ices as determined from the ν_3 mode, we conclude that these bands are not likely to be practical in future observational studies and therefore exclude them from the analysis of the OCS ice mixtures.

5.3.2 OCS ice mixtures

The profiles of the OCS ν_3 features at select temperatures in all of the ice mixtures investigated in this work are presented in Figure 5.3. In Figure 5.4, the extracted peak positions and FWHMs of the OCS ν_3 features from these experiments are overplotted with the peak positions and FWHMs extracted from Gaussian fits to the 4.9 μm feature observed toward massive protostars (or massive young stellar objects; MYSOs) by Boogert et al. 2022. (The binary OCS:CO mixtures and the OCS:CO:H_2S 1:20:1 mixtures are excluded from this fig-

Table 5.3: Band strengths of the fundamental vibrational modes of OCS ice, both pure and in mixtures with CH_3OH and CO in the case of the ν_3 mode, at 15 K.

Feature	Ice	Ratio	Peak position (cm^{-1})	Peak position (μm)	A' (cm $molec^{-1}$)	Integration range (cm^{-1})
ν_3	OCS	-	2033.7	4.917	$1.20(\pm0.12)\times10^{-16}$	2197-1909
	$OCS:CH_3OH$	1:20	2041.5	4.898	$1.21(\pm0.13)\times10^{-16}$	2106-1999
	$OCS:CH_3OH$	1:40	2041.5	4.898	$1.18(\pm0.13)\times10^{-16}$	2106-1999
	$OCS:CO:CH_3OH$	1:20:20	2040.8	4.900	$1.19(\pm0.13)\times10^{-16}$	2078-1999
	$OCS:CO:CH_3OH$	1:40:20	2041.3	4.899	$1.20(\pm0.13)\times10^{-16}$	2078-1999
	$OCS:CO:CH_3OH$	1:20:10	2041.2	4.899	$1.21(\pm0.13)\times10^{-16}$	2078-1999
	$OCS:CO:CH_3OH$	1:40:10	2044.7	4.891	$1.24(\pm0.13)\times10^{-16}$	2078-1999
ν_1	OCS	-	857.2	11.67	$8.86(\pm0.91)\times10^{-19}$	867-839
ν_2	OCS	-	514.2	19.45	$1.03(\pm0.11)\times10^{-18}$	530.5-505.8

ure due to their poor fits to the observations and substructures with multiple peaks.) Tables containing the peak positions, FWHMs, and relative integrated absorbances of the OCS ν_3 mode in these ice mixtures throughout their warm-up from 15 to 100 K are provided in the Supporting Information.

OCS:CH_3OH ice mixtures

In all of the binary OCS:CH_3OH mixtures, the OCS peak profile is symmetric and Gaussian-like, and its position is sensitive to temperature: it lies around ∼2041.5 cm^{-1} (4.898 μm) at 15 K and gradually blueshifts with increasing temperature to ∼2042.7 cm^{-1} (4.895 μm) at 100 K in all of the investigated OCS:CH_3OH mixing ratios. The FWHM, on the other hand, is sensitive to both temperature and the OCS:CH_3OH ratio. For example, the FWHM decreases from ∼23 to ∼19 cm^{-1} when the OCS:CH_3OH concentration decreases from 1:10 to 1:20 at 15 K, but a similar decrease in the FWHM also occurs during the warm-up of the OCS:CH_3OH 1:10 mixture. However, differences between the FWHMs of the OCS:CH_3OH 1:20 and 1:40 mixtures are much smaller. Based on this trend, we expect that increasing the dilution factor of OCS:CH_3OH beyond 1:40 would have very small effects on the OCS peak profile.

Notably, while several of the peak profiles observed by Boogert et al. 2022 can be well fit with our OCS:CH_3OH mixtures, many other observed peak positions are too redshifted (by 0.001-0.01 μm) to be sufficiently fit with them.

Given the similarity of these spectra to some of the observations, we derived apparent band strengths of the OCS ν_3 band in the OCS:CH_3OH 1:20 and 1:40 mixtures using the procedure described in the Methods section and report these values in Table 5.3. Within our uncertainties, these A' values are consistent with the A' value of pure OCS.

OCS:CO ice mixtures

Mixing OCS with CO results in an OCS peak blueshift of ∼5-10 cm^{-1} with respect to the OCS peak positions in the OCS:CH_3OH mixtures. Such a peak position is too blueshifted to fit observations. Furthermore, at the higher dilution factors (OCS:CO 1:20 and 1:40), the OCS feature splits into four blended but distinct peaks (see Figure 5.3). Similar splitting is observed in OCS:Ar and OCS:N_2 1:200 mixtures, where it has been attributed to isolated and aggregated OCS molecules within the Ar or N_2 matrices (Verderame & Nixon 1966), as the multiple peaks eventually disappear at even higher dilution factors. These split peak profiles do not match the observed Gaussian-like profile of interstellar OCS ice. Between 30-40 K, the multi-peak structures transform into very broad, asymmetric features similar to the peak structure of pure OCS ice because the CO ice desorbs between these temperatures, effectively distilling the ice and leaving behind nearly pure solid OCS.

OCS:CO:CH_3OH mixtures

Most of the investigated tertiary OCS:CO:CH_3OH mixtures have similar OCS profiles to the OCS:CH_3OH mixtures, but with two notable differences. First, the profiles of the OCS:CO:CH_3OH mixtures are slightly asymmetric at lower temperatures. The effect is most pronounced at 15 K and in the mixtures with the lowest CH_3OH concentrations (e.g., see the OCS:CO:CH_3OH 1:20:2 peak in Figure 5.3) but is still observed in the spectra up to ∼40

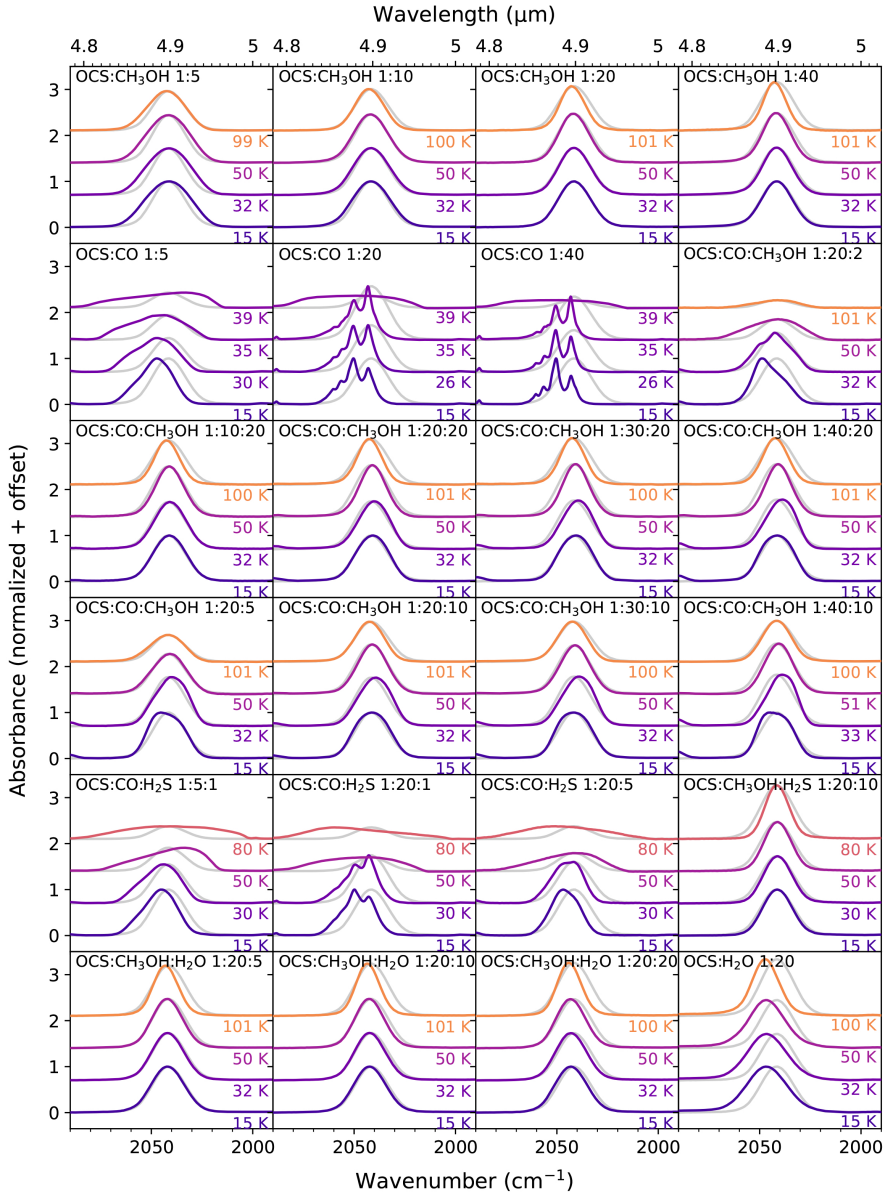


Figure 5.3: OCS ν_3 bands at select temperatures in all investigated binary and tertiary OCS-containing ice mixtures. All of the spectra are normalized so that the peak absorbance of the ν_3 mode at 15 K is equal to 1 in each set of spectra from a given mixture. The profile of the OCS ν_3 mode in the OCS:CH_3OH 1:20 ice mixture at 15 K is scaled to and plotted with all of the peaks (in gray) to facilitate comparisons of peak positions and profiles between the different mixtures.

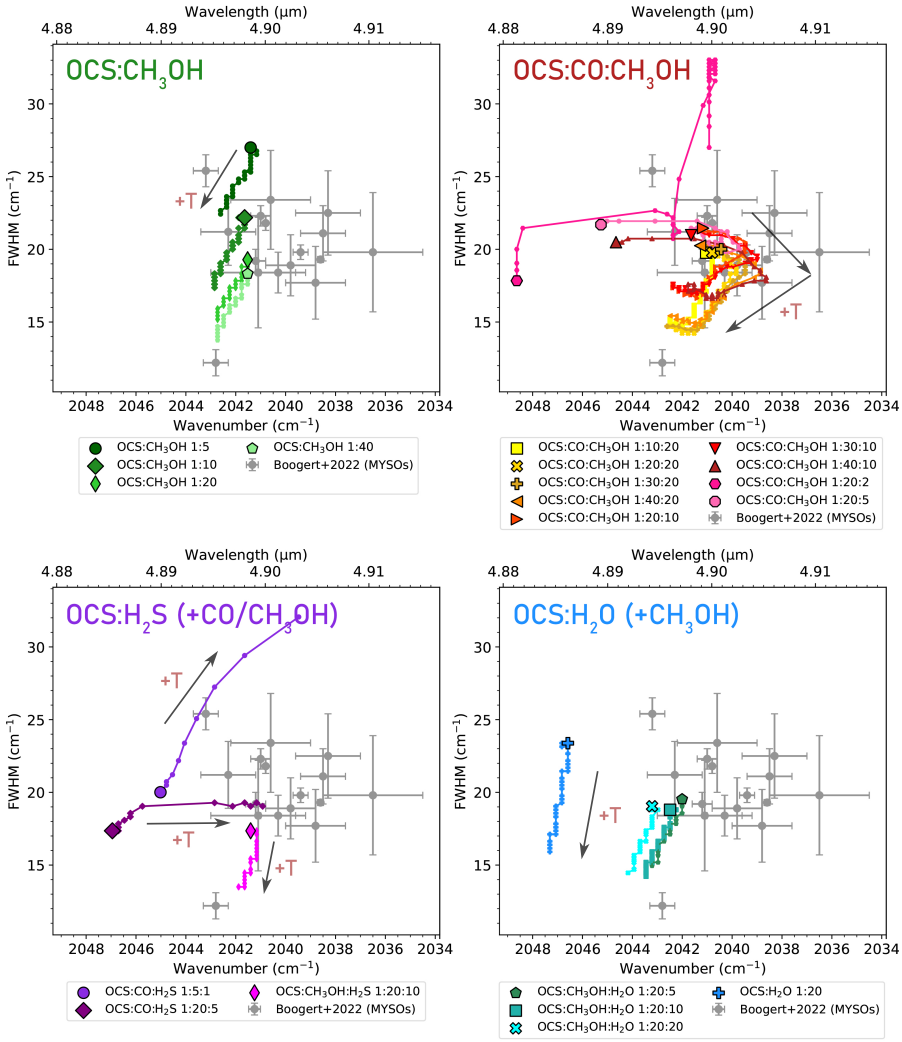


Figure 5.4: Peak positions and FWHMs of the OCS ν_3 mode in all of the investigated laboratory mixtures (color), excluding the binary OCS:CO mixtures and the OCS:CO:H_2S 1:20:1 mixture. The large outlined symbols denote mixtures at 15 K, while the traces and smaller symbols denote how the peak profile changes with increasing temperature. The black arrows indicate the direction of temperature increase. All mixtures are plotted up to 100 K except the OCS:CO:H_2S mixtures, which are only plotted up to 37 K because above this temperature, the OCS ν_3 feature in these mixtures becomes significantly broader than the peak in observations. The peak positions and FWHMs of the Gaussian profiles fit to the 4.9 μm band observed toward massive young stellar objects (MYSOs) by Boogert et al. 2022 are plotted in gray.

K, before a significant portion of the deposited CO begins to desorb. Second, the OCS peak positions in these mixtures tend to be slightly blueshifted relative to the OCS:CH_3OH mixtures at 15 K, but as the temperatures increase to ∼30-35 K, the peaks shift toward longer wavelengths. In the OCS:CO:CH_3OH 1:40:10 mixture, a maximum redshift is achieved at 35 K, with a peak position of 2038.6 cm^{-1} (4.905 μm). Such redshifted profiles provide substantially better fits to many of the redshifted observations.

It is important to note that these experiments demonstrate how even a small concentration of CH_3OH in the matrix has a pronounced effect on the OCS peak profile – i.e., the mixture does not have to be CH_3OH-dominated for the OCS peak to have a profile similar to that in the OCS:CH_3OH mixtures. For example, in the CO-dominated OCS:CO:CH_3OH 1:20:5 mixture, the OCS peak profile looks much more similar to the peak in the OCS:CH_3OH 1:5 mixture than in the OCS:CO 1:20 mixture (see Figure 5.3).

Given the match in redshifted peak position of several of the OCS:CO:CH_3OH mixtures to the MYSO observations in Boogert et al., we calculated the apparent band strengths of the OCS ν_3 mode in the 1:20:20, 1:40:20, 1:20:10, and 1:40:10 mixtures using the procedure outlined in the Methods section and report these values in Table 5.3. As was the case for the OCS:CH_3OH mixtures, these A' values are consistent with the A' value of pure OCS within our reported uncertainties.

OCS:CO:H_2S and OCS:CH_3OH:H_2S mixtures

The three investigated tertiary OCS:CO:H_2S mixtures have significantly blueshifted and markedly asymmetric OCS peaks at 15 K. As they are heated to 30-40 K, their peaks redshift toward the observed values but remain quite asymmetric, making them poor fits to the observations despite the apparent experimental overlap with the observational data in Figure 5.4. At higher temperatures, much of the deposited CO desorbs, and the OCS peaks become much broader than the observations as the OCS ice is effectively distilled. Further OCS distillation occurs in these mixtures between 70-80 K when H_2S desorbs.

The OCS peak profile of the OCS:CH_3OH:H_2S 1:20:10 mixture is nearly identical to that of the most dilute OCS:CH_3OH mixtures. Therefore, the OCS peak profile is not sensitive to the presence of H_2S in CH_3OH-dominated matrices.

OCS:H_2O and OCS:CH_3OH:H_2O mixtures

The OCS profile in the investigated H_2O-containing mixtures is symmetric and Gaussian-like, similar to the binary CH_3OH mixtures. The binary OCS:H_2O 1:20 mixture is far too blueshifted (by at least ∼5 cm^{-1}) to fit any of the observations, as noted previously by Palumbo et al. 1995. However, the tertiary mixtures of OCS:CH_3OH:H_2O explored here, even those with equivalent concentrations of CH_3OH and H_2O like the 1:20:20 mixture, have OCS peak profiles and positions that are very similar to those of the binary OCS:CH_3OH mixtures. They are also slightly blueshifted, but not by enough to lie outside of the observed OCS peak profile range considering errors. These results demonstrate again that the presence of CH_3OH in the ice matrix has a strong effect on the OCS peak profile, even if it is not the only dominant matrix species.

5.4 Astronomical implications

With the spectra collected in this work, we show that many of the observed OCS ν_3 peak positions that were too redshifted to be fit with any previously available nonirradiated laboratory ice mixtures can now actually be fit quite well with tertiary OCS:CO:CH_3OH mixtures. In the bottom two panels of Figure 5.5, we demonstrate how OCS:CO:CH_3OH mixtures provide good fits to the OCS ice features observed toward W33A and G029.8620-00.0444 (hereafter G029.8620), two embedded massive protostars (Boogert et al. 2022) observed via the NASA InfraRed Telescope Facility (IRTF). The massive protostar G029.8620 in particular has the highest quality OCS feature of the IRTF sample, and it is shifted significantly to longer wavelengths with respect to binary OCS:CH_3OH mixtures. This is the case even after the correction for a Doppler velocity shift of +100 km s^{-1} with respect to the Local Standard of Rest (Areal et al. 2020) and the motion of the Earth around the Sun at the date of the IRTF observations (this correction was not applied in Boogert et al. 2022).
These laboratory spectra therefore provide an alternative explanation to that presented by Boogert et al. 2022 for the observed OCS peak positions – namely, that solid-state interstellar OCS may be intimately mixed with both CO and CH_3OH ice. This result is one of many that supports a close chemical relationship between CO and CH_3OH (Watanabe & Kouchi 2002; Fuchs et al. 2009; Cuppen et al. 2011; Penteado et al. 2015) and is consistent with the hypothesis that CO is a chemical precursor of OCS (Shingledecker et al. 2020). Unfortunately, analysis of more precise physicochemical parameters like the OCS:CO:CH_3OH ratio and temperature of the ice matrix surrounding OCS cannot be reliably determined by analyzing the OCS ν_3 peak profile due to the degenerate effects of mixing ratios and temperatures on both the OCS peak position and FWHM in the OCS:CO:CH_3OH laboratory mixtures.

Conversely, our data do not provide conclusive evidence for OCS mixing with H_2S, another suggested OCS precursor (Ferrante et al. 2008; Santos et al. 2024a), in interstellar ices, although they do not refute the possibility, either. The OCS:CH_3OH:H_2S 1:20:10 mixture demonstrates that the presence of H_2S in a CH_3OH-dominated matrix does not have a strong effect on the OCS peak profile, even at relatively high (10:1) H_2S:OCS ratios. Significantly higher concentrations of H_2S are unlikely given that currently available H_2S ice upper limits in the literature result in H_2S:OCS ratio upper limits of $\lesssim$4 (Jiménez-Escobar & Muñoz Caro 2011; McClure et al. 2023). The asymmetric profiles of the OCS bands in the OCS:CO:H_2S mixtures investigated here do not match the more symmetric profiles of the OCS features reported in irradiated laboratory CO:H_2S ice mixtures (Ferrante et al. 2008; Garozzo et al. 2010), which may be due to the presence of several other irradiation products in the latter ices. It is possible that including CH_3OH in the nonirradiated OCS:CO:H_2S mixtures could result in more symmetric OCS features that would better match observations, but any changes in the OCS peak profile due to H_2S in such mixtures are likely to be small (given the tight constraints on H_2S ice abundances from the current upper limits) and perhaps also degenerate with other physicochemical effects.

Finally, we include in Figure 5.5 one of the first observations of OCS ice toward a dense core in front of a background star, J110621 McClure et al. (2023), observed by the *James Webb* Space Telescope (JWST). Although the feature is contaminated by CO gas absorption lines from the photosphere of the background star, a peak profile can be roughly extracted by fitting to the data points between the absorption lines, resulting in an extracted peak position that is blueshifted relative to the OCS:CH_3OH 1:20 position. The laboratory data from this

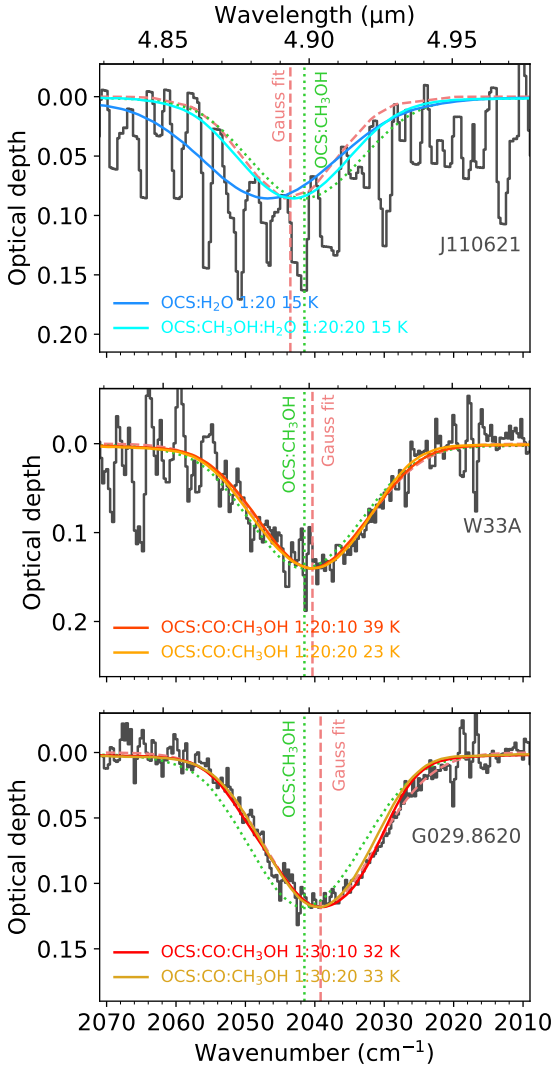


Figure 5.5: OCS ν_3 mode observed toward three icy sightlines (gray traces) overplotted with select laboratory OCS ice mixtures from this work (colored traces). A Gaussian fit to each observed feature (dashed coral trace) and the laboratory OCS:CH_3OH 1:20 15 K spectrum (dotted green trace), along with vertical lines marking their respective peak positions, are also overplotted to serve as points of reference and to facilitate visual comparisons between the different sources and laboratory data. The observational data include the dense core in front of a background star J110621 (top, McClure et al. 2023), the massive protostar W33A (middle, Boogert et al. 2022), and the massive protostar G029.8620 (bottom, Boogert et al. 2022). CO gas lines were removed from the MYSO spectra (see Boogert et al. 2022).

work that provides the best match to such a profile is the OCS:CH_3OH:H_2O 1:20:20 mixture. In their analysis of this source, McClure et al. 2023 found that the local cloud density may still be too low to support catastrophic CO freezeout, and that some portion of the detected CH_3OH ice may be mixed with H_2O, possibly due to early CH_3OH formation via a pathway like CH_4+OH in a H_2O-rich environment (Qasim et al. 2018). The blueshift in the OCS peak position toward this source could be considered evidence for early formation of both OCS and CH_3OH in a more H_2O-rich ice phase, although this evidence remains very tenuous given that the overlapping photospheric contamination may create distortions in the observed OCS profile, leading to higher uncertainties in the extracted peak position.

Given the spectroscopic degeneracies, we do not claim that our laboratory spectra provide unique fits to the OCS ice observations. Therefore, our fits do not strictly preclude other chemical environments, like those investigated by Ferrante et al. 2008 and Garozzo et al. 2010, providing equally satisfactory fits. Our fits do, however, provide evidence supporting plausible chemical environments of OCS ice comprising only simple ice species that are securely and abundantly observed in dense star-forming regions.

5.5 Conclusions

This work provides the astrochemical community with a library of new laboratory IR transmission spectra of OCS-containing ice mixtures to aid analysis of observations of OCS interstellar ices. Apparent band strengths, peak positions, and FWHMs of the OCS asymmetric stretching mode (ν_3) in these mixtures are reported. The main conclusions from this work can be summarized as follows:

- Tertiary laboratory mixtures of OCS:CO:CH_3OH provide the best fits to most of the OCS ice bands currently observed toward the ice envelopes of massive protostars, supporting the previously hypothesized link between these species. The match also supports the late OCS formation scenario, in which most of the observed OCS ice forms in the densest, coldest regions of ice clouds and envelopes where CO freezeout occurs.

- CH_3OH has a strong effect on the profile of the OCS band even when it is not the dominant ice component, and OCS features observed toward several massive protostars can be fit well with OCS:CO:CH_3OH laboratory ice mixtures whose dominant component is CO rather than CH_3OH.

- Specific conclusions regarding local OCS concentration or OCS ice temperature based on the OCS peak profile are hindered by the degenerate effects of these parameters. Taking into account previous work, this degeneracy also applies to proton-irradiated ices containing H_2S, CO, and H_2O (Ferrante et al. 2008).

- The apparent band strength of OCS in OCS:CH_3OH and OCS:CO:CH_3OH mixtures is consistent with that of pure OCS ice within our reported uncertainties. We recommend that a value of 1.2×10^{-16} cm molec^{-1} is used to calculate OCS column densities in interstellar ices.

- Our data neither support nor refute possible chemical links between H_2S and OCS, as the OCS:CO:H_2S mixtures collected as part of this work have asymmetric OCS profiles

that do not match any observations, but the investigated OCS:CH_3OH:H_2S mixture has a similar profile to binary OCS:CH_3OH mixtures that fit some of the observed OCS peaks well.

- While OCS:H_2O mixtures are too blueshifted to fit any current OCS observations, OCS:CH_3OH:H_2O mixtures may provide a good fit to an OCS feature observed toward a background star behind a dense cloud, suggesting that some OCS may form earlier in a phase of the ice that is still relatively H_2O-rich. However, this conclusion remains tenuous due to spectral contamination by photospheric CO gas absorptions complicating the OCS profile extraction toward this source.
- Given the weak apparent band strengths of the OCS symmetric stretching (ν_1) and bending (ν_2) modes and the relatively low abundance of OCS ice in dense star-forming regions, the very strong OCS asymmetric stretching (ν_3) mode remains the only likely detectable feature of this molecule in interstellar ices in the near future.

These laboratory spectra are made available for public use and enjoyment on the Leiden Ice Database (LIDA, (Rocha et al. 2022)).

5.6 Acknowledgements

This paper is dedicated to the memory of the late Harold Linnartz, who provided indispensable scientific guidance and inspiration throughout the collection and analysis of this data. K.S. thanks Ewine van Dishoeck for helpful scientific discussions, Julia Santos for experimental support, and Martijn Witlox and Robin Schrama for mechanical support. K.-J.C. is grateful for support from the Dutch Research Council (NWO) via the Veni fellowship. Astrochemistry at Leiden is supported by funding from the European Research Council (ERC) under the European Union's Horizon 2020 research and innovation programme (grant agreement No. 101019751 MOLDISK), the Netherlands Research School for Astronomy (NOVA), and the Danish National Research Foundation through the Center of Excellence "InterCat" (Grant agreement no.: DNRF150).

5.A Supplemental Information

5.A.1 OCS ν_3 peak positions, FWHMs, and relative integrated absorbances

This appendix presents the peak positions, FWHMs, and relative integrated absorbances (with respect to the integrated absorbance of each mixture at 15 K) of the OCS ν_3 feature in all OCS-bearing ice mixtures investigated in this work. The uncertainty of the peak positions and FWHMs is 0.5 cm^{-1}.

Table 5.A.4: Peak positions, FWHMs, and relative integrated absorbances (with respect to the integrated absorbance of each mixture at 15 K) of the OCS $\nu 3$ feature in pure and binary OCS ices at various temperatures.

Matrix	T	Peak		FWHM		Rel. integ. abs.
	(K)	cm^{-1}	μm	cm^{-1}	μm	(w.r.t. 15 K)
OCS*	15	2034.1	4.916	55.9	0.134	1.00
	50	2029.7	4.927	53.5	0.128	1.03
	65	2003.7	4.991	46.3	0.113	1.07
	83	2003.4	4.991	27.5	0.068	1.13
OCS:CH_3OH 1:5	15	2041.4	4.899	27.0	0.065	1.00
	52	2041.6	4.898	25.3	0.061	0.99
	66	2042.1	4.897	24.3	0.058	0.98
	80	2042.4	4.896	23.6	0.057	0.97
	95	2042.6	4.896	22.7	0.054	0.85
OCS:CH_3OH 1:10	15	2041.6	4.898	22.2	0.053	1.00
	50	2042.1	4.897	20.5	0.049	0.99
	60	2042.4	4.896	19.8	0.047	0.98
	71	2042.6	4.896	19.0	0.046	0.98
	81	2042.8	4.895	18.3	0.044	0.97
	99	2042.8	4.895	17.4	0.042	0.76
OCS:CH_3OH 1:20	15	2041.5	4.898	19.3	0.046	1.00
	48	2042	4.897	17.8	0.043	1.00
	59	2042.2	4.897	17.4	0.042	0.99
	69	2042.5	4.896	16.6	0.040	0.99
	80	2042.7	4.895	15.9	0.038	0.98
	99	2042.7	4.895	15.2	0.036	0.82
OCS:CH_3OH 1:40	15	2041.5	4.898	18.3	0.044	1.00
	48	2042	4.897	16.6	0.040	1.00
	60	2042.2	4.897	16.2	0.039	0.99
	71	2042.5	4.896	15.4	0.037	0.98
	81	2042.7	4.895	14.7	0.035	0.97
	99	2042.7	4.895	13.7	0.033	0.85
OCS:CO 1:5*	15	2047.3	4.884	19.8	0.047	1.00
	32	2047.6	4.884	30.1	0.072	0.92
	35	2043.7	4.893	35.7	0.085	0.90
OCS:CO 1:20*	15	2050.2	4.878	14.0	0.033	1.00
	26	2043.2	4.894	14.7	0.035	1.01
	30	2043.2	4.894	12.8	0.030	1.02
	35	2043.2	4.894	12.3	0.029	1.03
OCS:CO 1:40*	15	2050.7	4.876	5.3	0.013	1.00
	31	2043	4.895	5.1	0.012	1.00
	35	2043	4.895	4.8	0.012	0.97

* indicates that the OCS ν_3 mode in the marked ice has a strongly asymmetric or split (i.e., non-Gaussian) peak profile.

Table 5.A.5: Peak positions, FWHMs, and relative integrated absorbances (with respect to the integrated absorbance of each mixture at 15 K) of the OCS $\nu 3$ feature in select tertiary OCS:CO:CH_3OH mixtures at various temperatures.

Matrix	T (K)	Peak cm^{-1}	Peak μm	FWHM cm^{-1}	FWHM μm	Rel. integ. abs. (w.r.t. 15 K)
OCS:CO:CH_3OH 1:20:2*	15	2048.6	4.881	17.8	0.043	1.00
	25	2043.1	4.895	22.7	0.054	0.98
	41	2041.2	4.899	29.9	0.072	0.79
	50	2040.9	4.900	31.8	0.076	0.78
	71	2040.9	4.800	32.3	0.077	0.78
	90	2040.9	4.900	31.6	0.076	0.52
OCS:CO:CH_3OH 1:10:20	15	2041	4.899	19.8	0.047	1.00
	36	2040.8	4.900	18.6	0.045	1.00
	50	2041.3	4.899	17.1	0.041	0.98
	60	2041.5	4.898	15.9	0.038	0.98
	70	2041.8	4.898	15.2	0.036	0.98
	84	2042.2	4.897	14.7	0.035	0.97
	94	2042.5	4.896	15.2	0.036	0.90
OCS:CO:CH_3OH 1:20:20	15	2040.8	4.900	19.8	0.047	1.00
	33	2039.8	4.902	18.3	0.044	0.99
	47	2040.8	4.900	16.2	0.039	0.95
	60	2041.3	4.899	14.7	0.035	0.94
	72	2041.8	4.898	14.5	0.035	0.93
	90	2042.5	4.896	14.7	0.035	0.93
OCS:CO:CH_3OH 1:30:20	15	2040.4	4.901	20.0	0.048	1.00
	32	2039.5	4.903	18.6	0.045	1.00
	42	2040.4	4.901	16.6	0.040	0.97
	51	2040.9	4.900	15.7	0.038	0.96
	59	2041.2	4.899	14.9	0.036	0.96
	65	2041.4	4.899	14.5	0.035	0.96
	72	2041.6	4.898	14.5	0.035	0.95
	83	2042.1	4.897	14.7	0.035	0.94
	93	2042.6	4.896	14.7	0.035	0.89
OCS:CO:CH_3OH 1:40:20	15	2041.3	4.899	20.2	0.049	1.00
	22	2040.6	4.901	20.2	0.049	1.01
	32	2038.9	4.905	18.6	0.045	1.02
	41	2040.6	4.901	16.6	0.040	0.95
	50	2040.8	4.900	15.9	0.038	0.95
	60	2041.3	4.899	15.2	0.036	0.95
	71	2041.5	4.898	14.9	0.036	0.95
	80	2041.8	4.897	15.2	0.036	0.93
	90	2042.2	4.897	15.2	0.036	0.93
	99	2042.5	4.896	15.4	0.037	0.86

* indicates that the OCS ν_3 mode in the marked ice has a strongly asymmetric or split (i.e., non-Gaussian) peak profile.

Table 5.A.6: Peak positions, FWHMs, and relative integrated absorbances (with respect to the integrated absorbance of each mixture at 15 K) of the OCS $\nu 3$ feature in select tertiary OCS:CO:CH_3OH mixtures at various temperatures.

Matrix	T (K)	Peak cm^{-1}	Peak μm	FWHM cm^{-1}	FWHM μm	Rel. integ. abs. (w.r.t. 15 K)
OCS:CO:CH_3OH 1:20:5	15	2045.3	4.889	21.7	0.052	1.00
	22	2043.1	4.895	21.9	0.053	1.00
	35	2039.7	4.903	20.0	0.048	1.01
	50	2040.7	4.900	20.2	0.049	0.85
	60	2040.7	4.900	20.0	0.048	0.84
	71	2040.9	4.900	20.2	0.049	0.83
	80	2041.2	4.899	20.5	0.049	0.83
	90	2041.4	4.899	21.5	0.051	0.78
	96	2041.6	4.898	21.2	0.051	0.68
OCS:CO:CH_3OH 1:20:10	15	2041.2	4.899	21.5	0.051	1.00
	20	2040.7	4.900	21.2	0.051	1.00
	30	2039.5	4.903	20.0	0.048	1.00
	38	2040.2	4.901	19.0	0.046	0.95
	45	2040.7	4.900	18.3	0.044	0.94
	56	2041.2	4.899	17.1	0.041	0.93
	65	2041.4	4.899	16.9	0.040	0.93
	75	2041.6	4.898	16.9	0.040	0.92
	86	2042.1	4.897	17.4	0.042	0.90
	95	2042.4	4.896	17.4	0.042	0.82
OCS:CO:CH_3OH 1:30:10	15	2041.6	4.898	21.0	0.050	1.00
	21	2040.4	4.901	21.0	0.050	1.00
	32	2039	4.904	19.3	0.046	1.00
	44	2040.7	4.900	18.3	0.044	0.93
	56	2041.2	4.899	17.4	0.042	0.92
	66	2041.4	4.899	17.1	0.041	0.92
	75	2041.6	4.898	17.1	0.041	0.91
	86	2042.1	4.897	17.4	0.041	0.90
	95	2042.4	4.896	17.6	0.042	0.83
OCS:CO:CH_3OH 1:40:10	15	2044.7	4.891	20.5	0.049	1.00
	22	2040.3	4.901	20.2	0.049	1.01
	31	2038.6	4.905	18.1	0.043	1.01
	40	2040.3	4.901	16.9	0.041	0.92
	51	2040.6	4.901	16.9	0.041	0.93
	61	2040.6	4.901	16.6	0.040	0.93
	72	2040.8	4.900	16.6	0.040	0.93
	84	2041.3	4.899	17.1	0.041	0.92
	95	2041.8	4.898	17.1	0.041	0.83

* indicates that the OCS ν_3 mode in the marked ice has a strongly asymmetric or split (i.e., non-Gaussian) peak profile.

Table 5.A.7: Peak positions, FWHMs, and relative integrated absorbances (with respect to the integrated absorbance of each mixture at 15 K) of the OCS $\nu 3$ feature in tertiary H_2S-containing mixtures at various temperatures.

Matrix	T	Peak		FWHM		Rel. integ. abs.
	(K)	cm^{-1}	μm	cm^{-1}	μm	(w.r.t. 15 K)
OCS:CO:H_2S 1:5:1*	15	2045	4.890	20.0	0.048	1.00
	27	2044.5	4.891	21.2	0.051	0.98
	33	2042.8	4.895	27.2	0.065	0.92
	38	2037.1	4.909	34.0	0.082	0.89
	48	2034.2	4.916	36.4	0.087	0.90
	57	2030.8	4.924	44.4	0.107	0.85
OCS:CO:H_2S 1:20:1*	15	2050	4.880	18.3	0.044	1.00
	24	2040	4.900	18.6	0.044	1.01
	38	2040	4.900	16.4	0.039	0.93
	44	2040	4.900	47.7	0.114	0.80
	51	2040	4.890	50.9	0.121	0.78
	57	2040	4.900	57.6	0.137	0.79
OCS:CO:H_2S 1:20:5*	15	2046.9	4.885	17.4	0.041	1.00
	29	2042.8	4.895	19.3	0.046	1.00
	37	2040.9	4.900	19.0	0.046	0.98
	42	2040	4.902	29.7	0.071	0.82
	51	2040	4.902	39.1	0.093	0.81
	59	2040	4.902	52.6	0.125	0.82
OCS:CH_3OH:H_2S 1:20:10	15	2041.4	4.899	17.4	0.042	1.00
	50	2041.2	4.899	16.2	0.039	0.99
	60	2041.4	4.899	15.4	0.037	0.99
	80	2041.6	4.898	14.5	0.035	0.98
	96	2041.9	4.897	13.5	0.032	0.86

* indicates that the OCS ν_3 mode in the marked ice has a strongly asymmetric or split (i.e., non-Gaussian) peak profile.

Table 5.A.8: Peak positions, FWHMs, and relative integrated absorbances (with respect to the integrated absorbance of each mixture at 15 K) of the OCS $\nu 3$ feature in tertiary H_2S-containing mixtures at various temperatures.

Matrix	T	Peak		FWHM		Rel. integ. abs.
	(K)	cm^{-1}	μm	cm^{-1}	μm	(w.r.t. 15 K)
OCS:CH_3OH:H_2O 1:20:5	15	2042	4.897	19.5	0.047	1.00
	50	2042.2	4.897	18.1	0.043	0.99
	60	2042.5	4.896	17.4	0.042	0.98
	72	2042.7	4.895	16.9	0.040	0.97
	86	2043	4.895	15.9	0.038	0.96
	101	2043.2	4.894	14.9	0.036	0.85
OCS:CH_3OH:H_2O 1:20:10	15	2042.5	4.896	18.8	0.045	1.00
	50	2042.7	4.895	17.4	0.042	0.99
	65	2043	4.895	16.4	0.039	0.98
	75	2043.2	4.894	15.9	0.038	0.97
	87	2043.5	4.894	15.2	0.036	0.95
	101	2043.5	4.894	14.2	0.034	0.87
OCS:CH_3OH:H_2O 1:20:20	15	2043.2	4.894	19.0	0.046	1.00
	50	2043.2	4.894	17.6	0.042	0.99
	60	2043.5	4.894	17.1	0.041	0.98
	71	2043.7	4.893	16.4	0.039	0.97
	81	2043.9	4.893	15.7	0.038	0.96
	100	2044.2	4.892	14.5	0.035	0.89
OCS:H_2O 1:20	15	2046.6	4.886	23.4	0.056	1.00
	50	2046.8	4.886	21.0	0.050	0.98
	66	2047.1	4.885	19.0	0.045	0.97
	89	2047.3	4.884	17.1	0.041	0.95
	101	2047.3	4.884	15.9	0.038	0.88

* indicates that the OCS ν_3 mode in the marked ice has a strongly asymmetric or split (i.e., non-Gaussian) peak profile.

5.B Bibliography

Aikawa, Y., Kamuro, D., Sakon, I., et al. 2012, A&A, 538, A57
Areal, M. B., Paron, S., Fariña, C., et al. 2020, A&A, 641, A104
Boogert, A., Brewer, K., Brittain, A., & Emerson, K. 2022, ApJ, 941, 32
Boogert, A. A., Gerakines, P. A., & Whittet, D. C. 2015, ARA&A, 53, 541
Bouilloud, M., Fray, N., Bénilan, Y., et al. 2015, MNRAS, 451, 2145
Chen, Y.-J., Juang, K.-J., Nuevo, M., et al. 2014, ApJ, 798, 80
Cuppen, H., Penteado, E., Isokoski, K., van der Marel, N., & Linnartz, H. 2011, MNRAS, 417, 2809
Ferrante, R. F., Moore, M. H., Spiliotis, M. M., & Hudson, R. L. 2008, ApJ, 684, 1210
Fuchs, G., Cuppen, H., Ioppolo, S., et al. 2009, A&A, 505, 629
Garozzo, M., Fulvio, D., Kanuchova, Z., Palumbo, M., & Strazzulla, G. 2010, A&A, 509, A67
Geballe, T., Baas, F., Greenberg, J., & Schutte, W. 1985, A&A, 146, L6
Gerakines, P. A. & Hudson, R. L. 2015, ApJL, 808, L40
Gibb, E., Whittet, D., Boogert, A., & Tielens, A. 2004, ApJS, 151, 35
Hudgins, D., Sandford, S., Allamandola, L., & Tielens, A. 1993, ApJS, 86, 713
Hudson, R. L. & Gerakines, P. A. 2018, ApJ, 867, 138
Jiménez-Escobar, A. & Muñoz Caro, G. M. 2011, A&A, 536, A91
Laas, J. C. & Caselli, P. 2019, A&A, 624, A108
Loeffler, M., Moore, M., & Gerakines, P. 2016, ApJ, 827, 98
Luna, R., Millán, C., Domingo, M., Santonja, C., & Satorre, M. Á. 2022, ApJ, 935, 134
Luna, R., Molpeceres, G., Ortigoso, J., et al. 2018, A&A, 617, A116
McClure, M. K., Rocha, W., Pontoppidan, K., et al. 2023, Nat. Astro., 7, 431
Palumbo, M., Geballe, T., & Tielens, A. G. 1997, ApJ, 479, 839
Palumbo, M., Tielens, A., & Tokunaga, A. T. 1995, ApJ, 449
Penteado, E., Boogert, A., Pontoppidan, K., et al. 2015, MNRAS, 454, 531
Qasim, D., Chuang, K.-J., Fedoseev, G., et al. 2018, A&A, 612, A83
Rachid, M., Brunken, N., De Boe, D., et al. 2021, A&A, 653, A116
Rocha, W., Rachid, M., Olsthoorn, B., et al. 2022, A&A, 668, A63
Santos, J. C., Linnartz, H., & Chuang, K.-J. 2024a, A&A, 690, A24
Santos, J. C., van Gelder, M. L., Nazari, P., Ahmadi, A., & van Dishoeck, E. F. 2024b, A&A, 689, A248
Shingledecker, C. N., Lamberts, T., Laas, J. C., et al. 2020, ApJ, 888, 52
Slavicinska, K., Rachid, M. G., Rocha, W. R. M., et al. 2023, A&A, 677, A13
Tyagi, H., Manoj, P., Narang, M., et al. 2025, ApJ, 983, 110
Verderame, F. D. & Nixon, E. R. 1966, JCP, 44, 43
Vidal, T. H. & Wakelam, V. 2018, MNRAS, 474, 5575
Watanabe, N. & Kouchi, A. 2002, ApJ, 571, L173
Yarnall, Y. Y. & Hudson, R. L. 2022, ApJL, 931, L4
York, D. 1966, Can. J. Phys., 44, 1079

6

The hunt for formamide in interstellar ices

A toolkit of laboratory infrared spectra in astronomically relevant ice mixtures and comparisons to ISO, Spitzer, and JWST observations

Katerina Slavicinska, Marina G. Rachid, Will R. M. Rocha, Ko-Ju Chuang, Ewine F. van Dishoeck, Harold Linnartz

Astronomy & Astrophysics (2023), 677, A13

Abstract

Context. Although solid-state pathways are expected to dominate the formation mechanisms of many complex organic molecules (COMs), very few COMs have been securely identified in interstellar ices, in stark contrast with the many COM detections in the gas phase. The launch of the James Webb Space Telescope (JWST) and its increase in sensitivity and spectral resolution opens the possibility of identifying more COMs in ices, but additional laboratory data are necessary. Formamide (NH_2CHO) is one such COM that is of great interstellar and prebiotic relevance where more laboratory data are needed in the hunt for its presence in interstellar ices.
Aims. This work aims to characterize the mid-IR spectra of formamide in its pure form as well as in mixtures of the most abundant interstellar ices via laboratory simulation of such ices, as well as to demonstrate how these laboratory spectra can be used to search for formamide in ice observations.
Methods. Mid-IR spectra (4000 - 500 cm^{-1}/2.5 - 20 μm) of formamide, both in its pure form as well as in binary and tertiary mixtures with H_2O, CO_2, CO, NH_3, CH_3OH, H_2O:CO_2, H_2O:NH_3, CO:NH_3, and CO:CH_3OH, were collected at temperatures ranging from 15 - 212 K.
Results. Apparent band strengths and positions of eight IR bands of pure amorphous and crystalline formamide at various temperatures are provided. Three of these bands are identified as potential formamide tracers in observational ice spectra: the overlapping C=O stretch and NH_2 scissor bands at 1700.3 and 1630.4 cm^{-1} (5.881 and 6.133 μm), the CH bend at 1388.1 cm^{-1} (7.204 μm), and the CN stretch at 1328.1 cm^{-1} (7.529 μm). The relative apparent band strengths, positions, and full width half maxima (FWHM) of these features in mixtures at various temperatures were also determined. All of the laboratory spectra are available to the community on the Leiden Ice Database for Astrochemistry (LIDA) for use in the interpretation of both observations (e.g., from JWST) and laboratory spectroscopic data. Finally, the laboratory spectra are compared to observational spectra of a variety of low- and high-mass young stellar objects as well as prestellar cores observed with the Infrared Space Observatory, the Spitzer Space Telescope, and JWST. A comparison between the formamide CH bend in laboratory data and the 7.24 μm band in the observations tentatively indicates that, if formamide ice is contributing significantly to the observed absorption, it is more likely in a polar matrix. Upper limits ranging from 0.35-5.1% with respect to H_2O were calculated via scaling the formamide:H_2O laboratory spectrum to the observations. These upper limits are in agreement with gas-phase formamide abundances and take into account the effect of a H_2O matrix on formamide's band strengths.

6.1 Introduction

Of the >280 molecules that have been detected in interstellar environments (Endres et al. 2016), formamide (NH_2CHO) has become one of the most widely and deeply investigated in observational, modeling, computational, and laboratory studies in the last decade. Containing all four of the most abundant biological elements (C, H, N, and O), formamide is the simplest molecule that contains the biologically essential amide bond and has been suggested as a plausible prebiotic precursor to various nucleobases (e.g., Saladino et al. 2003; Barks et al.

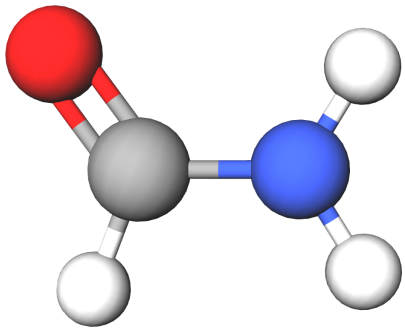


Figure 6.1: Molecular structure of NH_2CHO (hydrogen, white; carbon, gray; nitrogen, blue; and oxygen, red).

2010), the chemical building blocks of RNA and DNA. It has also been proposed as an alternative prebiotic solvent to promote condensation reactions, which form many vital biological molecules but are highly endergonic in purely aqueous solutions (e.g., phosphorylation), by lowering water activity (Gull et al. 2017; Pasek 2019; Lago et al. 2020).

Given this potential prebiotic relevance, the fact that formamide has been observed in numerous sources in the interstellar medium as well as on extraterrestrial bodies in our own Solar System has exciting implications for astrobiology. First detected in the interstellar medium in the gas phase by Rubin et al. (1971) in the Sagittarius B2 high-mass star-forming region, formamide has since been observed in over 30 massive young stellar objects (MYSOs) as well as low-mass YSOs (LYSOs) with hot corinos and protostellar shocks (López-Sepulcre et al. 2019 and references therein). Within our Solar System, gas-phase formamide has been found in the comae of the comets Lemmon, Lovejoy, and Hale-Bopp, with abundances ranging around 0.01-0.02% with respect to H_2O (Bockelée-Morvan et al. 2000; Biver et al. 2014). It was also detected in situ by the Rosetta mission on comet 67P Churyumov-Gerasimenko, both on the surface by the Cometary Sampling and Composition experiment (COSAC) instrument on the Philae lander (Goesmann et al. 2015) and in the coma by the Double Focusing Mass Spectrometer (DFMS) on the Rosetta Orbiter Spectrometer for Ion and Neutral Analysis (ROSINA) instrument (Altwegg et al. 2017; Rubin et al. 2019), where the formamide abundance was found to be $\sim$0.004% with respect to H_2O.

Notably, all of the interstellar sources in which gas-phase formamide has been securely detected have hot cores and corinos or shocked regions, where temperatures are high enough for formamide to thermally desorb from icy grains into the gas phase (López-Sepulcre et al. 2019). Additionally, in many of these sources, the formamide abundance correlates almost linearly with the abundance of isocyanic acid (HNCO) (Bisschop et al. 2007b; Mendoza et al. 2014; López-Sepulcre et al. 2015), and, in the case of the low-mass source IRAS 16293-2422, the two species are spatially correlated and have very similar deuteration ratios (Coutens et al. 2016).

These aspects of formamide observations could be considered evidence that formamide is formed in the solid state (i.e., via ice chemistry), possibly in a pathway chemically related to HNCO, and it is detected in the gas phase following desorption from icy grains. The ice formation and grain sublimation scenario is further supported by recent observational work

investigating excitation temperatures of N-bearing complex organic molecules (COMs) in 37 MYSOs from the ALMA Evolutionary study of High Mass Protocluster Formation in the Galaxy (ALMAGAL) survey, where formamide had the highest excitation temperatures of all the studied N-bearing COMs ($\gtrsim$250 K) (Nazari et al. 2022). These temperatures are consistent with thermal desorption experiments, in which formamide ice sublimes at high temperatures (typically ¿210 K) even when it is mixed with or deposited on top of more volatile species such as H_2O and CO, and at even higher temperatures (¿250 K) when the experiments are performed on certain dust grain analog substrates (Dawley et al. 2014; Urso et al. 2017; Chaabouni et al. 2018; Corazzi et al. 2020).

Experimentally, solid-state formamide has been identified as a product of processing via a variety of energetic sources (e.g., electron, UV, X-ray, and ion irradiation) of a myriad of simple ice mixtures, including (but not limited to) CO:NH_3 (Demyk et al. 1998; Hudson & Moore 2000; Jones et al. 2011; Bredehöft et al. 2017; Martín-Doménech et al. 2020) and H_2O:CO:NH_3 (Hudson & Moore 2000; Ciaravella et al. 2019; Chuang et al. 2022), NO:H_2CO:H and NO:CH_3OH:H (Fedoseev et al. 2016), H_2O:HCN (Gerakines et al. 2004), H_2O:CH_4:NH_3 and H_2O:CH_4:N_2 (Kaňuchová et al. 2016), and HNCO (Raunier et al. 2004) and CH_4:HNCO (Ligterink et al. 2018). Evidently, energetic processing of almost any ice mixture that contains H, N, C, and O is very likely to produce formamide. Such processing experiments mimic the radiation environments experienced by ices in protostellar envelopes and protoplanetary disks. Furthermore, recent experiments by Dulieu et al. (2019) demonstrate that hydrogenation of NO:H_2CO can also produce formamide, providing a plausible nonenergetic formation pathway that is relevant to cold, dark clouds.

While a plethora of observational, experimental, and theoretical works (see Section 6.2) have significantly progressed our understanding of formamide's interstellar presence and its plausible chemical history, whether its formation occurs in the solid state, gas phase, or both remains unclear. A secure detection of formamide in ices would be immensely valuable to resolve this debate regarding its formation mechanism. Such a detection, if well resolved, could provide parameters such as formamide's solid-state abundance and its physico-chemical environment, which are essential to elucidating its formation pathway.

Previously, formamide has been tentatively detected in the solid state in the Infrared Space Observatory Short Wavelength Spectrometer (ISO-SWS) spectra of the MYSOs W33A and NGC 7538 IRS 9. In the case of W33A, an upper limit of 2.1% with respect to H_2O via the CH bend at 7.22 μm/1385 cm^{-1} was derived, but the authors noted that the peak position in the observation (7.24 μm) was red-shifted relative to the formamide peak in their laboratory spectra (Schutte et al. 1999). For NGC 7538 IRS 9, no upper limit of formamide was provided – a laboratory spectrum of irradiated HNCO that showed IR evidence of formamide formation was qualitatively evaluated as a spectral fit to the observed 6 μm/1700 cm^{-1} band (Raunier et al. 2004). In both of these cases, the bands attributed to formamide were overlaid on top of or blended with other strong ice features.

Typically, reference laboratory IR spectra are used to assign and fit astronomically observed IR features to specific species, and band strengths acquired via systematic laboratory experiments are used to quantify the column densities of these species. For COMs such as formamide that are expected to be present in the ice in very low concentrations ($\lesssim$5%), it is important to obtain these spectra and band strengths not only for pure ices, but also in chemical conditions that are more realistic for interstellar ices. Namely, the molecule of interest should be diluted in the more abundant simple ice species (e.g., H_2O, CO, and CO_2), as interactions

with other species present in the ice matrix can significantly alter the positions, profiles, and apparent band strengths of a molecule's vibrational features. Morphological changes in the ice caused by thermal processing, such as transitions from amorphous to crystalline ice or matrix segregation, can also dramatically change an ice's spectral features, so spectra should be collected at a variety of temperatures as well. Considering such factors is not only important to accurately assign and quantify the molecule of interest, but it can also provide valuable information about the molecule's physico-chemical environment and history.

In previous IR characterization work, Brucato et al. (2006) derived the refractive index, density, and several band strengths of pure formamide, but integration ranges and errors were not provided for these band strengths, and no spectra of heated formamide or formamide in mixtures were collected. In order to tentatively assign the 7.24 μm band in W33A's spectrum to formamide, Schutte et al. (1999) collected spectra of formamide at 10 K in H_2O and H_2O:CH_3OH matrices, but only one band was characterized from these spectra, and it is unclear for what phase of formamide the band strength used in the upper limit calculation was derived. Urso et al. (2017) collected IR spectra of formamide in pure, H_2O-dominated, and CO-dominated ice matrices, but the band strengths, peak positions, and full width half maxima (FWHMs) of the formamide features in these mixtures are not given. Sivaraman et al. (2013) presented the peak positions of the bands of pure formamide in the 30 - 210 K temperature range, but no spectra of formamide in mixtures were collected.

Thus, in an effort to enable more secure assignments and accurate abundance and/or upper limit determinations of formamide in observed ice spectra, this work provides a comprehensive set of laboratory transmission IR spectra of pure formamide as well as formamide diluted in nine different astrophysically relevant ice mixtures of varying polarities. These spectra are provided at temperatures ranging from 15 - 212 K. Apparent band strengths were derived for eight integrated regions from the pure formamide spectra, and from these, three bands are evaluated as the most promising for future identification of formamide in observations. These bands are also fully characterized (i.e., peak positions, FWHMs, and relative band strengths are provided). Examples of how these spectra and values can be used in future analyses of ice observations are described, and new upper limits of formamide in a variety of objects (prestellar cores, low-mass protostars, and high-mass protostars) were calculated. Finally, all spectra are made publicly available on the Leiden Ice Database[1] (Rocha et al. 2022) for the community to use in fitting to their ice observations. This work is particularly timely given the recent launch of the James Webb Space Telescope (JWST), which may enable the detection of new COMs in interstellar ices due to its unprecedented sensitivity and spectral resolution.

6.2 Formamide formation mechanism debate

A variety of pathways have been suggested to explain the observed solid-state formamide formation in laboratory ice experiments. One initially proposed mechanism was the hydrogenation of HNCO, an attractive premise given that it provided a direct chemical link between HNCO and formamide to explain their correlation in gas-phase observations:

$$HNCO + 2\,{}^{\cdot}H \rightarrow NH_2CHO$$

[1] https://www.icedb.strw.leidenuniv.nl

This pathway was first suggested by Charnley (1997) and was stated as a possible formation mechanism of formamide when it was observed in VUV irradiation experiments of pure HNCO (Raunier et al. 2004). However, hydrogenation experiments by Noble et al. (2015) via H bombardment of HNCO ¡20 K did not produce detectable amounts of formamide, although the authors suggested that the reaction may be prevented in their experiments by the formation of very stable HNCO dimers or polymers, and that it could possibly proceed if HNCO is diluted in the matrix of an ice like H_2O. Indeed, subsequent experiments by Haupa et al. (2019) showed that, in a 3.3 K para-H_2 matrix, formamide can form from HNCO via a hydrogen addition-abstraction cycling mechanism, but in this reaction scheme, HNCO is still the favored product.

Another proposed formation pathway is the following radical-radical recombination:

$$\cdot NH_2 + \cdot CHO \rightarrow NH_2CHO$$

This mechanism is technically barrierless and can proceed at low temperatures ($\sim$10 K) but produces higher yields at higher temperatures ($\sim$20-40 K) due to increased mobility allowing the radicals to orient in the proper reaction geometry (Rimola et al. 2018; Martín-Doménech et al. 2020). In the laboratory, this mechanism requires some form of energetic processing to generate the NH_2 and CHO radicals, and its viability is supported by the presence of the CHO radical in the experimental spectra (Jones et al. 2011; Fedoseev et al. 2016; Ciaravella et al. 2019; Martín-Doménech et al. 2020; Chuang et al. 2022).

Various mechanisms have also been suggested where formamide is produced from the NH_2CO radical, which could form by the radical-molecule association of NH_2 and CO or CN and H_2O (Hudson & Moore 2000; Bredehöft et al. 2017; Rimola et al. 2018):

$$\cdot NH_2CO + \cdot H \rightarrow NH_2CHO$$
$$\cdot NH_2CO + H_2O \rightarrow NH_2CHO + \cdot OH$$
$$2\,\cdot NH_2CO \rightarrow NH_2CHO + HNCO$$

However, the formation of the NH_2CO radical via a pathway that does not involve hydrogen abstraction from already existing formamide, as seen in Haupa et al. (2019), has yet to be experimentally confirmed.

While these latter mechanisms do not provide an immediately obvious direct solid-state link between HNCO and NH_2CHO, some experimental studies have suggested alternative links consistent with these mechanisms. For example, once formed, formamide can decompose into HNCO via dehydrogenation and photolysis by H_2 loss (Brucato et al. 2006; Haupa et al. 2019; Chuang et al. 2022), so HNCO may be a product of NH_2CHO rather than the other way around. Fedoseev et al. (2016) proposed that the NH_2 radical can produce either HNCO or NH_2CHO depending on the degree of hydrogenation of the C- and O-containing molecule with which it reacts: the reaction of NH_2 with CO leads to HNCO, while NH_2 with HCO or H_2CO leads to formamide.

Thus, while formamide may not be a direct product of HNCO, the two species may be linked in a solid-state chemical network by common precursors. Astrochemical models using the rate constants from Fedoseev et al. (2016) further corroborate that, indeed, a direct chemical link between HNCO and NH_2CHO is not necessary to reproduce the observed linear correlation between them in models of various interstellar environments and suggest instead

that their correlation could be explained by their similar responses to physical (i.e., thermal) environments (Quénard et al. 2018).

In addition to these solid-state mechanisms, the plausibility of the following gas-phase formation route has been extensively debated in computational and modeling works since its proposal in Garrod et al. (2008):

$$^{\cdot}NH_2 + H_2CO \rightarrow NH_2CHO + {}^{\cdot}H$$

According to its first published electronic structure and kinetic calculations, this reaction is essentially barrierless at low temperatures and thus should proceed readily in interstellar environments (Barone et al. 2015; Vazart et al. 2016). Furthermore, chemical models of the protostar IRAS 16293-2422 and the molecular shocks L1157-B1 and B2 utilizing the calculated rate coefficients of this reaction produce formamide abundances that are consistent with observed values (Barone et al. 2015; Codella et al. 2017), and follow-up studies calculating rate coefficients of deuterated formamide formation via the same reaction show that formamide's observed deuteration ratio does not necessarily exclude the possibility of gas-phase formation (Skouteris et al. 2017).

However, the accuracy of these calculated rate coefficients has been called into question given that they neglect the zero point energy (ZPE) of one of the transition states. When the ZPE of the transition state is included, the reaction barrier becomes large enough that the reaction rate is negligible at low temperatures (Song & Kästner 2016), although some argue that inclusion of the ZPE is not warranted for this transition state and results in overestimation of the reaction barrier (Skouteris et al. 2017). Recent gas-phase experiments attempting to perform this route did not confirm any formamide formation, and their detection upper limits are consistent with the reaction barrier that includes the transition state ZPE (Douglas et al. 2022).

6.3 Methodology

All of the measurements were collected in the Laboratory for Astrophysics at Leiden Observatory on the IRASIS (InfraRed Absorption Setup for Ice Spectroscopy) chamber. The setup was described in detail in Rachid et al. (2021) and Rachid et al. (2022), and it has since undergone several upgrades, including a decrease of its base pressure to ¡1.0×10^{-9} mbar by the addition of new pumps, an exchange of the laser used for interference measurements to one with a wavelength of 543 nm (as the formamide ice refractive index was measured by Brucato et al. 2006 at this wavelength), and the implementation of an independent tri-dosing leak valve system that can be calibrated with a quadrupole mass spectrometer (QMS) following the procedure described in Appendix 6.A.3.

The optical layout of the chamber remains the same as that shown in Figure 1 in Rachid et al. (2021): a Ge substrate sits at the center of the chamber and is cooled by a closed-cycle He cryostat to 15 K. Ices are grown on the substrate via background deposition of gases and vapors dosed into the chamber through leak valves. Infrared transmission spectra are collected through two ZnSe viewports that are parallel to the Ge substrate and normal to the IR light beam. During deposition, laser interference patterns used to determine ice thickness are measured on both sides of the Ge substrate (which is opaque and reflective in the visible light

range) via photodiode detectors placed outside of viewports positioned 45° from the substrate normal. The patterns obtained from each side of the substrate during deposition show equal deposition rates on both sides. After deposition, the substrate can be heated to obtain IR spectra at different temperatures. In this work, 256 spectral scans with a 0.5 cm^{-1} resolution were collected and averaged while the substrate was heated at a rate of 25 K hr^{-1}, resulting in a temperature uncertainty of ±1.5 K in each heated spectrum. Spectra were collected during heating until reaching the temperature at which the major matrix component desorbed. Before their analysis, all spectra were baseline-corrected using a cubic spline function.

The liquids and gases used in this work were formamide (Sigma Aldrich, ≥99.5%), water (Milli-Q, Type I), carbon dioxide (Linde, ≥99.995%), carbon monoxide (Linde, ≥99.997%), ammonia (PraxAir, ≥99.96%), and methanol (Sigma Aldrich, ≥99.9%). The mixing ratios calculated for all of the spectra via the method outlined in Appendix 6.A.3 are presented in Table 6.1. Uncertainties in the column densities used to calculate these ratios are estimated to be ∼21% for the formamide column densities and ∼27% for the matrix species column densities (see Appendix 6.A.3). Prior to deposition, the liquid formamide sample was heated to 60°C and pumped on directly with a turbomolecular pump in order to remove contaminants (primarily water).

Table 6.1: Experimentally determined ratios of all mixtures presented in this work.

Mixture	Ratio
Pure NH_2CHO	–
$NH_2CHO:H_2O$	7:100
$NH_2CHO:CO_2$	7:100
$NH_2CHO:CO$	4:100
$NH_2CHO:CH_3OH$	8:100
$NH_2CHO:NH_3$	7:100
$NH_2CHO:H_2O:CO_2$	8:100:37
$NH_2CHO:H_2O:NH_3$	8:100:31
$NH_2CHO:CO:CH_3OH$	4:100:12
$NH_2CHO:CO:NH_3$	5:100:16

The apparent band strengths of pure formamide are determined via depositing formamide onto the substrate held at 15 K while simultaneously collecting the transmission IR spectra and the laser interference pattern. The thickness d of the ice can be derived from the laser interference pattern via the following equation:

$$d = \frac{m\lambda}{2\sqrt{n^2 - sin^2\theta}}, \tag{6.1}$$

where m is an integer number of constructive fringes, λ is the laser wavelength, n is the ice refractive index (1.361 for formamide at 543 nm, from Brucato et al. 2006), and θ is the angle of incidence.

Enough formamide is deposited so that four constructive fringes are acquired, the thick-

ness of the ice at each fringe peak is calculated, and the integrated absorbances of eight spectral regions (see Table 6.2) are calculated from the spectra collected at the time that a fringe peak was reached. Then, the integrated absorbance for each spectral region is plotted as a function of ice thickness, and the slope of this line, $\Delta \int abs(\nu)\, d\nu / \Delta d$, is obtained via a least-squares fit. From this value, the apparent band strengths A' can be approximated with an equation based on the Beer-Lambert Law (e.g., Hudson et al. 2014; Gerakines et al. 2023):

$$A' = \frac{2.303\, M}{\rho\, N_A} \times \frac{\Delta \int abs(\nu)\, d\nu}{\Delta d}, \tag{6.2}$$

where M is the molar mass of formamide (45.041 g mol^{-1}), ρ is the density of formamide ice (0.937 g cm^{-3}, from Brucato et al. 2006), and N_A is Avogadro's number. Using change in integrated absorbance over change in thickness in this equation rather than the absolute values of both variables ensures that there is no contribution of any residue from previous experiments on the substrate to the calculated ice thickness. It also does not require a constant ice growth rate.

The apparent band strengths reported in Table 6.2 are the averages of three repeated measurements following this method. The experimental uncertainties derived from the standard deviation of these three measurements range from 3-8% for the eight band strengths. However, simply using the standard deviations from the repeated measurements as the band strengths uncertainties neglects potential systemic sources of error such as uncertainties in the laser alignment geometry and the data analysis procedure. Thus, the uncertainties provided in Table 6.2 are calculated via error propagation of all of the experimental terms in Equation 6.2, using the same estimated uncertainties as Rachid et al. (2022) for the ice thickness (4%) and integrated absorbance (10%) as well as the ice density (10%). This calculation yields an uncertainty of 15% for the reported band strength values.

From the pure formamide apparent band strengths, the apparent band strengths of formamide in the investigated mixtures, A'_i, are calculated using the formamide column densities N_{mix} (obtained from the methods described in Appendix 6.A.3) via the following equation:

$$A'_i = 2.303 \times \frac{\int abs(\nu)\, d\nu}{N_{mix}}, \tag{6.3}$$

and the relative apparent band strengths, η, are subsequently found by:

$$\eta = \frac{A'_i}{A'}, \tag{6.4}$$

Following propagation of error from the pure apparent band strengths, integrated absorbances, and the formamide column densities in the mixtures (see Appendix 6.A.3), the uncertainties of the relative apparent band strengths presented here are estimated to be $\sim$28%.

6.4 Results

The spectra of pure amorphous and crystalline formamide are presented in Figure 6.2, and the eight apparent band strengths calculated at 15 K are presented in Table 6.2. Peak positions and vibrational mode assignments are also provided. Some integrated regions contain multiple overlapping peaks; in these cases, the peak positions and assignments were provided for all

Table 6.2: Apparent IR band strengths (and their peak positions, assignments, and corresponding integrated regions) of the IR bands of amorphous NH_2CHO ice at 15 K derived in this work.

Peak positions (cm^{-1} — μm)	Integrated region (cm^{-1})	Assignment*	A' (10^{-17} cm $molec^{-1}$)	A'**
3371.2 — 2.966	3719 - 2980	NH_2 antisymm. stretch (ν_{as} NH_2)	15.6 ± 2	13.49
3176.4 — 3.148		NH_2 symm. stretch (ν_s NH_2)		
2881.9 — 3.470	2980 - 2842	CH stretch (ν CH)	0.56 ± 0.08	0.47
2797.7 — 3.574	2842 - 2600	CH bend overtone (2δ CH)	0.23 ± 0.03	–
1700.3 — 5.881	2050 - 1532	C=O stretch (ν CO)	6.4 ± 0.9***	6.54
1630.4 — 6.133		NH_2 scissor (δ NH_2)		
1388.1 — 7.204	1532 - 1364	CH bend (δ CH)	0.9 ± 0.1***	0.68
1328.1 — 7.529	1364 - 1258	CN stretch (ν CN)	0.8 ± 0.1***	0.85
1108.1 — 9.024	1174 - 1030	NH_2 rock (ρ NH_2)	0.23 ± 0.03	–
1056.1 — 9.469		CH out-of-plane def. (γ CH)		
689.2 — 14.510	1030 - 575	NH_2 wag (ω NH_2)	2.3 ± 0.4	–
634.0 — 15.773		NH_2 twist (2τ NH_2)		

*Band assignments made according to the works of Räsänen 1983; Kwiatkowski & Leszczyński 1993; Torrie & Brown 1994; Lundell et al. 1998. Some band strengths contain multiple absorption modes in their corresponding integrated regions. **Values from Brucato et al. 2006. ***Bands that are also characterized in mixtures in this work.

peaks within the integrated region, but the peaks were not deconvolved to give an individual band strength for each peak. These band strengths have percent differences ranging from 1-

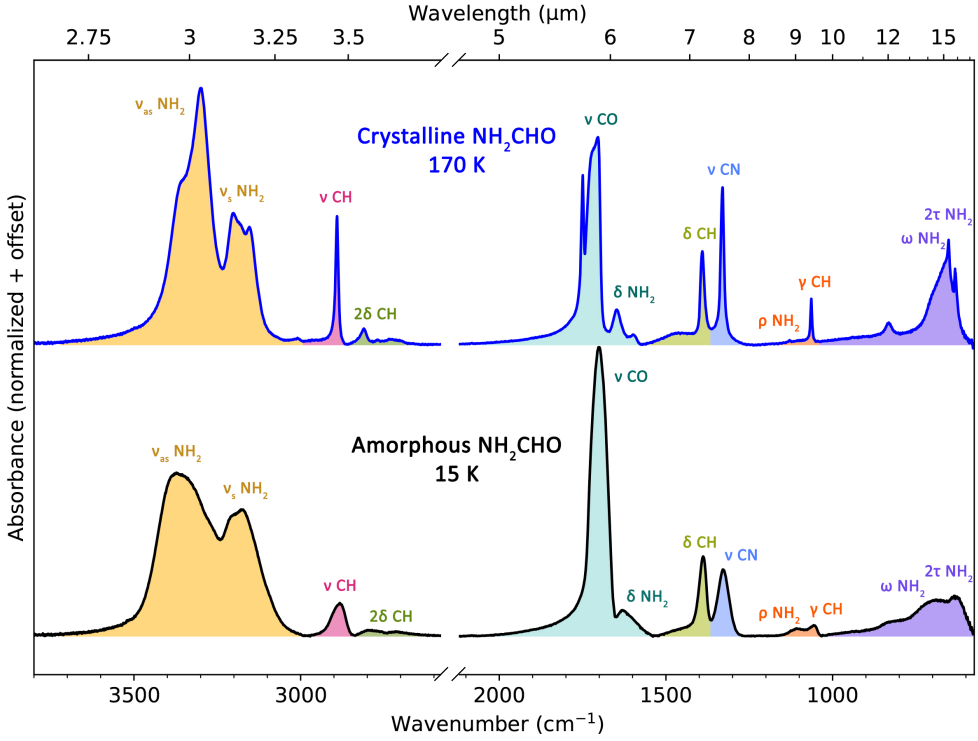


Figure 6.2: Infrared spectra in the range 3800 - 575 cm^{-1} of both amorphous and crystalline formamide (NH_2CHO). The integrated regions used to calculate the band strengths in Table 6.2 are indicated via the shaded areas under the peaks.

35% compared to those given for the same peak values in Brucato et al. (2006). As integration bounds were not provided by Brucato et al. (2006), any discrepancies in band strengths may be caused by differences in chosen integration regions.

The transition from amorphous to crystalline formamide is observed at 170 K, indicated by its bands becoming sharper and narrower and some peaks splitting. The amorphous nature of almost all of the pure and mixed ices collected at 15 K can be ascertained from their spectra, which have typical amorphous features that show evidence of matrix crystallization during the warm-up phase of the experiments. This excludes the mixtures containing CO, whose phase at 15 K in these experiments may be crystalline given recent investigations of CO ice structure $\geq$10 K He et al. (2021); Gerakines et al. (2023); Rachid et al. (in prep.).

Figure 6.3 presents the spectrum of pure formamide ice along with the spectra of the pure matrix components, all at 15 K. The formamide peaks indicated in the shaded areas were selected for full characterization (i.e., their peak positions, FWHMs, and relative band strengths are determined for mixtures): the overlapping C=O stretch and NH_2 scissor at 1700.3 cm^{-1}/5.881 μm and 1630.4 cm^{-1}/6.133 μm, respectively, and the slightly overlapping CH bend and CN stretch at 1388.2 cm^{-1}/7.204 μm and 1328.1 cm^{-1}/7.529 μm, respectively. These peaks were selected because they are strong, have sharp profiles, and overlap the least

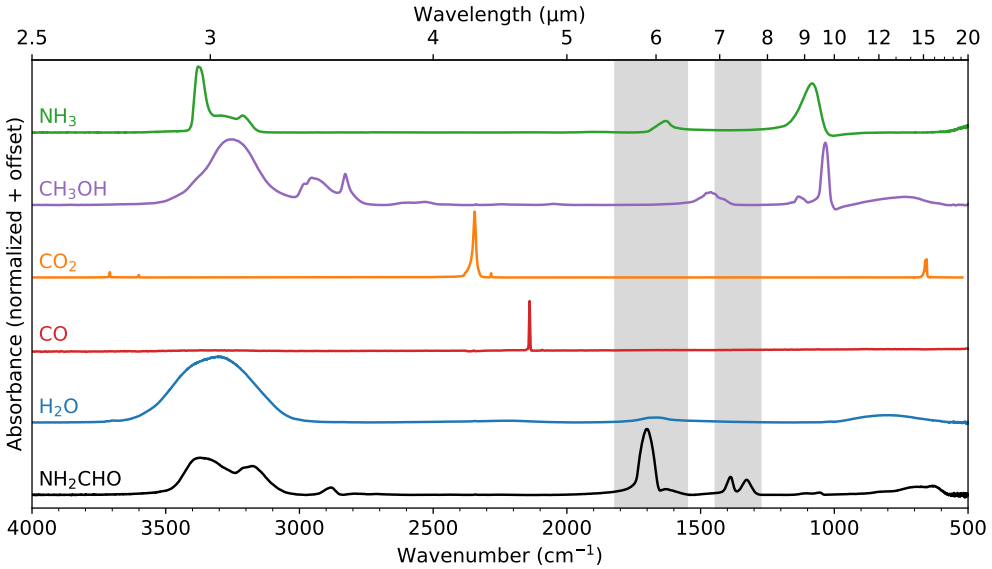


Figure 6.3: Infrared spectra of pure formamide (NH_2CHO) and five molecules observed in high abundances in interstellar ices that are present in the mixtures analyzed in this work (H_2O, CO, CO_2, CH_3OH, NH_3), all at 15 K. Peaks selected for further characterization in mixtures are indicated in the shaded areas.

with the major peaks of the most common interstellar ices, making them the best candidates for identifying formamide in interstellar ice spectra. There is still some overlap between these formamide peaks and some minor peaks of the matrix components, namely the water OH bend at ∼1600 cm^{-1}/6.25 μm, the methanol CH_3 and OH bends at ∼1460 cm^{-1}/6.85 μm, and the ammonia NH scissoring at 1624 cm^{-1}/6.16 μm. However, with sufficiently high formamide concentrations, it may still be possible to identify formamide in these spectral regions, as these matrix bands are relatively weak and broad.

The matrix- and temperature-dependent changes in these selected formamide ice bands are discussed in the following subsections, and their peak positions, FWHMs, and relative band strengths in different mixtures at various temperatures are reported in Appendices 6.A.1 and 6.A.2. The NH_2 stretching features at 3371.2 cm^{-1}/2.966 μm and 3176.4 cm^{-1}/3.148 μm and the NH_2 wagging and twisting features at 689.2 cm^{-1}/14.510 μm and 634.0 cm^{-1}/15.773 μm were excluded from further characterization despite their relatively large band strengths due to their direct overlap with the two most intense water features, the OH stretch at ∼3279 cm^{-1}/3.05 μm and the H_2O libration at ∼780 cm^{-1}/12.8 μm, respectively (Öberg et al. 2007). The remaining formamide bands, the CH stretch at 2881.9 cm^{-1}/3.470 μm, the CH bend overtone at 2797.7 cm^{-1}/3.574 μm, and the convolved NH_2 rock at 1108.1 cm^{-1}/9.024 μm and CH out-of-plane deformation at 1056.1 cm^{-1}/9.469 μm, have low band strengths and directly overlap with various methanol features: the CH_3 stretches at 2950 cm^{-1}/3.389 μm and 2830 cm^{-1}/3.533 μm, the CH_3 rock at 1126 cm^{-1}/8.881 μm, and the C-O stretch at 1027 cm^{-1}/9.737 μm (Luna et al. 2018).

6.4.1 C=O stretching and NH_2 scissoring features ($\sim$1700 and 1630 cm^{-1})

Figure 6.4 shows how the profile of the C=O band (1700.3 cm^{-1}/5.881 μm) changes in different mixtures and temperatures and presents the peak positions and FWHMs of these spectra in a scatter plot. This type of scatter plot can help to narrow down the possible thermochemical environments of molecules identified in observations (see Section 6.5). The right bottom plot in the figure shows the strengths of the band in the different mixtures at 15 K relative to the value of the band strength of pure formamide. The integrated regions used to calculate these band strengths also include the NH_2 scissoring mode, which presents as a weak, broad feature overlapping with the red shoulder of the C=O stretch (see Figure 6.4). The FWHM and relative band strengths of the formamide:NH_3 mixture are excluded from the bottom scatter plots in Figure 6.4 and the tables in Appendix 6.A.1 due to the significant overlap of this band with ammonia's NH scissoring mode at 1624 cm^{-1}/6.16 μm. The NH_3 peak is small enough in the NH_3-containing tertiary mixtures relative to the formamide C=O stretch to extract reliable peak positions and FWHMs, but relative band strengths were not calculated.

In pure amorphous formamide (<170 K), the C=O stretch appears as a single broad peak centered at 1704.2 cm^{-1}/5.868 μm. Generally, being in a mixture causes the feature to sharpen, most dramatically so in apolar mixtures in which CO or CO_2 are the dominant species. For example, the FWHM of the feature in formamide:CO_2 at 15 K is 51.1 cm^{-1}, over three times narrower than that in pure formamide. Also, in the CO, CO:CH_3OH, and crystalline CO_2 matrices, some peak splitting occurs before the formamide crystallization temperature is reached. Such sharpening and splitting is typical when a polar molecule is highly diluted in an apolar matrix and is caused by the polar molecule being isolated in the matrix as a monomer or dimer, unable to form the hydrogen bonds with other polar molecules that tend to broaden and blend vibrational features (e.g., Ehrenfreund et al. 1996). Urso et al. (2017) also previously observed the formamide peaks splitting due to monomer and dimer formation in their very dilute 1:40 formamide:CO mixture. In the polar mixtures, however, as hydrogen bonding with the matrix is still possible, the feature remains broad. The feature is the most blue-shifted in the binary CO and CO_2 mixtures, where its peak values are 1717.2 and 1703.7 cm^{-1}, respectively, in the 15 K ices, while in polar mixtures it tends to red-shift, with the most red-shifted peak position being that of the tertiary H_2O:CO_2 mixture, 1694.0 cm^{-1}. Despite containing a high fraction of apolar CO, the tertiary mixtures with CO:CH_3OH and CO:NH_3 have peak positions similar to the polar mixtures. The relative band strength of this formamide feature is >1 in all of the investigated matrices, with no observable trend related to polarity present in these values.

At formamide's crystalline phase transition temperature (170 K), the C=O peak blue-shifts and splits into multiple blended features. This is only observed in the pure formamide spectrum because all of the matrix molecules investigated here desorb below 170 K. An interesting trend to note is that, as the mixtures increase in temperature, the formamide C=O feature tends to broaden to have a FWHM value more similar to that of pure formamide. This trend can be easily identified in the scatter plot in Figure 6.4, where the scatter points of several of the mixtures move closer to the points of the pure amorphous spectrum as temperature increases. It is also particularly noticeable in Figure 6.4 in the spectra of mixtures containing H_2O, which have peak position and FWHM values at high temperatures (>150 K) that are the close to those of the pure spectrum. Sudden broadening of the FWHM to a value closer to that of pure formamide also tends to occur at the matrix crystallization temperatures (for example, in

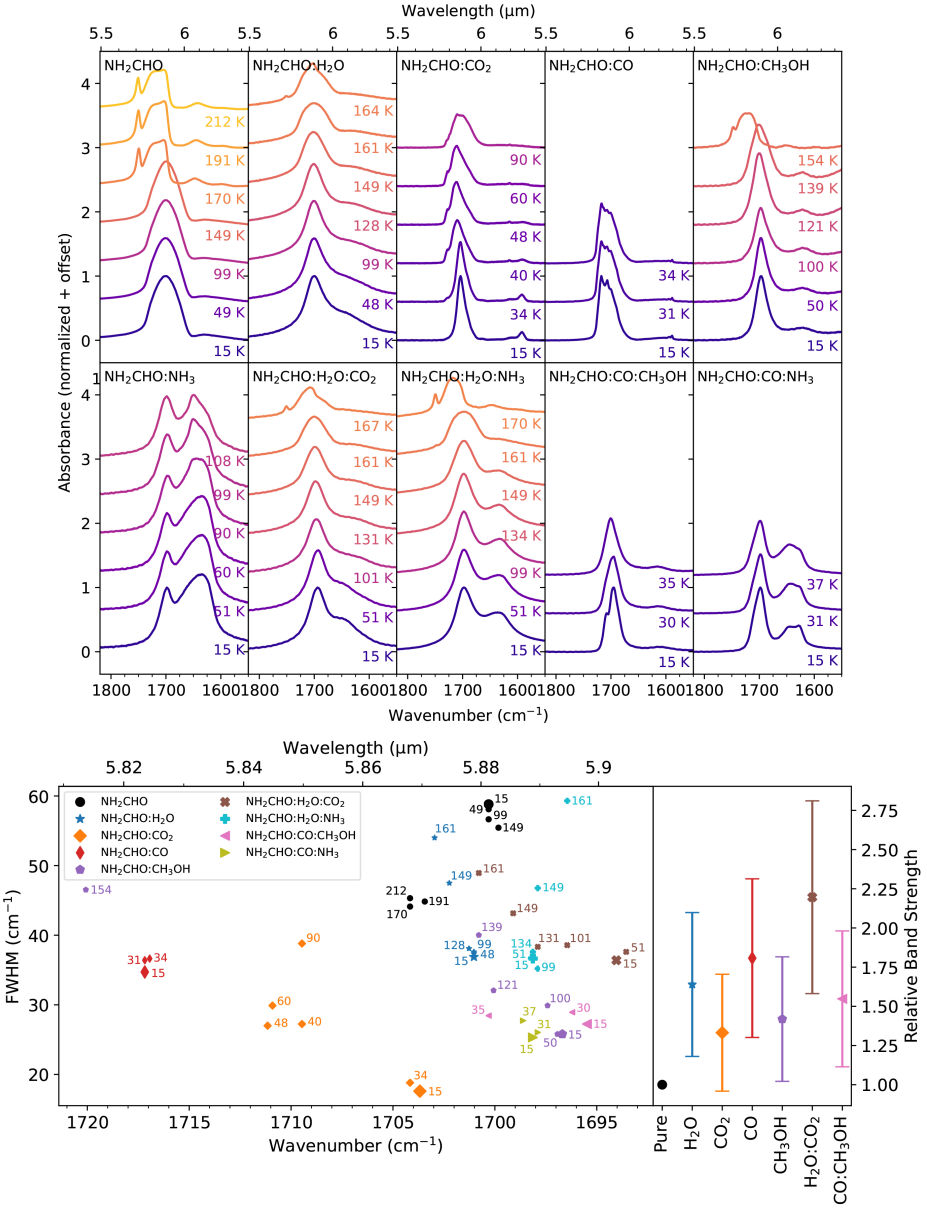


Figure 6.4: Characterization of the C=O stretching and NH_2 scissoring bands of NH_2CHO. Top: the C=O stretching and NH_2 scissoring bands of NH_2CHO in pure and mixed forms at selected temperatures. Bottom left: the peak position and FWHM of the formamide C=O stretch in pure and mixed forms at selected temperatures. Bottom right: the band strengths of the formamide C=O stretch and NH_2 scissor in mixtures relative to the pure band strength (all at 15 K).

the binary CO_2 mixture between ∼30 and 40 K and in the H_2O-containing mixtures between ∼130 and 150 K). These spectral changes indicate that formamide segregation is occurring in the matrix as the ice is heated and is particularly promoted when the ice undergoes a dramatic restructuring during matrix crystallization. The conclusion that solid-phase formamide diluted in a matrix is mobilized via heating is consistent with formamide thermal processing studies, in which formamide deposited on top of water ice diffused through the water during heating (Chaabouni et al. 2018).

6.4.2 CH bending and CN stretching features (∼1388 and 1328 cm^{-1})

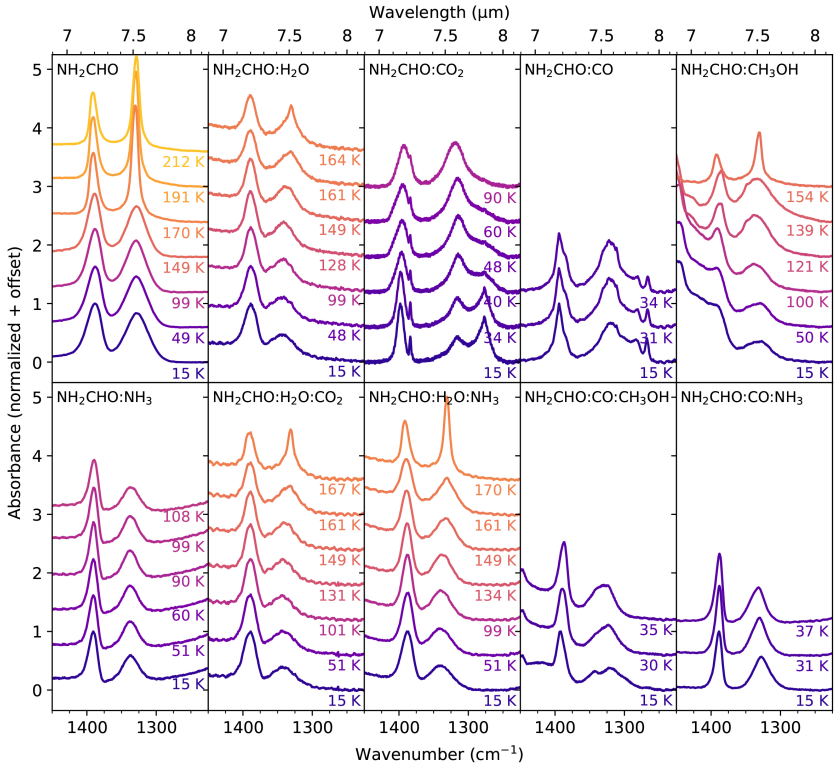


Figure 6.5: CH bending and CN stretching bands of NH_2CHO in pure and mixed forms at selected temperatures.

The shape and position of the CH bend (1388.1 cm^{-1}/7.204 μm) does not vary much depending on chemical environment or temperature, with peak positions only ranging from 1398.0 - 1387.2 cm^{-1} and FWHM values ranging from 11.1 - 27.5 cm^{-1} in the mixtures investigated here (see Figures 6.5 and 6.6). As in the C=O stretch band, the binary apolar mixtures with CO and CO_2 have the most blue-shifted and narrow peaks; however, a trend of the mixture band shifting during heating to peak position and FWHM values closer to those of the pure band is not as clear. The band strength of the CH bend increases in all of the mixtures

(e.g., η=1.63 at 15 K in the formamide:H_2O mixture) except for the CO_2 mixture, in which the band strength decreases slightly (η=0.85 at 15 K).

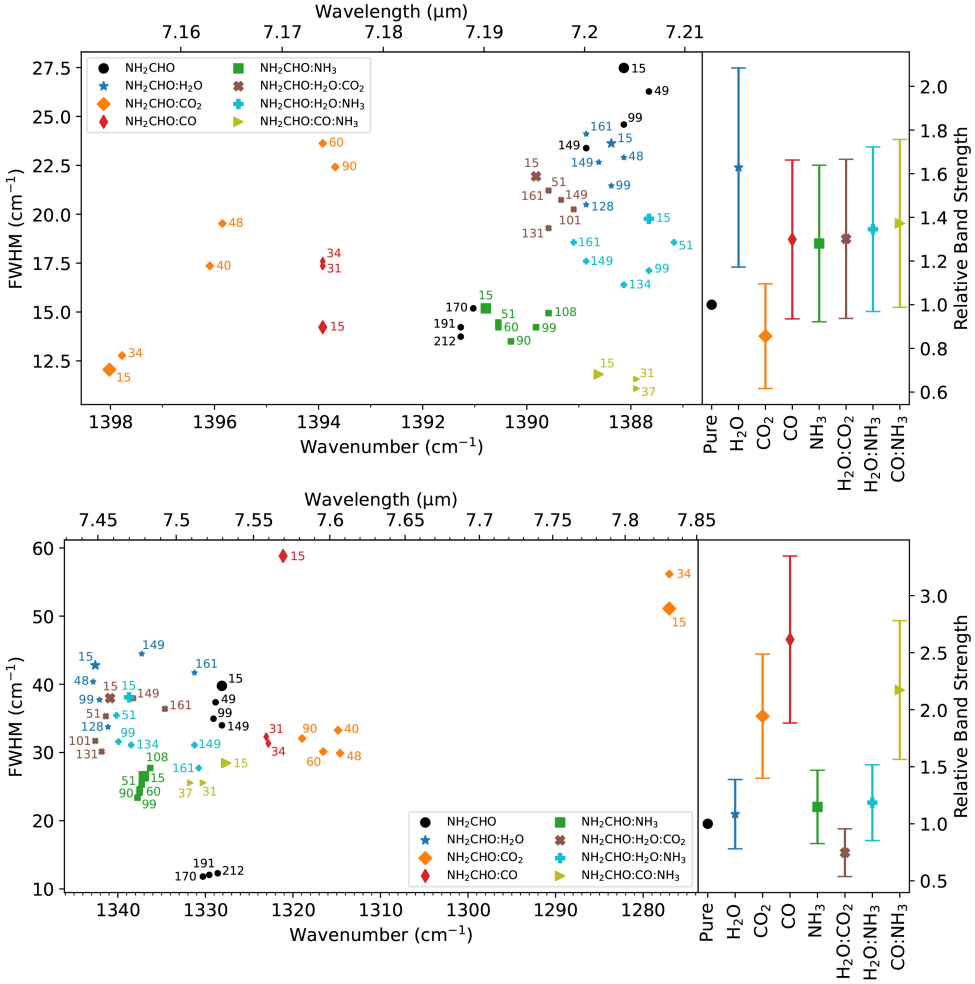


Figure 6.6: Characterization of the CH bending and CN stretching bands of NH_2CHO. Left top: the peak position and FWHM of the formamide CH bend in pure and mixed forms at selected temperatures. Right top: the band strengths of the formamide CH bend in mixtures relative to the pure band strength (all at 15 K). Left bottom: the peak position and FWHM of the formamide CN stretch in pure and mixed forms at selected temperatures. Right bottom: the band strengths of the formamide CN stretch in mixtures relative to the pure band strength (all at 15 K).

The CN stretching band (1328.1 cm^{-1}/7.529 μm) varies much more dramatically across different mixtures and temperatures (see Figures 6.5 and 6.6), particularly in the binary apolar mixtures, in which it red-shifts by up to $\sim$50 cm^{-1} and splits into multiple convolved features. In the formamide:CO_2 spectrum, two peaks are present at 15 K at 1316.8 and 1277.0

cm^{-1}, with the peak at 1277.0 cm^{-1} having a greater intensity until 40 K, at which point the intensity of the 1316.8 cm^{-1} peak increases and that of the 1277.0 cm^{-1} peak decreases. The 1277.0 cm^{-1} peak intensity then continues to decrease during heating until CO_2 sublimates at 90 K (see Figure 6.5). This trend is indicative of the 1277.0 cm^{-1} peak belonging to the formamide monomer and the 1316.8 cm^{-1} peak belonging to the formamide dimer, as it would be expected for the monomer peak to decrease and the dimer peak to increase if segregation occurs during heating, especially during a major ice structure rearrangement like matrix crystallization, which occurs for CO_2 at 40 K. Such assignments are consistent with the assignments in Mardyukov et al. (2007), who observed the formamide monomer and dimer in a xenon matrix at 1267.2 and 1305.4 cm^{-1}, respectively, and supported their assignments with computations. The peak in the formamide:CO spectrum also has a red component that appears to decrease in intensity during heating, but the monomer and dimer peaks are not as clearly distinguishable as more than two peaks appear to be overlapping in that spectrum. In the mixtures containing other polar molecules, the band is generally blue-shifted, broadened, and decreases in intensity relative to the CH bend. The relative strength of the band is close to 1 in most of the characterized polar mixtures, except for the H_2O:CO_2 mixture, which has a relative band strength of 0.75 at 15 K. In contrast, the relative band strength is closer to 2 in all of the primarily apolar mixtures.

While the CN stretch clearly has more potential than the CH bend as a diagnostic of the chemical environment of formamide, it is also much broader and less intense in most of the mixture spectra than in the pure spectra. This diminishes the ability to identify this band in a spectral region where several other astronomically relevant COMs also have features (see Section 6.5).

6.5 Astronomical implications

The ability of formamide to form via both atom addition and energetic processing in a variety of ices containing C, H, N, and O means that its solid-state presence is plausible in many interstellar environments, ranging from dark interstellar clouds to protoplanetary disks. However, in order to securely detect it, an absorption with a clear peak position and profile that is distinguishable from other ice features in the same spectral region must be identified.

The C=O stretch is amorphous formamide's strongest and sharpest feature, but it overlaps with the blue wing of the strong and broad 6.0 μm feature present in most interstellar ice spectra. Water and ammonia, which have been securely identified in ices, as well as formic acid and formaldehyde, which have been tentatively identified, have features in this spectral region (Boogert et al. 2008, 2015). Additionally, many other carbonyl group-containing COMs that have been detected in the gas-phase and may be present in the solid state, like acetaldehyde, acetone, and methyl formate, also have strong absorptions in this wavelength region (van Scheltinga et al. 2018; Rachid et al. 2020; Terwisscha van Scheltinga et al. 2021). While this limits the potential of using formamide's C=O band as its primary means of identification, the band can still be used for performing fits spanning a wider wavelength region in combination with other bands.

The CH bend and the CN stretch are medium-strength features that lie in the "COM-rich region" of interstellar ice spectra between 7-8 μm (Boogert et al. 2008). This region, where many organic functional groups have absorptions, sits on the tail of the strong 6.85 μm band

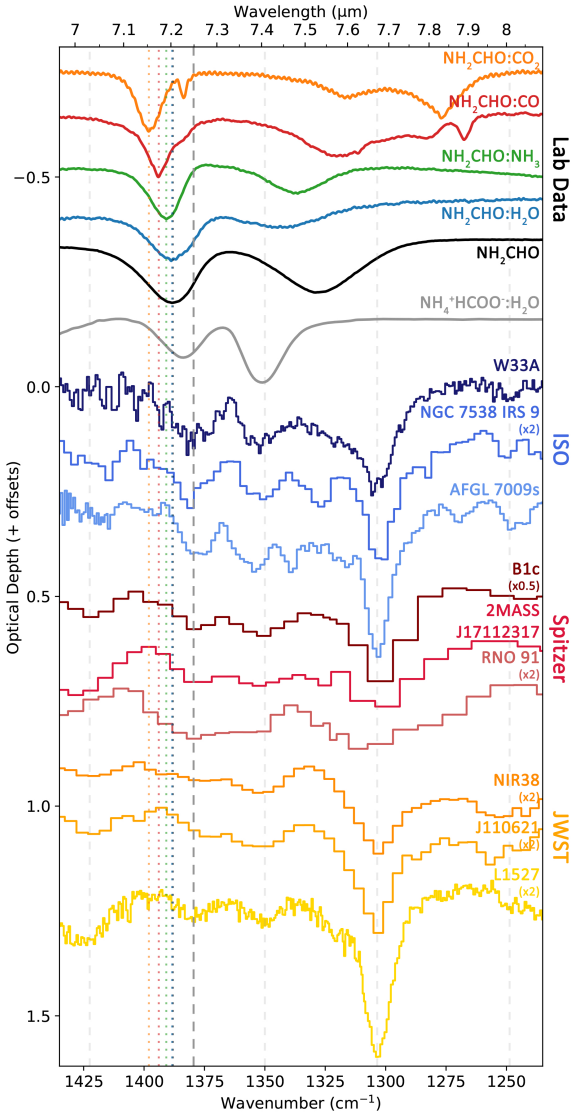


Figure 6.7: Laboratory spectra of several formamide mixtures (all at 15 K) as well as an ammonium formate:water mixture from Galvez et al. (2010) (at 150 K) versus local continuum-subtracted ISO spectra of three MYSOs (in blue), Spitzer spectra of three LYSOs (in red), and JWST spectra of both cold dense clouds in front of background stars and a LYSO (in gold). Optical depth scaling factors (if applied) are indicated via labels under the source names. Several of the band positions marked by gray dashed lines have been tentatively assigned to various COMs. The darkest gray dashed line indicates the peak position of the 7.24 μm band, and the colored dotted lines correspond to the peak positions of the formamide CH bend in the plotted formamide spectra. The wavelength calibration of the MIRI-LRS spectra, NIR38 and J110621, is still uncertain and was done for these spectra locally via the CH_4 band.

(whose assignment remains uncertain but likely contains absorptions by methanol and the ammonium cation, Boogert et al. 2008, 2015). The methane CH bending band at 7.68 μm is the most clearly and frequently observed ice band in this region (Öberg et al. 2008), but additional weaker features at 7.03, 7.24, 7.41, and 8.01 μm are also consistently observed toward some sources (Figure 6.7). Candidate carriers suggested for some of these absorptions include species like formic acid, ethanol, acetaldehyde, the formate anion, and, potentially, formamide (Schutte et al. 1999; Boogert et al. 2008; van Scheltinga et al. 2018).

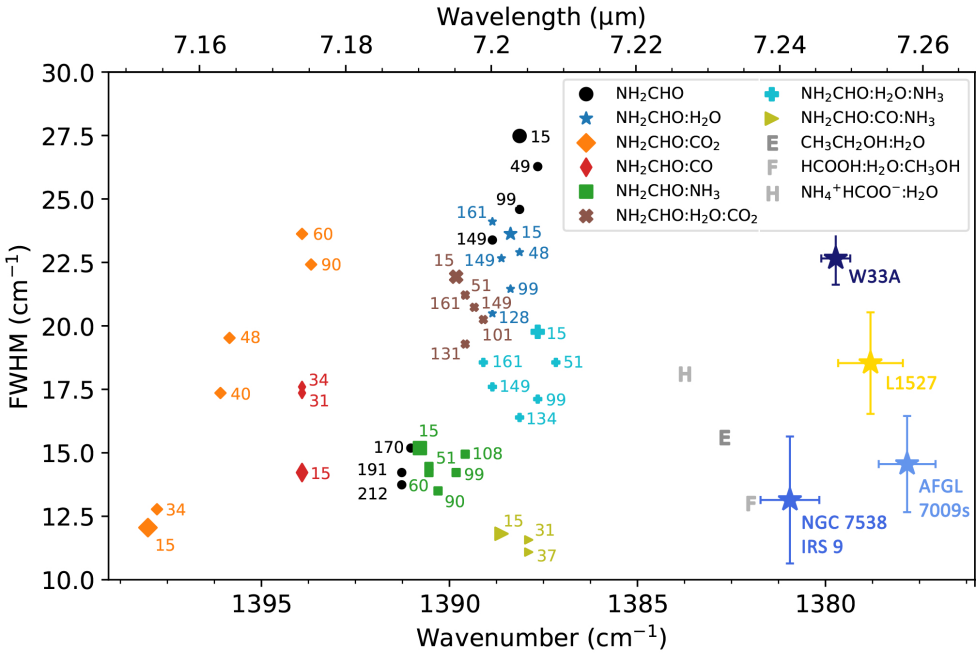


Figure 6.8: Scatter plot containing all the same peak position and FWHM values of formamide's CH bend from Figure 6.6 along with the peak positions and FWHM values of the 7.24 μm peaks in the W33A, NGC 7538 IRS 9, AFGL 7009s, and L1527 spectra shown in Figure 6.7 and laboratory spectra of CH_3CH_2OH:H_2O (van Scheltinga et al. 2018), HCOOH:H_2O:CH_3OH (Bisschop et al. 2007a) and $NH_4^+HCOO^-$:H_2O at 150 K (Galvez et al. 2010).

As mentioned previously, Schutte et al. (1999) tentatively assigned formamide as a plausible contributor to the 7.24 μm band in W33A using a formamide:H_2O spectrum and calculated a formamide ice upper limit of 2.1% with respect to H_2O, although they pointed out that in their lab data, the formamide peak position was blue-shifted by 0.02 μm relative to the observed band, and that an assignment to the CH bend of formic acid (HCOOH) may be more appropriate. Ethanol (CH_3CH_2OH) and the formate anion ($HCOO^-$) have also been considered candidates for this band (Boogert et al. 2008; Öberg et al. 2011; van Scheltinga et al. 2018; Rocha et al. 2024). No distinct and consistently observed bands are located at the peak position of the formamide CN stretch at ~7.5 μm. However, in mixtures (particularly those with polar components), the intensity and sharpness of this band weaken (relative to the intensity and sharpness of the CH bend). Such a profile change makes a distinction of the CN

stretch from the continuum in this region less feasible if formamide is present at the low ice abundances expected for COMs, especially given that around this wavelength, many sources also show a broad and significant absorption commonly attributed to SO_2 ice (Boogert et al. 1997; Öberg et al. 2008). On the other hand, the CH bend remains strong and sharp in all of the mixtures investigated here. All of the other absorption features of formamide either have profiles that are too broad or weak, or overlap directly with the strongest absorptions of the major ice components (see Figure 6.3), and will therefore not be utilized in our hunt for formamide ice.

Thus, if formamide is indeed present in interstellar ices, the CH bend is likely its best tracer. We focus our subsequent analysis on the comparison of the formamide CH bend in mixtures to the observed 7.24 μm band in nine spectra collected toward a variety of sources by ISO, Spitzer, and the recently launched JWST (Figure 6.7). The ISO (SWS) spectra include three massive young stellar objects (MYSOs), W33A, NGC 7538 IRS 9, and AFGL 7009s, and the Spitzer (IRS) spectra include three low-mass young stellar objects (LYSOs), B1c, 2MASS J17112317, and RNO 91. These archival spectra were selected due to their 7-8 μm regions having several deep and distinct features, indicating that they may be COM-rich, and because their profiles in this region slightly differ, demonstrating the variety of spectral features that have been observed here. In addition, three spectra recently collected by the JWST have been included: two pristine, high-extinction dark clouds toward background stars, NIR38 and J110621, observed with the Mid-InfraRed Instrument (MIRI) Low-Resolution Spectrometer (LRS) (McClure et al. 2023) in the ERS program Ice Age (program 1309, PI: M. McClure), and a Class 0/I low-mass protostar, L1527, observed with the MIRI Medium-Resolution Spectrometer (MRS) in the GTO program JOYS (program 1290, PI: E. F. van Dishoeck, van Dishoeck et al. 2023). These are some of the first spectra ever collected of such low-flux sources. While the resolution of the ISO data is comparable to that of the JWST data, the resolution of the Spitzer data is significantly lower (R$\sim$60-100), limiting its use in the analysis of weak and narrow bands.

The 7.24 μm band is present to some extent in all of the sources, usually at an optical depth similar to the 7.41 μm band in the local continuum-subtracted spectra. The position and FWHM of the band were extracted from the spectra that have spectral resolutions high enough to clearly define the shape and position of the peak – that is, the ISO-SWS and JWST MIRI-MRS MYSO spectra – by fitting a Gaussian profile to the peak. Figure 6.8 shows these observed peak positions and FWHMs (indicated with star shapes) in a scatter plot with the peak positions and FWHMs of the CH bend extracted from the laboratory spectra. The peak positions and FWHMs extracted from laboratory spectra of ethanol in a H_2O mixture (van Scheltinga et al. 2018), formic acid in a H_2O:CH_3OH mixture (Bisschop et al. 2007a), and ammonium formate in a H_2O mixture at 150 K (Galvez et al. 2010) are also included in this figure (indicated with the letters E, F, and H respectively) to enable a comparison between formamide and the other commonly proposed carriers. From this plot, it is evident that, while the polar mixtures have the band position and profile closest to the observations, they are all still too blue-shifted (by $\sim$7 cm^{-1}/0.04 μm) from the astronomical values for formamide to be the major carrier of this band. In contrast, ethanol, formic acid, and the formate anion in polar mixtures are much better candidates.

It is still possible that formamide could be contributing to the blue wing of this band. However, to result in non-negligible upper limits, the formamide must be present in a matrix containing other polar molecules, as the band is far too blue-shifted in the purely apolar

mixtures to contribute significantly to the observed absorption. Therefore, we derived upper limits of formamide by fitting the CH bend in the laboratory spectrum of the formamide:H_2O mixture at 15 K to the 7.24 μm band in the local continuum-subtracted observed spectra (see example fits in Figure 6.9). The water mixture was chosen for the fit for simplicity's sake and due to the fact that water is by far the most abundant interstellar ice component. The water contribution was subtracted out of the laboratory ice spectrum using a spectrum of pure water ice to ensure that absorption by the broad water bending band did not contribute to the calculated formamide upper limit. The band strength used to perform the upper limit calculation was 1.5×10^{-17} cm molec^{-1}, the band strength of the CH bend in pure formamide at 15 K (from Table 6.2) multiplied by the relative band strength of formamide in H_2O at 15 K (1.63, from Appendix 6.A.2).

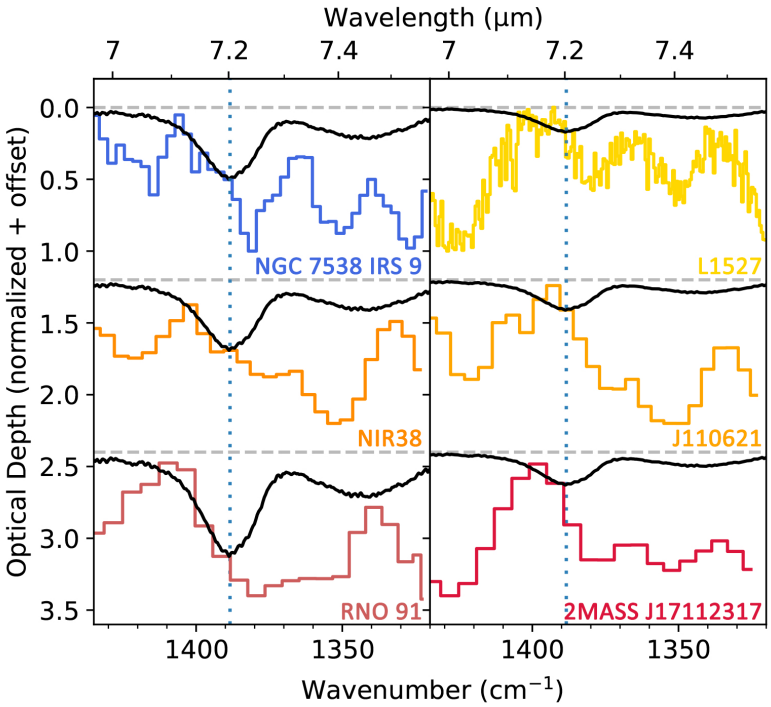


Figure 6.9: Examples of fits of the CH bending band in the formamide:H_2O laboratory spectrum (in black, water contribution subtracted out) to the local-continuum subtracted observed spectra (in color) used to derive solid-state formamide upper limits. The peak position of the CH bend in the laboratory spectrum is marked with a dotted blue vertical line. These selected fits showcase the variation in the profile of the observed 7.24 μm band across the selected sources. In the observed spectra on the left, excess absorption on the blue wing of the observed 7.24 μm band allows for relatively high formamide upper limits ($\sim\leq$1.5-5.1% with respect to H_2O), while the observed spectra on the right lack such a wing, resulting in lower formamide upper limits ($\sim\leq$0.35-0.68% with respect to H_2O).

When deriving upper limits, it is prudent to ensure that the laboratory spectrum fits to the observed spectrum across a wider wavelength range, as upper limits can be easily overestimated if only one band is considered. Subtracting out the contributions of other ices that

absorb in the analyzed spectral region, if their abundances can be unambiguously determined from other spectral regions, also prevents further upper limit overestimations. Therefore, we ensured that the calculated upper limits in Table 6.3 do not result in a C=O stretch absorption that exceeds the observed optical depth of the $\sim$6 μm band in our selected objects. Prior to checking the C=O absorption in this region, the spectral contribution of water's OH bend $\sim$1655 cm^{-1}/6.04 μm was removed from the observed spectra by scaling a laboratory water spectrum at 15 K from Öberg et al. (2007), so that the water column density of the scaled spectrum was the same as what was previously determined for these objects, and then performing a subtraction. (For the ISO and Spitzer data, the water column densities from Boogert et al. (2008) were used for scaling; for the JWST MIRI-LRS data, the water column densities from McClure et al. (2023) were used. For the JWST MIRI-MRS spectrum (L1527), the water column density was determined by first subtracting the silicate contribution by fitting the GCS3 spectrum to the 10 μm silicate band and then fitting the laboratory water spectrum from Öberg et al. 2007 to the water libration band.)

The resulting upper limits of solid-state formamide, presented in column densities as well as with respect to the abundance of water in each source, are presented in Table 6.3. These upper limits (ranging from 0.35-5.1% with respect to H_2O) are all at least an order of magnitude greater than (but consistent with) the observed gas-phase formamide abundances in three comets (0.016-0.021% with respect to H_2O) as well as the average beam dilution-corrected abundance of 22 MYSOs from the ALMAGAL survey ($\sim$0.05% with respect to H_2O, assuming a CH_3OH/H_2O ratio of $\sim$5%). As a beam dilution-corrected gas-phase formamide abundance has also been obtained for the LYSO B1c ($\sim$0.05%), one of the sources investigated here, it can be directly compared to our solid-state formamide upper limit derived from the object's low-resolution Spitzer data. While our upper limit ($\leq$0.93%) is consistent with this gas-phase abundance, it is an order of magnitude greater. We expect the precision of this upper limit to be further refined by future high-resolution observations of B1c, planned to be observed by MIRI-MRS in the JOYS program.

A formamide upper limit of 2.1% with respect to H_2O was previously derived for W33A in Schutte et al. (1999) by assuming that the entire 7.24 μm band consisted of formamide and using a band strength of 3.2 $\times$ 10^{-18} cm molec^{-1} attributed to Wexler (1967), where it is unclear for what phase of formamide this band strength was derived. Despite our very different approaches, we have fortuitously arrived at nearly the same upper limit value for W33A (2.2%).

In the higher resolution observational data of MYSOs explored here, the lack of a formamide CH bending feature distinct from other COM absorptions prevents a secure formamide ice detection. However, it is clear from the example upper limit fits shown in Figure 6.9 that the profile of the 7.24 μm feature is not uniform across different sources, and several sources, such as NGC 7538 IRS 9, NIR38, and RNO 91, may have a blue wing on this band that spectrally overlaps with the CH bend of formamide. Therefore, it is possible that a more distinct absorption at the expected 7.20 μm will emerge more clearly in sources targeted by future JWST MIRI-MRS observations. The first ice spectra arriving now from MIRI-MRS illuminate a promising future. In the spectrum of the LYSO IRAS 15398-3359 acquired by the JWST CORINOS program (program 2151, PI: Y. -L. Yang, Yang et al. 2022), the COM features between 7-8 μm previously detected barely above 3σ levels in the spectra in Figure 6.7 are beautifully resolved (although a distinct absorption centered at 7.20 μm is not present). More sources known to have strong COM absorptions in this spectral region

Table 6.3: Upper limits of formamide with respect to H_2O compared to observed abundances of formamide in various objects.

Object	$N(NH_2CHO)$ 10^{17} molec cm^{-2}	% H_2O
MYSOs		
W33A	$\leq$2.8	$\leq$2.2
NGC 7538 IRS 9	$\leq$2.0	$\leq$3.1
AFGL 7009s	$\leq$1.4	$\leq$1.2
LYSOs		
B1c	$\leq$2.8	$\leq$0.93
2MASS J17112317	$\leq$1.3	$\leq$0.68
RNO 91	$\leq$2.2	$\leq$5.1
L1527	$\leq$1.0	$\leq$0.50
Prestellar cores		
NIR38	$\leq$1.0	$\leq$1.5
J110621	$\leq$0.47	$\leq$0.35
LYSOs		
B1c (gas)	-	$\sim$0.05[a]
MYSOs		
ALMAGAL average (gas)	-	$\sim$0.05[b]
Comets		
67P (dust and gas)	-	0.004[c]
Lemmon (gas)	-	0.016[d]
Lovejoy (gas)	-	0.021[d]
Hale-Bopp (gas)	-	0.02[e]

[a] Value calculated via the beam dilution-corrected NH_2CHO/CH_3OH ratio from Nazari et al. subm., assuming a CH_3OH/H_2O ratio of $\sim$5%. [b] Value calculated via the beam dilution-corrected NH_2CHO/CH_3OH ratio of 22 MYSO sources from Nazari et al. subm., assuming a CH_3OH/H_2O ratio of $\sim$5%. [c] Value from Rubin et al. 2019. [d] Value from Biver et al. 2014. [e] Value from Bockelée-Morvan et al. 2000.

have been specifically targeted by the JOYS program as well as the JWST proposals "It's COMplicated" (program 1854, PI: M. McClure, McClure et al. 2021) and "Ice chemical complexity toward the Ophiuchus molecular cloud" (program 1959, PI: W. R. M. Rocha, Rocha et al. 2021), and these sources are scheduled to be observed throughout the remainder of this year. As demonstrated by the examples of spectral analysis of ices in this section, the laboratory spectra from this work can serve as a toolkit for formamide identification in such ice observations.

6.6 Conclusions

In an effort to facilitate the hunt for formamide in interstellar ices, laboratory spectra of pure formamide and formamide in various astronomically relevant ice mixtures ranging from temperatures of 15 - 212 K have been collected and made freely available to the astronomical community on the Leiden Ice Database for Astrochemistry (LIDA). The band strengths at 15 K for all pure formamide features between 4000 - 500 cm^{-1}/2.5 - 20 μm are presented, and the peak positions, FWHMs, and relative apparent band strengths of the three bands identified as the most promising for future formamide detection were extracted from the pure and mixed formamide spectra. These spectra and extracted data were used to assess present and future detectability of ices in various interstellar objects. The primary conclusions drawn from this work are as follows:

1. Out of the eight formamide features in the investigated IR spectral region, the C=O stretch (1700.9 cm^{-1}/5.881 μm), the CH bend (1388.3 cm^{-1}/7.203 μm), and the CN stretch (1328.0 cm^{-1}/7.530 μm) are likely to be the most useful for future formamide identification due to their strength, sharp profile, and low overlap with the strongest features of the major ice components, with the CH bending feature being the most promising. The NH_2 stretching features (3371.2 cm^{-1}/2.966 μm and 3176.4 cm^{-1}/3.148 μm) and the NH_2 wagging and twisting features (689.2 cm^{-1}/14.510 μm and 634.0 cm^{-1}/15.773 μm) directly overlap with strong water absorptions, while the CH stretch (2881.9 cm^{-1}/3.470 μm), the CH bend overtone (2797.7 cm^{-1}/3.574 μm), and the convolved NH_2 rock and CH out-of-plane deformation (1108.1 cm^{-1}/9.024 μm and 1056.1 cm^{-1}/9.469 μm) have both low band strengths and direct overlap with methanol absorptions, making them less suitable for formamide identification.

2. In the mixtures investigated here, the CN stretch is the most affected by ice composition – its peak position varies by up to $\sim$68 cm^{-1} and its FWHM by up to $\sim$50 cm^{-1} across the mixtures investigated here, with peak splitting observed in the apolar mixtures. The C=O stretch can also change significantly, depending on the matrix, by up to $\sim$27 cm^{-1} in peak position and up to $\sim$40 cm^{-1} in FWHM, although peak splitting in the apolar mixtures is not as prominent as in the CN stretch. The CH bend is relatively unaffected by ice composition, with its peak position and FWHM only varying by $\sim$11 cm^{-1} and $\sim$15 cm^{-1}, respectively, across the different mixtures. Relative to the pure spectrum, the band strength of the C=O stretch increases in all of the investigated mixtures. The CH bend band strength also increases in all of the mixtures except the binary CO_2 mixture, while a significant increase in the band strength of the CN stretch is only observed in the mixtures dominated by an apolar component.

3. Although the polar formamide mixtures provide the closest match to the 7.24 μm band observed toward nine lines of sight (including dense clouds, LYSOs, and MYSOs) with three different space telescopes (ISO, Spitzer, and JWST), none provide a convincing fit, with all having their CH bend peak position approximately 7 cm^{-1}/0.04 μm too far to the blue from the clearly observed band at 1381 cm^{-1}/7.24 μm. Instead, formic acid and ethanol mixtures containing H_2O provide a better fit. However, this does not exclude the possibility of formamide being present in these ices. The calculated formamide upper limits in these objects range from 0.35-5.1% with respect to H_2O, which

are consistent with gas-phase abundances of formamide in several LYSOs, MYSOs, and comets. The upper limit value derived for W33A, 2.2% with respect to H_2O, is fortuitously in agreement with that derived by Schutte et al. (1999).

While a more secure formamide detection is not possible with the telescopic data explored in this work, the first ice observations arriving from JWST demonstrate an unprecedented sensitivity and spectral resolution that will enable us in the near future to broaden the search for formamide ice in both objects previously observed by Spitzer, whose analysis is limited by low spectral resolution, as well as newly observed objects that were too dim to be observed by Spitzer or ISO.

6.7 Acknowledgements

This work is supported by funding from the European Research Council (ERC) under the European Union's Horizon 2020 research and innovation programme (grant agreement No. 101019751 MOLDISK), the Netherlands Research School for Astronomy (NOVA), and the Danish National Research Foundation through the Center of Excellence "InterCat" (Grant agreement no.: DNRF150). The authors acknowledge the Ice Age (program 1309, PI: M. McClure) and JOYS (program 1290, PI: E. F. van Dishoeck) observing programs for the JWST astronomical data used in this work. KS acknowledges Thanja Lamberts and Pooneh Nazari for helpful discussions about the formamide formation mechanism and Sergio Ioppolo for helpful discussions about the QMS calibration methodology.

6.A Appendix

6.A.1 Peak positions and FWHMs of formamide in pure and mixed ices

This appendix contains the peak positions and FWHMs of the formamide features selected for complete IR characterization in this work. The values are listed for the formamide features in pure ice as well as in mixtures containing H_2O, CO_2, CO, CH_3OH, and NH_3. The peak position is the wavelength at which the absorption reaches its maximum, and the FWHM is the width of the peak between the half-maximum values on each side. A Savitzky-Golay filter with a second-order polynomial was applied to many of the mixture spectra here before extraction of the peak position and FWHM to eliminate shifts in these values caused by noise. The smoothing windows used ranged from 10-100 depending on level of noise present in each spectrum, and care was taken that these smoothing windows did not warp the shape of any features. Values were extracted until the temperatures at which the major matrix component desorbed were reached.

For formamide features in mixtures where there is direct overlap with weaker matrix component bands (e.g., the C=O stretch in the NH_2CHO:H_2O mixture), the spectrum of the matrix component without formamide collected using identical experimental parameters at the corresponding temperature was scaled to the formamide mixture spectrum via a feature without overlap with formamide features and subtracted prior to peak position and FWHM extraction. These cases are denoted with a ^{M}. For formamide features in mixtures where the formamide features lie on the tails of bands or on very wide bands without sharp features (e.g., the CH

bend and CN stretch in the NH_2CHO:NH_3 mixture), a second-order polynomial was used to perform a local continuum subtraction. These cases are denoted with a ^{P}. For formamide features in mixtures where overlap with a strong matrix component band was very substantial and difficult to reliably subtract (e.g., the C=O stretch in the NH_2CHO:NH_3 mixture), only peak positions are given. These cases are denoted with a ^{N}. For formamide features that contain multiple peaks, all peak positions are given, and the FWHM of the strongest peak is given. However, if a weaker peak maximum occurs within the two half maximum values of the stronger peak (e.g., the CN stretch in the NH_2CHO:CO 15 K mixture), it is included in the FWHM. These cases are denoted with a ^{B}.

Table 6.A.4: Peak positions and FWHMs of the C=O stretch and NH_2 scissor bands of pure formamide and formamide in various binary mixtures at temperatures from 15-212 K (part 1).

Matrix	T (K)	Peak		FWHM	
		(cm^{-1})	(μm)	(cm^{-1})	(μm)
Pure	15	1700.3	5.881	58.8	0.203
		1630.4	6.133	-	-
	49	1700.3	5.881	58.1	0.201
		1632.6	6.125	-	-
	99	1700.3	5.881	56.6	0.196
		1631.1	6.131	-	-
	149	1699.8	5.883	55.4	0.192
		1629.4	6.137	-	-
	170	1704.2	5.868	44.1	0.149
		1749.2	5.717	-	-
		1647.0	6.072	-	-
	191	1703.4	5.870	44.8	0.152
		1750.0	5.714	-	-
		1644.6	6.080	-	-
	212	1704.2	5.868	45.3	0.154
		1750.4	5.713	-	-
		1642.2	6.089	-	-
H_2O^M	15	1701.0	5.879	36.9	0.128
	49	1701.0	5.879	37.4	0.129
	99	1701.0	5.879	37.6	0.130
	129	1701.3	5.878	38.1	0.132
	149	1702.2	5.875	47.5	0.164
	161	1703.0	5.872	54.0	0.187
CO_2	15	1703.7	5.870	17.6	0.061
		1591.6	6.283	-	-
	34	1704.2	5.868	18.8	0.065
		1591.6	6.283	-	-
	40	1709.5	5.850	27.2	0.093
		1591.6	6.283	-	-
	49	1711.2	5.844	27.0	0.093
		1615.2	6.191	-	-
	60	1710.9	5.845	29.9	0.103
		1614.0	6.196	-	-
	90	1709.5	5.850	38.8	0.134
		1613.8	6.197	-	-

Table 6.A.5: Peak positions and FWHMs of the C=O stretch and NH_2 scissor bands of pure formamide and formamide in various binary mixtures at temperatures from 15-212 K (part 2).

Matrix	T (K)	Peak		FWHM	
		(cm^{-1})	(μm)	(cm^{-1})	(μm)
CO	15	1717.2	5.824	34.7	0.119
		1588.9	6.294	-	-
	31	1717.2	5.824	36.4	0.125
		1588.7	6.294	-	-
	34	1716.9	5.824	36.6	0.126
		1588.7	6.294	-	-
CH_3OH^M	15	1696.7	5.894	25.8	0.090
		1623.5	6.159	-	-
	50	1696.9	5.893	25.8	0.090
		1623.3	6.160	-	-
	100	1697.4	5.891	29.9	0.104
		1621.4	6.168	-	-
	121	1700.1	5.882	32.1	0.111
		1621.4	6.168	-	-
	139	1700.8	5.880	40.0	0.139
		1621.4	6.168	-	-
	154	1720.1	5.814	46.5	0.156
		1646.9	6.072	-	-
$NH_3{}^N$	15	1698.4	5.888	-	-
	51	1698.1	5.889	-	-
	60	1697.9	5.890	-	-
	90	1696.9	5.893	-	-
	99	1697.7	5.890	-	-
	108	1698.9	5.886	-	-

Table 6.A.6: Peak positions and FWHMs of the C=O stretch and NH_2 scissor bands of formamide in various tertiary mixtures at temperatures from 15-161 K.

Matrix	T (K)	Peak		FWHM	
		(cm^{-1})	(μm)	(cm^{-1})	(μm)
$H_2O{:}CO_2{}^M$	15	1694.0	5.903	36.4	0.127
	51	1693.6	5.905	37.6	0.131
	101	1696.4	5.895	38.6	0.134
	131	1697.9	5.890	38.3	0.133
	149	1699.1	5.885	43.1	0.150
	161	1700.8	5.880	48.9	0.169
$H_2O{:}NH_3{}^M$	15	1698.1	5.889	36.6	0.127
	51	1698.1	5.889	37.1	0.129
	99	1697.9	5.890	35.2	0.122
	134	1698.1	5.889	37.6	0.131
	149	1697.9	5.890	46.8	0.162
	161	1696.4	5.895	59.3	0.206
$CO{:}CH_3OH^P$	15	1695.5	5.898	27.2	0.095
		1615.2	6.191	-	-
	30	1696.2	5.896	28.9	0.100
		1615.2	6.191	-	-
	35	1700.3	5.881	28.4	0.099
		1617.1	6.184	-	-
$CO{:}NH_3{}^M$	15	1698.1	5.889	25.3	0.088
	30	1697.9	5.890	26.0	0.090
	37	1698.6	5.887	27.7	0.096

Table 6.A.7: Peak positions and FWHMs of the CH bend band of pure formamide and formamide in various binary and tertiary mixtures at temperatures from 15-212 K.

Matrix	T (K)	Peak		FWHM	
		(cm^{-1})	(μm)	(cm^{-1})	(μm)
Pure	15	1388.1	7.204	27.5	0.142
	49	1387.7	7.206	26.3	0.136
	99	1388.1	7.204	24.6	0.127
	149	1388.9	7.200	23.4	0.121
	170	1391.0	7.189	15.2	0.079
	191	1391.3	7.188	14.2	0.074
	212	1391.3	7.188	13.7	0.071
H_2O^M	15	1388.4	7.203	23.6	0.122
	49	1388.1	7.204	22.9	0.119
	99	1388.4	7.203	21.5	0.111
	129	1388.9	7.200	20.5	0.106
	149	1388.6	7.201	22.7	0.117
	161	1388.9	7.200	24.1	0.125
CO_2	15	1398.0	7.153	12.1	0.062
		1383.7	7.227	-	-
	34	1397.8	7.154	12.8	0.065
		1383.7	7.227	-	-
	40	1396.1	7.163	17.4	0.089
		1383.9	7.226	-	-
	49	1395.8	7.164	19.5	0.100
		1383.9	7.226	-	-
	60	1393.9	7.174	23.6	0.122
		1383.9	7.226	-	-
	90	1393.7	7.175	22.4	0.116
		1384.4	7.223	-	-
CO	15	1393.9	7.174	14.2	0.073
	31	1393.9	7.174	17.4	0.090
	34	1393.9	7.174	17.6	0.091
$NH_3{}^P$	15	1390.8	7.190	15.2	0.078
	51	1390.5	7.191	14.5	0.075
	60	1390.5	7.191	14.2	0.073
	90	1390.3	7.193	13.5	0.070
	99	1389.8	7.195	14.2	0.074
	108	1389.6	7.196	14.9	0.077
$H_2O{:}CO_2{}^M$	15	1389.9	7.195	21.9	0.114
	51	1389.6	7.196	21.2	0.110
	101	1389.1	7.199	20.2	0.105
	131	1389.6	7.196	19.3	0.100
	149	1389.3	7.198	20.7	0.107
	161	1389.6	7.196	21.2	0.110
$H_2O{:}NH_3{}^P$	15	1387.7	7.206	19.8	0.103
	51	1387.2	7.209	18.6	0.096
	99	1387.7	7.206	17.1	0.089
	134	1388.1	7.204	16.4	0.085
	149	1388.9	7.200	17.6	0.091
	161	1389.1	7.199	18.6	0.096
$CO{:}NH_3{}^M$	15	1388.6	7.201	11.8	0.061
	30	1387.9	7.205	11.1	0.058
	37	1387.9	7.205	11.6	0.060

Table 6.A.8: Peak positions and FWHMs of the CN stretch band of pure formamide and formamide in various binary and tertiary mixtures at temperatures from 15-212 K.

Matrix	T (K)	Peak		FWHM	
		(cm^{-1})	(μm)	(cm^{-1})	(μm)
Pure	15	1328.1	7.529	39.8	1.226
	49	1328.8	7.525	37.4	0.212
	99	1329.1	7.524	35.0	0.198
	149	1328.1	7.529	34.0	0.192
	170	1330.3	7.517	11.8	0.067
	191	1329.6	7.521	12.1	0.068
	212	1328.6	7.527	12.3	0.070
H_2O^M	15	1342.6	7.448	42.8	0.237
	49	1342.8	7.447	40.4	0.223
	99	1342.1	7.451	37.7	0.209
	129	1341.1	7.456	33.7	0.188
	149	1337.3	7.478	44.5	0.248
	161	1331.2	7.512	41.7	0.234
CO_2	15	1277.0	7.831	51.1	0.305
		1316.8^B	7.594	-	-
	34	1277.0	7.831	56.2	0.334
		1316.8^B	7.594	-	-
	40	1314.9	7.605	33.3	0.194
	49	1314.6	7.607	29.9	0.173
	60	1316.5	7.596	30.1	0.174
	90	1319.0	7.582	32.1	0.184
CO	15	1321.1	7.569	58.8	0.344
		1283.3^B	7.793	-	-
		1267.6	7.889	-	-
	31	1323.0	7.558	32.3	0.185
		1280.9	7.807	-	-
		1266.9	7.893	-	-
	34	1322.8	7.560	31.3	0.179
		1280.6	7.809	-	-
		1266.4	7.896	-	-
$NH_3{}^P$	15	1337.0	7.479	26.5	0.148
	51	1337.3	7.478	25.3	0.142
	60	1337.5	7.477	24.6	0.138
	90	1337.8	7.475	23.4	0.131
	99	1337.5	7.477	24.1	0.135
	108	1336.3	7.483	27.7	0.155
$H_2O{:}CO_2{}^M$	15	1340.9	7.458	38.0	0.211
	51	1341.4	7.455	35.3	0.196
	101	1342.6	7.448	31.7	0.176
	131	1341.9	7.452	30.1	0.167
	149	1338.2	7.473	38.0	0.211
	161	1334.6	7.493	36.4	0.204
$H_2O{:}NH_3{}^P$	15	1338.7	7.470	38.1	0.212
	51	1340.2	7.462	35.4	0.198
	99	1339.9	7.463	31.6	0.176
	134	1339.0	7.468	30.9	0.173
	149	1331.2	7.512	31.1	0.175
	161	1330.8	7.514	27.7	0.157
$CO{:}NH_3{}^M$	15	1327.6	7.532	28.4	0.162
	30	1330.3	7.517	25.6	0.144
	37	1331.7	7.509	25.6	0.144

6.A.2 Relative apparent band strengths of formamide in pure and mixed ices

This appendix provides the relative apparent band strengths (η) of formamide, calculated via Equation 6.4, where the value of *A'* used in the calculations is the apparent band strength of the respective band in the pure amorphous formamide ice at 15 K (given in Table 6.2). Thus, the η value of each band in the pure ice at 15 K is unity. The integration ranges used to calculate the integrated absorbances are stated for each mixture individually, as the same integration ranges were not used for all mixtures due to shifting peak positions and FWHMs. Different integration ranges were used to calculate the integrated absorbances of the amorphous and crystalline pure formamide peaks for the same reason.

These η values can be used to calculate column densities or upper limits of formamide in a specific mixture and at a specific temperature by simply multiplying the corresponding relative apparent band strength by the appropriate apparent band strength in Table 6.2.

Table 6.A.9: Relative apparent band strengths of the three selected bands of pure formamide and formamide in various binary and tertiary mixtures at temperatures from 15-212 K (part 1).

Matrix	T (K)	Rel. Band Strength C=O stretch + NH_2 bend 1700.3 cm^{-1} (5.881 μm)	Rel. Band Strength CH bend 1388.1 cm^{-1} (7.204 μm)	Rel. Band Strength CN stretch 1700.3 cm^{-1} (7.529 μm)
Pure		Int. Range: 2050-1532 cm^{-1}	Int. Range: 1532-1364 cm^{-1}	Int. Range: 1364-1258 cm^{-1}
	15	1.00	1.00	1.00
	49	0.99	1.00	0.97
	99	0.96	0.99	0.93
	149	0.95	0.97	0.91
		Int. Range: 2050-1570 cm^{-1}	Int. Range: 1570-1364 cm^{-1}	Int. Range: 1364-1258 cm^{-1}
	170	0.70	1.01	1.015
	191	0.70	1.01	1.014
	212	0.60	0.82	0.857
H_2O		Int. Range: 1961-1553 cm^{-1}	Int. Range: 1532-1368 cm^{-1}	Int. Range: 1368-1258 cm^{-1}
	15	1.64	1.63	1.08
	49	1.66	1.67	1.13
	99	1.71	1.61	1.16
	129	1.63	1.57	1.18
	149	1.73	2.22	2.01
	161	1.32	2.10	2.00
CO_2		Int. Range: 1961-1532 cm^{-1}	Int. Range: 1532-1364 cm^{-1}	Int. Range: 1364-1240 cm^{-1}
	15	1.33	0.85	1.94
	34	1.34	0.84	1.88
	40	1.31	0.78	1.85
	49	1.31	0.79	1.88
	60	1.33	0.83	1.92
	90	1.36	0.93	1.91
CO		Int. Range: 1900-1500 cm^{-1}	Int. Range: 1532-1364 cm^{-1}	Int. Range: 1364-1240 cm^{-1}
	15	1.81	1.30	2.62
	31	1.81	1.34	2.71
	34	1.80	1.38	2.72
CH_3OH		Int. Range: 1800-1550 cm^{-1}	-	-
	15	1.42	-	-
	50	1.41	-	-
	100	1.39	-	-
	121	1.75	-	-
	139	1.70	-	-
	154	0.79	-	-

Table 6.A.10: Relative apparent band strengths of the three selected bands of pure formamide and formamide in various binary and tertiary mixtures at temperatures from 15-212 K (part 2).

Matrix	T (K)	Rel. Band Strength C=O stretch + NH_2 bend 1700.3 cm^{-1} (5.881 μm)	Rel. Band Strength CH bend 1388.1 cm^{-1} (7.204 μm)	Rel. Band Strength CN stretch 1700.3 cm^{-1} (7.529 μm)
NH_3		-	Int. Range: 1484-1374 cm^{-1}	Int. Range: 1374-1258 cm^{-1}
	15	-	1.28	1.14
	51	-	1.28	1.11
	60	-	1.28	1.10
	90	-	1.24	1.05
	99	-	1.39	1.13
	108	-	1.41	1.15
H_2O:CO_2		Int. Range: 1961-1553 cm^{-1}	Int. Range: 1437-1368 cm^{-1}	Int. Range: 1368-1279 cm^{-1}
	15	2.20	1.30	0.75
	51	2.18	1.23	0.67
	101	1.89	1.10	0.51
	131	1.85	0.99	0.50
	149	1.88	1.55	1.24
	161	1.57	1.42	1.33
H_2O:NH_3		-	Int. Range: 1437-1368 cm^{-1}	Int. Range: 1368-1279 cm^{-1}
	15	-	1.35	1.19
	51	-	1.36	1.21
	99	-	1.32	1.27
	134	-	1.19	1.27
	149	-	1.11	1.24
	161	-	1.01	1.22
CO:CH_3OH		Int. Range: 1810-1524 cm^{-1}	-	-
	15	1.57	-	-
	30	1.64	-	-
	35	1.68	-	-
CO:NH_3		-	Int. Range: 1460-1370 cm^{-1}	Int. Range: 1370-1256 cm^{-1}
	15	-	1.41	2.23
	30	-	1.49	2.14
	37	-	1.54	1.85

6.A.3 QMS calibration of an independent tri-dosing leak valve system and mixing ratio determination

Calibration procedure and mixing ratio determination

The new tri-dosing system mentioned in Section 6.3 allows for simultaneous but independent deposition of gases and vapors via three leak valves, each connected to a separate gas line. Compared to our previous method in which gases and vapors were premixed in the desired ice ratio in a gas bulb and then dosed into the chamber through a single valve, the new method allows for codepositing multiple gases and vapors without experimental errors in the ratio caused by mixing gases with different volatilities in a single bulb or dosing gases that may have different flow, pumping, and substrate deposition rates through the same valve. Subsequently, it greatly improves the ability to create mixtures with precisely determined ratios of molecules with low volatilities like formamide, which is challenging in traditional premixing procedures. The benefits of independent multidosing systems were also described for similar systems with two leak valves in Gerakines et al. (1995) and Yarnall & Hudson (2022).

There are several ways to calibrate such a system to ensure a certain ratio of ice components. One such method is calibrating the deposition rate on the substrate to a specific leak valve position with a specific pressure of the gas or vapor of choice in its manifold line. However, because formamide has a very low vapor pressure compared to liquids like H_2O and CH_3OH and tends to stick to and condense in various parts of the line, reproducing a specific line pressure throughout multiple experiments using this method is difficult. Therefore, to conduct a systematic and thorough IR characterization of formamide in a wide variety of ices with precisely constrained mixing ratios, a different method is necessary.

For this purpose, we calibrate molecules' ice deposition rates with the intensity of their mass signals during the deposition with a QMS. In this calibration procedure, a pure molecule is dosed at a constant rate into the chamber, with the substrate cooled to the desired deposition temperature and the IR spectrometer continuously collecting IR spectra, while the QMS continuously collects mass peak intensity values of selected mass-to-charge ratios (m/z) in the selected ion monitoring (SIM) mode. The IR spectrometer is used to measure the ice column density rather than the laser interference because the formamide deposition pressure does not remain stable over the long period of time necessary to generate multiple interference fringes ($>$18 hours), which is necessary to reliably extract a deposition rate. Conversely, a deposition rate can be extracted from integrated absorbance growth rates (obtained via a least-squares fit to the integrated absorbance over time) in $\sim$30 mins, during which time the formamide deposition rate remains stable (as indicated by the linearity of the integrated absorbance increase over time). The integrated absorbance growth rate for that molecule can then be correlated to a specific mass peak's signal intensity (typically the molecule's base peak) in the QMS (obtained via averaging the mass peak's signal intensity values collected during the deposition and simultaneous IR data collection). The integrated absorbance growth rate can then be converted to the ice column density growth rate, *dN/dt*, via the following equation if the band strength of the pure molecule, *A*, is known:

$$\frac{dN}{dt} = \frac{2.303}{A} \times \frac{d \int abs(\nu)\, d\nu}{dt}. \tag{6.A.5}$$

Table 6.1 provides the peak used for the calibration of each pure molecule and its corre-

sponding band strength and reference.

Table 6.A.11: Peaks and their band strengths used to obtain calibration curves of the pure molecules.

Molecule	Calibration peak (cm^{-1} — μm)	Band strength used (10^{-17} cm $molec^{-1}$)
NH_2CHO	1701 — 5.88	6.4 (this work)
H_2O*	3280 — 3.05	20. (Bouilloud et al. 2015)
	1660 — 6.02	1.1 (Bouilloud et al. 2015)
CO_2*	2343 — 4.27	13. (Bouilloud et al. 2015)
	665 — 15.3	1.8 (Bouilloud et al. 2015)
CO	2139 — 4.67	0.87 (González Díaz et al. 2022)
CH_3OH*	1027 — 9.74	1.61 (Luna et al. 2018)
	1460 — 6.85	1.1 (Luna et al. 2018)
NH_3	1071 — 9.34	1.95 (Hudson et al. 2022)

* If two calibration peaks are listed, then both peaks were utilized to create the calibration curve, with the peak with a lower band strength used to calculate the ice's column density at the higher deposition rates to avoid saturation effects in the calibration curve.

Via this method, a calibration curve relating a mass peak's signal intensity in the QMS to its column density growth rate can be determined, with the slope of this curve referred to here as a molecule's *sensitivity* (see Figure 6.A.10 for an example of such a calibration). When starting a deposition, the leak valve can then be opened accordingly so that the mass signal of the molecule in the QMS corresponds to the desired column density growth rate. In this work, such calibration curves were completed for all molecules used in these spectra with a Spectra Microvision Plus QMS. The relationship between column density growth rate and QMS signal intensity is linear for all molecules within the deposition pressure ranges used (R^2 values of the linear fits ranged from 0.9699-0.9999 with an average of 0.9936).

After the experiment, the mass signal data during the deposition can be converted via the equation from the calibration curve to a column density growth rate, which is then integrated over time to give the absolute column density of each species at the end of the deposition. However, in the case that some of the species in a given mixture share their strongest mass peaks and have no alternative strong peaks without overlap with the other mixture components (which is the case for several mixtures in this work), the individual column density growth rates must be extracted from the mass spectra by utilizing ratios of a given molecule's base peak to another mass peak that is not shared with any other molecules in a given mixture. For example, the mass spectrum of formamide contains a peak at 28, the base peak of CO. Thus, during the deposition of the formamide:CO mixture, the 28 m/z signal contains contribution from both formamide and CO. The contribution of formamide to the signal at 28 m/z was calculated by dividing the signal at 45 m/z (which, in this mixture, only formamide contributed to) by the ratio of the 45 and 28 m/z peaks during pure formamide deposition. This calculated contribution was then subtracted from the 28 m/z signal to yield the CO 28 m/z signal.

In order to estimate the error of the calculated column density of each component and, subsequently, the mixing ratios in each ice, multiple sources of error have been considered.

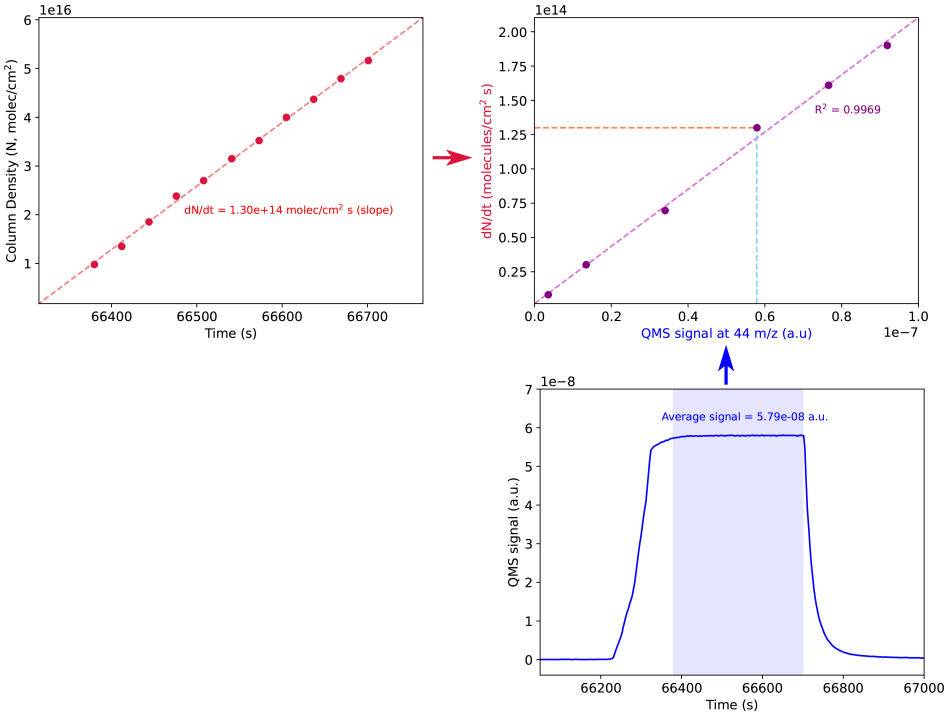


Figure 6.A.10: Example of how a calibration curve is obtained, shown here for CO. The rate of ice growth is found via monitoring the molecule's integrated absorbance of a selected peak, which can be converted to column densities via known pure band strengths, and relating them to the time of the spectrum collected (top left). Then the average value of a given mass signal (28 m/z for CO), measured by the QMS during the same time interval as the collection of the IR spectra, is calculated (bottom right). The calibration curve is obtained by correlating the two values to each other for a range of ice deposition rates (top right).

These are discussed in the following subsections.

Ion interference effect

Ion interactions within the instrument, such as ion-molecule interactions or ions interacting with the QMS filament or rods, during the dosing of multiple species into the chamber can effect a molecule's sensitivity. Such interactions between two different species can cause their sensitivities to deviate from the values determined in the calibration of each species in pure form. This phenomenon is often referred to as the *ion interference effect*, and it complicates using a mass spectrometer to quantify gases or vapors in a mixture (Basford et al. 1993; Yongjun et al. 2022).

The magnitude of this effect is highly dependent on the species as well as the instrument. It increases with total pressure and decreases for a given species as its proportion in a mixture increases (Nemanič & Žumer 2018; Sun et al. 2020). Thus, the sensitivities that are most

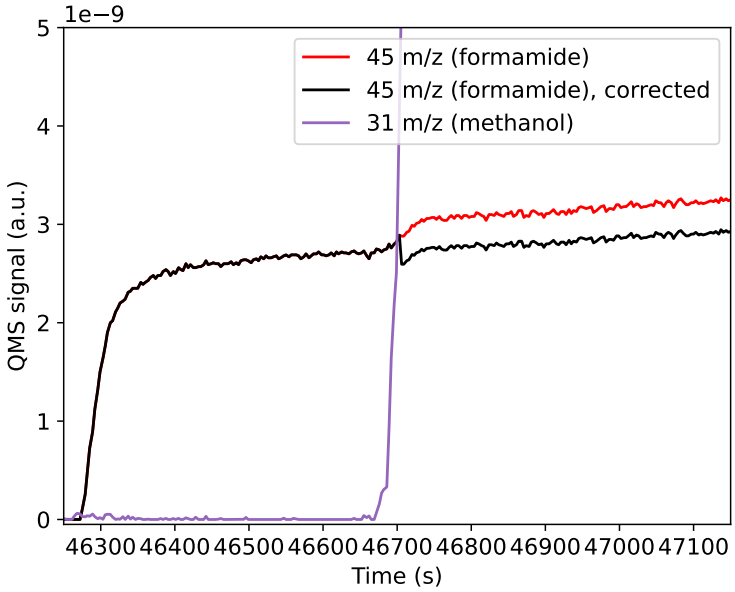


Figure 6.A.11: Correction of the ion interference effect observed in the formamide 45 m/z signal during CH_3OH codeposition.

affected by this effect are those of species that are present in the lowest proportions in a mixture. Given that our formamide dosing pressure was in the range of a couple 10^{-9} mbar and that the intended ratio of formamide to matrix components was ∼5:100 in the case of binary mixtures and 5:100:25 in the case of tertiary mixtures, we treated the interference effect of formamide on the matrix components as negligible and accounted for ion interference only in the formamide signal. While the formamide absolute column densities are necessary to calculate its relative band strengths (see Section 6.3), the absolute column densities of the matrix components are not needed to find any values other than the mixing ratios.

In order to quantify the ion interference effect on formamide in each mixture, at the start of each deposition, formamide was first dosed alone, and its mass signal was given ∼5 min to stabilize before the other matrix components were introduced into the chamber. Although this meant that each experiment started with a very brief deposition of pure formamide, the deposition rate of formamide was so slow in all of the experiments (on the order of tens of monolayers per hour) that this brief pure deposition was usually not even noticeable above the noise level in the IR spectra. Then, the ratio between formamide's signal before and after the matrix molecules were added to the chamber was used as a correction factor to remove the ion interference effect from formamide's signal. An example of this correction is shown in Figure 6.A.11 for the formamide:CH_3OH mixture, which had the highest correction factor of all the mixtures (1.11).

The ion interference effect on formamide was noticeable in all of the mixtures where the major matrix component was polar, while it was not detected above the noise level in the

mixtures in which the major matrix component was apolar. In order to provide a conservative estimate of the error caused by the ion interference effect on the calculated column density of formamide, the percent difference of the formamide column density before and after the ion interference effect correction was obtained for all mixtures in which the effect was detected above the noise level. The average percent difference was ∼5%, with the highest percent difference being that of the formamide:CH_3OH mixture (∼10%). To avoid underestimating the error in any of the mixtures, we use this maximum error, ∼10%, as the uncertainty in the column density caused by the ion interference effect.

The sensitivity of a QMS can also drift over time. However, such drift is typically only significant over timescales spanning several months to a couple years, and it is more significant for absolute sensitivities than for relative sensitivities (Ellefson et al. 1987; Lieszkovszky et al. 1990). The contribution of this drift to the method error was assumed to be negligible here given that all the formamide mixture spectra were collected within a span of two months, and that the calibration curves were usually either determined within a few days of their use to create an ice mixture or were frequently updated with new values that were consistent with the fits to the previous values.

Error calculation

In this method of determining ice column densities, multiple sources of error must be considered. First, there is the error in the method used to determine the ice column density growth rate (*dN/dt*). This error can be estimated by propagating uncertainties of the variables in Equation 6.A.5. For all ices, the integrated absorbance growth rate uncertainty is estimated to be 10%, as mentioned in Section 6.3. For formamide, the uncertainty in the band strengths reported in this work is estimated to be 15% (also see Section 6.3). For the matrix components, literature band strength values were used (see Table 6.A.11). However, in the literature, variations between the band strengths reported in different publications can be large (e.g., Bouilloud et al. 2015). For this reason, we estimate a 25% uncertainty for the literature band strengths used.

Then, we determine the uncertainty resulting from converting the integrated QMS measurement to a column density experimentally by finding the difference between the column density calculated from the QMS signal and the column density calculated from the integrated IR absorbance at the end of a pure molecule's IR measurement. Comparing these differences in formamide, H_2O, and CO deposition experiments resulted in an average error ∼2.5%. To be conservative, we estimate the error from converting the QMS measurement to a column density to be 5%.

Propagating all of these uncertainties, along with the 10% uncertainty from the ion interference effect for the formamide measurements, results in an uncertainty of ∼21% for the formamide column densities and ∼27% for the matrix column densities in the ice mixtures.

6.B Bibliography

Altwegg, K., Balsiger, H., Berthelier, J.-J., et al. 2017, MNRAS, 469, S130
Barks, H. L., Buckley, R., Grieves, G. A., et al. 2010, Chem. Bio. Chem., 11, 1240
Barone, V., Latouche, C., Skouteris, D., et al. 2015, MNRASL, 453, L31
Basford, J. A., Boeckmann, M. D., Ellefson, R. E., et al. 1993, J. Vac. Sci. Technol. A: Vacuum, Surfaces, and Films, 11, A22
Bisschop, S., Fuchs, G., Boogert, A., Van Dishoeck, E., & Linnartz, H. 2007a, A&A, 470, 749
Bisschop, S., Jørgensen, J., Van Dishoeck, E., & De Wachter, E. 2007b, A&A, 465, 913
Biver, N., Bockelée-Morvan, D., Debout, V., et al. 2014, A&A, 566, L5
Bockelée-Morvan, D., Lis, D., Wink, J., et al. 2000, A&A, 353, 1101
Boogert, A., Schutte, W., Helmich, F., Tielens, A., & Wooden, D. 1997, A&A, 317, 929
Boogert, A. A., Gerakines, P. A., & Whittet, D. C. 2015, ARA&A, 53, 541
Boogert, A. C., Pontoppidan, K. M., Knez, C., et al. 2008, ApJ, 678, 985
Bouilloud, M., Fray, N., Bénilan, Y., et al. 2015, MNRAS, 451, 2145
Bredehöft, J. H., Böhler, E., Schmidt, F., Borrmann, T., & Swiderek, P. 2017, ACS Earth Space Chem., 1, 50
Brucato, J. R., Baratta, G. A., & Strazzulla, G. 2006, A&A, 455, 395
Chaabouni, H., Diana, S., Nguyen, T., & Dulieu, F. 2018, A&A, 612, A47
Charnley, S. 1997, Editrice Compositiori, 89
Chuang, K.-J., Jäger, C., Krasnokutski, S., Fulvio, D., & Henning, T. 2022, ApJ, 933, 107
Ciaravella, A., Jiménez-Escobar, A., Cecchi-Pestellini, C., et al. 2019, ApJ, 879, 21
Codella, C., Ceccarelli, C., Caselli, P., et al. 2017, A&A, 605, L3
Corazzi, M. A., Fedele, D., Poggiali, G., & Brucato, J. R. 2020, A&A, 636, A63
Coutens, A., Jørgensen, J., Van der Wiel, M., et al. 2016, A&A, 590, L6
Dawley, M. M., Pirim, C., & Orlando, T. M. 2014, JPCA, 118, 1220
Demyk, K., Dartois, E., d'Hendecourt, L., et al. 1998, A&A, 339, 553
Douglas, K. M., Lucas, D. I., Walsh, C., et al. 2022, ApJL, 937, L16
Dulieu, F., Nguyen, T., Congiu, E., Baouche, S., & Taquet, V. 2019, MNRASL, 484, L119
Ehrenfreund, P., Schutte, W. A., & Gerakines, P. 1996, A&A, 312, 263
Ellefson, R. E., Cain, D., & Lindsay, C. N. 1987, J. Vac. Sci. Technol. A: Vacuum, Surfaces, and Films, 5, 134
Endres, C. P., Schlemmer, S., Schilke, P., Stutzki, J., & Müller, H. S. 2016, J. Mol. Spectrosc., 327, 95
Fedoseev, G., Chuang, K.-J., van Dishoeck, E. F., Ioppolo, S., & Linnartz, H. 2016, MNRAS, 460, 4297
Galvez, O., Maté, B., Herrero, V. J., & Escribano, R. 2010, ApJ, 724, 539
Garrod, R. T., Weaver, S. L. W., & Herbst, E. 2008, ApJ, 682, 283
Gerakines, P., Moore, M., & Hudson, R. 2004, Icarus, 170, 202
Gerakines, P., Schutte, W., Greenberg, J., & van Dishoeck, E. F. 1995, A&A, 296, 810
Gerakines, P. A., Materese, C. K., & Hudson, R. L. 2023, MNRAS, stad1164
Goesmann, F., Rosenbauer, H., Bredehöft, J. H., et al. 2015, Science, 349, aab0689
González Díaz, C., Carrascosa, H., Muñoz Caro, G. M., Satorre, M. Á., & Chen, Y. 2022, MNRAS, 517, 5744
Gull, M., Cafferty, B. J., Hud, N. V., & Pasek, M. A. 2017, Life, 7, 29

Haupa, K. A., Tarczay, G., & Lee, Y.-P. 2019, JACS, 141, 11614
He, J., Toriello, F. E., Emtiaz, S. M., Henning, T., & Vidali, G. 2021, ApJL, 915, L23
Hudson, R., Ferrante, R., & Moore, M. 2014, Icarus, 228, 276
Hudson, R. & Moore, M. 2000, A&A, 357, 787
Hudson, R. L., Gerakines, P. A., & Yarnall, Y. Y. 2022, ApJ, 925, 156
Jones, B. M., Bennett, C. J., & Kaiser, R. I. 2011, ApJ, 734, 78
Kaňuchová, Z., Urso, R., Baratta, G., et al. 2016, A&A, 585, A155
Kwiatkowski, J. S. & Leszczyński, J. 1993, J. Mol. Struct., 297, 277
Lago, J. L., Burcar, B. T., Hud, N. V., et al. 2020, OLEB, 50, 1
Lieszkovszky, L., Filippelli, A., & Tilford, C. 1990, J. Vac. Sci. Technol. A: Vacuum, Surfaces, and Films, 8, 3838
Ligterink, N., Terwisscha van Scheltinga, J., Taquet, V., et al. 2018, MNRAS, 480, 3628
López-Sepulcre, A., Balucani, N., Ceccarelli, C., et al. 2019, ACS Earth Space Chem., 3, 2122
López-Sepulcre, A., Jaber, A. A., Mendoza, E., et al. 2015, MNRAS, 449, 2438
Luna, R., Molpeceres, G., Ortigoso, J., et al. 2018, A&A, 617, A116
Lundell, J., Krajewska, M., & Räsänen, M. 1998, JPCA, 102, 6643
Mardyukov, A., Sánchez-Garcia, E., Rodziewicz, P., Doltsinis, N. L., & Sander, W. 2007, JPCA, 111, 10552
Martín-Doménech, R., Öberg, K. I., & Rajappan, M. 2020, ApJ, 894, 98
McClure, M., Bergin, E. A., Boogert, A. C., et al. 2021, JWST Proposal. Cycle 1, 1854
McClure, M. K., Rocha, W., Pontoppidan, K., et al. 2023, Nat. Astro., 1
Mendoza, E., Lefloch, B., López-Sepulcre, A., et al. 2014, MNRAS, 445, 151
Nazari, P., Meijerhof, J., van Gelder, M., et al. 2022, A&A, 668, A109
Nazari, P., Tabone, B., Rosotti, G., & van Dishoeck, E. subm., A&A
Nemanič, V. & Žumer, M. 2018, AIP Advances, 8, 015128
Noble, J., Theule, P., Congiu, E., et al. 2015, A&A, 576, A91
Öberg, K. I., Boogert, A. A., Pontoppidan, K. M., et al. 2008, ApJ, 678, 1032
Öberg, K. I., Boogert, A. A., Pontoppidan, K. M., et al. 2011, ApJ, 740, 109
Öberg, K. I., Fraser, H. J., Boogert, A. A., et al. 2007, A&A, 462, 1187
Pasek, M. A. 2019, Chem. Rev., 120, 4690
Quénard, D., Jiménez-Serra, I., Viti, S., Holdship, J., & Coutens, A. 2018, MNRAS, 474, 2796
Rachid, M., Brunken, N., De Boe, D., et al. 2021, A&A, 653, A116
Rachid, M., van Scheltinga, J. T., Koletzki, D., & Linnartz, H. 2020, A&A, 639, A4
Rachid, M. et al. in prep., A&A
Rachid, M. G., Rocha, W., & Linnartz, H. 2022, A&A, 665, A89
Räsänen, M. 1983, J. Mol. Struct., 101, 275
Raunier, S., Chiavassa, T., Duvernay, F., et al. 2004, A&A, 416, 165
Rimola, A., Skouteris, D., Balucani, N., et al. 2018, ACS Earth Space Chem., 2, 720
Rocha, W., Jorgensen, J., Karska, A., Kristensen, L. E., & Perotti, G. 2021, JWST Proposal. Cycle 1, 1959
Rocha, W., Rachid, M., Olsthoorn, B., et al. 2022, A&A, 668, A63
Rocha, W., van Dishoeck, E., Ressler, M., et al. 2024, A&A, 683, A124
Rubin, M., Altwegg, K., Balsiger, H., et al. 2019, MNRAS, 489, 594
Rubin, R., Swenson Jr, G., Benson, R., Tigelaar, H., & Flygare, W. 1971, ApJ, 169, L39

Saladino, R., Ciambecchini, U., Crestini, C., et al. 2003, Chem. Bio. Chem., 4, 514
Schutte, W., Boogert, A., Tielens, A., et al. 1999, A&A, 343, 966
Sivaraman, B., Sekhar, B. R., Nair, B., Hatode, V., & Mason, N. 2013, Spectrochim. Acta A Mol. Biomol. Spectrosc., 105, 238
Skouteris, D., Vazart, F., Ceccarelli, C., et al. 2017, MNRASL, 468, L1
Song, L. & Kästner, J. 2016, PCCP, 18, 29278
Sun, W., Wu, C., Cheng, Y., et al. 2020, Measurement, 164, 108099
Terwisscha van Scheltinga, J., Marcandalli, G., McClure, M. K., Hogerheijde, M. R., & Linnartz, H. 2021, Astronomy & Astrophysics, 651, A95
Torrie, B. & Brown, B. 1994, J. Raman Spectrosc., 25, 183
Urso, R. G., Scirè, C., Baratta, G. A., et al. 2017, PCCP, 19, 21759
van Dishoeck, E., Grant, S., Tabone, B., et al. 2023, Faraday Discuss.
van Scheltinga, J. T., Ligterink, N., Boogert, A., Van Dishoeck, E., & Linnartz, H. 2018, A&A, 611, A35
Vazart, F., Calderini, D., Puzzarini, C., Skouteris, D., & Barone, V. 2016, J. Chem. Theory Comput., 12, 5385
Wexler, A. S. 1967
Yang, Y.-L., Green, J. D., Pontoppidan, K. M., et al. 2022, ApJL, 941, L13
Yarnall, Y. Y. & Hudson, R. L. 2022, ApJL, 931, L4
Yongjun, C., Meng, D., Wenjun, S., et al. 2022, Meas. Sci. Technol., 33, 065019

English summary

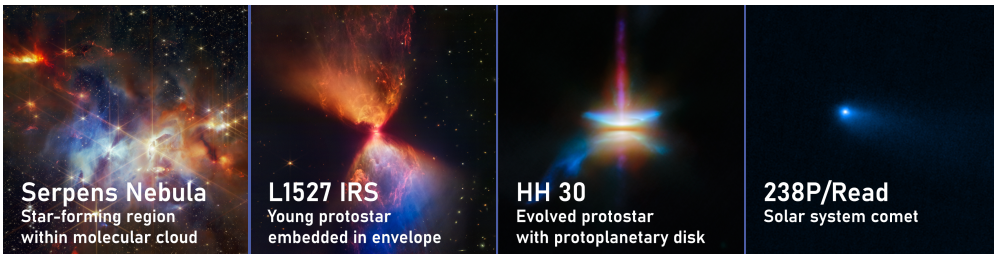


Figure 1: Four cosmic objects representing different stages of the star and planet formation sequence captured with the *James Webb* Space Telescope (JWST). All of their spectra indicate chemical inventories rich in icy volatiles. Image credits: NASA/ESA/CSA/STScI and, from left to right, 1. Klaus Pontoppidan (NASA-JPL)/Joel Green (STScI). 2. Joseph DePasquale (STScI)/Alyssa Pagan (STScI)/Anton Koekemoer (STScI). 3. Ryo Tazaki et al. 4. Mike Kelley/Henry Hsieh (PSI)/Alyssa Pagan (STScI).

Deep in the remote interstellar medium, clouds of gas and microscopic dust grains are shaped by physical processes into swirling webs of pillars, globules, and filaments. The densest depths of these clouds are largely shielded from the surrounding interstellar radiation, creating exceptionally cold and dark conditions that are, perhaps counterintuitively, ideal for chemical reactions. The cooling of the dust grains within these clouds turns them into catalytic surfaces – gaseous species stick to them and subsequently react with each other to form a plethora of volatile biogenic molecules in the form of ice layers that grow on top of the dust grains.

The most abundant of these molecules is water, which is produced particularly efficiently under such dark and dusty conditions. However, a variety of other species like methanol, formaldehyde, and ammonium salts can also be found in these ices. Eventually, the dust cloud may collapse due to its own gravity, allowing a *protostar* to begin forming at its center. The icy dust particles from the cloud – now enriched with volatile molecules – then feed the growing star and the surrounding protoplanetary disk, where its planets form. In this way, the ices grown in interstellar dust clouds become one of the primary ingredients of planetary systems and serve as a key source of biogenic volatiles during planet formation.

The work presented in this thesis investigates 1) the chemistry that occurs in interstellar ices during these earliest stages of star and planet formation, and 2) how that chemistry sets the stage for the formation of solar systems like our own and the distributions of volatiles within them. To do so, it employs infrared (IR) spectroscopy in a combined experimental and observational approach, where data collected in Earth-based laboratories that simulate interstellar conditions are used to analyze interstellar spectra observed by powerful IR facilities like the *James Webb* Space Telescope (JWST) and its predecessors. The presented studies largely target molecules that have been detected in volatile-rich and primitive small solar system bodies – particularly comets – to assess the chemical link between the interstellar medium and planetary systems.

Ice chemistry during star and planet formation

The chemical inventory of the interstellar medium (ISM) mainly consists of hydrogen and some helium atoms formed via fusion shortly after the Big Bang. Additionally, outflows from exploding dying stars supply trace amounts of heavier elements like carbon, nitrogen, oxygen, sulfur, and silicon in the form of atoms, ions, and microscopic grains of highly radiation-resistant molecules like polycyclic aromatic hydrocarbons (PAHs) and silicate minerals.

These grains shield, absorb, and scatter interstellar radiation and catalyze reactions on their surfaces, cooling their surroundings and enabling chemical reactions. In the densest regions of interstellar dust clouds, temperatures can be as low as 10 K (-263.15°C). At these temperatures, gaseous atoms and molecules that stick to the grains form layers of ices. The high abundance and mobility of hydrogen atoms on the surfaces of these grains lead to the production of reduced species such as H_2O, CH_4, and NH_3, with water being by far the most abundant. Species that are acidic can react with the base NH_3 to form ammonium salts, like NH_4SH and NH_4OCN. Organic molecules like H_2CO and CH_3OH can also form via the hydrogenation of CO that freezes out onto the grains from the gas phase. During the evolution of the cloud, different species dominate the ice chemistry at different cloud stages and cloud locations, resulting in a chemical stratification within the ice layers formed throughout a cloud's lifetime (Fig. 2). Namely, ice layers rich in water are produced largely at early, less dense cloud stages, while ice layers rich in CO and its products like CH_3OH are produced in the later, denser cloud stages.

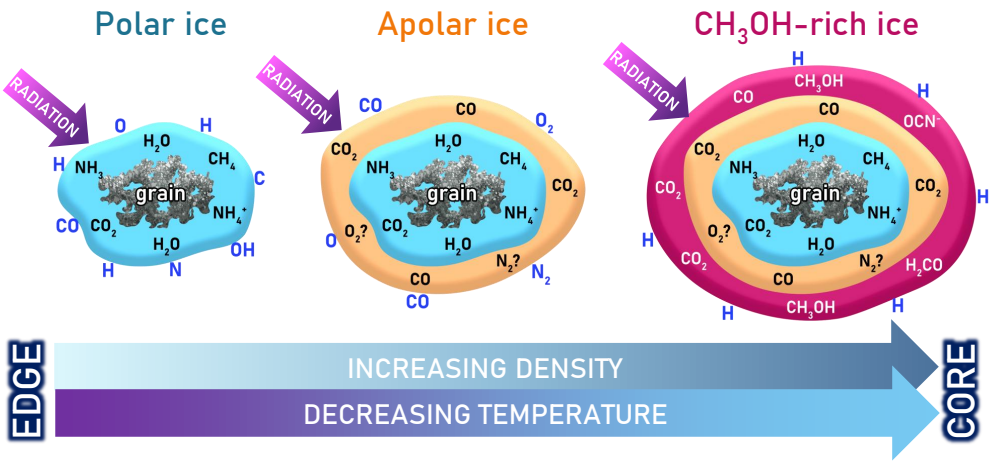


Figure 2: Different stages of ice growth in molecular clouds. In the first ice layers grown in the less dense translucent regions closer to the cloud edges, H_2O, CO_2, and hydrogenated species like NH_3 and CH_4 form. As densities increase, temperatures drop, enabling the growth of an apolar layer dominated by CO and CO_2. In the densest regions, CO is efficiently hydrogenated to form CH_3OH, resulting in a CH_3OH-rich layer that includes other species formed from CO like CO_2, OCS, and OCN^-.

If a molecular cloud is sufficiently massive and dense, gravitational instabilities and turbulence can trigger the cloud's gravitational collapse, initiating the formation of a protostellar core. The nascent protostar follows an evolutionary sequence that ends in the formation of a

star and sometimes planets. First, molecular cloud material feeds the core source, and gravitational potential energy is converted into thermal energy as the material collapses, heating the surrounding envelope of material. As the protostar continues to accrete surrounding envelope material, conservation of angular momentum results in outflows of accreted material from the source poles as well as the flattening of the inner portion of the envelope into a *protoplanetary disk*. Matter within the disk starts to coagulate into larger bodies, marking the beginnings of planetary formation. Eventually the envelope material is completely depleted via outflows and accretion, leaving only the disk and a central pre-main sequence star. Finally, the disk material is also depleted via disk winds and accretion by the source or disk planetesimals.

Ices from the molecular cloud stage are inherited by the protostellar envelope and disk, where they can transform through various physical processes (Fig. 3). One of the processes most central to this transformation is the desorption of ice species into the gas phase, which is governed by molecular *snowlines*: the thermal boundaries that define the regions where envelope or disk temperatures become warm enough to sublimate specific ice species.

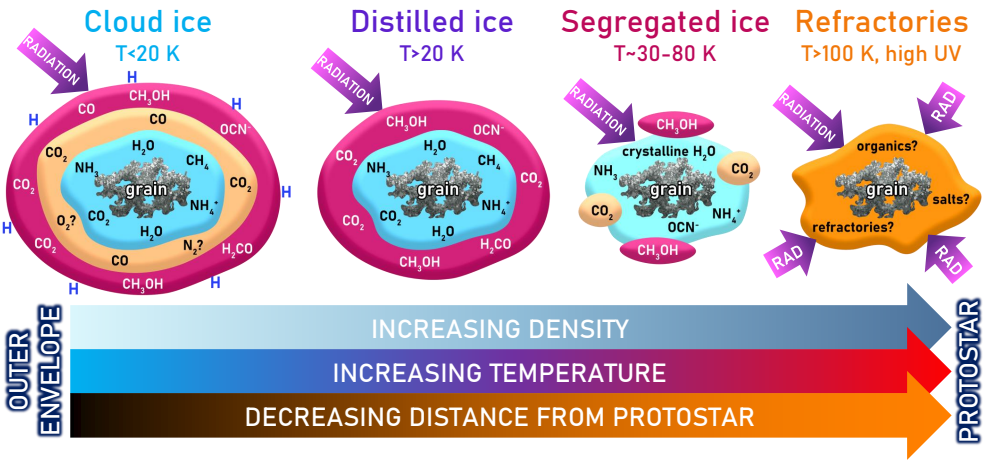


Figure 3: Changes in ice chemistry during processing in protostellar envelopes and protoplanetary disks. In the coldest envelope and disk regions, ice structures mimic those seen toward molecular clouds. As the ices move into warmer regions, hypervolatile species desorb into the gas phase, distilling the ice. Even warmer temperatures drive the segregation of certain species within the ice matrix and crystallization of the amorphous ices. Past 100 K, most of the volatile ices are expected to have desorbed into the gas, leaving behind on the grain more refractory species like salts and larger complex organics.

In younger and colder protostellar envelopes as well as the coldest, outermost regions of more evolved protostellar envelopes and the cold midplanes of protoplanetary disks, molecular cloud ices remain largely intact. As the ices move into warmer regions, they cross molecular snowlines in order of decreasing volatility, effectively *distilling* the ice layers as various ice species desorb into the gas phase, where they can further react with other gaseous species. Before inducing desorption, warmer temperatures also increase the mobility of species within the ices, leading to restructuring of the ice matrix. Additionally, increased mobility can increase rates of reactions that involve heavier species.

Snowlines in protoplanetary disks are a key factor that partially dictates the compositions

of planetary objects based on their formation locations within the disk. A given species can be accreted by planetesimals that form outside of the snowline of that species, so the starting material that forms a planetary body will depend on where that body lies in the protoplanetary disk in relation to molecular snowlines. This initial chemical record is subsequently altered by snowline changes during disk evolution, the dynamic scattering of planetary objects into different disk regions, and the geologic, atmsopheric, and space-weathering processes that planetary bodies undergo.

Small airless bodies formed in the outermost reaches of the solar system are thought to contain some of the most pristine records of volatiles inherited from interstellar ices because their small sizes preclude significant geologic or atmospheric processing, and their formation locations in the cold outer solar system allowed them to retain volatiles after their formation. Comets are a prime example, and comparisons between their volatile inventories and those of interstellar ices and protostellar gases have revealed some striking similarities. However, systematic differences between cometary and interstellar chemical inventories also point toward cometary material undergoing at least some degree of chemical processing within the protoplanetary disk.

Infrared spectroscopy of ices

Molecules absorb or emit light by transitioning between their quantized energy states. Molecules in space can be identified and quantified by their unique emission or absorption features in telescopic spectra. The ice chemistry described in this thesis is uncovered using absorption features at infrared (IR) wavelengths, which probe vibrational energy transitions.

The positions, shapes, and intensities of IR absorption peaks observed toward interstellar regions contain information about the chemical identities, quantities, and the physical and chemical environments of interstellar ices. Extracting this information requires an integrated approach in which observations are compared to models that use laboratory data.

Observational methods

Fig. 4 provides a schematic of the observing geometry used to acquire interstellar ice spectra. The telescope is aimed toward an IR light source, which can be either a background star located behind an interstellar cloud, or a protostar that is embedded within the cloud. Species located along the line of sight from the light source to the telescope are then observed against the (proto)stellar continuum. A large portion of the observational work utilized in this thesis was collected with the JWST, which has superior sensitivity, wavelength coverage, and spectral and spatial resolution compared to most previous IR telescopes. An example JWST spectrum of interstellar ices observed toward a protostar is presented in Fig. 5.

A specific molecule can be identified or ”assigned” in an interstellar IR spectrum if its characteristic IR features, defined via controlled laboratory experiments or theoretical quantum calculations, are observed. Assignments can be ascertained by comparing how closely observed peak shapes and wavelengths match those in laboratory data. Once assigned, an IR peak can be used to quantify molecules along a line of sight. In addition, peak shapes can be used to infer the physical and chemical properties of their ice carriers.

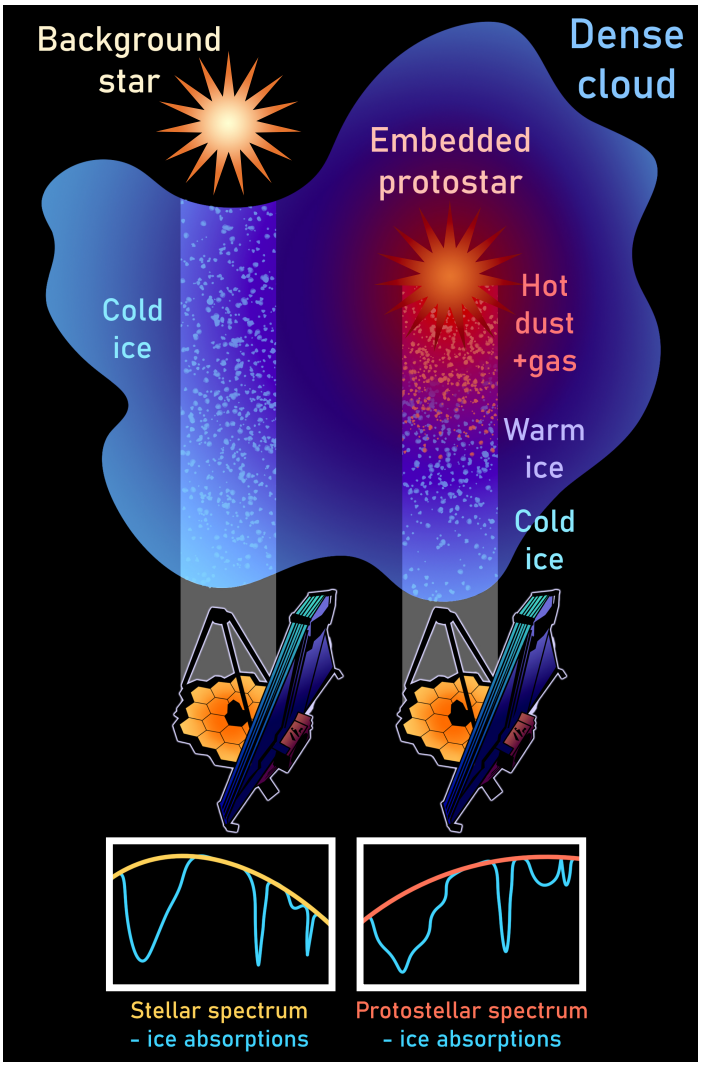


Figure 4: A schematic of how telescopes observe absorption features of interstellar ices in dense clouds and protostellar envelopes. The ices are observed along a pencil beam that traces the path from an IR light source (either an extincted background star or a protostar) to the telescope.

Laboratory methods

Laboratory measurements provide experimental data that is essential to interpreting ice observations. In such experiments, interstellar ice analogs are deposited upon a cryo-cooled flat substrate within an ultrahigh vacuum chamber with typical pressures on the order of $\leq 10^{-8}$-10^{-10} mbar (up to trillions of times lower than standard atmospheric pressure on Earth). The resulting lab-grown ice is a physical approximation of the ice layers on top of interstellar dust grains. Laboratory IR spectra of these ices are then collected, which can in some cases

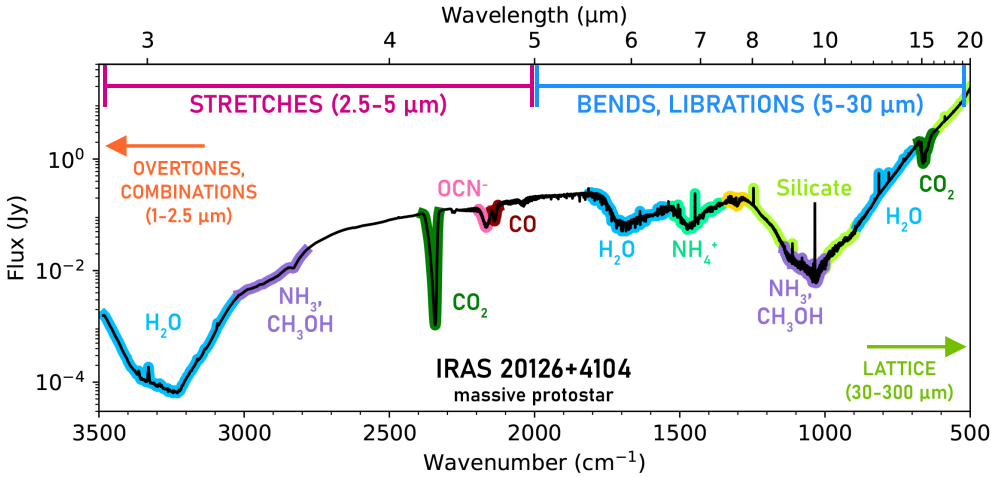


Figure 5: Example IR spectrum of a massive protostar (IRAS 20126+4104) showing interstellar ice and dust absorption features upon the protostellar continuum.

be directly compared to ice observations to identify species present in ices. Apparent band strengths of ice features can also be calculated, which can be used to quantify ice species in observations. The laboratory work presented in this thesis was conducted on the Infrared Absorption Set-up for Ice Spectroscopy (IRASIS) in the Leiden Laboratory for Astrophysics.

Thesis overview

Infrared spectroscopy has continually revealed that interstellar ices are hosts to a rich chemistry foundational to the formation and transport of volatiles in planetary systems. However, a number of questions about this chemistry remained unanswered when this thesis work began: *To what extent is interstellar ice inherited versus chemically reprocessed in protostellar envelopes and protoplanetary disks before its accretion into planetary objects? What species are the major sulfur sinks in the densest stages of star formation? Which of the many complex organic molecules detected in the gas phase in protostars can be found also in ices, and what does that tell us about their formation histories?* The chapters in this thesis address these questions.

Chapter 2: This work makes the first robust detections of the O-D stretching mode of HDO ice at 4.1 μm with JWST. It then presents a method for quantifying ice HDO/H_2O ratios toward protostars and uses this method to find this ratio toward two massive protostars observed with JWST. Ice HDO/H_2O ratios of $4.6\pm1.8\times10^{-3}$ and $2.6\pm1.2\times10^{-3}$ are obtained for the two sources. These ratios are similar to the highest reported gas HDO/H_2O ratios measured toward massive protostars and the hot inner regions of isolated low-mass protostars, suggesting that at least some of the gas HDO/H_2O ratios measured toward massive hot cores are representative of those in ices.

Chapter 3: This work presents the first detection of the 4.1 μm HDO ice feature with JWST toward a low-mass Sun-like protostar, L1527 IRS. The method developed in Chapter 2 is used to measure an ice HDO/H_2O ratio of $4.4^{+3.7}_{-1.7}\times10^{-3}$, similar to the gas HDO/H_2O ratios measured in the warm inner cores of other low-mass protostellar envelopes and protoplanetary disks found in comparably isolated star-forming regions. Such a similarity tentatively supports the assumption that water vapor detected in these regions is not significantly altered by gas-phase reactions following ice sublimation. It also supports the hypothesis that pre- and protostellar water ice is largely inherited in a chemically unaltered state by outer protoplanetary disks. However, the fraction is a factor of ∼4-10 times higher than the gas HDO/H_2O ratios measured toward comets and low-mass protostars in clustered star-forming regions, perhaps due to gas-phase water reprocessing in protostellar envelopes and protoplanetary disks or differences between prestellar conditions of isolated dense cores and the clustered star-forming regions that are more analogous to the environment in which our Sun formed.

Chapter 4: Laboratory IR spectra and apparent band strengths of ices containing NH_4SH salt were collected to investigate whether NH_4SH could be a major sulfur reservoir and a carrier of the 6.85 μm band in interstellar ices. The laboratory IR spectra were compared to those of four protostars and two dense clouds. The observed 6.85 μm feature toward these sources is fit well with laboratory NH_4SH:H_2O ice spectra. Calculated NH_4^+ column densities range from 8–23% with respect to H_2O. The apparent band strength of the SH^- feature is likely too low for the feature to be detectable, but the 5.3 μm NH_4SH combination mode may be an alternative means of detection. Its tentative assignment supports the presence of NH_4^+ salts in ices and is the first tentative observation of the SH^- anion toward interstellar ices. If the majority ($\gtrsim$80–85%) of the NH_4^+ cations quantified toward the investigated sources are bound to SH^- anions, then NH_4SH salts could account for up to 17–18% of their sulfur budgets.

Chapter 5: This chapter provides a library of new laboratory IR spectra and apparent band strengths of OCS in CH_3OH- and CO-rich ice mixtures, some of which also include H_2S and H_2O, to aid future studies of the abundance, physicochemical environment, and evolutionary history of interstellar OCS ice. Of these new laboratory spectra, tertiary OCS:CO:CH_3OH ice mixtures provide the best fits to observations of high-mass protostars, providing further evidence that OCS forms with CH_3OH, possibly via chemical pathways involving CO. A mass spectrometric calibration method for producing ice mixtures using gases and high vapor pressure liquids is described.

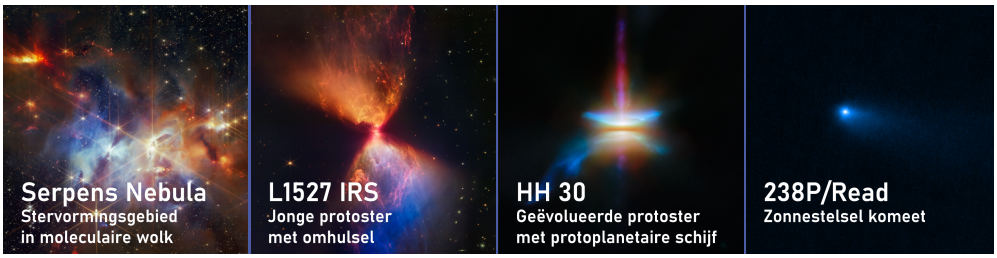
Chapter 6: Gaseous formamide has been detected in many interstellar regions, but whether it forms in the ice or gas is a topic of great debate. This chapter characterizes the IR spectra and apparent band strengths of pure and mixed formamide in interstellar ice analogs. Three formamide bands are identified as potential tracers in observational ice spectra. The laboratory spectra are compared to the 7.24 μm band in spectra of protostars and prestellar cores. If formamide ice contributes significantly to the observed band, it is more likely in a polar ice matrix, but other species provide better fits and are more likely to be the main carriers. Upper limits ranging from 0.35-5.1% with respect to H_2O were calculated, in agreement with gas-phase protostellar as well as cometary formamide abundances.

Scientific significance and future directions

- HDO ice is now robustly detectable in star-forming regions with JWST. Similarities between ice and gas water D/H ratios measured toward protostars and the gas water D/H measured toward protoplanetary disks suggest interstellar ice inheritance between protostellar envelopes and protoplanetary disks.
- Comparisons between water D/H values in protostellar ices and cometary comae suggest either some level of gas-phase water reprocessing in the protoplanetary disk *or* or an environmentally-driven diversity in prestellar water ice D/H values across different star-forming regions in our galaxy.
- Up to $\sim$20% of the sulfur in dense star-forming regions like molecular clouds and protostellar envelopes may be locked up in salts like NH_4SH, potentially resolving the decades-long puzzle of why H_2S is not detected in interstellar ices despite predictions from chemical models.
- Given their higher desorption temperatures relative to their neutral acid-base counterparts, salts like NH_4SH may have facilitated the transport of the volatile elements N and S into the inner solar system, where they could eventually be accreted by volatile-rich bodies like carbonaceous asteroids.
- Even with JWST, it may not be possible to unambiguously detect the absorption features of many of the less abundant and semi-refractory complex organic molecules like formamide due to overlaps with absorptions from more abundant and volatile organics.

Looking forward, a larger sample of ice water D/H measured toward protostars spanning a variety of environments will be needed to better constrain the ice water D/H ratio that was inherited by our solar system. Furthermore, a large fraction of the interstellar sulfur still remains missing. If it is in minerals or allotropes, chances for direct detections of such species are not promising. But wherever this missing sulfur may be, it is time for an updated sulfur ice survey with JWST data to update previous constraints. The laboratory data presented in this thesis enable such surveys. And finally, observationally targeting lines of sight with low ice-to-dust ratios but high dust columns (*i.e.*, protostellar envelopes that are still dense but have been highly thermally or energetically processed) may provide better opportunities for identifying more refractory trace ice species whose absorptions are typically overshadowed by the strong absorptions of more abundant volatiles.

Nederlandse samenvatting



Figuur 1: Vier kosmische objecten die verschillende stadia van de ster- en planeetvormingsvolgorde vertegenwoordigen, vastgelegd met de *James Webb* Space Telescope (JWST). Al hun spectra duiden op een chemische samenstelling rijk aan vluchtige ijzen. Credits: NASA/ESA/CSA/STScI en, van links naar rechts, 1. Klaus Pontoppidan (NASA-JPL)/Joel Green (STScI). 2. Joseph DePasquale (STScI)/Alyssa Pagan (STScI)/Anton Koekemoer (STScI). 3. Ryo Tazaki et al. 4. Mike Kelley/Henry Hsieh (PSI)/Alyssa Pagan (STScI).

Diep in het verre interstellaire medium worden wolken van gas en microscopische stofdeeltjes door fysische processen gevormd tot pilaren, bolwolken en filamenten. De dichtste gebieden van deze wolken zijn grotendeels afgeschermd van de omringende interstellaire straling, wat uitzonderlijk koude en donkere omstandigheden creëert die, wellicht contra-intuïtief, ideaal zijn voor chemische reacties. De afkoeling van de stofdeeltjes binnen deze wolken verandert ze in katalytische oppervlakken – gasdeeltjes hechten zich eraan en reageren vervolgens met elkaar om een overvloed aan vluchtige prebiotische moleculen te vormen in de vorm van ijslagen die bovenop de stofdeeltjes groeien.

Het meest abondante molecuul is water, dat bijzonder efficiënt wordt geproduceerd onder dergelijke donkere en stoffige omstandigheden. Er worden echter ook een verscheidenheid aan andere moleculen zoals methanol, formaldehyde en ammoniumzouten in deze ijzen gevonden. Uiteindelijk kan de stofwolk onder invloed van de zwaartekracht ineenstorten, waardoor er in het centrum een protoster kan beginnen te vormen. De ijzige stofdeeltjes uit de wolk – nu verrijkt met vluchtige stoffen – voeden vervolgens de groeiende ster en de omliggende protoplanetaire schijf, waar de planeten worden gevormd. Op deze manier worden de ijzen uit interstellaire stofwolken één van de primaire ingrediënten van planetaire systemen en dienen ze als een belangrijke bron van biogene vluchtige stoffen tijdens de planeetvorming.

Het werk gepresenteerd in dit proefschrift onderzoekt 1) de chemie die plaatsvindt in interstellair ijs tijdens deze vroegste stadia van ster- en planeetvorming, en 2) hoe die chemie de basis legt voor de vorming van zonnestelsels zoals het onze en de distributie van vluchtige stoffen daarin. Om dit te doen, maakt het gebruik van infrarood (IR) spectroscopie in een gecombineerde experimentele en observationele benadering, waarbij gegevens verzameld in aardse laboratoria die interstellaire omstandigheden simuleren, worden gebruikt om interstellaire spectra te analyseren die zijn waargenomen door state-of-the-art IR-faciliteiten zoals de *James Webb* Space Telescope (JWST) en zijn voorgangers. De studies richten zich grotendeels op moleculen die zijn gedetecteerd in primitieve kleine objecten in ons zonnestelsel – met name kometen – om de chemische link tussen het interstellaire medium en planetaire systemen te bepalen.

Ijschemie tijdens ster- en planeetvorming

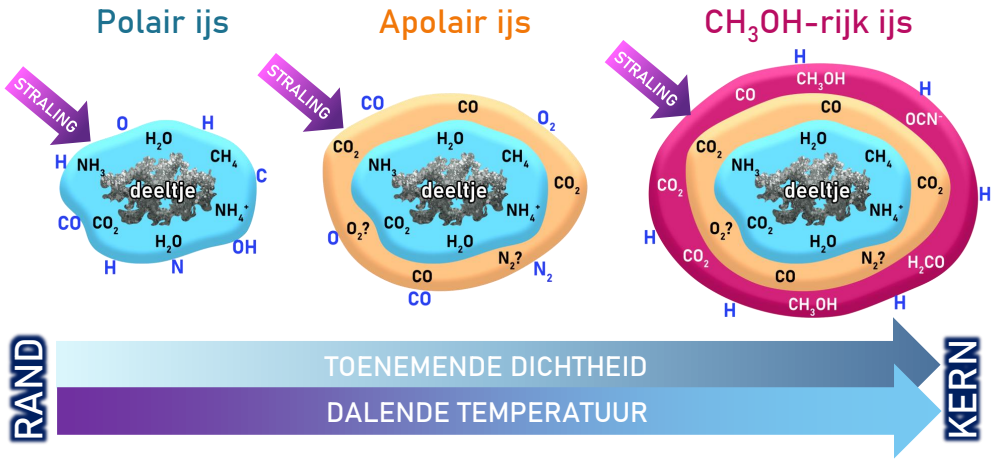
De chemische inventaris van het interstellaire medium (ISM) bestaat voornamelijk uit waterstof en enkele heliumatomen die kort na de oerknal zijn gevormd. Zwaardere elementen worden door kernfusie in het inwendige van sterren gevormd. Uitstromen van exploderende stervende sterren leveren dan miniscule hoeveelheden van zwaardere elementen zoals koolstof, stikstof, zuurstof, zwavel en silicium in de vorm van atomen, ionen en microscopische korrels van zeer stralingsbestendige moleculen zoals polycyclische aromatische koolwaterstoffen (PAK's) en silicaatmineralen.

Deze stofdeeltjes beschermen, absorberen en verstrooien interstellaire straling en katalyseren reacties op hun oppervlakken, waardoor hun omgeving afkoelt en chemische reacties mogelijk worden. In de dichtste gebieden van interstellaire wolken kunnen temperaturen zo laag zijn als 10 K (-263.15°C). Bij deze temperaturen vormen de gasvormige atomen en moleculen die aan de stofdeeltjes blijven kleven ijslaagjes. De grote overvloed en mobiliteit van waterstofatomen op de oppervlakken van deze deeltjes leidt tot de vorming van gereduceerde verbindingen zoals H_2O, CH_4 en NH_3, waarbij water verreweg het meest abondant is. Verbindingen die in chemisch opzicht een zuur zijn, kunnen reageren met een base zoals NH_3 om ammoniumzouten te vormen, zoals NH_4SH en NH_4OCN. Organische moleculen zoals H_2CO en CH_3OH kunnen ook ontstaan via de hydrogenering van CO dat vanuit de gasfase op de stofdeeltjes uitvriest. Tijdens de evolutie van de wolk domineren verschillende verbindingen de ijschemie in verschillende stadia en op verschillende locaties in de wolk, wat resulteert in een chemische gelaagdheid (Fig. 2). Namelijk, ijslagen rijk aan water worden grotendeels geproduceerd in vroege, minder dichte stadia van de wolk, terwijl ijslagen rijk aan CO en de daarvan gemaakte producten, zoals CH_3OH, worden gemaakt in de latere, dichtere stadia.

Als een moleculaire wolk voldoende massief en dicht is, kan het ineenstorten door gravitationele instabiliteiten en turbulentie, wat resulteert in de vorming van een protostellaire kern. De ontluikende protoster volgt een evolutionaire reeks die eindigt in de vorming van een ster en soms planeten. Eerst wordt de protoster gevoed door materiaal uit de moleculaire wolk, en wordt gravitationele potentiële energie omgezet in thermische energie, waardoor het omringende omhulsel van materiaal wordt verwarmd. Terwijl de protoster omringend materiaal uit het omhulsel blijft aantrekken, resulteert het behoud van impulsmoment in uitstromen van materiaal vanaf de polen van de bron. Ook wordt het binnenste gedeelte van het omhulsel afgeplat tot een *protoplanetaire schijf*. Materie binnen de schijf begint samen te klonteren tot grotere lichamen, wat het begin van planeetvorming markeert. Uiteindelijk raakt het materiaal in het omhulsel volledig uitgeput door uitstromen en accretie van materiaal op de jonge ster, waardoor alleen de schijf en een centrale pre-hoofdreeksster overblijven. Ten slotte raakt ook het schijfmateriaal uitgeput door winden en accretie, of door vorming van planetesimalen in de schijf.

IJzen uit de moleculaire wolk worden getransporteerd door het protostellaire omhulsel en de schijf, waar ze kunnen worden omgezet door verschillende fysische processen (Fig. 3). Eén van de processen die het meest centraal staat in deze transformatie is de desorptie van ijsverbindingen naar de gasfase, die plaatsvinden bij zogenaamde moleculaire *sneeuwlijnen*: de grenzen die de gebieden definiëren waar de temperaturen in het omhulsel of de schijf warm genoeg worden om specifieke ijsverbindingen te sublimeren.

In de koudere delen van protostellaire omhulsels en in de koude middenvlakken van protoplanetaire schijven, blijven de ijzen uit de moleculaire wolk grotendeels intact. Naarmate

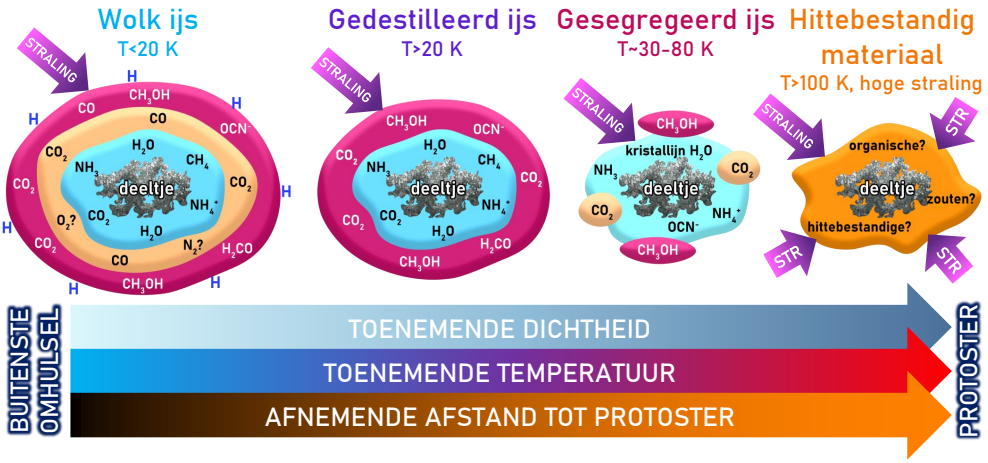


Figuur 2: Verschillende stadia van ijsgroei in moleculaire wolken. De eerste ijslagen groeien in de minder dichte, half-doorzichtige gebieden dichter bij de randen van de wolk, en bestaan uit H_2O, CO_2 en gehydrogeneerde moleculen zoals NH_3 en CH_4. Naarmate de dichtheid toeneemt, daalt de temperatuur, wat de groei van een apolaire ijslaag mogelijk maakt die wordt gedomineerd door CO en CO_2. In de dichtste gebieden wordt CO efficiënt gehydrogeneerd tot CH_3OH, wat resulteert in een CH_3OH-rijke laag die ook andere deeltjes bevat die uit CO zijn gevormd, zoals CO_2, OCS en OCN^-

de ijzen naar warmere gebieden bewegen, passeren ze moleculaire sneeuwlijnen in volgorde van afnemende vluchtigheid, waardoor de ijslagen effectief worden *gedestilleerd* terwijl verschillende ijsverbindingen sublimeren naar de gasfase, waar ze verder kunnen reageren met andere gassen. Voordat ze sublimeren, verhogen hogere temperaturen ook de mobiliteit van deeltjes binnen het ijs, wat leidt tot een herstructurering van de ijsmatrix. Daarnaast kan een verhoogde mobiliteit de snelheid verhogen van reacties waarbij zwaardere deeltjes betrokken zijn.

Sneeuwlijnen in protoplanetaire schijven zijn een sleutelfactor die gedeeltelijk de samenstelling van planetaire objecten bepaalt op basis van hun vormingslocatie binnen de schijf. Een bepaalde verbinding kan worden aangetrokken door planetesimalen die zich buiten de sneeuwlijn van die verbinding bevinden. Het startmateriaal dat uiteindelijk een planeet vormt, hangt dus af van waar dat lichaam zich in de protoplanetaire schijf bevindt ten opzichte van de sneeuwlijnen. Deze initiële chemische ordering wordt vervolgens gewijzigd door veranderingen in de sneeuwlijn tijdens de evolutie van de schijf, de dynamische verstrooiing van planetaire objecten naar verschillende schijfregio's, en de geologische, atmosferische en ruimtelijke verweringsprocessen die planetaire lichamen ondergaan.

Kleine objecten die in de buitenste delen van het zonnestelsel zijn gevormd, worden geacht de meest ongerepte samenstelling van vluchtige stoffen te bevatten die zijn overgeërfd van interstellaire ijzen: hun kleine omvang sluit aanzienlijke geologische of atmosferische verwering uit, en hun vormingslocaties in het koude buitenste deel van het zonnestelsel stelden hen in staat om vluchtige stoffen na hun vorming te behouden. Kometen zijn hier een uitstekend voorbeeld van, en vergelijkingen tussen hun samenstelling aan vluchtige stoffen en die van interstellaire ijzen en protostellaire gassen hebben enkele opvallende overeenkomsten



Figuur 3: Veranderingen in de ijschemie tijdens de evolutie van protostellaire omhulsels en protoplanetaire schijven. In de koudste gebieden van het omhulsel en de schijf lijken de ijsstructuren op die van moleculaire wolken. Naarmate de ijzen naar warmere gebieden bewegen, sublimeren de meest vluchtige deeltjes naar de gasfase, waardoor het ijs wordt gedestilleerd. Nog hogere temperaturen drijven de segregatie van bepaalde moleculen binnen de ijsmatrix en de kristallisatie van de amorfe ijzen. Boven de 100 K zijn het merendeel van de vluchtige ijzen naar de gasfase gesublimeerd, waarbij meer hittebestandige deeltjes zoals zouten en grotere complexe organische stoffen op de stofdeeltjes achterblijven.

aan het licht gebracht. Echter, systematische verschillen tussen de chemische inventaris van kometen en die van het interstellaire medium wijzen er ook op dat kometair materiaal tenminste een zekere mate van chemische bewerking heeft ondergaan binnen de protoplanetaire schijf.

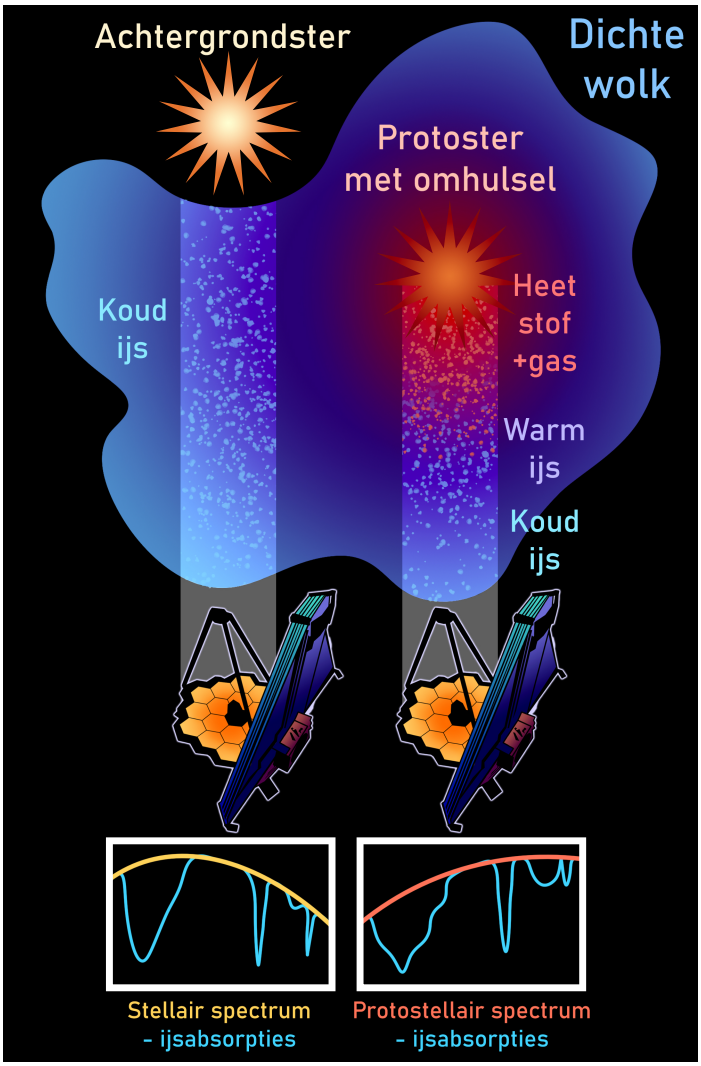
Infraroodspectroscopie van ijzen

Moleculen absorberen of zenden licht uit door overgangen tussen hun gekwantiseerde energietoestanden. Moleculen in de ruimte kunnen worden geïdentificeerd en gekwantificeerd door hun unieke emissie- of absorptiekenmerken in waargenomen spectra. De ijschemie die in dit proefschrift wordt beschreven, wordt onthuld met behulp van absorptiekenmerken op infrarode (IR) golflengten, geassocieerd met vibratie-overgangen.

De posities, vorm en intensiteiten van de IR-absorptiebanden die worden waargenomen in interstellaire gebieden bevatten informatie over de chemische identiteit, de hoeveelheden en de fysische en chemische omgevingen van interstellaire ijzen. Het extraheren van deze informatie vereist een geïntegreerde aanpak waarbij waarnemingen worden vergeleken met modellen die gebruikmaken van laboratoriumgegevens.

Observationele methoden

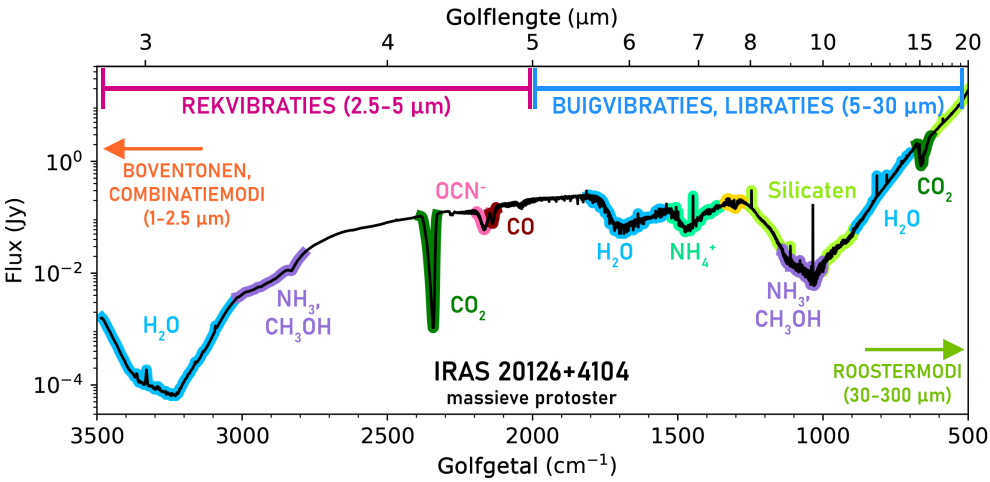
Fig. 4 geeft een schema weer van de geometrie die wordt gebruikt om interstellaire ijsspectra waar te nemen. De telescoop wordt gericht op een IR-lichtbron, hetgeen een achtergrondster



Figuur 4: Schema hoe telescopen de absorptiekenmerken van interstellaire ijzen in dichte wolken en protostellaire omhulsels waarnemen. De ijzen worden waargenomen langs een smalle lichtbundel ("pencil beam") die het pad volgt van een IR-lichtbron (hetzij een achtergrondster hetzij een protoster) naar de telescoop.

kan zijn die zich achter een interstellaire wolk bevindt, of een protoster die in de wolk is ingebed. Deeltjes die zich langs de gezichtslijn van de lichtbron naar de telescoop bevinden, worden vervolgens waargenomen tegen het (proto)stellaire continuüm. Een groot deel van de waarnemingen die in dit proefschrift zijn gebruikt, is verzameld met de James Webb Space Telescope (JWST), die een superieure gevoeligheid, golflengtebereik en spectrale en ruimtelijke resolutie heeft in vergelijking met de meeste eerdere IR-telescopen. Een voorbeeld van

een JWST-spectrum van interstellaire ijzen waargenomen bij een protoster is gepresenteerd in Fig. 5.



Figuur 5: Voorbeeld van een IR-spectrum van een massieve protoster (IRAS 20126+4104) dat absorptiekenmerken van interstellair ijs en stof laat zien gesuperponeerd op het protostellaire continuüm.

Een specifiek molecuul kan worden geïdentificeerd of "toegewezen" als de karakteristieke IR-kenmerken ervan, bepaald via gecontroleerde laboratoriumexperimenten of theoretische kwantummechanische berekeningen, worden waargenomen. Toewijzingen kunnen worden vastgesteld door te vergelijken hoe nauwkeurig de waargenomen piekvormen en golflengten overeenkomen met die in laboratoriumgegevens. Eenmaal toegewezen kan een IR-piek worden gebruikt om moleculen langs een gezichtslijn te kwantificeren. Bovendien kunnen piekvormen worden gebruikt om de fysische en chemische eigenschappen van hun ijsdragers af te leiden.

Laboratoriummethoden

Laboratoriummetingen leveren experimentele gegevens die essentieel zijn voor het interpreteren van ijswaarnemingen. In dergelijke experimenten worden interstellaire ijsanalogen uitgevroren op een cryogeen gekoeld substraat in een ultrahoge vacuümkamer met typische drukken in de orde van $\leq 10^{-8}$-10^{-10} mbar (tot biljoenen malen lager dan de standaard atmosferische druk op aarde). Dit in het lab gemaakte ijs is een fysische benadering van de ijslagen bovenop interstellaire stofdeeltjes. Vervolgens worden laboratorium-IR-spectra van deze ijzen verzameld, die in sommige gevallen direct kunnen worden vergeleken met ijswaarnemingen om de moleculen te identificeren. Ook kunnen de bandsterktes van specifieke ijzen worden gemeten, die kunnen worden gebruikt om de hoeveelheid waargenomen ijsdeeltjes te kwantificeren. Het laboratoriumwerk dat in dit proefschrift wordt gepresenteerd, is uitgevoerd op de Infrared Absorption Set-up for Ice Spectroscopy (IRASIS) in het Laboratorium voor Astrofysica in Leiden.

Overzicht van het proefschrift

Infraroodspectroscopie heeft laten zien dat interstellaire stofdeeltjes een rijke ijschemie hebben, die aan de basis ligt van de vorming en het transport van vluchtige stoffen in planetaire systemen. Echter, een aantal vragen over deze chemie bleven onbeantwoord toen dit promotieonderzoek begon: *In welke mate wordt interstellair ijs overgeërfd versus chemisch omgevormd in protostellaire omhulsels en protoplanetaire schijven voordat het opgenomen wordt in planetaire objecten? Welke deeltjes zijn de belangrijkste reservoirs voor zwavel in de dichtste stadia van stervorming? Welke van de vele complexe organische moleculen die in de gasfase bij protosterren zijn gedetecteerd, kunnen ook in ijzen worden gevonden, en wat vertelt dat ons over hun ontstaansgeschiedenis?* De hoofdstukken in dit proefschrift behandelen deze vragen.

Hoofdstuk 2: Dit werk presenteert de eerste robuuste detecties van de O-D strekkingsvibratie van HDO-ijs bij 4,1 μm met JWST. Vervolgens wordt een methode gepresenteerd voor het kwantificeren van ijs-HDO/H_2O-verhoudingen bij protosterren, en wordt de verhouding bepaald voor twee massieve protosterren die met JWST zijn waargenomen. Voor deze twee bronnen worden ijs-HDO/H_2O-verhoudingen van $4{,}6\pm1{,}8\times10^{-3}$ en $2{,}6\pm1{,}2\times10^{-3}$ verkregen. Deze verhoudingen zijn vergelijkbaar met de hoogste gerapporteerde gas-HDO/H_2O-verhoudingen gemeten bij massieve protosterren en bij geïsoleerde protosterren met een lage massa, wat suggereert dat ten minste een deel van de gas-HDO/H_2O-verhoudingen gemeten bij massieve hete kernen representatief is voor die in ijzen.

Hoofdstuk 3: Dit werk presenteert de eerste detectie van de 4,1 μm HDO-ijsband met JWST bij een zonsachtige protoster met een lage massa, L1527 IRS. De in Hoofdstuk 2 ontwikkelde methode wordt gebruikt om een ijs-HDO/H_2O-verhouding van $4{,}4^{+3,7}_{-1,7}\times10^{-3}$ te meten, vergelijkbaar met de gas-HDO/H_2O-verhoudingen gemeten in de warme kernen van andere geisoleerde lage massa protostellaire omhulsels en protoplanetaire schijven. Een dergelijke gelijkenis ondersteunt voorzichtig de aanname dat waterdamp gedetecteerd in deze gebieden niet significant wordt gewijzigd door gasfasereacties na ijssublimatie. Het ondersteunt ook de hypothese dat pre- en protostellair waterijs grotendeels in een chemisch ongewijzigde staat wordt overgeërfd door de buitenste delen van protoplanetaire schijven. Echter, de fractie is een factor $\sim$4-10 hoger dan de gas-HDO/H_2O-verhoudingen gemeten bij kometen en lage massa protosterren in stervormingsgebieden met een cluster van sterren. Wellicht komt dit door het opnieuw verwerken van water in de gasfase in de protostellaire fase en protoplanetaire schijven of door verschillen tussen de koude prestellaire condities van geïsoleerde dichte wolken en de warmere geclusterde stervormingsgebieden die meer analoog zijn aan de omgeving waarin onze zon is gevormd.

Hoofdstuk 4: Laboratorium-IR-spectra en bandsterktes van ijzen die NH_4SH-zout bevatten zijn verzameld om spectroscopisch te onderzoeken of NH_4SH een zwavelreservoir kan zijn en ook de drager van de 6,85 μm-band in interstellaire ijzen. De laboratorium-IR-spectra zijn vergeleken met die van vier protosterren en twee dichte wolken. De waargenomen 6,85 μm-band wordt goed gefit met laboratoriumspectra van NH_4SH:H_2O-ijs, en de fits leveren $NH_4{}^+$-kolomdichtheden op die variëren van 8–23% ten opzichte van H_2O. De bandsterkte van de SH^--band is waarschijnlijk te laag om detecteerbaar te zijn, maar de 5,3 μm NH_4SH combinatiemode zou een alternatieve manier van detectie kunnen zijn. De voorzichtige toewij-

zing hiervan ondersteunt de aanwezigheid van NH_4^+-zouten in ijzen en is de eerste mogelijke waarneming van het SH^--anion in interstellaire ijzen. Als het merendeel ($\gtrsim$80–85%) van de gekwantificeerde NH_4^+-kationen gebonden is aan SH^--anionen, dan zouden NH_4SH-zouten tot 17–18% van hun zwavelbudget kunnen verklaren.

Hoofdstuk 5: Dit hoofdstuk biedt een bibliotheek van nieuwe laboratorium-IR-spectra en bandsterktes van OCS in CH_3OH- en CO-rijke ijsmengsels, waarvan sommige ook H_2S en H_2O bevatten, om toekomstige studies naar de hoeveelheid, chemische omgeving en evolutionaire geschiedenis van interstellair OCS-ijs te ondersteunen. Van deze nieuwe laboratoriumspectra bieden tertiaire OCS:CO:CH_3OH-ijsmengsels de beste fits aan waarnemingen van protosterren met een hoge massa, wat verder bewijs levert dat OCS samen met CH_3OH wordt gevormd, mogelijk via chemische routes waarbij CO betrokken is. Een massaspectrometrische kalibratiemethode voor het produceren van ijsmengsels met behulp van gassen en vloeistoffen met een hoge dampdruk wordt beschreven.

Hoofdstuk 6: Formamide is regelmatig als gas in interstellaire gebieden gedetecteerd, maar of het zich in het ijs of in het gas vormt, is een onderwerp van significant debat. Dit hoofdstuk karakteriseert de IR-spectra en bandsterktes van puur en gemengd formamide in interstellaire ijsanalogen. Drie formamidebanden zijn geïdentificeerd als potentiële indicatoren in observationele ijsspectra. De laboratoriumspectra worden vergeleken met de 7,24 μm-band in spectra van protosterren en prestellaire kernen. Als formamide-ijs significant bijdraagt aan de waargenomen band, is dit waarschijnlijker in een water-rijke polaire ijsmatrix, maar andere moleculen zorgen voor betere fits en zijn waarschijnlijker de hoofddragers. Bovengrenzen variërend van 0,35-5,1% ten opzichte van H_2O werden berekend, wat in overeenstemming is met de hoeveelheid formamide in zowel de gasfase bij protosterren als in kometen.

Conclusies en toekomstige richtingen

- HDO-ijs kan nu robuust gedetecteerd worden in stervormingsgebieden met JWST. Overeenkomsten tussen de D/H-verhoudingen van water in ijs en gas gemeten bij protosterren en de D/H-verhouding van watergas gemeten bij schijven suggereren dat interstellair ijs wordt overgeërfd van protostellaire omhulsels naar protoplanetaire schijven.

- Vergelijkingen tussen D/H-waarden van water in protostellaire ijzen en de coma van kometen suggereren ofwel een zekere mate van waterherverwerking in de gasfase in de protoplanetaire schijf, *of* een omgevingsgestuurde diversiteit in D/H-waarden van prestellair waterijs tussen verschillende stervormingsgebieden in ons sterrenstelsel.

- Tot $\sim$20% van het zwavel in dichte stervormingsgebieden kan opgesloten zitten in zouten zoals NH_4SH, wat mogelijk het decennialange raadsel oplost waarom H_2S niet wordt gedetecteerd in interstellaire ijzen ondanks voorspellingen uit chemische modellen.

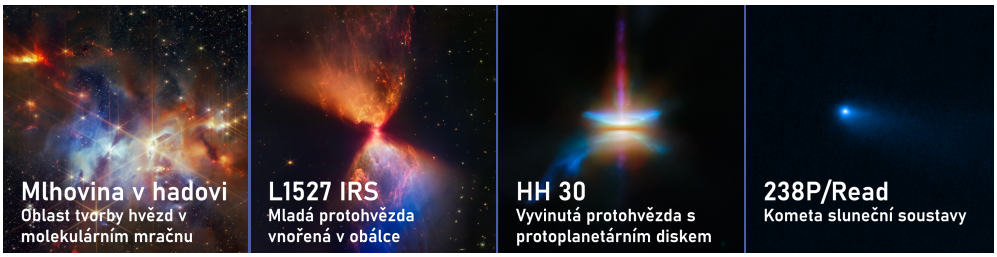
- Gezien hun hogere desorptietemperaturen ten opzichte van hun neutrale zuur-base tegenhangers, hebben zouten zoals NH_4SH mogelijk het transport van de vluchtige elementen N en S naar het binnenste deel van ons zonnestelsel vergemakkelijkt, waar ze

uiteindelijk opgenomen konden worden door lichamen die rijk zijn aan vluchtige verbindingen zoals koolstofhoudende planeto{iden.

- Zelfs met JWST is het wellicht niet mogelijk om de absorptiekenmerken van veel van de minder abondante en minder vluchtige complexe organische moleculen zoals formamide ondubbelzinnig te detecteren, vanwege overlappende absorptiebanden van meer overvloedige en vluchtige organische stoffen.

Vooruitkijkend zal een grotere steekproef van ijs-water-D/H gemeten bij protosterren in verschillende omgevingen nodig zijn om de ijs-water-D/H-verhouding die door ons zonnestelsel is overgeërfd beter te begrijpen. Bovendien blijft een groot deel van het interstellaire zwavel nog steeds vermist. Als het zich in mineralen of allotropen bevindt, zijn de kansen op directe detectie van dergelijke deeltjes niet veelbelovend. Maar waar deze ontbrekende zwavel zich ook bevindt, het is tijd voor een hernieuwd onderzoek naar zwavelijs met JWST-gegevens om eerdere beperkingen te herzien. De laboratoriumgegevens gepresenteerd in dit proefschrift maken dergelijke onderzoeken mogelijk. En tot slot: waarnemingen van gezichtslijnen met lage ijs-tot-stof-verhoudingen maar hoge stofkolommen (*d.w.z.* protostellaire omhulsels die thermisch of energetisch sterk zijn beinvloed) kan betere mogelijkheden bieden voor het identificeren van minder vluchtige ijsdeeltjes, waarvan de absorpties doorgaans worden overschaduwd door de sterke absorpties van meer abondante vluchtige stoffen.

České shrnutí



Obrázek 1: Čtyři kosmické objekty zachycené Vesmírným dalekohledem *Jamese Webba* (JWST), které představují různé fáze sekvence formování hvězd a planet. Všechna jejich spektra poukazují na chemické složení bohaté na ledové těkavé látky. Kredit snímků: NASA/ESA/CSA/STScI a zleva doprava: 1. Klaus Pontoppidan (NASA-JPL)/Joel Green (STScI). 2. Joseph DePasquale (STScI)/Alyssa Pagan (STScI)/Anton Koekemoer (STScI). 3. Ryo Tazaki et al. 4. Mike Kelley/Henry Hsieh (PSI)/Alyssa Pagan (STScI).

Hluboko ve vzdáleném mezihvězdném prostředí jsou mračna plynu a mikroskopických prachových zrn tvarována fyzikálními procesy do vířících sítí pilířů, globulí a filamentů. Nejhutnější oblasti těchto mračen jsou z velké části odstíněny od okolního mezihvězdného záření, což vytváří výjimečně chladné a temné podmínky, které jsou – možná paradoxně – ideální pro chemické reakce. Ochlazování prachových zrn uvnitř těchto mračen z nich činí katalytické povrchy; plynné částice na nich ulpívají a následně spolu reagují, čímž vytvářejí nepřeberné množství těkavých biogenních molekul v podobě ledových vrstev, které rostou na povrchu prachových zrn.

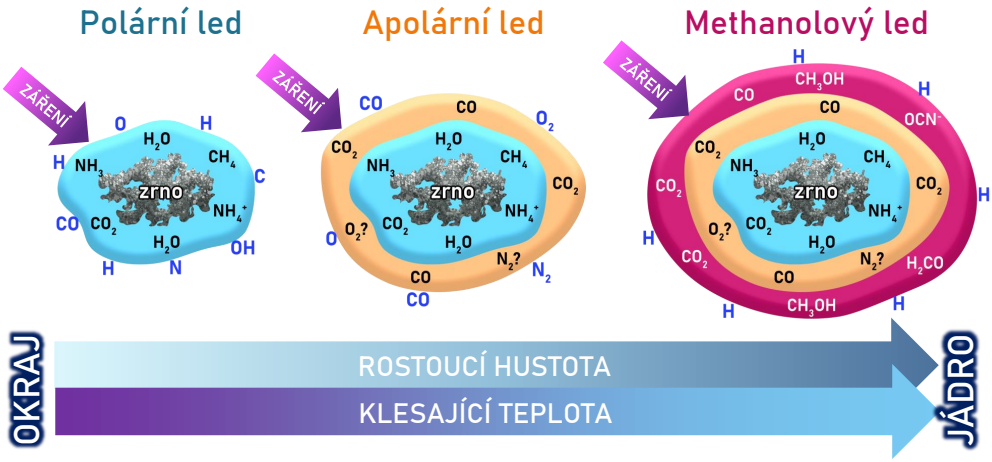
Nejhojnější z těchto molekul je voda, která vzniká v těchto temných a prašných podmínkách obzvláště účinně. V těchto ledech však lze nalézt i řadu dalších látek, jako je methanol, formaldehyd a amonné soli. Časem se prachové mračno může v důsledku vlastní gravitace zhroutit, což umožní, aby v jeho centru začala vznikat *protohvězda*. Ledové prachové částice z mračna – nyní obohacené o těkavé molekuly – následně sytí rostoucí hvězdu a okolní protoplanetární disk, ve kterém se formují její planety. Tímto způsobem se ledy vzniklé v mezihvězdných prachových mračnech stávají jednou z primárních složek planetárních systémů a slouží jako klíčový zdroj biogenních těkavých látek během formování planet.

Práce předložená v této disertaci zkoumá 1) chemii, která probíhá v mezihvězdných ledech během těchto nejranějších fází vývoje hvězd a planet, a 2) způsob, jakým tato chemie připravuje půdu pro vznik slunečních soustav, jako je ta naše, a pro distribuci těkavých látek v nich. K tomuto účelu využívá infračervenou (IR) spektroskopii v kombinovaném experimentálním a observačním přístupu, kdy jsou data získaná v pozemských laboratořích simulujících mezihvězdné podmínky využívána k analýze mezihvězdných spekter pozorovaných výkonnými IR zařízeními, jako je Vesmírný dalekohled *Jamese Webba* (JWST) a jeho předchůdci. Předkládané studie se zaměřují především na molekuly, které byly detekovány v primitivních malých tělesech sluneční soustavy bohatých na těkavé látky – zejména v kometách –, s cílem posoudit chemickou souvislost mezi mezihvězdným prostředím a planetárními systémy.

Chemie ledu během formování hvězd a planet

Chemické složení mezihvězdného prostředí (ISM) se skládá převážně z vodíku a určitého množství atomů helia vzniklých fúzí krátce po velkém třesku. Hmota vyvržená do vesmíru z explodujících hvězd navíc dodává stopová množství těžších prvků, jako je uhlík, dusík, kyslík, síra a křemík, a to ve formě atomů, iontů a mikroskopických zrn vysoce radiačně odolných molekul, jako jsou polycyklické aromatické uhlovodíky (PAH) a silikátové minerály.

Tato zrna odstiňují, absorbují a rozptylují mezihvězdné záření a katalyzují reakce na svém povrchu, čímž ochlazují své okolí a umožňují chemické reakce. V nejhustších oblastech mezihvězdných prachových mračen mohou teploty klesat až na 10 K (-263,15 °C). Při těchto teplotách tvoří plynné atomy a molekuly, které ulpívají na zrnech, vrstvy ledů. Vysoké zastoupení a mobilita atomů vodíku na povrchu těchto zrn vede k produkci redukovaných forem látek, jako jsou H_2O, CH_4 a NH_3, přičemž voda je zdaleka nejhojnější. Látky kyselé povahy mohou reagovat se zásaditým NH_3 za vzniku amonných solí, jako jsou NH_4SH a NH_4OCN. Organické molekuly jako H_2CO a CH_3OH mohou vznikat také hydrogenací CO, který na zrna vymrzá z plynné fáze. Během vývoje mračna dominují chemii ledu v různých fázích a místech různé látky, což vede k chemické stratifikaci (vznik vrstev s rozdílným chemickým složením) v rámci ledových vrstev vytvořených během existence mračna (Obr. 2). Konkrétně ledové vrstvy bohaté na vodu vznikají převážně v raných, méně hustých fázích mračna, zatímco ledové vrstvy bohaté na CO a jeho produkty, jako je CH_3OH, vznikají v pozdějších, hustších fázích.

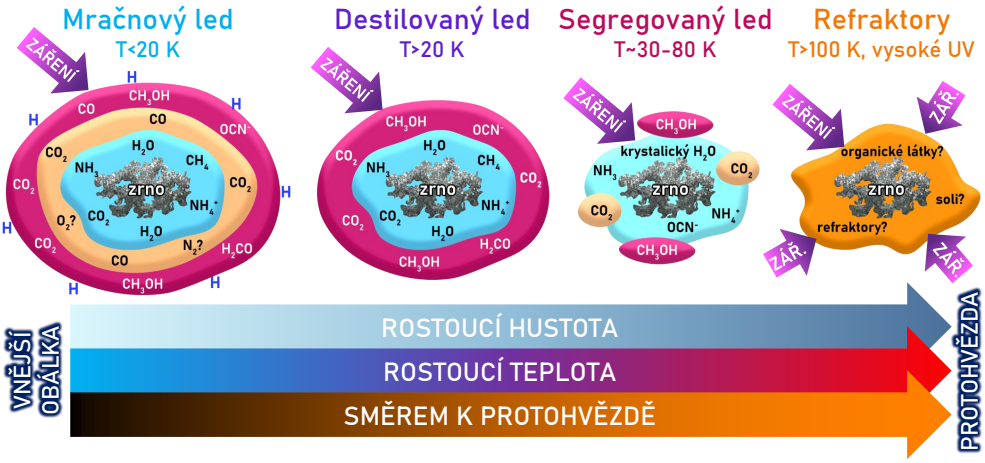


Obrázek 2: Různé fáze růstu ledu v molekulárních mračnech. V prvních vrstvách ledu, které vznikají v méně hustých, translucentních (poloprůsvitných) oblastech blíže k okrajům mračna, se tvoří H_2O, CO_2 a hydrogenované sloučeniny jako NH_3 a CH_4. S rostoucí hustotou klesají teploty, což umožňuje růst apolární vrstvy s převahou CO a CO_2. V nejhustších oblastech dochází k účinné hydrogenaci CO za vzniku CH_3OH, což vede k vytvoření vrstvy bohaté na CH_3OH, která zahrnuje i další látky vzniklé z CO, jako jsou CO_2, OCS a OCN^-.

Pokud je molekulární mračno dostatečně hmotné a husté, mohou gravitační nestability a turbulence vyvolat jeho gravitační kolaps, čímž započne tvorba protohvězdného jádra. Rodící

se protohvězda prochází evoluční sekvencí, která končí vznikem hvězdy a někdy i planet. Nejprve materiál z molekulárního mračna sytí centrální zdroj a gravitační potenciální energie se při kolapsu materiálu přeměňuje na energii tepelnou, která zahřívá okolní obálku materiálu. Jak protohvězda pokračuje v akreci okolního materiálu z obálky, zákon zachování momentu hybnosti vede k výtokům akreovaného materiálu z pólů zdroje a také ke zploštění vnitřní části obálky do *protoplanetárního disku*. Hmota v disku se začíná shlukovat do větších těles, což značí počátky planetárního formování. Nakonec je materiál obálky zcela vyčerpán výtoky a akrecí, přičemž zůstává pouze disk a centrální hvězda před hlavní posloupností. Nakonec je i materiál disku vyčerpán větry z disku a akrecí centrálním zdrojem nebo planetesimálami v disku.

Ledy z fáze molekulárního mračna jsou zděděny protohvězdnou obálkou a diskem, kde se mohou transformovat prostřednictvím různých fyzikálních procesů (Obr. 3). Jedním z procesů, které jsou pro tuto transformaci nejpodstatnější, je desorpce ledových složek do plynné fáze, která se řídí molekulárními *sněžnými čarami* (snowlines): tepelnými hranicemi, které definují oblasti, kde jsou teploty v obálce nebo disku dostatečně vysoké na to, aby specifické druhy ledu sublimovaly.



Obrázek 3: Změny v chemii ledu během zpracování v protohvězdných obálkách a protoplanetárních discích. V nejchladnějších oblastech obálek a disků struktura ledu odpovídá strukturám pozorovaným v molekulárních mračnech. Jak se ledy přesouvají do teplejších oblastí, hyper-těkavé látky desorbují do plynné fáze, čímž dochází k destilaci ledu. Ještě vyšší teploty způsobují segregaci určitých látek v rámci ledové matice a krystalizaci amorfních ledů. Předpokládá se, že po překročení 100 K většina těkavých ledů desorbovala do plynu, přičemž na zrnu zůstaly odolnější (refraktorní) látky, jako jsou soli a větší komplexní organické molekuly.

V mladších a chladnějších protohvězdných obálkách, stejně jako v nejchladnějších, nejvzdálenějších oblastech vyvinutějších obálek a v chladných středových rovinách (midplanes) protoplanetárních disků, zůstávají ledy z molekulárních mračen z velké části nedotčeny. Jak se ledy přesouvají do teplejších oblastí, překračují molekulární sněžné čáry v pořadí podle klesající těkavosti, čímž dochází k efektivní *destilaci* ledových vrstev, jak různé složky desorbují do plynné fáze, kde mohou dále reagovat s jinými plynnými látkami. Předtím, než vyvolají

desorpci, zvyšují vyšší teploty také mobilitu látek uvnitř ledů, což vede k restrukturalizaci ledové matice. Zvýšená mobilita může navíc zvýšit rychlost reakcí zahrnujících těžší částice.

Sněžné čáry v protoplanetárních discích jsou klíčovým faktorem, který částečně určuje složení planetárních objektů na základě místa jejich vzniku v disku. Daná látka může být akreována planetesimálami, které vznikají vně sněžné čáry této látky, takže výchozí materiál tvořící planetární těleso bude záviset na tom, kde se toto těleso nachází v protoplanetárním disku vzhledem k molekulárním sněžným čárám. Tento počáteční chemický záznam je následně pozměněn změnami sněžných čar během vývoje disku, dynamickým rozptylem planetárních objektů do různých oblastí disku a geologickými, atmosférickými procesy a procesy vesmírného zvětrávání, kterým planetární tělesa podléhají.

Má se za to, že malá tělesa bez atmosféry vzniklá v nejvzdálenějších oblastech sluneční soustavy obsahují jedny z nejvíce původních záznamů o těkavých látkách zděděných z mezihvězdných ledů, protože jejich malá velikost vylučuje významné geologické nebo atmosférické zpracování a místo jejich vzniku v chladné vnější sluneční soustavě jim umožnilo uchovat si těkavé látky i po jejich zformování. Primárním příkladem jsou komety; srovnání jejich zásob těkavých látek se zásobami v mezihvězdných ledech a protohvězdných plynech odhalilo některé pozoruhodné podobnosti. Systematické rozdíly mezi kometárním a mezihvězdným chemickým složením však také poukazují na to, že kometární materiál prošel alespoň určitým stupněm chemického zpracování v rámci protoplanetárního disku.

Infračervená spektroskopie ledů

Molekuly absorbují nebo emitují světlo prostřednictvím přechodů mezi svými kvantovanými energetickými stavy. Molekuly ve vesmíru lze identifikovat a kvantifikovat pomocí jejich jedinečných emisních nebo absorpčních prvků v teleskopických spektrech. Chemie ledu popsaná v této práci je odhalována pomocí absorpčních prvků v infračervených (IR) vlnových délkách, které zkoumají vibrační energetické přechody.

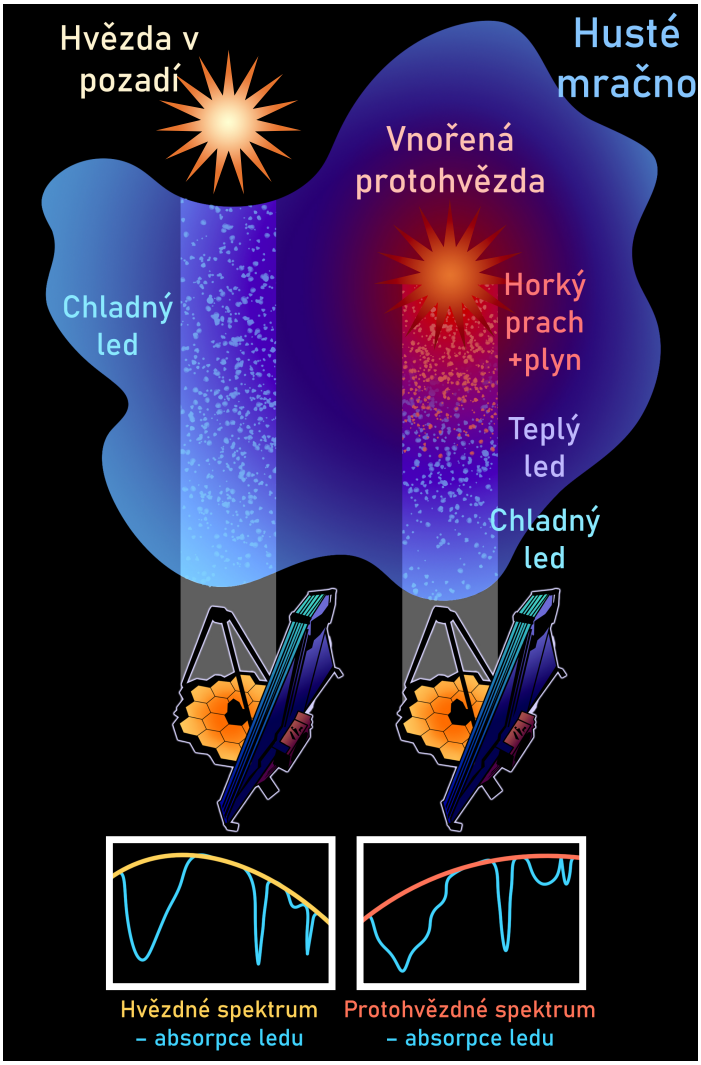
Pozice, tvary a intenzity IR absorpčních vrcholů (peaků) pozorovaných směrem k mezihvězdným oblastem obsahují informace o chemické identitě, množství a fyzikálním a chemickém prostředí mezihvězdných ledů. Získávání těchto informací vyžaduje integrovaný přístup, v němž jsou pozorování porovnávána s modely využívajícími laboratorní data.

Pozorovací metody

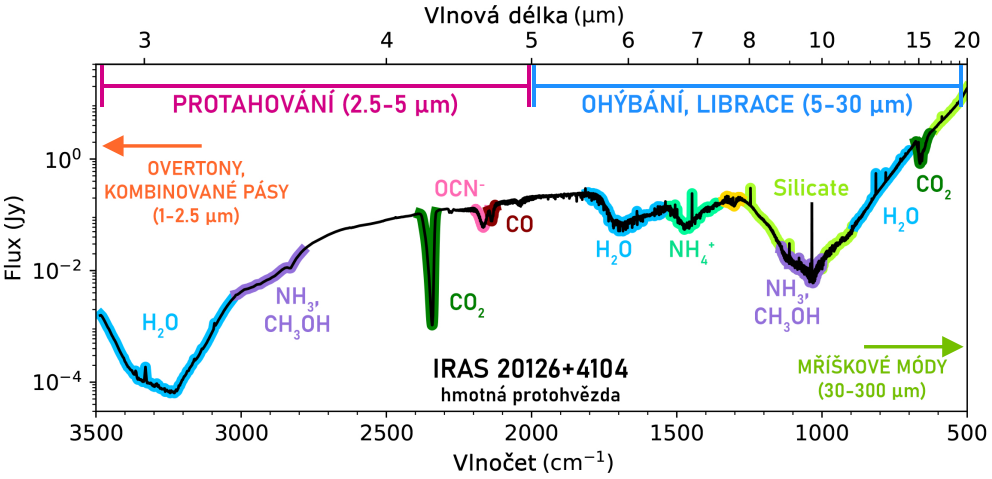
Obr. 4 poskytuje schéma pozorovací geometrie používané k získávání spekter mezihvězdného ledu. Dalekohled je zaměřen na zdroj IR záření, kterým může být buď hvězda v pozadí nacházející se za mezihvězdným mračnem, nebo protohvězda, která je v mračnu vnořena. Látky nacházející se podél zorné přímky od světelného zdroje k dalekohledu jsou pak pozorovány proti (proto)hvězdnému kontinuu (elektromagnetické záření). Velká část pozorovacích údajů použitých v této práci byla shromážděna pomocí JWST, který má ve srovnání s většinou předchozích IR dalekohledů vynikající citlivost, vlnový rozsah a spektrální i prostorové rozlišení. Příklad spektra mezihvězdných ledů pozorovaných pomocí JWST směrem k protohvězdě je uveden na Obr. 5.

Konkrétní molekulu lze v mezihvězdném IR spektru identifikovat nebo jí „přiřadit“ (assign), pokud jsou pozorovány její charakteristické IR rysy definované pomocí kontrolovaných

laboratorních experimentů nebo teoretických kvantových výpočtů. Přiřazení lze potvrdit porovnáním toho, jak těsně tvary vrcholů a vlnové délky odpovídají laboratorním datům. Po přiřazení lze IR vrchol použít ke kvantifikaci molekul podél zorné přímky. Kromě toho lze tvary vrcholů využít k odvození fyzikálních a chemických vlastností jejich ledových nosičů.



Obrázek 4: Schéma toho, jak dalekohledy pozorují absorpční rysy mezihvězdných ledů v hustých mračnech a protohvězdných obálkách. Ledy jsou pozorovány podél úzkého svazku (tzv. pencil beam), který sleduje dráhu od zdroje IR záření (buď zastíněné hvězdy v pozadí, nebo protohvězdy) k dalekohledu.



Obrázek 5: Příklad IR spektra masivní protohvězdy (IRAS 20126+4104) ukazující absorpční rysy mezihvězdného ledu a prachu na protohvězdném kontinuu.

Laboratorní metody

Laboratorní měření poskytují experimentální data, která jsou nezbytná pro interpretaci pozorování ledu. V takových experimentech jsou analogy mezihvězdného ledu nanášeny na kryogenně chlazený plochý substrát v ultravakuové komoře s typickými tlaky řádu $\leq 10^{-8}$-10^{-10} mbar (až bilionkrát nižšími než standardní atmosférický tlak na Zemi). Výsledný v laboratoři vypěstovaný led je fyzikální aproximací ledových vrstev na povrchu mezihvězdných prachových zrn. Následně jsou snímána laboratorní IR spektra těchto ledů, která lze v některých případech přímo porovnat s pozorováními ledu a identifikovat tak látky přítomné v ledech. Lze také vypočítat intenzity pásů (band strengths) ledových prvků, které lze použít ke kvantifikaci druhů ledu v pozorováních. Laboratorní práce prezentovaná v této disertaci byla provedena na zařízení Infrared Absorption Set-up for Ice Spectroscopy (IRASIS) v Leidenské laboratoři pro astrofyziku.

Přehled disertační práce

Infračervená spektroskopie opakovaně odhaluje, že mezihvězdné ledy jsou hostitelem bohaté chemie, která je základem pro vznik a transport těkavých látek v planetárních systémech. Nicméně v době zahájení této práce zůstávala řada otázek ohledně této chemie nezodpovězena: *Do jaké míry je mezihvězdný led zděděn a do jaké míry chemicky přepracován v protohvězdných obálkách a protoplanetárních discích před jeho akrecí do planetárních objektů? Které látky jsou hlavními rezervoáry síry v nejhustších fázích formování hvězd? Které z mnoha komplexních organických molekul detekovaných v plynné fázi u protohvězd lze nalézt také v ledech a co nám to říká o historii jejich vzniku?* Kapitoly této práce se těmito otázkami zabývají.

Kapitola 2: Tato práce představuje první spolehlivou detekci vibračního módu natahování

vazby O-D v ledu HDO na vlnové délce 4,1 μm pomocí dalekohledu JWST. Dále předkládá metodu pro kvantifikaci poměru ledu HDO/H2O směrem k protohvězdám a používá tuto metodu ke zjištění tohoto poměru u dvou masivních protohvězd pozorovaných pomocí JWST. U těchto dvou zdrojů byly získány poměry ledu HDO/H2O ve výši $4{,}6\pm1{,}8\times10^{-3}$ a $2{,}6\pm1{,}2\times10^{-3}$. Tyto poměry jsou podobné nejvyšším uváděným poměrům plynného HDO/H_2O naměřeným u masivních protohvězd a horkých vnitřních oblastí izolovaných protohvězd o nízké hmotnosti, což naznačuje, že alespoň některé poměry plynného HDO/H_2O naměřené v masivních horkých jádrech odpovídají poměrům v ledech.

Kapitola 3: Tato práce uvádí první detekci spektrálního rysu ledu HDO na 4,1 μm pomocí JWST u sluneční protohvězdy nízké hmotnosti, L1527 IRS. Metoda vyvinutá v kapitole 2 je zde použita k měření poměru HDO/H_2O v ledu s hodnotou $4{,}4^{+3{,}7}-1{,}7\times10^{-3}$, což je podobné poměrům HDO/H_2O v plynu naměřeným v teplých vnitřních jádrech jiných obálek protohvězd nízké hmotnosti a protoplanetárních disků v obdobně izolovaných oblastech tvorby hvězd. Tato podobnost předběžně podporuje předpoklad, že vodní pára detekovaná v těchto oblastech není po sublimaci ledu významně měněna reakcemi v plynné fázi. Podporuje také hypotézu, že pre- a protohvězdný vodní led je do vnějších protoplanetárních disků z velké části zděděn v chemicky nezměněném stavu. Tento podíl je však přibližně 4-10krát vyšší než poměry HDO/H_2O v plynu naměřené u komet a protohvězd nízké hmotnosti v hustých hvězdokupách, což může být způsobeno přepracováním plynné vody v obálkách a discích nebo rozdíly mezi prehvězdnými podmínkami izolovaných jader a oblastmi s tvorbou hvězdokup, které jsou spíše podobné prostředí, v němž vzniklo naše Slunce.

Kapitola 4: Byla získána laboratorní IR spektra a intenzity pásů ledů obsahujících sůl NH_4SH za účelem výzkumu, zda by NH_4SH mohl být hlavním rezervoárem síry a nosičem pásu 6,85 μm v mezihvězdných ledech. Laboratorní IR spektra byla porovnána se spektry čtyř protohvězd a dvou hustých mračen. Pozorovaný rys na 6,85 μm u těchto zdrojů dobře odpovídá laboratorním spektrům ledu NH_4SH:H_2O. Vypočtené sloupcové hustoty NH_4^+ se pohybují v rozmezí 8–23 % vzhledem k H_2O. Síla pásu rysu SH^- je pravděpodobně příliš nízká na to, aby byl tento rys detekovatelný, ale kombinační mód NH_4SH na 5,3 μm může představovat alternativní způsob detekce. Jeho předběžné přiřazení podporuje přítomnost solí NH_4^+ v ledech a je prvním předběžným pozorováním aniontu SH^- v mezihvězdných ledech. Pokud je většina ($\gtrsim$80-85%) kationtů NH_4^+ kvantifikovaných u zkoumaných zdrojů vázána na anionty SH^-, pak by soli NH_4SH mohly tvořit až 17-18% jejich celkového rozpočtu síry.

Kapitola 5: Tato kapitola poskytuje knihovnu nových laboratorních IR spekter a intenzit pásů OCS v ledových směsích bohatých na CH_3OH a CO, z nichž některé obsahují také H_2S a H_2O. Cílem je podpořit budoucí studie o zastoupení, fyzikálně-chemickém prostředí a evoluční historii mezihvězdného ledu OCS. Z těchto nových laboratorních spekter poskytují nejlepší shodu s pozorováním masivních protohvězd terciární směsi ledu OCS:CO:CH_3OH, což přináší další důkaz, že OCS vzniká společně s CH_3OH, pravděpodobně chemickými cestami zahrnujícími CO. Popsána je také kalibrační metoda hmotnostní spektrometrie pro přípravu ledových směsí s využitím plynů a kapalin s vysokým tlakem par.

Kapitola 6: Plynný formamid byl detekován v mnoha mezihvězdných oblastech, ale otázka, zda vzniká v ledu nebo v plynu, je předmětem velkých debat. Tato kapitola charakterizuje IR

spektra a intenzity pásů čistého a smíšeného formamidu v analozích mezihvězdného ledu. Tři pásy formamidu jsou identifikovány jako potenciální indikátory (tracery) v observačních spektrech ledu. Laboratorní spektra jsou porovnána s pásem na 7,24 μm ve spektrech protohvězd a prehvězdných jader. Pokud k pozorovanému pásu významně přispívá led formamidu, je pravděpodobnější, že se nachází v polární ledové matici; jiné druhy molekul však vykazují lepší shodu a je pravděpodobnější, že hlavními nosiči jsou ony. Byly vypočteny horní limity v rozmezí 0,35-5,1% vzhledem k H_2O, což je v souladu s hojností formamidu v plynné fázi u protohvězd i u komet.

Vědecký význam a budoucí směřování

- Led HDO je nyní díky JWST robustně detekovatelný v oblastech tvorby hvězd. Podobnosti mezi poměry D/H ve vodním ledu a plynu naměřenými u protohvězd a poměrem D/H v plynné vodě u protoplanetárních disků naznačují, že mezihvězdný led je děděn z protohvězdných obálek do protoplanetárních disků.
- Srovnání hodnot D/H ve vodě mezi protohvězdnými ledy a kometárními komami naznačuje buď určitou míru přepracování plynné vody v protoplanetárním disku, *nebo* diverzitu hodnot D/H v prehvězdném vodním ledu napříč různými oblastmi tvorby hvězd v naší galaxii, která je řízena okolním prostředím.
- Až ∼20% síry v hustých oblastech tvorby hvězd, jako jsou molekulární mračna a protohvězdné obálky, může být vázáno v solích typu NH_4SH. To potenciálně řeší desítky let trvající záhadu, proč není v mezihvězdných ledech detekován H_2S, přestože to chemické modely předpovídají.
- Vzhledem k jejich vyšším desorpčním teplotám v porovnání s jejich neutrálními acidobazickými protějšky mohly soli jako NH_4SH usnadnit transport těkavých prvků N a S do vnitřní sluneční soustavy, kde mohly být nakonec akreovány tělesy bohatými na těkavé látky, jako jsou uhlíkaté asteroidy.
- Ani s JWST nemusí být možné jednoznačně detekovat absorpční rysy mnoha méně hojných a polorefraktorních komplexních organických molekul, jako je formamid, a to kvůli překryvům s absorpcemi hojnějších a těkavějších organických látek.

Do budoucna bude zapotřebí větší vzorek měření D/H ve vodním ledu u protohvězd v různých prostředích, aby bylo možné lépe vymezit poměr D/H ve vodním ledu, který zdědila naše sluneční soustava. Velká část mezihvězdné síry navíc stále zůstává pohřešována. Pokud se nachází v minerálech nebo alotropech, vyhlídky na přímou detekci takových látek nejsou slibné. Avšak bez ohledu na to, kde se tato chybějící síra nachází, nastal čas pro nový průzkum ledů obsahujících síru s využitím dat z JWST, který by aktualizoval předchozí poznatky. Laboratorní data prezentovaná v této práci takové průzkumy umožňují. A konečně, zaměření pozorování na zorné přímky s nízkým poměrem ledu k prachu, ale vysokými sloupci prachu (*tj.* protohvězdné obálky, které jsou stále husté, ale byly silně tepelně nebo energeticky zpracovány), může poskytnout lepší příležitosti pro identifikaci refraktornějších stopových druhů ledu, jejichž absorpce jsou obvykle zastíněny silnými absorpcemi hojnějších těkavých látek.

Publications

Refereed publications as first author

1. *Laboratory infrared spectra and band strengths of carbonyl sulfide (OCS) in CH_3OH- and CO-rich ice mixtures for analyzing interstellar ice observations*
K. Slavicinska, C. Coone, B. Benz, H. Linnartz, A. C. A. Boogert, K. -J. Chuang. *ACS Earth & Space Chemistry*, 2025, 9(8), 2148-2158

2. *HDO ice detected toward an isolated low-mass protostar with JWST*
K. Slavicinska, Ł. Tychoniec, M. G. Navarro, E. F. van Dishoeck, J. J. Tobin, M. L. van Gelder, Y. Chen, A. C. A. Boogert, W. B. Dreschsler, H. Beuther, A. Caratti o Garatti, S. T. Megeath, P. Klaassen, L. W. Looney, P. J. Kavanagh, N. G. C. Brunken, P. Sheehan, W. J. Fischer. *The Astrophysical Journal Letters*, 2025, 986(2), L19

3. *Ammonium hydrosulfide (NH_4SH) as a potentially significant sulfur sink in interstellar ices*
K. Slavicinska, A. C. A. Boogert, Ł. Tychoniec, E. F. van Dishoeck, M. L. van Gelder, M. G. Navarro, J. C. Santos, P. D. Klaassen, P. J. Kavanagh, K. -J. Chuang. *Astronomy & Astrophysics*, 2025, 693, A146

4. *JWST detections of amorphous and crystalline HDO ice toward massive protostars*
K. Slavicinska, E. F. van Dishoeck, Ł. Tychoniec, P. Nazari, A. E. Rubinstein, R. Gutermuth, H. Tyagi, Y. Chen, N. G. C. Brunken, W. R. M. Rocha, P. Manoj, M. Narang, S. T. Megeath, Y. -L. Yang, L. W. Looney, J. J. Tobin, H. Beuther, T. L. Bourke, H. Linnartz, S. Federman, D. M. Watson, H. Linz. *Astronomy & Astrophysics*, 2024, 688, A29

5. *The hunt for formamide in interstellar ices: A toolkit of laboratory infrared spectra in astronomically relevant ice mixtures and comparisons to ISO, Spitzer, and JWST observations*
K. Slavicinska, M. G. Rachid, W. R. M. Rocha, K. -J. Chuang, E. F. van Dishoeck, H. Linnartz. *Astronomy & Astrophysics*, 2023, 677, A13

6. *Link between polycyclic aromatic hydrocarbon size and aqueous alteration in carbonaceous chondrites revealed by laser mass spectrometry*
K. Slavicinska, D. Duca, D. Egorov, T. Mitra, Y. Carpentier, C. Focsa, C. J. Bennett, C. Pirim. *ACS Earth & Space Chemistry*, 2022, 6(6), 1413-1428

Refereed publications as co-author

1. *JOYS: Launching and destruction of dust in protostellar jets. The case of BHR71-IRS1 with JWST/MIRI*
Ł. Tychoniec, L. Francis, M. G. Navarro, J. M. Vorster, E. F. van Dishoeck, K. Assani, V. J. M. Le Gouellec, B. Tabone, P. Klaassen, A. G. M. Janssen, K. Justtanont, D. Harsono, P. Nazari, S. Reyes, **K. Slavicinska**, C. Gieser, T. Bourke, Y. -L. Yang, B.

Nisini, T. Giannini, H. Beuther, R. Devaraj, T. P. Ray, N. G. C. Brunken, Y. Chen, M. L. van Gelder. *Astronomy & Astrophysics*, 2026, in press

2. *JOYS: Linking the molecular ice and gas phase composition toward the high-mass hot core IRAS 18089-1732*
C. Gieser, W. R. M. Rocha, Y. Chen, **K. Slavicinska**, E. F. van Dishoeck, P. Nazari, N. G. C. Brunken, L. Francis, H. Beuther, S. Reyes, A. Caratti o Garatti, P. D. Klaassen, J. M. Vorster, M. G. Navarro. *Astronomy & Astrophysics*, 2026, in press

3. *Investigating the nested structure of the outflow from the low luminosity protostar IRAS 16253-2429 using JWST and ALMA*
M. Narang, H. Tyagi, N. Ohashi, P. Manoj, S. T. Megeath, J. J. Tobin, E. F. van Dishoeck, N. J. Evans, D. M. Watson, A. Caratti o Garatti, J. K. Jørgensen, R. Gutermuth, Y. Aso, H. Beuther, L. W. Looney, D. A. Neufeld, G. Anglada, M. Osorio, A. E. Rubinstein, S. Federman, L. W. Hartmann, P. Nazari, N. Karnath, H. Linz, T. Stanke, T. L. Bourke, Y. -L. Yang, R. Kuiper, J. Green, P. Klaassen, W. Zakri, N. Habel, N. G. C. Brunken, J. Muzerolle, **K. Slavicinska**, A. M. Stutz, Ł. Tychoniec, S. Wolk, W. R. M. Rocha, W. J. Fischer. *The Astrophysical Journal*, 2026, 1000(2), 184

4. *IPA: Accretion rate of a low-mass class 0 protostar, measured via mid-IR fluorescent OH emission*
D. M. Watson, M. Narang, C. V. Pittman, H. Tyagi, R. Gutermuth, A. E. Rubinstein, N. J. Evans, L. W. Hartmann, S. T. Megeath, P. Manoj, C. C. Espaillat, N. Calvet, A. Caratti o Garatti, E. F. van Dishoeck, T. L. Bourke, J. D. Green, C. M. Lisse, P. Klaassen, L. W. Looney, P. Nazari, D. A. Neufeld, J. J. Tobin, S. J. Wolk, G. Anglada, P. Atnagulov, H. Beuther, N. G. C. Brunken, S. Federman, E. Furlan, N. Habel, N. Karnath, H. Linz, J. Muzerolle Page, M. Osorio, R. Pokhrel, R. Rahatgaonkar, W. R. M. Rocha, P. D. Sheehan, **K. Slavicinska**, T. Stanke, A. M. Stutz, Ł. Tychoniec, Y. -L. Yang, W. J. Fischer. *The Astrophysical Journal*, 2026, 999(2), 264

5. *JWST observations of segregated $^{12}CO_2$ and $^{13}CO_2$ ices in protostellar envelopes*
N. G. C. Brunken, A. C. A. Boogert, E. F. van Dishoeck, N. J. Evans, C. A. Poteet, **K. Slavicinska**, Ł. Tychoniec, P. Nazari, L. W. Looney, H. Tyagi, M. Narang, P. Klaassen, Y. -L. Yang, P. J. Kavanagh, S. T. Megeath, M. E. Ressler. *ACS Earth & Space Chemistry*, 2025, 9(8), 1992-2003

6. *JWST Observations of Young protoStars (JOYS): Overview of program and early results*
E. F. van Dishoeck, W. R. M. Rocha, **K. Slavicinska**, L. Francis, M. L. van Gelder, T. P. Ray, H. Beuther, A. Caratti o Garatti, N. G. C. Brunken, Y. Chen, R. Devaraj, V. C. Geers, C. Gieser, T. P. Greene, K. Justtanont, V. J. M. Le Gouellec, P. J. Kavanagh, P. D. Klaassen, A. G. M. Janssen, M. G. Navarro, P. Nazari, S. Notsu, G. Perotti, M. E. Ressler, S. D. Reyes, A. D. Sellek, B. Tabone, C. Tap, N. C. M. A. Theijssen, L. Colina, M. Güdel, Th. Henning, P. -O. Lagage, G. Östlin, B. Vandenbussche, G. S. Wright. *Astronomy & Astrophysics*, 2025, 699, A361

7. *JWST-IPA: Chemical inventory and spatial mapping of ices in the protostar HOPS 370 – Evidence for an opacity hole and thermal processing of ices*
H. Tyagi, P. Manoj, M. Narang, S. T. Megeath, W. R. M. Rocha, N. G. C. Brunken, A. E.

Rubinstein, R. Gutermuth, N. J. Evans, E. F. van Dishoeck, S. Federman, D. M. Watson, D. A. Neufeld, G. Anglada, H. Beuther, A. Caratti o Garatti, L. W. Looney, P. Nazari, M. Osorio, T. Stanke, Y. -L. Yang, T. L. Bourke, W. J. Fischer, E. Furlan, J. Green, N. Habel, P. Klaassen, N. Karnath, H. Linz, J. Muzerolle, J. J. Tobin, P. Atnagulov, R. Rahatgaonkar, P. Sheehan, **K. Slavicinska**, A. M. Stutz, Ł. Tychoniec, S. Wolk, W. Zakri. *The Astrophysical Journal*, 2025, 983, 110

8. *JWST Observations of Young protoStars (JOYS): Overview of gaseous molecular emission and absorption in low-mass protostars*
M. L. van Gelder, L. Francis, E. F. van Dishoeck, T. P. Ray, H. Beuther, A. Caratti o Garatti, Y. Chen, R. Devaraj, C. Gieser, K. Justtanont, P. J. Kavanagh, P. Nazari, S. Reyes, W. R. M. Rocha, **K. Slavicinska**, M. Güdel, Th. Henning, P. -O. Lagage, G. Wright. *Astronomy & Astrophysics*, 2024, 692, A197

9. *JOYS+ study of solid-state $^{12}C/^{13}C$ isotope ratios in protostellar envelopes: Observations of CO and CO_2 ice with the James Webb Space Telescope*
N. G. C Brunken, E. F. van Dishoeck, **K. Slavicinska**, V. J. M. le Gouellec, W. R. M. Rocha, L. Francis, Ł. Tychoniec, M. L. van Gelder, M. G. Navarro, A. C. A. Boogert, P. J. Kavanagh, P. Nazari, T. Greene, M. E. Ressler, L. Majumdar. *Astronomy & Astrophysics*, 2024, 692, A163

10. *JOYS+: link between ice and gas of complex organic molecules: Comparing JWST and ALMA data of two low-mass protostars*
Y. Chen, W. R. M. Rocha, E. F. van Dishoeck, M. L. van Gelder, P. Nazari, **K. Slavicinska**, L. Francis, B. Tabone, M. E. Ressler, P. D. Klaassen, H. Beuther, A. C. A. Boogert, C. Gieser, P. J. Kavanagh, G. Perotti, V. J. M. Le Gouellec, L. Majumdar, M. Güdel, Th. Henning. *Astronomy & Astrophysics*, 2024, 690, A205

11. *JOYS: Linked accretion and ejection in a Class I protobinary system*
Ł. Tychoniec, M. L. van Gelder, E. F. van Dishoeck, L. Francis, W. R. M. Rocha, A. Caratti o Garatti, H. Beuther, C. Gieser, K. Justtanont, H. Linnartz, V. J. M. Le Gouellec, G. Perotti, R. Devaraj, B. Tabone, T. P. Ray, N. G. C. Brunken, Y. Chen, P. J. Kavanagh, P. Klaassen, **K. Slavicinska**, M. Güdel, G. Östlin. *Astronomy & Astrophysics*, 2024, 687, A36

12. *Hunting for complex cyanides in protostellar ices with the JWST: A tentative detection of CH_3CN and C_2H_5CN*
P. Nazari, W. R. M. Rocha, A. E. Rubinstein, **K. Slavicinska**, M. G. Rachid, E. F. Van Dishoeck, S. T. Megeath, R. Gutermuth, H. Tyagi, N. G. C. Brunken, M. Narang, P. Manoj, D. M. Watson, N. J. Evans, S. Federman, J. Muzerolle Page, G. Anglada, H. Beuther, P. Klaassen, L. W. Looney, M. Osorio, T. Stanke, Y. -L. Yang. *Astronomy & Astrophysics*, 2024, 686, A71

13. *JWST observations of $^{13}CO_2$ ice: Tracing the chemical environment and thermal history of ices in protostellar envelopes*
N. G. C. Brunken, W. R. M. Rocha, E. F. Van Dishoeck, R. Gutermuth, H. Tyagi, **K. Slavicinska**, P. Nazari, S. T. Megeath, N. J. Evans II, M. Narang, P. Manoj, A. E. Rubinstein, D. M. Watson, L. W. Looney, H. Linnartz, A. Caratti o Garatti, H. Beuther,

H. Linz, P. Klaassen, C. A. Poteet, S. Federman, G. Anglada, P. Atnagulov, T. L. Bourke, W. J. Fischer, E. Furlan, J. Green, N. Habel, L. Hartmann, N. Karnath, M. Osorio, J. Muzerolle Page, R. Pokhrel, R. Rahatgaonkar, P. Sheehan, T. Stanke, A. M. Stutz, J. J. Tobin, Ł. Tychoniec, S. Wolk, Y. -L. Yang. *Astronomy & Astrophysics*, 2024, 685, A27

14. *JOYS: Detecting icy complex organic molecules and ions - I. CH_4, SO_2, $HCOO^-$, OCN^-, H_2CO, HCOOH, CH_3CH_2OH, CH_3CHO, CH_3OCHO, and CH_3COOH*
W. R. M. Rocha, E. F. Van Dishoeck, M. E. Ressler, M. L. Van Gelder, **K. Slavicinska**, N. G. C. Brunken, H. Linnartz, T. P. Ray, H. Beuther, A. Caratti o Garatti, V. Geers, P. J. Kavanagh, P. D. Klaassen, K. Justtanont, Y. Chen, L. Francis, C. Gieser, G. Perotti, M. Barsony, L. Majumdar, V. J. M. Le Gouellec, L. E. U. Chu, B. W. P. Lew, Th. Henning, G. Wright. *Astronomy & Astrophysics*, 2024, 683, A124

15. *JOYS: MIRI/MRS spectroscopy of gas-phase molecules from the high-mass star-forming region IRAS 23385+6053*
L. Francis, M. L. van Gelder, E. F. van Dishoeck, C. Gieser, H. Beuther, Ł. Tychoniec, G. Perotti, A. Caratti o Garatti, P. J. Kavanagh, T. Ray, P. Klaassen, K. Justtanont, H. Linnartz, W. R. M. Rocha, **K. Slavicinska**, M. Güdel, Th. Henning, P. -O. Lagage, G. Östlin. *Astronomy & Astrophysics*, 2024, 683, A249

16. *IPA. Class 0 protostars viewed in CO emission using JWST/NIRSpec*
A. E. Rubinstein, N. J. Evans, H. Tyagi, M. Narang, P. Nazari, R. Gutermuth, S. Federman, P. Manoj, J. D. Green, D. M. Watson, S. T. Megeath, W. R. M. Rocha, N. G. C. Brunken, **K. Slavicinska**, E. F. van Dishoeck, H. Beuther, T. L. Bourke, A. Caratti o Garatti, L. Hartmann, P. Klaassen, H. Linz, L. W. Looney, J. Muzerolle, T. Stanke, J. J. Tobin, S. J. Wolk, Y. -L. Yang. *The Astrophysical Journal*, 2024, 974, 112

17. *Discovery of a collimated jet from the low-luminosity protostar IRAS 16253-2429 in a quiescent accretion phase with the JWST*
M. Narang, P. Manoj, H. Tyagi, D. M. Watson, S. T. Megeath, S. Federman, A. E. Rubinstein, R. Gutermuth, A. Caratti o Garatti, H. Beuther, T. L. Bourke, E. F. van Dishoeck, N. J. Evans, G. Anglada, M. Osorio, T. Stanke, J. Muzerolle, L. W. Looney, Y. -L. Yang, P. Klaassen, N. Karnath, P. Atnagulov, N. G. C. Brunken, W. J. Fischer, E. Furlan, J. Green, N. Habel, L. Hartmann, H. Linz, P. Nazari, R. Pokhrel, R. Rahatgaonkar, W. R. M. Rocha, P. Sheehan, **K. Slavicinska**, A. M. Stutz, J. J. Tobin,Ł. Tychoniec, S. Wolk. *The Astrophysical Journal Letters*, 2024, 962, L16

18. *Investigating protostellar accretion-driven outflows across the mass spectrum: JWST NIRSpec Integral Field Unit 3–5 m spectral mapping of five young protostars*
S. A. Federman, S. T. Megeath, A. E. Rubinstein, R. Gutermuth, M. Narang, H. Tyagi, P. Manoj, G. Anglada, P. Atnagulov, H. Beuther, T. L. Bourke, N. G. C. Brunken, A. Caratti o Garatti, N. J. Evans, W. J. Fischer, E. Furlan, J. D. Green, N. Habel, L. Hartmann, N. Karnath, P. Klaassen, H. Linz, L. W. Looney, M. Osorio, J. Muzerolle Page, P. Nazari, R. Pokhrel, R. Rahatgaonkar, W. R. M. Rocha, P. Sheehan, **K. Slavicinska**, T. Stanke, A. M. Stutz, J. J. Tobin, Ł. Tychoniec, E. F. van Dishoeck, D. M. Watson, S. Wolk, Y. -L. Yang. *The Astrophysical Journal*, 2024, 966, 41

19. *JOYS: Disentangling the warm and cold material in the high-mass IRAS 23385+6053 cluster*

C. Gieser, H. Beuther, E. F. van Dishoeck, L. Francis, M. L. van Gelder, Ł. Tychoniec, P. J. Kavanagh, G. Perotti, A. Caratti o Garatti, T. P. Ray, P. Klaassen, K. Justtanont, H. Linnartz, W. R. M. Rocha, **K. Slavicinska**, L. Colina, M. Güdel, Th. Henning, P. -O. Lagage, G. Östlin, B. Vandenbussche, C. Waelkens, G. Wright. *Astronomy & Astrophysics*, 2023, 679, A108

20. *JWST Observations of Young protoStars (JOYS): Outflows and accretion in the high-mass star-forming region IRAS 23385+ 6053*
H. Beuther, E. F. van Dishoeck, Ł. Tychoniec, C. Gieser, P. J. Kavanagh, G. Perotti, M. L. van Gelder, P. Klaassen, A. Caratti o Garatti, L. Francis, W. R. M. Rocha, **K. Slavicinska**, T. Ray, K. Justtanont, H. Linnartz, C. Waelkens, L. Colina, Th. Greve, M. Güdel, Th. Henning, P. -O. Lagage, B. Vandenbussche, G. Östlin, G. Wright. *Astronomy & Astrophysics*, 2023, 673, A121

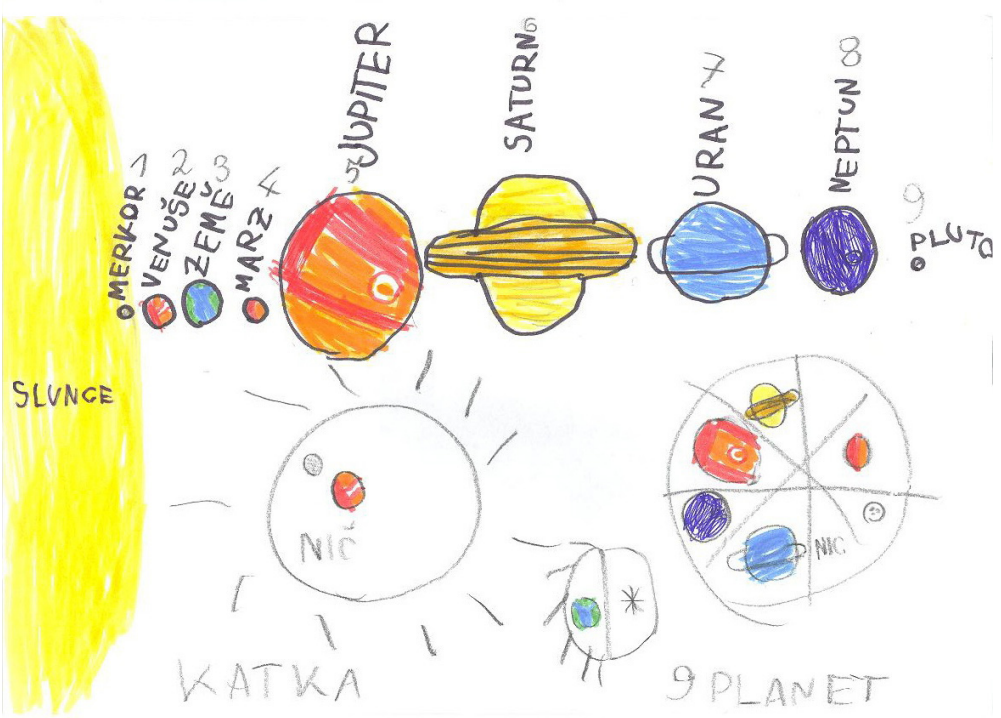
21. *Role of suprathermal chemistry on the evolution of carbon oxides and organics within interstellar and cometary ices*
B. C. Ferrari, **K. Slavicinska**, C. J. Bennett. *Accounts of Chemical Research*, 2021, 54, 1067-1079

Submitted publications as co-author

1. *CORINOS V: Radiative transfer effects in protostellar ice observations*
W. E. Thompson, J. B. Bergner, N. J. Evans, Y. -L. Yang, V. Kreft, L. Anderson, K. Pontoppidan, L. I. Cleeves, E. F. van Dishoeck, R. E. Gross, J. -E. Lee, M. K. McClure, N. Sakai, **K. Slavicinska**. *The Astrophysical Journal*, in press

2. *JOYS+: Analyses of OCN^-, N_2O, NO, and complex cyanides in ices. Thermal processing results in modest enhancement of OCN^- ice*
P. Nazari, N. Brunken, Y. Chen, **K. Slavicinska**, E. F. van Dishoeck, W. R. M. Rocha, A. C. A. Boogert, M. G. Navarro, V. J. M. Le Gouellec, L. Francis, Ł. Tychoniec, A. Caratti o Garatti, C. Gieser, T. P. Greene, P. J. Kavanagh. *Astronomy & Astrophysics*, accepted

3. *Probing the ubiquity of complex ices in protostars with JWST: the first systematic quantification of weak ice bands between 6.8 and 7.9 μm*
Y. Chen, E. F. van Dishoeck, **K. Slavicinska**, Ł. Tychoniec, M. L. van Gelder, L. Francis, A. C. A. Boogert, M. Narang, C. A. Schravendijk, H. Beuther, A. Caratti o Garatti, E. K. Eenhorst, C. Gieser, Th. Henning, M. Guedel, V. J. Le Gouellec, M. K. McClure, P. Nazari, S. Reyes, M. Tolman, Y. -L. Yang. *The Astrophysical Journal Letters*, under review



My first astronomical work (2003).

Curriculum vitae

I was born on January 15, 1997 in Brno, Czech Republic, a city infamous for its comically-shaped astronomical clock. Neither of my parents are astronomers or scientists, but my mother frequently took my brother and me to various public astronomy events in Brno. One of my earliest memories is a visit to the local planetarium, where we watched a movie about Pluto and received a booklet about the (back then) 9 planets of the solar system.

In 2004, my family immigrated to the United States. I did most of my schooling there, but my parents sent my brother and me back to the Czech Republic every summer to live with my grandparents. Eager to explore our new home, my parents also took my brother and me on road trips across the US, during which we visited the Kennedy and Johnson NASA centers. These visits cemented my early fascination with space, but this was only one of my many childhood obsessions – besides an affinity for science (especially chemistry), I also loved writing, visual art, music (I played the clarinet), and theater. As I grew older, I found myself approaching, with increasing stress, a critical crossroads: should I pursue a career in science, or the arts? Encouraged by the support of my high school science teachers, excellent performances in chemistry classes, and an internal pull, I enrolled in a chemistry BS with a physics minor at a college near my family, Kennesaw State University, in fall 2015. Simultaneously, I worked for my family's wedding photography business as a photographer's assistant, photo editor, and wedding album designer. I resolved to maintain high class loads each semester so that I could graduate early and save on college fees. I also worked various jobs throughout, including supplemental chemistry instructor, grocery store cake decorator, and waitress at a French café.

In my second freshman semester, I was eager to start applying the concepts I was learning in my classes to hands-on research. I approached Prof. Dr. Heather Abbott-Lyon to ask to join her research group in *astrochemistry*, which sounded like a perfect topic for my interests. Heather immediately put me to work, getting me trained on the ultrahigh vacuum (UHV) equipment in her lab. KSU had no chemistry PhD students or postdocs, so undergrads like me (and occasional master's students) ran the show in the lab. While such conditions are not optimal for a lab's productivity and output, I believe they are optimal for young students to develop an early sense of independence and empowerment. The Abbott Lab was also a part of the Center for Chemical Evolution (CCE), a consortium of groups from multiple universities studying the chemical origins of life. Being a CCE member gave me the opportunity to go on research visits to other labs at Georgia Tech and University of South Florida, where I worked with PhD students and postdocs and got a taste of what graduate school was like.

I quickly fell in love with research, astrochemistry, and UHV science, and I decided early on that I wanted to continue such research in graduate school. One of the first people I met in the Abbott Lab was a master's student, Danna Qasim, who went on to pursue a PhD in the Laboratory for Astrophysics (LfA) in Leiden University. Danna stayed in touch with me after leaving KSU, and after hearing from her what the LfA was like, I decided to make it my goal to work there one day. However, I also wanted to apply for US citizenship once I became eligible in 2018, and the application required that I continuously lived in the US until I was naturalized. So I devised a plan: I would apply for citizenship at the end of my bachelor's, get a US master's degree while waiting for naturalization, and then apply for a PhD in Leiden. In the meantime, I worked hard to become the perfect LfA PhD candidate. I spent every semester doing research in the lab, worked as a paid research assistant every summer, received several research awards and stipends, and presented at conferences all over

the US, including the Origins of Life Gordon Research Conference in 2018 thanks to a kind invite from CCE collaborator Prof. Dr. Matthew Pasek. I graduated with my BS after 3 years and spent what would have been my final BS year employed as a technician in the Abbott lab.

I filed my application for US citizenship the day I became eligible in November 2018. Around this time, Danna introduced me to Dr. Christopher Bennett at the University of Central Florida, who was looking for graduate students for his new astrochemistry lab. Chris was supportive of my plan and encouraged me to apply to the UCF PhD program and then master out, which would give me a flexible graduation timeline and a better stipend that would allow me to study without needing outside income. So in fall 2019, I entered UCF as a PhD student in physics on the planetary sciences track. In Chris's lab, I worked on a variety of projects, including electron irradiation of cosmic ice analogs and designing a UHV chamber for simulating space weathering of carbonaceous asteroids. Under the latter project, I applied for the NASA FINESST grant, one of the few NASA opportunities available to non-US citizen graduate students, and was awarded it. I also fell in love with Chris's other PhD student, Brian Ferrari (now my husband). Brian was supportive of my dream to go to Leiden and expressed interest in mastering out with me, but I figured there was little chance of two LfA PhD positions being open simultaneously and thus tabled my dream in favor of us being together.

In November 2020, I was finally naturalized as a US citizen. Then, in the spring of 2021, we heard the Leiden LfA was hiring two new PhDs. Given the timing, it seemed like a sign, so Brian and I reached out to Prof. Dr. Harold Linnartz to apply. He told us the positions had just been filled, but that another PhD position had opened for a combined laboratory and observational project to be co-supervised with Prof. Dr. Ewine van Dishoeck, along with an additional PhD opening in the theoretical chemistry group. Ultimately, we were offered and accepted these positions. During my final summer at UCF, I traveled to the University of Lille in France to work with Dr. Claire Pirim on a project analyzing PAHs in carbonaceous chondrite meteorites with a state-of-the-art two-step laser mass spectrometry setup. This work resulted in my first first-author publication, submitted right after I received my master's.

In January 2022, three weeks after the JWST launch, I fulfilled my dream and arrived in the Leiden LfA to conduct a PhD using laboratory and JWST data to analyze the chemical composition of interstellar ices. The PhD was co-supervised by Harold, Ewine, and eventually Dr. Ko-Ju Chuang following Harold's untimely passing in December 2023. Over the past four years, I have worked on a variety of experimental and observational projects that culminated in 5 first-author publications, 2 of which had accompanying press releases, and 20 co-author publications. I conducted experiments on the IRASIS setup and modified it in my final year to include a UV lamp and a quartz crystal microbalance. I learned how to propose for and analyze JWST observations and was awarded 36 total hours as PI of two JWST programs in cycles 3 and 4. I was a member of multiple JWST observing teams including JOYS+, IPA, and HEFE, and worked closely with external collaborators, including Dr. John Tobin at NRAO and Dr. Adwin Boogert at the University of Hawai'i at Manoa, whom I visited on a 2-week research trip. I presented my work in conferences and seminars in the Netherlands, Denmark, Germany, Italy, Spain, and 5 US states. I was also a teaching assistant for the Astronomical Spectroscopy course for 3 semesters and supervised the lab research projects of 4 bachelor students and 3 high school students. Following my defense, I will return to the US to explore the chemical links between interstellar and planetary ices as a Caltech Center for Comparative Planetary Evolution (^{3}CPE) Postdoctoral Fellow with Prof. Dr. Michael Brown.

Acknowledgments

The science in my PhD may have been conducted in physical vacuums, but it was not conducted in social ones. If I had to quantify all the support I have received throughout my life leading up to this milestone, it would be a *quadrillion* times higher than the $\sim 10^{-9}$ mbar vacuum of IRASIS – like the $\sim$1000 bar pressures in the deepest parts of the ocean.

I was lucky to have dedicated PhD advisors and mentors that also allowed me to forge my own path. Ewine: your devotion to your students is unbelievable – you truly embody leadership through service. Thank you for believing in me, holding me to high standards, and always finding time to talk about science. Ko-Ju: even before you formally became my advisor, you were always willing to guide me, discuss my ideas, and hear my frustrations over tea in your office. It was a privilege to work in the lab with you. Harold: I will always remember your kind and gentle nature, paper cakes, and funny stories. You were gone too soon. Adwin: getting to collaborate with someone whose work I admire and respect so much has been exhilarating. Thank you for engaging with my work and graciously hosting me in Hawai'i. John: thank you for entrusting me with your data, inspiring and supporting the HDO ice projects, and enriching my work with your gas expertise. Marina: when I was thrown into deep ends at the beginning of my PhD, you were there to swim alongside me and make sure I didn't drown. You are not only a brilliant scientist and mentor but also a deeply good person.

I also worked with incredible colleagues. Nashanty: when we're together, it's like we're simultaneously the stars and audience of a two-woman comedy-drama show. With you, dire situations turn into opportunities for camaraderie, reflection, and memes – I wouldn't have survived this PhD without you. Julia: you are such an immensely caring and supportive friend in so many ways. Our hangouts with you and Fabio made life in the Netherlands feel whole. Yuan: you are this brilliant combination of authentic, hilarious, and introspective that makes conversations with you delightful, whether they are about science or life. Łukasz: you were my gateway into the world of observations and are the reason my JWST programs exist. You are an incredibly devoted scientist. Thank you for all the patient explanations and passionate science chats. Logan: thanks for being down to bro out about regular science *and* bro science. Sierra: you have been both a role model and a friend – it means a lot to have someone to whom I can look up *and* relate. Jerry and Nienke: thank you for taking excellent care of Tina whenever Brian and I needed to get out of this country for some sun. Anita, Carlos, Domenik, Franciele, Helgi, Jeroen, Jessalyn, Julian, Lars, Laura, Lina, Pavi, Pranjal, Tara: I will fondly remember our lab scavenging sessions, setup jury-rigging, borrel drinks, and the riveting *Shrek de Musical* performance. Thanh, Milan, Cecilie, Pippa, Roshini: the future of the LfA is so bright in your hands. Alice, Andrés, Andrew, Giulio, Margot, Marissa, Martijn, Milou, Lisa, Lucas, Nico, Pooneh, Teresa, Will, Xunchuan: I loved learning about astronomy and traveling the world together. Bryce, Charlotte C, Femke, Daan, Charlotte S, Eyze, Mees: it was a joy to be a part of your journeys into science; I learned so much from working with you. Martijn and Robin: thank you for your mechanical work and building the QCM with me! Huib and Bram: you wrangled the most important tools I used in my PhD (and faced the horrors of Windows OS for me). Alina, Nancy, Somayeh, Robin: thank you for taking such great care of the institute and always helping me with a smile.

Before Leiden, many exceptional people helped me grow into the person I am today. Claire: you are such an astute problem solver, dedicated mentor, and one of my favorite people with whom I've ever worked. I aspire to be a scientist like you. Chris: thank you

for supporting my professional dreams. I hope the next chapter of your life brings you the peace and happiness you deserve. Joe: the skills your astrodata class taught me served as the foundation for all of my subsequent scientific work. Kerri: likewise, your observational astronomy course laid the foundation for my JWST work. Riley: it has been a blast meeting up in various corners of the world and always picking up right where we left off. Allison, Eric, Kenny, Alle, Brynn, Ryan, Jenny: you made our years at UCF memorable and fun.

Heather: you took me in as a curious undergrad freshman and turned me into a scientist. This thesis is a direct result of all the time and care you poured into mentoring me and nurturing my spirit during some of the most difficult years of my life. Stef: in addition to being an immensely shrewd and dedicated scientist, you are such a caring person. I was lucky to have met you in the ALL. TJ: I am grateful that I learned most of my UHV lab skills from someone so resourceful and *whimsical*. Danna: you were my first scientific role model and have been so instrumental throughout my research career. Thank you for all the support over the years. The CCE (especially Christine, Matt, Martin, David, Bradley): thank you for making me feel like a valued part of a research team even as a derpy undergrad. Jen Wallace: thank you for believing in my potential in the most angsty and erratic era of my life.

Dominique: you have been the longest-standing constant in my life over the past 13 years. I will always be down to help you carry your bags full of rocks (but I will *never* play Zoo again). Carmona-Ferrari and Brazilian friends family: I am so grateful to have married into such a loving family that immediately treated me as one of their own. Dědo a babičko: kdekoliv jsem byla ve světě, vždy jste mě podporovali. Děkuji za všechna společná léta, buchty, haldy ponožek a povzbudivé hovory přez skype. Jan: you are the only person who understands the unique microculture of our childhood, and you never fail to make me laugh. I'm so glad I grew up with you as my brother. Mummy: you are the strongest, most courageous, and most loving person I know. I was able to do this PhD because you nurtured my interests and raised me to feel free to live my life authentically, in the way that made me happiest. What a privilege it is to have received such a gift. Brian: meeting you was the greatest luck of my life. You push me to pursue my dreams, challenge me when I need it, and make me laugh until I cry. Without you, I wouldn't have made it to Leiden like I dreamed – this thesis is a result of your *promessa*, something I will always cherish.